Institute of Fundamental Technological Research
Polish Academy of Sciences

Doctoral Thesis

ANISOTROPY OF COMPOSITE MATERIAL PROPERTIES INDUCED BY MICROSTRUCTURE MOPRHOLOGY - MICROMECHANICAL AND NUMERICAL MODELLING IN NON-LINEAR REGIME

by

Kamil Krystian Bieniek

Supervisor:
Prof. Katarzyna Kowalczyk-Gajewska

Warsaw 2025

First and foremost, I am deeply grateful to my supervisor, prof. Katarzyna Kowalczyk-Gajewska, for her great amount of patience, empathy and strong support during the entire process of writing the thesis.

I want to thank colleagues at IPPT PAN, whose advice and contribution to the subject have been indispensable.

I acknowledge the financial support of Polish National Science Center within projects: OPUS NCN 2016/23/B/ST8/03418 and OPUS NCN 2021/41/B/ST8/03345, which this thesis was part of.

Last but not least, heartfelt thanks to my family and friends who supported and motivated me in all times.

Abstract

The thesis is focused on understanding the relation between microstructure morphological features, in particular spatial distribution of phases and anisotropy of macroscopic properties of heterogeneous materials. The main tool used for this purpose is a mean-field cluster model, originally proposed by Molinari & El Mouden (1996) for particulate composites. The goal of the thesis is to extend this semi-analytical scheme and provide its numerical verification in the non-linear regime of material response (elasto-plasticity and elasto-viscoplasticity), as well as to formulate computationally efficient procedures for applying this model in finding the optimal composite microstructure at the preliminary stage of material design process.

First, the performance of the cluster model is explored for a linear thermoelastic composites to identify its limitations. Computationally effective, closed-form formulas for finding the interaction tensor, which describes the impact of microstructure morphology in the model, are formulated for the most often used regular inclusion arrangements.

In case of elastic properties, the cluster model is verified with results of computational homogenisation performed using the finite elements method (FEM). It is demonstrated that the cluster model gives consistent results, with the impact of the microstructure on the anisotropy of the macroscopic material parameters correctly captured. The maximum applicable volume fraction of inhomogeneities for the cluster model is identified as $f_i = 40\%$. Additionally, a set of 3D-printed porous samples are employed for a limited experimental validation of the model. The results are in good qualitative agreement, especially showing the impact of porosity, microstructure type, as well as the similar effect of loading direction on the macroscopic Young's modulus. However, the quantitative assessment of real-life samples is significantly challenging, mainly due to inherent inaccuracy of 3D-printed geometries.

Extension of the cluster model to the elastic-plastic composites is performed with incorporation of three additional steps to the original scheme: linearisation, uniformisation and isotropisation. Stress fluctuations in the form of the second moments of stresses are introduced to the algorithm in a modified tangent linearisation. Results show that for the elastic-plastic case, the cluster model also gives consistent results with the finite element method, for both deviatoric and hydrostatic loading cases.

Multi-criteria optimisation procedures are proposed for composites working in the elastic and elastic-plastic regime. A time-efficient algorithm for finding the optimal microstructure, volume fraction of inclusions or material composition is developed. Performed analyses of many different scenarios shows the potential of the cluster model for initial stages of the design process of composite materials.

Following Kowalczyk-Gajewska et al. (2021), the extension of the cluster model to the elastic-viscoplastic cases, described by the additive Maxwell-type model and the non-linear Perzyna viscoplastic law for the matrix, is explored. It is shown that estimates strongly rely on the selected isotropisation method applied to the viscous tangent stiffness. Multiple isotropisation strategies are examined which hints that the model calibration in this respect should be performed at the beginning of the calculation process for the viscoplastic regime. By the FEM validation, the ranges of pure elasticity and advanced viscoplastic flow are assessed to be well represented in the cluster model. However, the transition from the elastic to viscoplastic regime is the most difficult range to estimate, requiring further adjustments in this field.

Additionally, a new geometrical morphology indicator is proposed, based on the concept of "boreholes", as a way to quantify macroscopic material anisotropy. Possible instabilities in sub-local level are explored for porous materials with a high volume fraction of voids.

Streszczenie

Niniejsza rozprawa koncentruje się na próbie zrozumienia związku pomiędzy cechami morfologicznymi mikrostruktury, w szczególności przestrzennego rozłożenia faz, a anizotropią makroskopowych właściwości materiałów niejednorodnych. Głównym narzędziem wykorzystanym w tym celu jest model klastra (ang. *cluster model*) - model pola średniego (ang. *mean-field*) zaproponowany pierwotnie przez Molinariego i El Moudena (Molinari & El Mouden, 1996) dla kompozytów typu osnowa-wtrącenie. Celem pracy jest rozwinięcie tego pół-analitycznego modelu mikromechanicznego i przeprowadzenie jego numerycznej weryfikacji w nieliniowym zakresie odpowiedzi materiału (sprężystoplastyczność oraz sprężysto-lepkoplastyczność), jak również sformułowanie efektywnych obliczeniowo procedur służących zastosowaniu tego modelu do znajdywania optymalnych microstruktur na wstępnych etapach procesu projektowania materiałów.

W celu zidentyfikowania ograniczeń modelu klastra, na samym początku zbadano jego działanie dla kompozytów w zakresie liniowej termosprężystości. Dla najczęściej wykorzystywanych regularnych układów wtrąceń sformułowane zostały zamknięte, wydajne obliczeniowo wzory na tensor interakcji, który opisuje wpływ morfologii mikrostruktury w modelu.

W zakresie sprężystym model klastra został poddany weryfikacji homogenizacją numeryczną przy użyciu metody elementów skończonych (MES). Wykazano, że model ten daje spójne wyniki, poprawnie odwzorowując wpływ mikrostruktury na anizotropię makroskopowych parametrów materiałowych. Maksymalny możliwy do zastosowania udział objętościowy wtrąceń dla modelu został zidentyfikowany jako $f_i = 40\%$. Ponadto, w ograniczonym zakresie, zestaw próbek otrzymanych techniką druku 3D został wykorzystany do doświadczalnej walidacji modelu. Wyniki wskazują na zgodność jakościową, zwłaszcza pod względem odwzorowania wpływu porowatości, typu mikrostruktury, jak również kierunku obciążenia na makroskopowy moduł Younga. Niemniej, zgodność ilościowa jest większym wyzwaniem głównie ze względu na nieuniknione błędy w procesie produkcji próbek.

Rozwinięcie modelu klastra do zakresu sprężystoplastycznego zostało przeprowadzone w trzech dodatkowych krokach względem oryginalnej procedury, mianowicie: linearyzacji, uniformizacji i izotropizacji. W proponowanej zmodyfikowanej linearyzacji stycznej zostały uwzględnione fluktuacje pola naprężeń poprzez tzw. "drugie momenty" (ang. *second moments of stress*). Otrzymane wyniki wskazują, że model klastra daje wartości zgodne z MES również dla zakresu sprężystoplastycznego, zarówno dla dewiatorowego, jak i hydrostatycznego układu obciążenia.

Zaproponowano procedury wielokryterialnej optymalizacji dla kompozytów pracujących w zakresie sprężystym i sprężystoplastycznym. Opracowano algorytm służący do znajdywania optymalnej mikrostruktury, udziału objętościowego wtrąceń oraz składu materiałowego, który cechuje się krótkim czasem obliczeń. Analizy przeprowadzone dla wielu różnych scenariuszy wskazują na potencjał modelu klastra do wykorzystania na pierwszych etapach procesu projektowania kompozytów.

Za Kowalczyk-Gajewska et al. (2021) przeanalizowano rozwinięcie modelu klastra do zakresu sprężystolepkoplastycznego, opisanego addytywnym modelem Maxwella oraz nieliniowym prawem lepkoplastycznym Perzyny dla osnowy. Otrzymane wyniki wskazują na silną zależność estymatorów od wybranej metody izotropizacji lepkiego modułu sztywności. Sprawdzono różne strategie izotropizacji, które wskazują na zasadność kalibracji modelu pod tym względem. Powinna być ona przeprowadzana na początku procesu obliczeniowego. Porównując z MES, można stwierdzić, że zakres czystej sprężystości oraz zaawansowanego płynięcia lepkoplastycznego są dobrze odzworowane w modelu klastra. Problematyczne jest zaś samo przejście między zakresem sprężystym a lepkoplastycznym, które wymaga dalszych udoskonaleń.

Zaproponowano nową metodę geometrycznego opisu morfologii mikrostruktury, opierającą się na koncepcji "odwiertów", jako sposób na skwantyfikowanie makroskopowej anizotropii materiału. Zbadano również możliwe niestabilności na poziomie sublokalnym dla porowatych materiałów o dużym udziale objętościowym pustek.

Contents

Chapter 1

Introduction

1.1 Motivation

Heterogeneity has always been a complicated topic in science and engineering, compared with the much simpler treatment of homogeneous materials. Steel, concrete and aluminium, for example, are widely used in many industries. Even though their real microstructures are heterogeneous, in the fields such as civil engineering (including official normatives and guidebooks), these materials are generally treated as homogeneous which massively simplifies the process of design making it easier and more time-effective. However, with the wider use of composites, polycrystalline and porous materials (examples shown in figure 1.1), with the possibilities of tailoring and designing microstructures opened by additive manufacturing, as well as with the demand for more accurate assessments of the material parameters, much more sophisticated theories and models were proposed in the last decades, dedicated to the description of the influence of material heterogeneity.

While the use of numerical homogenisation, in which the actual microstructure of a material can be directly subjected to mechanical analysis (e.g. with the finite elements method), seems to be the obvious choice at the present stage of development of computer technology, such a "brute force" approach is still relatively resource-inefficient and time-consuming. This is the reason for the continuing development of analytical solutions, such as the mean-field models. The use of quick analytical or semi-analytical computational tools allows for testing many scenarios (e.g. modifying parameters of phases, spatial distribution of inclusions or their volume fraction), understanding of the leading trends in the microstructure–property relationship and finding optimal solutions depending on the foreseen applications of a given composite. Thanks to short calculation times and ease of automation, many different scenarios may be tested efficiently. Examples are: finding the lowest weight of an element along with a sufficient level of stiffness, or choosing the best arrangement of inclusions for the highest level of thermal insulation. More complex approaches may also take into account applying an external load while overseeing stresses in different phases or include inclusion failure.

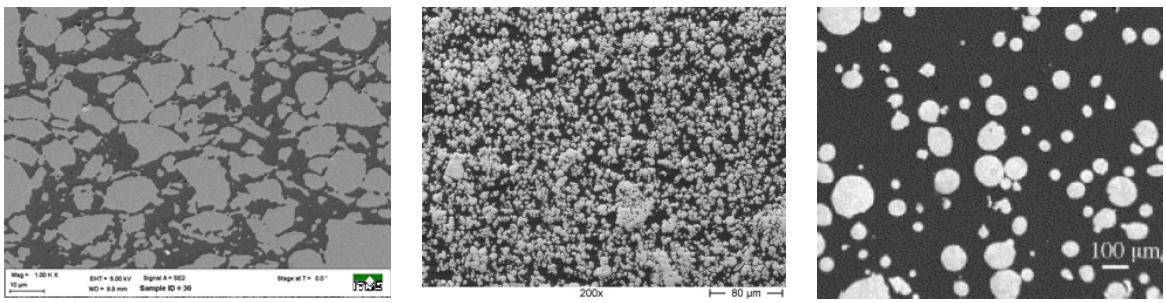

(a) (b) (c)

Figure 1.1: Microstructure images of composites: NiAl reinforced with Al_2O_3 (Majewski, 2019) (a); W-30 matrix reinforced with CuCr1Zr, reprinted from (Zivelonghi & You, 2014) with permission from Elsevier (b); Al matrix with TiAl inclusions of different sizes, reprinted from (Muñoz-Morris et al., 2006) with permission from Elsevier (c).

1.2 Literature review

Many different micromechanical mean-field models have been developed throughout the years to describe the relationship between microstructure of a composite material and its macroscopic properties. There are various existing micromechanical models, many of them based on the Eshelby solution (Eshelby, 1957). Eshelby's problem assumes a single ellipsoidal inclusion in an infinite linearly elastic medium, subjected to a homogeneous external load located at infinity. Among mean-field models originating from this fundamental solution, the Mori–Tanaka method is the most widely used for composite materials (Mori & Tanaka, 1973). In this model, the medium material is the matrix material, while the far-field values are replaced with the average fields in the matrix phase. The model assumes that a single inclusion interacts only with the surrounding matrix, while direct interactions between inclusions are neglected which limits the applicability of the model to relatively small volume fractions. The other possibilities are the self-consistent and generalised self-consistent models, or differential and incremental schemes (Nemat-Nasser & Hori, 1999). These methods differ between each other by specific definition of the properties of the infinite medium or by the way by which inclusion phase is embedded into the medium (see discussion in Kursa et al. (2018)).

Unfortunately, the above-mentioned classical models fail to describe properly the scale effects related to the inclusion size as well as their spatial distribution within the sample, which may be an important source of a material's anisotropy even if it is composed of isotropic phases. As an answer to these issues, more sophisticated models were proposed. Vilchevskaya et al. (2021) distinguished two classes of approaches to dealing with the effect of regular particle distribution: homogenisation models based on the one particle approximation; and analytical or semi-analytical solutions for periodic arrangements of identical inhomogeneities. As concerns the second class, the effect of regular particle distribution was first studied in the context of thermal conductivity. One of the very first contributions was given by Rayleigh (1892) and concerns a regular cubic lattice of spheres. Subsequently the issue was studied by McPhedran & McKenzie (1978); McPhedran et al. (1978) and Sangani & Acrivos (1982) who derived the overall thermal conductivity of a periodic array of spheres. Lu & Shih-Yuan (1999) and Mercier et al. (2000) additionally analysed the effect of the aspect ratio of the unit cell. As far as elastic properties are concerned, equivalent estimates of the effective properties of composite materials with regular inclusion arrangements were found analytically using different methods by Nemat-Nasser et al. (1982), Nunan & Keller (1984), Sangani & Lu (1987), Rodin (1993), Kushch (1997), Cohen (2004), Schjødt-Thomsen & Pyrz (2005) and Kushch et al. (2011).

Within the first class of methods, variational estimates accounting for the spatial distribution of inclusions were formulated by Ponte Castañeda & Willis (1995). The authors provided Hashin–Shtrikman-type estimates which, using two-point correlation functions, enable one to independently account for the shape and spatial distribution of inclusions. The results were restricted to the spatial correlations of an "ellipsoidal" form. Hu & Weng (2000) demonstrated that the proposed method delivers results similar to the ones obtained by the double inclusion model by Hori & Nemat-Nasser (1993) when the outer shape of the double inclusion is assumed to carry information about the inhomogeneity arrangements. A similar concept was discussed by Kanaun & Levin (2008) who introduced the so-called "spatial correlation zone" surrounding each inhomogeneity. Additionally, Sevostianov (2014) and Sevostianov et al. (2019) demonstrated that the Ponte Castañeda & Willis (1995) approach coincides with the Maxwell model in which the "effective inclusion" is identified with the correlation zone. In all the above approaches, the shape of this zone must be ellipsoidal which limits the anisotropy of the overall properties, that is induced solely by the particles' spatial distribution, to three symmetry classes corresponding to the symmetry group of the second-order tensor describing the shape of the effective ellipsoid: orthotropy, transverse isotropy and isotropy. Thus, for example, the cubic symmetry of elastic properties, which is induced by a regular array of spherical particles, cannot be accounted for by such approaches. This may also lead to the limited capability of those models to describe periodic composites, as concluded by Vilchevskaya et al. (2021).

The packing effect (but not the spatial distribution effect) can also be accounted for by the so-called morphologically representative pattern (MRP) approach developed in Bornert et al. (1996), Marcadon et al. (2007) and verified through comparison with numerical homogenisation in Majewski et al. (2017) and Majewski et al. (2020) for elastic and elastic–plastic composites, respectively. The MRP approach originates from the composite sphere Hashin model and its modification into the generalised self-consistent model by Christensen. The basic idea of the MRP approach is the description of a composite not with a representative volume element, but with multiple representative patterns with

a given volume fraction of inclusions. Additionally, each inclusion has a region of the matrix linked to it, described as an interphase region.

Finally, there is a group of even more sophisticated models, that consider impact of spatial distribution of inhomogeneities, like the cluster model. Its core idea, proposed by Molinari & El Mouden (1996), is to extend the classical Mori-Tanaka model by taking into account the interactions between pairs of inclusions within the analysed space, in addition to the interactions between the inclusions and the matrix. In that model, an elementary cubic volume (a unit cell) containing a finite number of inclusions is created which is then periodically reproduced to fill the whole space, representing the entire material. Any given spatial layout of inclusions can be represented, be it regular or random. Initial solution proposed for the elastic problem was later extended to linear thermoelasticity (Mercier et al., 2000; El Mouden & Molinari, 2000) and viscoplasticity (Kowalczyk-Gajewska et al., 2021).

Throughout the thesis, the analysis includes calculation not only in the pure elastic, but also in the elastic-plastic and elastic-viscoplastic regimes, for which the constitutive laws are non-linear. Thus, similarly to other classical mean-field models which are based on analytical solutions obtained in the frame of linear elasticity, some additional steps must be taken to extend the cluster scheme to the non-linear laws (Suquet, 1997). First, the constitutive law of the matrix has to be effectively linearised and next the selected linearised stiffness, which is in general spatially non-uniform within the matrix, needs to be approximated by some uniform values. There are several possibilities for the linearisation and "uniformisation" steps available in the literature: the oldest model proposed by Kröner (1961), the classical incremental tangent method due to Hill (1965) and the non-incremental secant method of Tandon & Weng (1988) or its modified version employing the second moments for uniformisation proposed by Suquet (1995). Another related class of approaches, employing algorithmic incremental tangent or secant stiffness and originating from the finite element implementations of the elastic-plastic constitutive model, together with the use of the second moments of stress, were proposed in the series of papers (Doghri & Friebel, 2005; Doghri et al., 2011; El Ghezal & Doghri, 2018; Naili & Doghri, 2023) or by Song et al. (2020). There is also a family of variational approaches which hold some connections with the modified secant approach, cf. (Ponte Castañeda & Suquet, 1997; Lahellec & Suquet, 2013; Lucchetta et al., 2021). Some of these methods, when combined with the mean-field models neglecting interactions between inclusions, were subjected to numerical verification in (González et al., 2004; Kursa et al., 2018) and other papers mentioned above.

It has been observed that most of the mean-field models formulated for elastic-plastic heterogeneous materials fail to correctly predict the plasticity developed in the processes with pure hydrostatic stress or even with high stress triaxialities, in particular, for porous materials. It is especially true for the approaches which are solely based on the mean stress or strain per phase (the so-called first moments). An extensive discussion on this issue can be found in El Ghezal & Doghri (2018); Naili & Doghri (2023). It was demonstrated that the problem can be overcome, at least to some extent, when using the second stress moments in the "uniformisation" step.

Regarding the elastic-viscoplastic case, mean-field micromechanical modelling based on the Eshelby's solution poses difficulties when the non-linear Maxwell-type constitutive law is used for elasto-viscoplasticity. First, it involves different orders of time differentiation, which leads to long-term memory effect so that an aggregate of Maxwellian constituents is no more Maxwellian (Suquet, 1987)). Second, the adaptation of linear homogenisation methods to such non-linear behaviour still needs some refinements to reach enough predictive capability as compared to full-field calculations. Hashin (1969) found an analytical solution for the linear viscoelastic problem of a spherical inclusion embedded in an infinite matrix using the Laplace transform technique and the correspondence principle. The material response was of the Maxwell type in both phases and incompressibility was assumed. Correspondence principle was also applied in Brenner & Masson (2005) in the context of non-linear viscoelasticity. Later, the tangent linearisation was proposed by Molinari et al. (1987), as well as additive interaction law for solving inclusion problems, for non-linear, anisotropic, compressible material responses, including elasto-viscoplasticity (Molinari et al., 1997; Molinari, 2002). Moreover, it was verified by Mercier et al. (2005) that, for elastic-viscoplastic materials, the predictions of the additive interaction law for the single inclusion problem were in good agreement with the finite element simulations for various loading conditions and strain paths. It was observed in the literature (Lahellec & Suquet (2007); Czarnota et al. (2015)) that Mori-Tanaka scheme was not sufficient to properly capture the response of a composite with elastic-viscoplastic matrix and elastic inclusions for larger volume fractions of inclusions. Li & Hu (2007) considered elastic inclusions with a linear-viscoelastic matrix where they proposed to solve the two-particle interaction problem in the Laplace domain, adopting

the Kuster-Toksoz model. By considering the direct interaction between particles and introducing the probability distribution function of presence of inclusion centres in the composite, they developed an enhanced model valid for finite concentration of inclusions. They proved that the new model predicts more stiff overall response than the Mori-Tanaka approach. In addition, a strong effect of the particle distribution was detected, showing that the packing of inclusions being a significant factor in obtaining reliable results.

The main tool used for the validation of the cluster model is the numerical homogenisation employing the finite element method (FEM). FEM is practically the most popular method of numerical approximation, with its central idea being the partition the analysed body into an assembly of discrete subdomains, called finite elements. This approach allows for transforming a complicated problem into a systems of computationally manageable equations. The implementation, theory and application of FEM is a subject to decades-long development dating back to Courant (1943). Worth noting is that proper definition of mesh and size of finite elements is vital for obtaining reliable results, which is considered in the thesis.

The numerical homogenisation consists of analysing a statistically representative sample of material, called representative volume element (RVE), recreating a piece of the real microstructure. Each phase is distinct, with a detailed recreation of its shape, spatial distribution and material parameters. For such virtual samples, the "relation between averages", i.e. volume-averaged macroscopic parameters is computed (Zohdi & Wriggers, 2004). It results in a specific homogenised values of investigated characteristics, e.g. Young's modulus, Poisson's ratio or thermal conductivity, which can later be used in a macroscopic analysis (e.g. static analysis of larger structures). The RVE must be big enough to contain a sufficient number of heterogeneities, or a sufficient part of the microstructure, if tackles regular lattices on one hand, and small enough to be treated as a material point in large-scale calculations on the other hand. With an increasing computer power and development of high resolution imaging techniques (e.g. computer tomography), the projection and definition of microstructure in computer analysis can better and better resemble the actual material (Kouznetsova et al., 2001; Zohdi & Wriggers, 2004). However, the FE-based homogenisation technique has its limitations, with the main obstacle usually being time and resource consumption. Due to a high computational cost, a reduced number of microstructure representative volumes can only be considered, so that the extensive parametric study, required for the optimal design process, is often burdensome or even impossible.

Last decade was marked by rapid growth of additive manufacturing techniques, commonly known as three-dimensional (3D) printing. Its flexibility, together with diminishing cost of printing devices and ease of geometry definition by various CAD-like software, makes experimental studies of custom samples more accessible. They may include both closed- and open-porosity systems of a predefined form from the mechanical point of view. The topic of uniform and irregular porosity present in 3D printed components is reviewed in Al-Maharma et al. (2020), while Dizon et al. (2018) provides general characterisation of additively manufactured polymers. Experimental uniaxial tensile stress test of samples of different infill patterns was described in Moradi et al. (2021). In general, microstructures of the same volume fraction of pores, but distinct internal geometry, present different macroscopic elastic properties. Highly porous periodic geometries were also investigated in Mao et al. (2020, 2021); Mueller & Shea (2018).

As stated in the motivation, reliant, quick and resource-efficient analytical or semi-analytical models could open new possibilities in design process of complex materials. This includes optimisation, i.e. a process of finding the proper design solutions of a composite material for specific application. For this reason, part of the thesis concerns this topic. Preliminary selection of the material for a selected component can be done with the use of material charts, as discussed in Ashby (2011). When a composite material is chosen, the further steps aim to find an optimal compromise between objectives for desired parameters, e.g., a high thermal conductivity and a low coefficient of thermal expansion. The background for the respective optimisation methodology has been described in Ashby & Bréchet (2003) and Ashby (2011). Within this method, the allowable region of thermomechanical properties of the pre-selected composite system is identified in the space of performance metrics. The optimum solution is found using and objective function formulated as a weighted function of single objectives. The choice of weight coefficients reflects the relative importance of each analysed property. In most cases, the objective function is formulated as a linear weighted function of single objectives expressed in non-dimensional quantities (Ashby & Bréchet, 2003; Ashby, 2011).

In an alternative, mathematically-based optimisation of heterogeneous materials, its target application and processing method are usually not taken into consideration directly. The objective function

is formulated for selected properties for which established methods of homogenisation exist, such as linear thermomechanical or transport properties (Hashin, 1983; Fullwood et al., 2010). This approach delivers more accurate estimates of the selected macroscopic properties of the composite, nevertheless neglecting other factors of possible importance in the application oriented material design process. As an example, an optimal distribution of phases inside a unit cell can be searched to ensure maximised stiffness and conductivity of macroscopic material (de Kruijf et al., 2007; Challis et al., 2008). Another examples are the optimisation of the unit cell of heterogeneous material is with respect to a single macroscopic property, however, described by a tensorial quantity of multiple components, namely elastic stiffness (Paulino et al., 2009) or anisotropic conductivity (Zhou & Li, 2008). In these studies, the objective function is formulated as a sum of weighted square differences between the required and effective tensor components. Weights in these formulations govern proximity between desired and homogenised properties. Kursa et al. (2014) proposed a mathematically-based multi-objective optimisation of a composite, aiming to find a compromise between conflicting optimality criteria corresponding to different thermomechanical properties obtained using analytical micromechanical models. Their example were metal and ceramic phases for specific applications of valves and brake disks, with volume fraction of ceramic inclusions being the optimised input.

1.3 Aim and scope of the thesis

The aim of the thesis are:

- to extend and provide verification of the micromechanical mean-field cluster model in the non-linear regime of material response (elasto-plasticity and elasto-viscoplasticity);
- to propose and test procedures for finding the optimal microstructure of the composite, given its desired properties for various applications.

The first point consists of exploring the behaviour and limitations of the cluster model, as well as its accordance with predictions of full-field numerical models in elastic, plastic and viscoplastic regimes. The second point consist of developing multi-criteria optimisation procedures that would allow to find an optimal microstructure (i.e. material choice, lattice, volume fraction of inclusions, etc.), obtaining proper balance between all of the used fractions to achieve desired parameters.

The thesis is divided into several chapters:

- Chapter 2 explains the principles of the cluster model, its theory, application procedure, as well as explores its behaviour and convergence of results.
- Chapter 3 includes the validation of the cluster model in the case of thermoelastic properties. The main tool used for this purpose is the finite elements method. Additionally, some experimental data from initial experiments on 3D-printed porous samples are used for the comparison. These results have been included in the article Kowalczyk-Gajewska et al. (2024), so the content of this section aligns to some extent with the material included therein. Finally, multi-criteria optimisation procedures are proposed for composites working in the elastic regime, including mechanical (stiffness) and thermal properties (thermal conductivity, coefficient of thermal expansion).
- Chapter 4 provides the extension of the cluster model to elasto-plasticity, with necessary steps such as: linearisation, uniformisation and isotropisation. So called "second moments of stress" are introduced to tackle the issues of proper prediction of stress-strain curve in pure hydrostatic cases. Results are compared with the finite elements method. These results have already been published in the article Bieniek et al. (2024). As the content of this article aligns with the material included in this chapter, its certain sections reproduce parts of this publication. Additionally, multi-criteria optimisation procedures are proposed for composites working in the elastic-plastic regime.
- Chapter 5 provides the extension of the cluster model to elasto-viscoplasticity, with focus on the choice of the isotropisation method and its influence on the results. Results are compared with the outcomes of the full-field numerical analyses of representative unit cells performed with use finite elements method.

- Chapter 6 includes a supplementary study on geometric traits of the microstructure of two most prevailing regular lattices: regular cubic (RC) and body-centred cubic (BCC). It explores the differences between results achieved for both lattices, as well as risk of possible geometrical instabilities of matrix in porous materials.
- The thesis concludes with chapter 7 with summary of main findings of the thesis and possible future works.

Chapter 2

Cluster model for linear constitutive laws

2.1 Theoretical formulation

The cluster model is an extension of the classical Mori-Tanaka mean-field model proposed by Molinari & El Mouden (1996). It aims to describe the average macroscopic parameters of a material with a given microstructure. In that model, an elementary cubic volume (a unit cell) containing a finite number of inclusions is created which is then periodically reproduced to fill the whole space, representing the entire material. Within this cell we allow any given spatial layout of inclusions, be it regular or random. To each inclusion of a unit cell we may assign a set of inclusions which are periodically related in space and are supposed to carry the same mechanical fields. This set of inclusions is called a family. If all the inclusions within the unit cell are symmetrically equivalent like e.g. in the Regular Cubic (RC), Body-Centred Cubic (BCC) or Face-Centred Cubic (FCC) lattices of inclusions of the same size, then we deal with the one-family case. However, when the inclusions within the cell are not symmetrically equivalent, in which case they may exhibit different mean strains and stresses, like for example in random arrangements, then multiple families must be considered. In this thesis, only the single-family situation is analysed for the sake of simplicity, as the main focus is on the overall material anisotropy induced by the spatial distribution of inclusions.

The three mentioned regular layouts are the most prevalent lattices in the field of micromechanics and are visualised in figure 2.1. In the literature on crystallography, the first lattice is sometimes referred as "simple cubic". Throughout the thesis, the name regular cubic (RC) is used for this lattice in order to avoid confusion with the abbreviation of the self-consistent micromechanical model (SC).

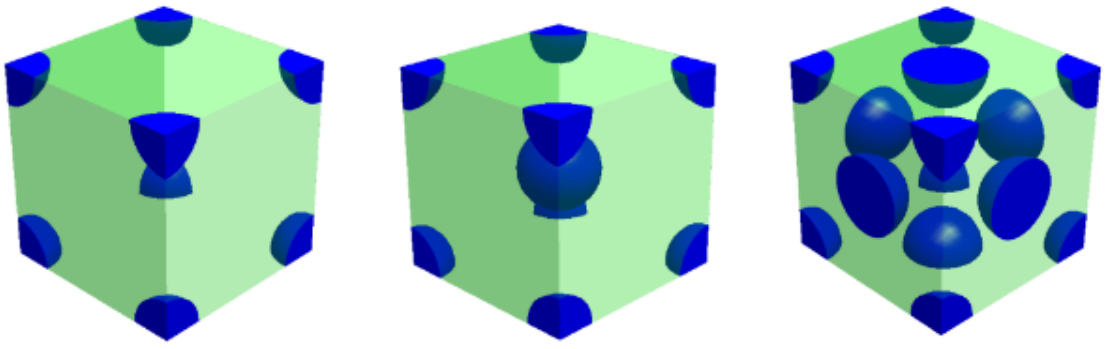

Figure 2.1: Different patterns: Regular Cubic (left); Body-Centred Cubic (middle); and Face-Centred Cubic (right).

The core idea of Molinari and El Mouden (1996) is to extend classical mean-field models by taking into account the interactions between each pair of inclusions within the analysed space, in addition

to the interactions between the inclusions and the matrix. Due to the character of the fundamental solution by Green's function technique (Berveiller et al. (1987)) such interactions decay when the distance between the inclusions increases, thus we may restrict the analysis to the pairs included in some material sub-volume, which is called a cluster. In order to establish a cluster, a reference inclusion is chosen within the basic unit cell of size a (usually, the centremost one) and then a sphere, with its centre point in this reference inclusion, is defined. In calculations, only N inclusions with centre points that lie within this sphere are considered, as depicted in figure 2.2. For the purposes of this analysis, the unit cell size a is defined as the distance between the inclusions belonging to the RC "net" (BCC and FCC containing extra inclusions inside the RC "net"). The cluster size is defined as the diameter (or radius) of a sphere reaching the furthermost inclusion of the RC "net".

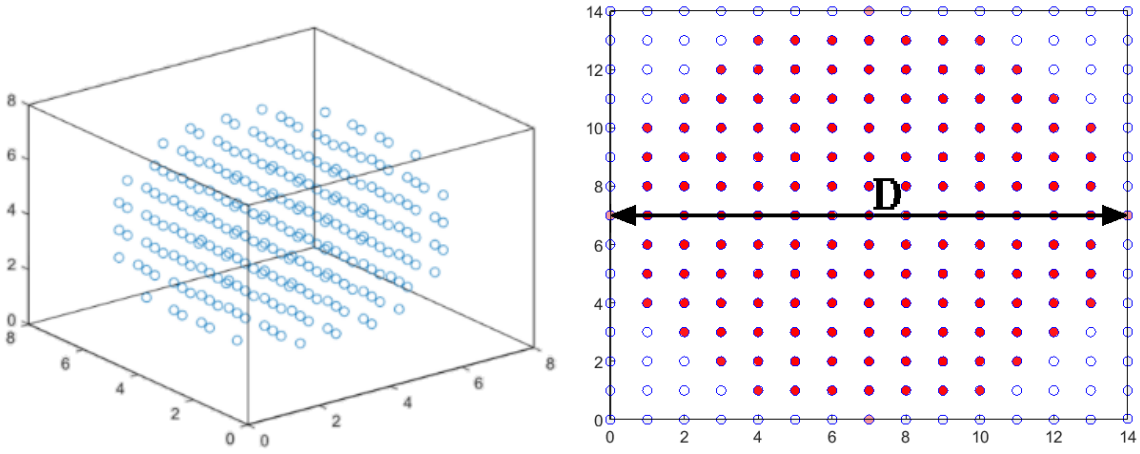

Figure 2.2: Visualisation of a cluster in 3D (left); and its cross section in 2D (right). The cluster contains only red inclusions that fit within diameter D. In this case the size (diameter) of $D = 14a$.

2.1.1 Linear thermoelasticity

In brief, the input to the model is the material parameters for each phase, geometry and external (macroscopic) stresses or strains. The results are homogenised macroscopic parameters of the entire sample, such as: elastic stiffness moduli, thermal conductivity, the coefficient of thermal expansion or field stress, as well as tresses and strains for each phase. These stresses and strains are assumed to be uniform within each phase.

The starting point is the constitutive equations for the thermoelastic material locally relating the stress $\boldsymbol{\sigma}$ and strain $\boldsymbol{\varepsilon}$ in each phase r, which is valid also for the respective mean values $\boldsymbol{\sigma}_r = \langle \boldsymbol{\sigma} \rangle_r$ and $\boldsymbol{\varepsilon}_r = \langle \boldsymbol{\varepsilon} \rangle_r$ per volumes V_r occupied by the phase r:

$$\boldsymbol{\sigma} = \mathbb{C} \cdot \varepsilon - \boldsymbol{\beta}_r \theta \quad \rightarrow \quad \boldsymbol{\sigma}_r = \mathbb{C} \cdot \boldsymbol{\varepsilon}_r - \boldsymbol{\beta}_r \theta \tag{2.1}$$

where: $\langle \quad \rangle_r \equiv \int_{V_r} (\quad) dV_r$ denotes operation of volume averaging; $\boldsymbol{\sigma}$, $\boldsymbol{\varepsilon}$ are second-order tensors; $\mathbb{C}$ is fourth-order stiffness tensor for phase r; and $\beta_r \theta$ is thermal stress at temperature increment θ in the composite.

As in any mean-field model, the effective stiffness tensor $\bar{\mathbb{C}}$ and effective thermal stress $\bar{\boldsymbol{\beta}}_r \theta$ for the composite representative volume V, such that:

$$\bar{\boldsymbol{\sigma}} = \sum_r f_r \boldsymbol{\sigma}_r = \bar{\mathbb{C}} \cdot \bar{\boldsymbol{\varepsilon}} - \bar{\boldsymbol{\beta}} \theta, \quad \bar{\boldsymbol{\varepsilon}} = \sum_r f_r \boldsymbol{\varepsilon}_r \tag{2.2}$$

are found as a weighted sum of respective mean quantities for each phase, where the weights are the relevant strain localisation tensors $\mathbb{A}_r$:

$$\bar{\mathbb{C}} = \sum_r f_r \mathbb{C}_r \mathbb{A}_r, \quad \bar{\beta} = \sum_r f_r \boldsymbol{\beta}_r \cdot \mathbb{A}_r \tag{2.3}$$

and f_r is the volume fraction of phase r. The strain localisation relations take a standard form:

$$\boldsymbol{\varepsilon}_r = \mathbb{A}_r \cdot \bar{\boldsymbol{\varepsilon}} + \boldsymbol{e}_r \theta \tag{2.4}$$

When the strain localisation tensors $\mathbb{A}_r$ and $\boldsymbol{e}_r$ are known, the set of above-stated relations enable to find the mean stresses and strains per phases and macroscopic stress or strain depending which of these two quantities is prescribed by boundary conditions. It has been demonstrated by Kowalczyk-Gajewska et al. (2021) that for the single-family case the strain localisation tensor and the free term e_r of the cluster model are calculated differently for the inclusions and for the matrix:

$$\mathbb{A}_\mathrm{i} = (\mathbb{I} + ((1-f_\mathrm{i})\mathbb{P}_0 - \bar{\boldsymbol{\Gamma}}))(\mathbb{C}_\mathrm{i} - \mathbb{C}_\mathrm{m})^{-1}, \quad \mathbb{A}_\mathrm{m} = \frac{1}{1-f_\mathrm{i}}(\mathbb{I} - f_\mathrm{i}\mathbb{A}_\mathrm{i}) \tag{2.5}$$

$$\boldsymbol{e}_i = \mathbb{A}_\mathrm{i}((1-f_i)\mathbb{P}_0 - \bar{\boldsymbol{\Gamma}})(\boldsymbol{\beta}_i - \boldsymbol{\beta}_m), \quad \boldsymbol{e}_m = \frac{1}{1-f_\mathrm{i}} e_i \tag{2.6}$$

where $\bar{\boldsymbol{\Gamma}}$ is interaction tensor; $\mathbb{P}_0$ is polarisation tensor; and $\mathbb{I}$ is fourth order identity tensor. Subscript "m" denotes the respective parameters for the matrix, while subscript "i" for the inclusions. Substituting equations (2.5)-(2.6) into (2.3) one obtains:

$$\bar{\mathbb{C}} = \mathbb{C}_\mathrm{m} + f_i \left[(1-f_i)\mathbb{P}_0 - \bar{\boldsymbol{\Gamma}} + (\mathbb{C}_\mathrm{i} - \mathbb{C}_\mathrm{m})^{-1}\right]^{-1}, \quad \bar{\boldsymbol{\beta}} = \boldsymbol{\beta}_m + f_i(\boldsymbol{\beta}_i - \boldsymbol{\beta}_m) \cdot \mathbb{A}_i \tag{2.7}$$

The interaction tensor $\bar{\boldsymbol{\Gamma}}$ is the core of the cluster model. It is a fourth-order tensor that accounts for the interactions between the inclusions and is specified as:

$$\bar{\boldsymbol{\Gamma}} = \sum_{J \neq I} \boldsymbol{\Gamma}^{IJ} \tag{2.8}$$

The symmetry group of this tensor results from the symmetry of the unit cell. The fourth order tensors $\boldsymbol{\Gamma}^{IJ}$ are defined by:

$$\boldsymbol{\Gamma}^{IJ} = \frac{1}{V_I} \int_{V_I} \int_{V_J} \boldsymbol{\Gamma}(\boldsymbol{x}_I - \boldsymbol{x}_J) d\boldsymbol{x}_J d\boldsymbol{x}_I \tag{2.9}$$

where integrations are preformed on the domains V_I and V_J occupied by inclusions I and J respectively. $\boldsymbol{\Gamma}^{IJ}$ depends on the shape of two inclusions and the relative distance between inclusion centres. $\boldsymbol{\Gamma}^{IJ}$ is also function of $\mathbb{C}_m$ through the kernel $\boldsymbol{\Gamma}$ in equation (2.9) which is obtained from Green functions related to the elastic stiffness $\mathbb{C}_m$ of the matrix. For two spherical inclusions embedded in an isotropic elastic medium, $\boldsymbol{\Gamma}^{IJ}$ can be analytically expressed, as per equations (2.16)-(2.22) (Berveiller et al. (1987)).

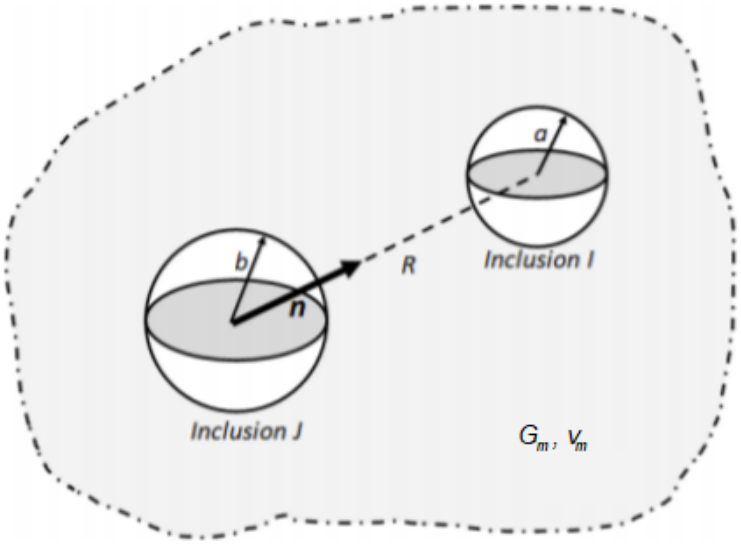

Figure 2.3: Pair of inclusions.

In the cluster model, $\mathbf{\Gamma}^{IJ}$ is calculated as an interaction tensor between the reference inclusion I and every other inclusion J within the cluster (a separate tensor for each pair I-J, as per figure 2.3). The procedure of finding effective values is described in subsection 2.2 as a step-by-step algorithm for the readers' convenience, if they wish to implement the model or test it by themselves. Note that, contrary to the Ponte Castañeda & Willis (1995) approach and related ones, the effect of the spatial distribution is described in the cluster model by a fourth order tensor (not a second order tensor), so there are eight symmetry classes of anisotropy which could be accounted for within the cluster approach, including the cubic symmetry class (Forte and Vianello, 1996). It is worth mentioning then when $\bar{\mathbf{\Gamma}}$ is set to zero in the formulas above, the classical Mori-Tanaka model for a two-phase composite is recovered.

2.1.2 Thermal conductivity

For the thermal conductivity problem, the constitutive equation is the linear Fourier law of thermal conduction:

$$\mathbf{q}_r = -\mathbf{k}_r \cdot (\nabla\theta)_r \tag{2.10}$$

where $\mathbf{q}_r$ is a mean heat flux in phase r; $(\nabla\theta)^r$ is a mean temperature gradient in phase r; and $\mathbf{k}_r$ is a second order tensor of thermal conductivity. The effective thermal conductivity tensor $\bar{\mathbf{k}}$ for the composite representative volume V, such that is found as a weighted sum of respective mean quantities for each phase, where the weights are the relevant temperature gradient localisation tensors $\mathbf{a}_r$:

$$\bar{\mathbf{k}} = \sum_r f_r \mathbf{k}_r \mathbf{a}_r, \tag{2.11}$$

and f_r is the volume fraction of phase r. The temperature gradient localisation relation takes the form:

$$(\nabla\theta)_r = \mathbf{a}_r \cdot (\bar{\nabla\theta}) \tag{2.12}$$

For a single-family case, the thermal localisation tensor is calculated as follows:

$$\mathbf{a}_i = \left(\mathbf{I} + \left((1-f_i)\mathbf{p}_0 - \bar{\mathbf{T}}\right)(\mathbf{k}_i - \mathbf{k}_m)\right)^{-1}, \quad \mathbf{a}_m = \frac{1}{1-f_i}(\mathbf{I} - f_i\mathbf{a}_i) \tag{2.13}$$

where $\boldsymbol{p}_0$ is thermal polarisation tensor; and $\bar{\boldsymbol{T}}_i$ is thermal interaction tensor. Subscript "m" denotes the respective parameters for the matrix, while subscript "i" for the inclusions. Substituting equation (2.11) into (2.13) one obtains:

$$\bar{\mathbf{k}} = \mathbf{k}_m + f_i[(1-f_i)\mathbf{p}_0 - \bar{\mathbf{T}} + (\mathbf{k}_i - \mathbf{k}_m)^{-1}]^{-1} \tag{2.14}$$

The thermal interaction tensor $\bar{\mathbf{T}}$ is analogue to the interaction tensor $\bar{\mathbf{\Gamma}}$ in the mechanical problem. It is a second order tensor that accounts for the interactions between the inclusions and is specified as:

$$\bar{\mathbf{T}} = \sum_{J \neq I} \mathbf{T}^{IJ} \tag{2.15}$$

where $\mathbf{T}^{IJ}$ describes thermal interactions between two inclusions in an infinite medium and, in a general case, is calculated based on the formulas analogical to (2.9) with a Green function specific for the thermal problem. The cluster model for thermal conductivity problem outlined above was originally proposed by Mercier et al. (2000).

2.2 Step-by-step algorithm for the cluster model

This point contains a step-by-step computational algorithm for the cluster model as applied to a two-phase composite with isotropic phases, from the beginning (setting input parameters) to the end (obtaining effective values for the composite). It allows the reader to implement and try it using examples and parameters of their choice. The linear elasticity and thermal conductivity problems are treated separately:

2.2.1 Linear elasticity

The procedure for linear elasticity consists of the following steps:

0. "Step zero" is to create input data for the model. These data consist of material parameters of all phases, as well as the geometry of the sample:
   (a) elastic constants for both phases, i.e.: bulk modulus, shear modulus and Poisson's ratio: K_r, G_r, ν_r, $(r = i, m)$;
   (b) coordinates (x, y, z) of the centres and radii of all inclusions within the unit cell; the number of inclusions will be denoted by M and we are assuming here that they are all symmetrically equivalent – in particular, their radii are equal;
   (c) diameter D of the cluster (we assume for simplicity that D is a multiple of the unit cell size a).

1. Find the centermost inclusion I in the unit cell and its coordinates (x^I, y^I, z^I). It will serve as the base inclusion of reference.

2. Construct a cluster of diameter D by repeating the unit cell periodically in three dimensions until the assembly of cells accommodates a sphere of radius D centred at the base inclusion. Then select from the assembly those inclusions which are within distance $D/2$ (measured centre to centre) from the base inclusion. The number of inclusions in the cluster is denoted by N.

3. Calculate the interaction tensor $\mathbf{\Gamma}^{IJ}$ for each pair of inclusions: I and any other inclusion J (as in figure 2.3). There should be N–1 pairs and thus N–1 tensors $\mathbf{\Gamma}^{IJ}$. The components of the interaction tensor are calculated as follows:

$$\mathbf{\Gamma}^{IJ}_{1111} = \mathbf{\Gamma}^{IJ}_{2222} = \frac{-V_J}{16\pi R^3}\frac{1}{G_m(1-\nu_m)}(1 - 4\nu_m + \frac{9}{5}\rho^2) \tag{2.16}$$

$$\mathbf{\Gamma}^{IJ}_{1122} = \mathbf{\Gamma}^{IJ}_{2211} = \frac{-V_J}{16\pi R^3}\frac{1}{G_m(1-\nu_m)}(-1 + \frac{3}{5}\rho^2) \tag{2.17}$$

$$\mathbf{\Gamma}^{IJ}_{1133} = \mathbf{\Gamma}^{IJ}_{2233} = \mathbf{\Gamma}^{IJ}_{3311} = \mathbf{\Gamma}^{IJ}_{3322} = \frac{-V_J}{16\pi R^3}\frac{1}{G_m(1-\nu_m)}(2 - \frac{12}{5}\rho^2) \tag{2.18}$$

$$\mathbf{\Gamma}^{IJ}_{1212} = \mathbf{\Gamma}^{IJ}_{1221} = \mathbf{\Gamma}^{IJ}_{2112} = \mathbf{\Gamma}^{IJ}_{2121} = \frac{-V_J}{16\pi R^3}\frac{1}{G_m(1-\nu_m)}(1 - 2\nu_m + \frac{3}{5}\rho^2) \tag{2.19}$$

$$\mathbf{\Gamma}^{IJ}_{1313} = \mathbf{\Gamma}^{IJ}_{1331} = \mathbf{\Gamma}^{IJ}_{3113} = \mathbf{\Gamma}^{IJ}_{3131} = \frac{-V_J}{16\pi R^3}\frac{1}{G_m(1-\nu_m)}(1 + \nu_m - \frac{12}{5}\rho^2) \tag{2.20}$$

$$\mathbf{\Gamma}^{IJ}_{2323} = \mathbf{\Gamma}^{IJ}_{2332} = \mathbf{\Gamma}^{IJ}_{3223} = \mathbf{\Gamma}^{IJ}_{3232} = \frac{-V_J}{16\pi R^3}\frac{1}{G_m(1-\nu_m)}(1 + \nu_m - \frac{12}{5}\rho^2) \tag{2.21}$$

$$\mathbf{\Gamma}^{IJ}_{3333} = \frac{-V_J}{16\pi R^3}\frac{1}{G_m(1-\nu_m)}(-8 + 8\nu_m - \frac{24}{5}\rho^2) \tag{2.22}$$

   where:

$$\rho^2 = (a^2 + b^2)/R^2 \tag{2.23}$$

   and V_J is volume of inclusion no J; G_m is shear modulus for matrix; ν_m is Poisson's ratio for matrix; R is distance between inclusion no J and base inclusion I; a is radius of base inclusion I; and b is radius of inclusion no J.

4. Sum up all N–1 interaction tensors $\mathbf{\Gamma}^{IJ}$. This gives the global tensor of interaction $\bar{\mathbf{\Gamma}}$:

$$\bar{\mathbf{\Gamma}} = \sum_{J \neq I} \mathbf{\Gamma}^{IJ} \tag{2.24}$$

   Note that before summation the components (2.16)–(2.22) of subsequent $\mathbf{\Gamma}^{IJ}$ tensors must be transformed into the common reference frame. Otherwise, the basis-free formula can be used:

$$\mathbf{\Gamma}^{IJ} = \frac{1}{3G_{\mathrm{m}}(1-\nu_{\mathrm{m}})(R/b)^3}\left(\Gamma_1^{IJ}\mathbb{P}_{12}(\mathbf{n}) + 2(\Gamma_3^{IJ}+\Gamma_4^{IJ})\mathbb{P}_2(\mathbf{n}) - \Gamma_3^{IJ}\mathbb{P}_3(\mathbf{n}) - \Gamma_4^{IJ}\mathbb{P}_4(\mathbf{n})\right) \quad (2.25)$$

where $\mathbf{n}$ is the unit vector along the line connecting the centres of inclusions I and J; and:

$$\mathbb{P}_{12}(\mathbf{n}) = \frac{\sqrt{2}}{6}\left((3\mathbf{N}-\mathbf{I})\otimes\mathbf{I} + \mathbf{I}\otimes(3\mathbf{N}-\mathbf{I})\right) \quad (2.26)$$

$$\mathbb{P}_2(\mathbf{n}) = \frac{1}{6}(3\mathbf{N}-\mathbf{I})\otimes(3\mathbf{N}-\mathbf{I}) \quad (2.27)$$

$$\mathbb{P}_3(\mathbf{n}) = \frac{1}{2}\left([(\mathbf{I}-\mathbf{N})\otimes(\mathbf{I}-\mathbf{N})]^{T(23)+T(24)} - (\mathbf{I}-\mathbf{N})\otimes(\mathbf{I}-\mathbf{N})\right) \quad (2.28)$$

$$\mathbb{P}_4(\mathbf{n}) = \frac{1}{2}\left[\mathbf{N}\otimes(\mathbf{I}-\mathbf{N}) + (\mathbf{I}-\mathbf{N})\otimes\mathbf{N}\right]^{T(23)+T(24)} \quad (2.29)$$

with: $(\mathbb{A}^{T(23)+T(24)})_{ijkl} \equiv (\mathbb{A})_{ikjl} + (\mathbb{A})_{ilkj}$; $\mathbf{N} = \mathbf{n}\otimes\mathbf{n}$; and $\mathbf{I}$ being the second-order identity tensor. The three scalar coefficients $\Gamma_k^{IJ} = \Gamma_k^{IJ}(R/b, a/b)$, $k = 1, 3, 4$, are specified by the following formulas:

$$\Gamma_1^{IJ} = \frac{1}{\sqrt{2}}(1-2\nu_{\mathrm{m}}), \quad \Gamma_3^{IJ} = \frac{1}{10}(5-10\nu_{\mathrm{m}}+3\rho^2), \quad \Gamma_4^{IJ} = \frac{1}{10}(5+5\nu_{\mathrm{m}}-12\rho^2) \quad (2.30)$$

5. Calculate the polarisation tensor $\mathbb{P}_0$:

$$\mathbb{P}_0 = h^P_{polar}\mathbb{I}^P + h^D_{polar}\mathbb{I}^D \quad (2.31)$$

where:

$$h^P_{polar} = \frac{1}{4G_m + 3K_m}, \quad h^D_{polar} = \frac{3}{5G_m}\frac{K_m+2G_m}{4G_m+3K_m} \quad (2.32)$$

and:

$$\mathbb{I}^P = \frac{1}{3}\mathbf{I}\otimes\mathbf{I} \quad (I^P_{ijkl} = \frac{1}{3}\delta_{ij}\delta_{kl}), \quad \mathbb{I}^D = \mathbb{I} - \mathbb{I}^P \quad (I_{ijkl} = \frac{1}{2}(\delta_{ik}\delta_{jl}+\delta_{il}\delta_{jk})) \quad (2.33)$$

with $\mathbb{I}$ being the fourth-order identity tensor.

6. Compose the stiffness tensors for the matrix and inclusions:

$$\mathbb{C}_r = 3K_r\mathbb{I}^P + 2G_r\mathbb{I}^D \quad (r = i, m) \quad (2.34)$$

7. Calculate localisation tensors for the matrix and inclusions using equation (2.5).

8. Calculate the effective stiffness tensor for the entire sample using equation (2.3) or (2.7). The effective stiffness tensor is one of the output values – an effective parameter of the composite that was the subject of mathematical homogenisation.

9. If the external strain (or stress) applied to the sample was a part of the problem, it is possible to calculate the effective stress (or strain) from the overall relation:

$$\bar{\boldsymbol{\sigma}} = \bar{\mathbb{C}}\cdot\bar{\boldsymbol{\varepsilon}} \quad (2.35)$$

10. Stresses and strains for each phase r are calculated as follows:

$$\boldsymbol{\varepsilon}_r = \mathbb{A}_r\cdot\bar{\boldsymbol{\varepsilon}}, \quad \boldsymbol{\sigma}_r = \mathbb{B}_r\cdot\bar{\boldsymbol{\sigma}}, \quad (r = i, m), \quad (2.36)$$

where $\mathbb{B}_r = \mathbb{C}_r\mathbb{A}_r\bar{\mathbb{C}}^{-1} (r = i, m)$ are stress localisation tensors.

Note that the above algorithm is written for the elastic analysis. In the case of the elastic–plastic analysis, the algorithm needs to be executed at each time step and, in the case of tangent linearisation, formulas in steps 9 and 10 concern stress and strain rates. Extension to elastic-plastic and elastic-viscoplastic analysis will be described in chapters 4 and 5.

2.2.2 Thermal conductivity

The procedure for thermal conductivity consists of the following steps:

0. "Step zero" is to create input data for the model. These data consist of material parameters of all phases, as well as the geometry of the sample:
   (a) thermal constant for both phases, i.e.: thermal conductivity k_r $(r = i, m)$;
   (b) coordinates (x, y, z) of the centres and radii of all inclusions within the unit cell; the number of inclusions will be denoted by M and we are assuming here that they are all symmetrically equivalent – in particular, their radii are equal;
   (c) diameter D of the cluster (we assume for simplicity that D is a multiple of the unit cell size a).
1. Find the centermost inclusion I in the unit cell and its coordinates (x^I, y^I, z^I). It will serve as the base inclusion of reference.
2. Construct a cluster of diameter D by repeating the unit cell periodically in three dimensions until the assembly of cells accommodates a sphere of radius D centred at the base inclusion. Then select from the assembly those inclusions which are within distance $D/2$ (measured centre to centre) from the base inclusion. The number of inclusions in the cluster is denoted by N.
3. Calculate the thermal interaction tensor $\mathbf{T}^{IJ}$ for each pair of inclusions: I and any other inclusion J (as in figure 2.3). There should be N–1 pairs and thus N–1 tensors $\mathbf{T}^{IJ}$. The thermal interaction tensor is calculated as follows:
$$\mathbf{T}^{IJ} = \frac{V_J}{4\pi R_J^3 k_\mathrm{m}} \mathbf{d}(\mathbf{n}_J), \quad \mathbf{d}(\mathbf{n}) = 3\mathbf{n}_J \otimes \mathbf{n}_J - \mathbf{I} \quad (d_{ij}(n_k) = 3n_i n_j - \delta_{ij}) \tag{2.37}$$
   where V_J, R_J and $\mathbf{n}_J$ are defined as for the linear elasticity algorithm; and $\mathbf{I}$ is the second-order identity tensor.
4. Sum up all $N-1$ thermal interaction tensors $\mathbf{T}^{IJ}$. This gives the global tensor of thermal interaction $\bar{\mathbf{T}}$:
$$\bar{\mathbf{T}} = \sum_{J \neq I} \mathbf{T}^{IJ} \tag{2.38}$$
5. Calculate the polarisation tensor $\mathbf{p}_0$:
$$\mathbf{p}_0 = \frac{1}{3k_m} \mathbf{I} \tag{2.39}$$
6. Compose the thermal conductivity tensors for the matrix and inclusions:
$$\mathbf{k}_r = k_r \mathbf{I}, \quad (r = i, m) \tag{2.40}$$
7. Calculate temperature gradient localisation tensors for the matrix and inclusions using equation (2.13).
8. Calculate the effective thermal conductivity tensor for the entire sample using equation (2.11) or (2.14). The effective thermal conductivity tensor is one of the output values – an effective parameter of the composite that was the subject of mathematical homogenisation.
9. If the external heat flux (or temperature gradient) applied to the sample was a part of the problem, it is possible to calculate the effective temperature gradient (or heat flux) from the constitutive relation:
$$\mathbf{q}_r = -\mathbf{k}_r \cdot (\nabla\theta)_r \tag{2.41}$$
10. Heat flux and temperature gradient for each phase r are calculated as follows:
$$(\nabla\theta)_r = \mathbf{a}_r \cdot (\bar{\nabla\theta}), \quad \mathbf{q}_r = \mathbf{b}_r \cdot \bar{\mathbf{q}}, \quad (r = i, m), \tag{2.42}$$
    where $\mathbf{b}_r = \mathbf{k}_r \mathbf{a}_r \bar{\mathbf{k}}^{-1} (r = i, m)$ is a heat flux localisation tensor.

2.3 Effect of the cluster size

The cluster model aims to describe average macroscopic parameters of a material with a given microstructure. In that model, an elementary cubic volume (a unit cell), containing a finite number of inclusions, is created and then periodically reproduced to fill the whole space, representing the entire material in a form of a cluster. This creates an important question of how big such a cluster should be in order to capture and represent the proper behaviour of the material, while not unnecessarily consuming too much computing power. In this section, the answer for this question is sought. The procedure is to calculate effective macroscopic material parameters for clusters of different sizes, starting with the smallest possible sample and increasing the size with each step, comparing the outcome values from the one before - similar to a mesh convergence test in the finite elements method.

The results from the cluster model are either a 3x3x3x3 fourth order tensor (for the stiffness) or a 3x3 second order tensor (for the thermal conductivity, strain and stresses). The macroscopic properties are anisotropic or approximately isotropic for regular or random particle distribution, respectively. The anisotropy of macroscopic properties follows the symmetry of the unit cell. If the particles are distributed in the RC, BCC or FCC lattice, the macroscopic elastic stiffness tensor will be of cubic symmetry, while the macroscopic thermal conductivity tensor will be isotropic. For this reason, the tracked outcomes are: macroscopic bulk modulus ($\bar{K}$), effective shear moduli ($\bar{G_1}$,$\bar{G_2}$), macroscopic thermal conductivity ($\bar{k}$) and average von Mises stresses in inclusions (σ_{eq}). Stresses for inclusions are chosen, as they show bigger discrepancies compared with the stresses in the matrix. The difference between $\bar{G_1}$ and $\bar{G_2}$ marks the anisotropy degree of the effective elastic properties. These parameters are introduced to simplify the data interpretation and presentation, and are calculated as following:

$$3\bar{K} = 1/3\left(\bar{C}_{1111} + \bar{C}_{2222} + \bar{C}_{3333}\right) + 2/3\left(\bar{C}_{1122} + \bar{C}_{1133} + \bar{C}_{2233}\right) \tag{2.43}$$

$$2\bar{G_1} = 1/3\left(\bar{C}_{1111} + \bar{C}_{2222} + \bar{C}_{3333}\right) - 1/3\left(\bar{C}_{1122} + \bar{C}_{1133} + \bar{C}_{2233}\right)\ , \tag{2.44}$$

$$\bar{G_2} = 1/3\left(\bar{C}_{2323} + \bar{C}_{1313} + \bar{C}_{1212}\right)\ . \tag{2.45}$$

$$\bar{k} = \frac{1}{3}(\bar{k}_{11} + \bar{k}_{22} + \bar{k}_{33}) \tag{2.46}$$

$$\sigma_{eq} = \sqrt{\frac{1}{2}\left((\sigma_{11} - \sigma_{22})^2 + (\sigma_{22} - \sigma_{33})^2 + (\sigma_{11} - \sigma_{33})^2 + 6(\sigma_{12}^2 + \sigma_{13}^2 + \sigma_{23}^2)\right)} \tag{2.47}$$

where $\bar{K}$ is macroscopic bulk modulus; $\bar{G_1}$ is first macroscopic shear modulus; $\bar{G_2}$ is second macroscopic shear modulus; $\bar{k}$ is macroscopic thermal conductivity; σ_{eq} is equivalent von Mises stress; $\bar{C}_{ijkl}$ are components of the macroscopic stiffness tensor $\bar{\mathbb{C}}$; and $\bar{k}$ is macroscopic thermal conductivity tensor. It is worth noting that for a perfect cubic symmetry, following relations are true:

$$\bar{C}_{1111} = \bar{C}_{2222} = \bar{C}_{3333}, \quad \bar{C}_{1122} = \bar{C}_{1133} = \bar{C}_{2233}, \quad \bar{C}_{1212} = \bar{C}_{1313} = \bar{C}_{2323} \tag{2.48}$$

Three lattices are considered: RC, BCC and FCC. The unit cell size is equal to $a = 1$ (see figure 2.1). In each step, the cluster size (cluster diameter) varies from $D = 2a$ up to $D = 19a$. Effective properties can be calculated without considering specific boundary conditions. For tracking the σ_{eq} and other stress related quantities, it was assumed that each sample is subjected to uniaxial tension of $\bar{\sigma} = 1$ MPa along the unit cell edge. Volume fraction of inclusions has been chosen separately for each lattice: $f_i = 50\%$ for RC, $f_i = 65\%$ for BCC and $f_i = 70\%$ for FCC. Such values have been chosen in order to create the most demanding conditions for the model, as they are close to what is the limit volume fraction for each lattice ($f_i = 52.36\%$, $f_i = 68.01\%$ and $f_i = 73.70\%$ respectively) which mark the value at which inclusions in a given arrangement touch each other. For the same reason, a set of non-real, "theoretical" material parameters for the matrix and inclusions with a extremely high contrast are used in order to emphasize and better visualise the effects of the model, as per table 2.1.

Table 2.1: Parameters of "theoretical" materials used for the cluster convergence test.

	Matrix: soft	Inclusions: ultra hard
bulk modulus, K [GPa]	2.1667	21667
shear modulus, G [GPa]	1.0000	10000
Poisson's ratio, ν [-]	0.3	0.3
thermal conductivity, k [W/(m·K)]	1	10000

Table 2.2: Results for different lattices for the largest analysed cluster size ($D = 19d$).

Lattice	f_i [-]	$\bar{K}$ [MPa]	$\bar{G}_1$ [MPa]	$\bar{G}_2$ [MPa]	k [W/(m·K)]	$\bar{\sigma}_{eq}$ [kPa]	$\sigma_{eq.m}$ [kPa]	$\sigma_{eq.i}$ [kPa]
RC	0.50	5666.9	4312.5	2688.0	3.9994	1.0000	463.71	1.536
BCC	0.65	8660.8	4632.0	5094.3	6.5642	1.0000	616.43	1.2067
FCC	0.70	10332.8	5231.0	6475.6	7.9963	1.0000	637.267	1.1554

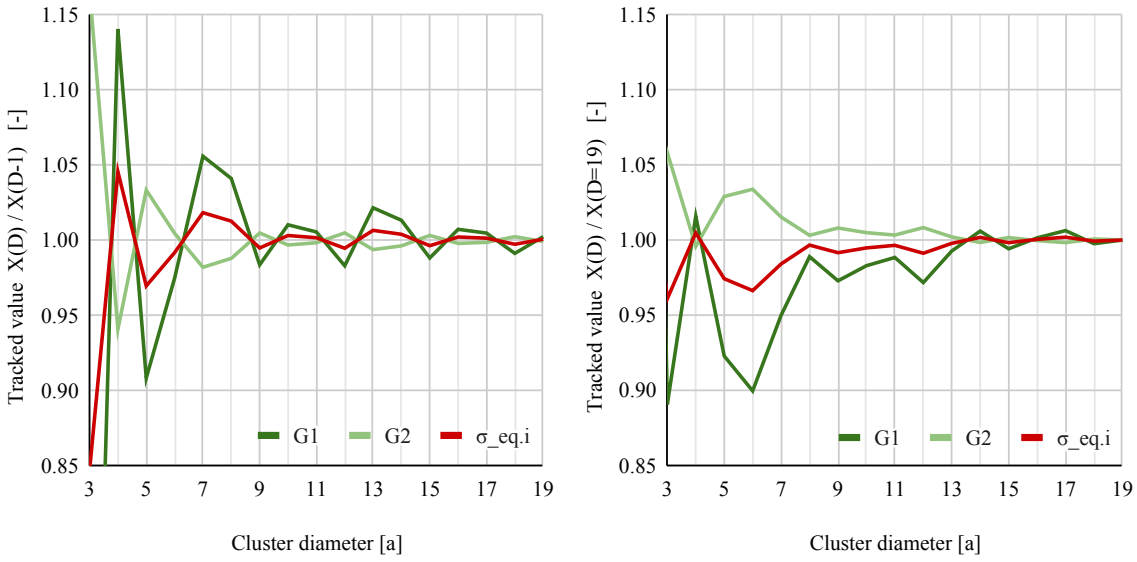

(a) (b)

Figure 2.4: Discrepancies of tracked values for the RC lattice relative to previous (D–1) sample (a); and to the reference ($D = 19a$) sample (b). Volume fraction of inclusions $f_i = 50\%$.

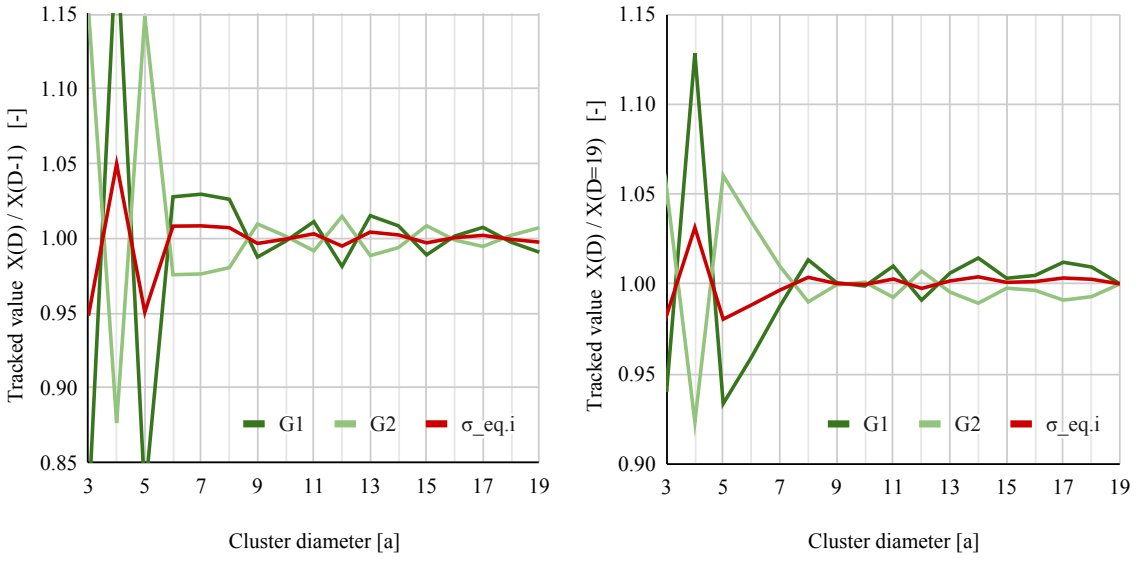

(a) (b)

Figure 2.5: Discrepancies of tracked values for the BCC lattice relative to previous (D–1) sample (a); and to the reference ($D = 19a$) sample (b). Volume fraction of inclusions $f_i = 65\%$.

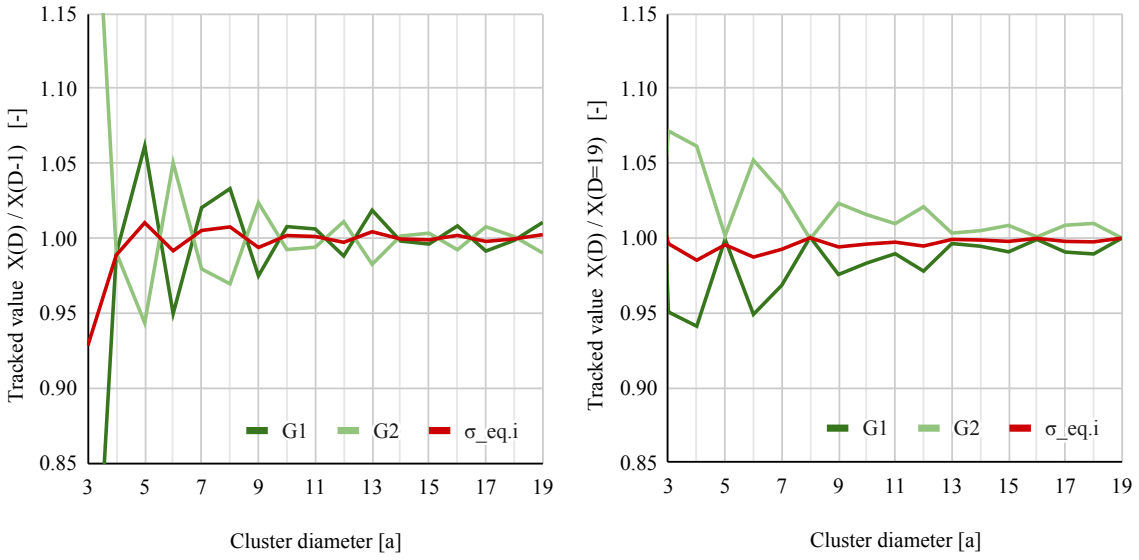

(a) (b)

Figure 2.6: Discrepancies of tracked values for the FCC lattice relative to previous (D–1) sample (a); and to the reference ($D = 19a$) sample (b). Volume fraction of inclusions $f_i = 70\%$.

In table 2.2 there are results for each lattice for the largest analysed cluster size ($D = 19a$) which are set as the reference values. Figures 2.4 - 2.6 show how the tracked values are changing relative to a previous smaller sample or to the reference sample. The bulk modulus and thermal conductivity are omitted in the figures for the sake of readability, as their value stay practically the same for each cluster size. As it can be seen, the effective values from each iteration differ one from another if the samples are small, showing a semi-oscillating behaviour. One of the causes might be the fact that in the cluster model a base inclusion I needs to be chosen and then the interaction tensors $\mathbf{\Gamma}^{IJ}$ are calculated relative to it. In the script, the base inclusion I is an inclusion closest to the centre of the cluster. Depending on the layout, not always is there an inclusion in the very centre, with "eccentricity" being relatively bigger in smaller samples (e.g. for the RC lattice with even number of inclusions in a row). Thermal properties are very stable, showing negligible discrepancies, so the observation of the mechanical parameters is more important. If the acceptable threshold of discrepancies is set to 1%, the results converge starting from a sample of diameter $D = 16a$ for the RC and BCC lattices, or $D = 15a$ for the FCC lattice.

2.4 Pre-defined gamma functions

The cluster model allows to perform calculations for different regular and irregular layouts. This allows for flexibility of adjusting inclusion sizes, their location or sample proportion. However, calculations always take time and the most time-consuming part of the cluster model is the interaction tensor $\bar{\mathbf{\Gamma}}$. It is a fourth-order tensor that needs to be calculated as a sum of contributions $\mathbf{\Gamma}^{IJ}$ for each inclusion pair constituted of base inclusion I and inclusion no J. As explained in section 2.2, the formulas for the components of interaction tensor $\mathbf{\Gamma}^{IJ}$ describing the contribution of a given pair $I - J$ are given by equations (2.16)-(2.23). For large cluster sizes, including multiple inclusions, this can pose a significant efficiency problem. However, the interaction tensor $\mathbf{\Gamma}^{IJ}$ depends only on: inclusion size, cell size and material parameters of the matrix. Thus, as long as the inclusions are spherical, the lattice remains the same and identical material properties for the matrix are applied, the interaction tensor $\bar{\mathbf{\Gamma}}$ will always be the same. This opens a gate for optimising this most resource-expensive part of calculations.

Regular lattices from previous sections are considered: regular cubic (RC), body-centred cubic (BCC) and face-centred cubic (FCC). A spherical sample of diameter equal to 40 unit cells (i.e. $D = 40a$, see section) was generated for each lattice and implemented into the cluster model. Mathematica

software was used to automatically simplify the formulas and perform calculations in a symbolic mode. The result are the following formulas defining components of the global interaction tensor:

$$\bar{\mathbf{\Gamma}}_{1111} = \bar{\mathbf{\Gamma}}_{2222} = \bar{\mathbf{\Gamma}}_{3333} = X \tag{2.49}$$

$$\bar{\mathbf{\Gamma}}_{1122} = \bar{\mathbf{\Gamma}}_{1133} = \bar{\mathbf{\Gamma}}_{2233} = -\frac{1}{2}X \tag{2.50}$$

$$\bar{\mathbf{\Gamma}}_{1212} = \bar{\mathbf{\Gamma}}_{1313} = \bar{\mathbf{\Gamma}}_{2323} = -\frac{1}{2}X \tag{2.51}$$

with X being described by following formulas, depending on the lattice (RC, BCC, FCC):

$$X_{RC} = \frac{(r/d)^3}{3G_m(1-\nu_m)}(2.3322 - 7.4597(r/a)^2) \tag{2.52}$$

$$X_{BCC} = \frac{(r/d)^3}{3G_m(1-\nu_m)}(-1.4414 + 7.4555(r/a)^2) \tag{2.53}$$

$$X_{FCC} = \frac{(r/a)^3}{3G_m(1-\nu_m)}(-2.5643 + 18.0617(r/d)^2) \tag{2.54}$$

where X_{RC}, X_{BCC}, X_{FCC} are simplified functions for different layouts; r is radius of inclusions; a is cell size; G_m is shear modulus of matrix; and ν_m is Poisson's ratio of matrix.

Above stated formulas are compact and consume much less calculation time when implemented which is a significant factor in the design process. In figure 2.7, there is a comparison of time needed for different cluster diameters varying between $2a$ and $40a$. The more detailed the model, the longer it takes to perform the calculations. As the cluster size rises, the number of inclusions in the analyses rises even faster, thus affecting the needed time. This task consisted only of finding the effective mechanical parameters for the elastic regime. If viscoplasticity was considered, such calculation would need to be repeated in each time increment. This shows that pre-defined functions can serve as an efficient way of calculating effective material parameters for the most prevalent regular lattices, making the cluster model even more time-efficient.

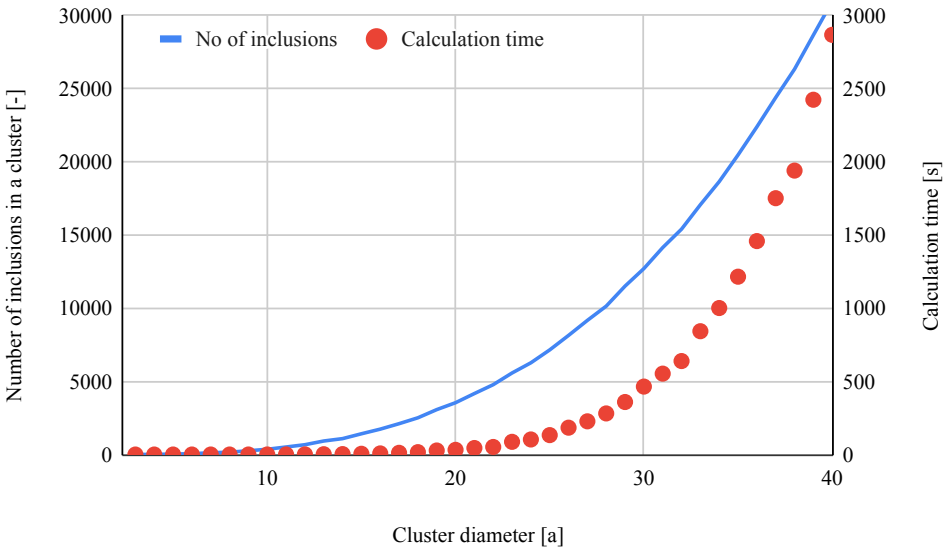

Figure 2.7: Number of inclusions and calculation time related to diameter of a cluster.

2.5 Comparison of the cluster and Mori-Tanaka models

The cluster model originates from the Mori-Tanaka scheme and aims to take into consideration the spatial distribution of inclusions which the original approach lacks. It is worth comparing how they behave in detail, i.e.: in what circumstances are geometry effects visible, how big they are and how they affect the results.

2.5.1 Two inclusions

First, let us consider an infinite matrix with only two inclusions and see what is the impact on the results depending on the distance between them. The inclusion diameter is equal to $d = 1$ ($r = 0.5$). The volume fraction of inclusions is assumed as zero ($f_i = 0\%$), with their volume being insignificant relative to the matrix and the same in each step. Parameters of used materials are listed in table 2.3. Please note that these are only "theoretical" materials with non-real values of an extreme contrast, used in order to emphasize and better visualise the effects of the model.

Table 2.3: Parameters of "theoretical" materials used for comparison with the Mori-Tanaka model.

	Matrix: soft	Inclusions: ultra hard
bulk modulus, K [GPa]	2.1667	21667
shear modulus, G [GPa]	1.0000	10000
Poisson's ratio, ν [-]	0.3	0.3

For the cluster model, in analogy to the Eshelby problem, we consider two inclusions in the infinite medium. We start with the inclusions touching each other, so the distance between their centres is equal to $L = 1d$. With each step the distance between them rises until it reaches the $L = 10d$.

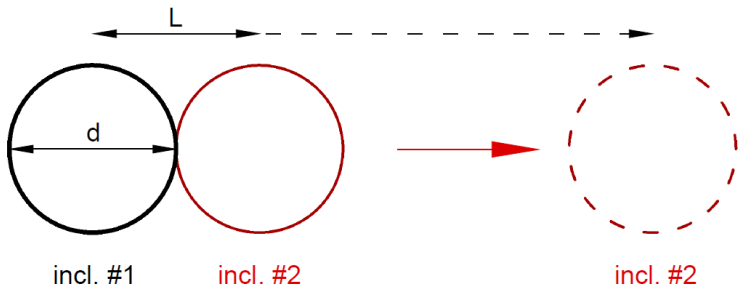

Figure 2.8: Distance between inclusions.

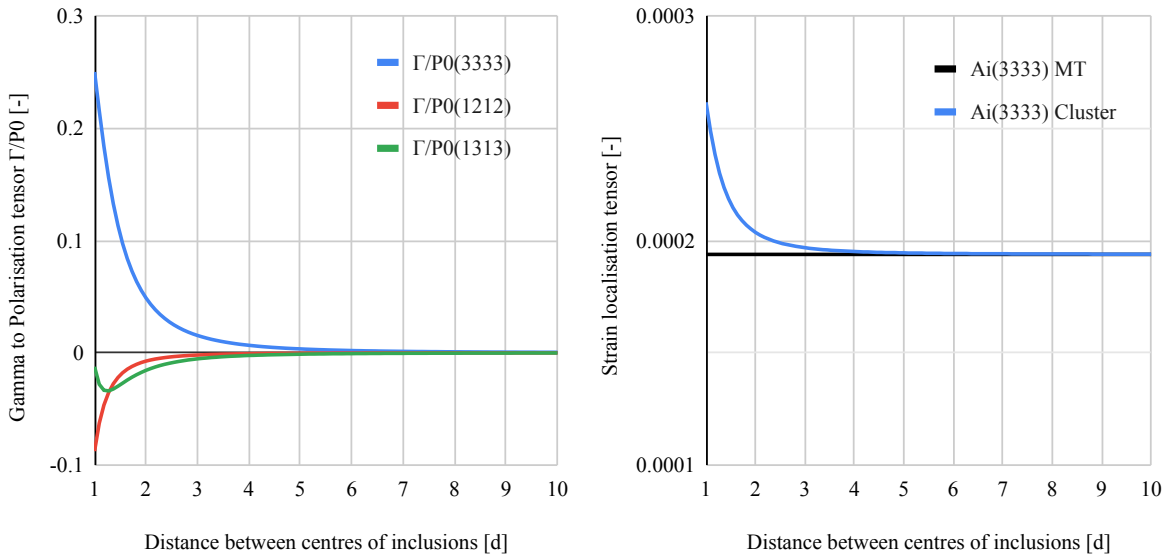

(a) (b)

Figure 2.9: Quotient $\bar{\mathbf{\Gamma}}_{ijkl}/\mathbb{P}_{0ijkl}$ for different distances between inclusions. Three independent tensor components: (3,3,3,3), (1,2,1,2) and (1,3,1,3) (a); and strain localisation tensor $\mathbb{A}_i$ for different distances between inclusions. Tensor component (3,3,3,3) (b). Note different scale on Y axes.

As explained before, the core of the cluster model is the interaction tensor $\bar{\mathbf{\Gamma}}$ which makes the difference from the classical Mori-Tanaka scheme. The interaction tensor $\bar{\mathbf{\Gamma}}$ appears in the equation for the strain localisation tensor $\mathbb{A}_i$, as per equation (2.5). If the volume fraction of inclusions is assumed as zero (negligible in an infinite matrix), this equation simplifies to:

$$\mathbb{A}_\mathrm{i} = (\mathbb{I} + (\mathbb{P}_0 - \bar{\mathbf{\Gamma}}))(\mathbb{C}_\mathrm{i} - \mathbb{C}_\mathrm{m})^{-1} \tag{2.55}$$

where $\mathbb{A}_\mathrm{i}$ is strain localisations tensor for inclusions; $\mathbb{I}$ is fourth order identity tensor; $\mathbb{P}_0$ is polarisation tensor; $\mathbb{C}_i, \mathbb{C}_m$ are stiffness tensors for inclusions and matrix; and $\bar{\mathbf{\Gamma}}$ is interaction tensor (here, as it is the case of only two inclusions, $\bar{\mathbf{\Gamma}} = \mathbf{\Gamma}^{12}$). The key to find the impact of interactions is to observe the relation between the $\bar{\mathbf{\Gamma}}$ and $\mathbb{P}_0$. They are presented in the form of a quotient $\bar{\mathbf{\Gamma}}_{ijkl}/\mathbb{P}_{0ijkl}$ (for several tensor components). The higher the quotient, the bigger the impact of interactions. This quotient has been calculated for each step and presented figure 2.9a. As it can be seen, the quotient $\bar{\mathbf{\Gamma}}_{ijkl}/\mathbb{P}_{0ijkl}$, and thus the impact of the interaction between inclusions, diminishes as the inclusions drift further apart. If the significance threshold is set to 1%, then the interaction might be described as insignificant after reaching a distance of 4.00 inclusion diameters between their centres. Additionally, for a better illustration, the strain interaction tensor $\mathbb{A}_\mathrm{i}$ was also calculated and is presented on figure 2.9b. For simplicity, only one tensor component $\mathbb{A}_{\mathrm{i}.3333}$ is shown, as for this component the impact of distance between inclusions is most visible.

2.5.2 Multiple inclusions

The next step is to perform the comparison between the cluster model and Mori-Tanaka scheme for the examples of entire composite microstructure. We consider a representative unit cell with either RC or BCC lattice (FCC is skipped for simplicity). In this case, the size of the unit cell is constant, while only the volume fraction of inclusions (i.e. their radius) changes.

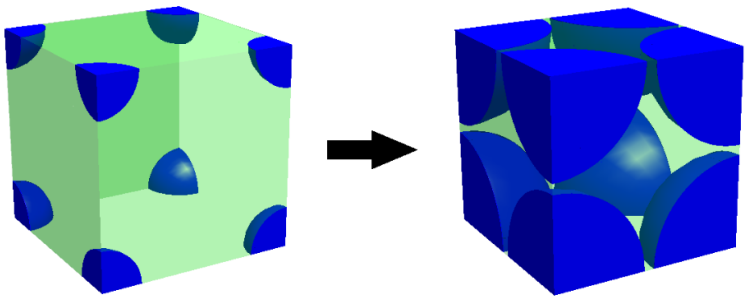

Figure 2.10: Different volume fraction of inclusions for a unit cell with RC lattice.

Volume fraction of inclusions varies between $f_i = 0\%$ and $f_i = 52\%$ (for RC) or $f_i = 0\%$ and $f_i = 65\%$ (for BCC and Mori-Tanaka). These particular values are chosen, as they are the maximum volume fraction of inclusions possible for each lattice respectively. Similarly to the previous point, we observe the relation between the $\bar{\mathbf{\Gamma}}$ and $\mathbb{P}_0$ which is presented in the form of a quotient $\bar{\mathbf{\Gamma}}_{ijkl}/\mathbb{P}_{0ijkl}$ (for two independent tensor components) in figure 2.11 for both RC and BCC. As it can be seen, interaction effects are much more visible compared with the previous example of only two inclusions in an infinite matrix, and the effect of interactions can be described as insignificant only for the tiniest volume fractions of inclusions (below $f_i = 1\%$ for a significance threshold set to 1%). It is interesting that the $\bar{\mathbf{\Gamma}}_{ijkl}/\mathbb{P}_{0ijkl}$ quotient rises, reaching the maximum value around $f_i = 33 - 34\%$ of volume fraction of inclusions, and then decreases. It means that the difference between the cluster model and Mori-Tanaka scheme is the biggest at this value. Moreover, it seems that the BCC lattice produces smaller interaction effects than the RC lattice. Possibly, the BCC lattice has a more unified spatial distribution of inclusions, being "less anisotropic" than the RC lattice.

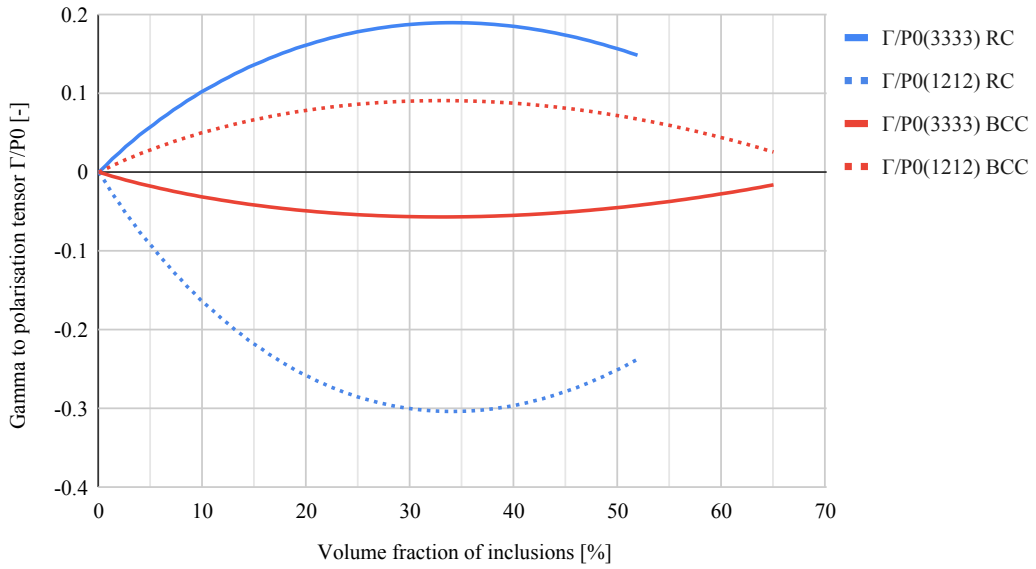

Figure 2.11: Quotient $\bar{\mathbf{\Gamma}}/\mathbb{P}_0$ for different volume fractions of inclusions. RC (blue) and BCC (red) lattices. Two independent tensor components: (3,3,3,3) and (1,2,1,2).

Additionally, for better illustration, the strain interaction tensor $\mathbb{A}_i$ has also been calculated, as well as the macroscopic material parameters: the effective bulk modulus ($\bar{K}$) and two effective shear moduli ($\bar{G}_1$, $\bar{G}_2$), as in section 2.3. These values are shown in figures 2.12-2.13. Figures 2.14-2.15 present the ratio of each value obtained from the cluster model to value obtained from the Mori-Tanaka scheme. The FCC lattice was omitted for simplicity, as it gives results very close to the BCC lattice.

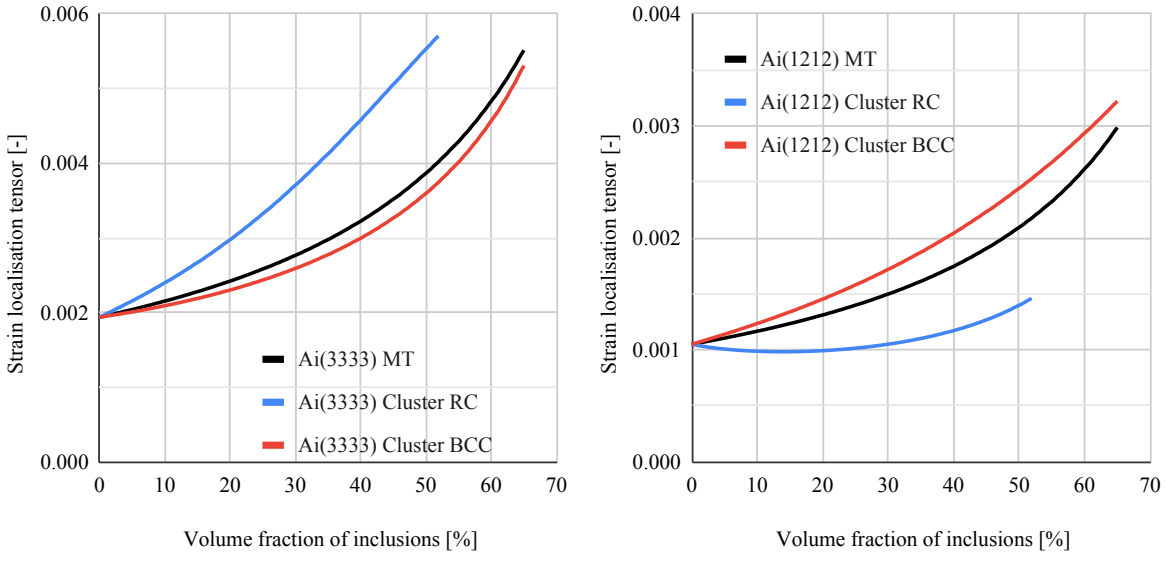

(a) (b)

Figure 2.12: Strain localisation tensor $\mathbb{A}_i$ for Mori-Tanaka and cluster model. RC (blue) and BCC (red) lattices. Tensor component (3,3,3,3) (a); and (1,2,1,2) (b). Note different scale on Y axes.

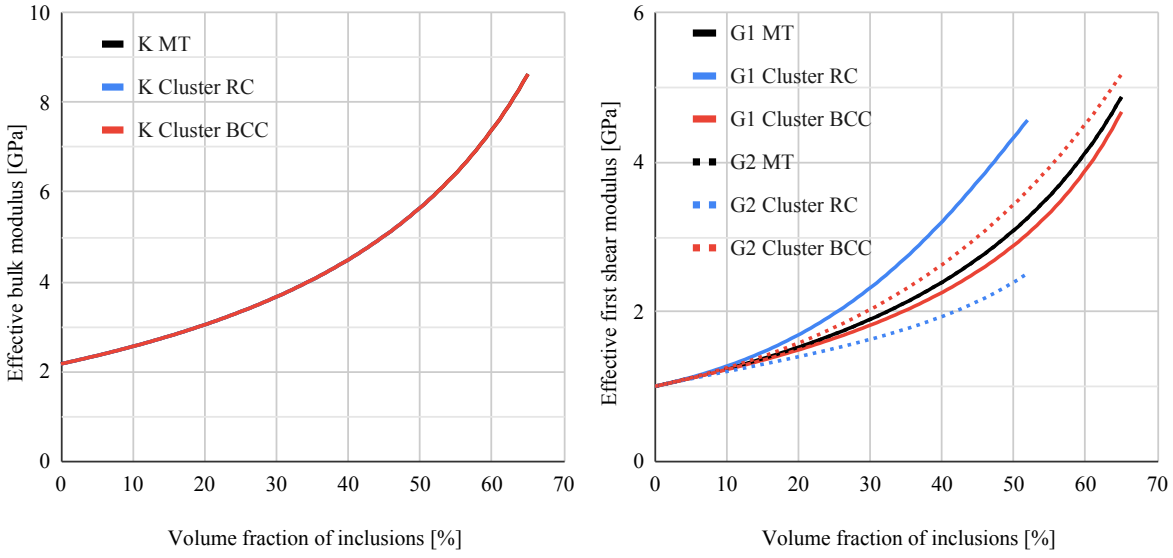

(a) (b)

Figure 2.13: Effective bulk modulus $\bar{K}$ (a); and Effective shear moduli $\bar{G}_1$, $\bar{G}_2$ (b) for Mori-Tanaka and cluster model. RC (blue) and BCC (red) lattices.

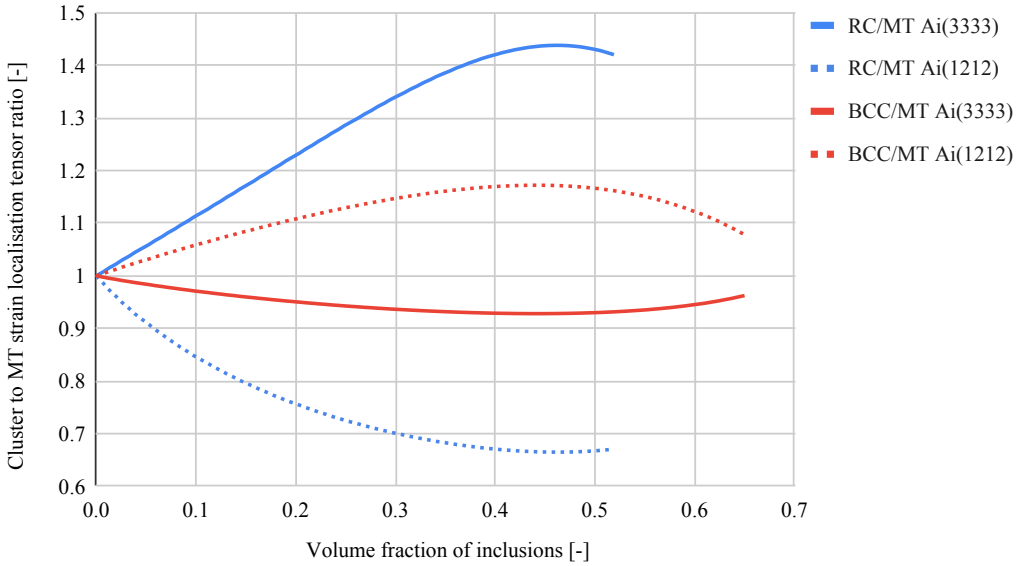

Figure 2.14: Cluster-to-Mori-Tanaka ratio for strain localisation tensor $\mathbb{A}_i$. RC (blue) and BCC (red) lattices. Two independent tensor components: (3,3,3,3) and (1,2,1,2).

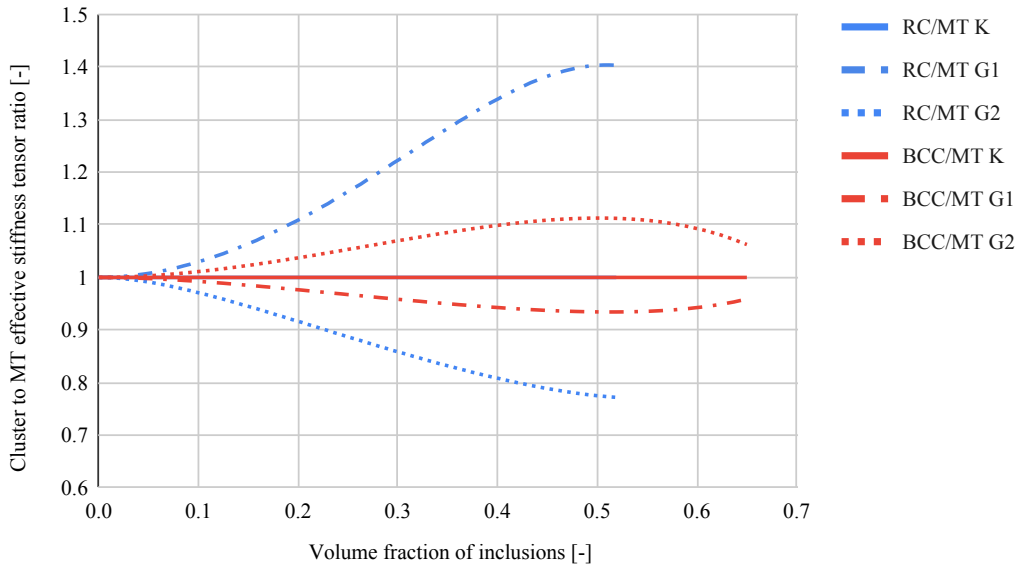

Figure 2.15: Cluster-to-Mori-Tanaka ratio for bulk modulus $\bar{K}$ and shear moduli $\bar{G}_1$, $\bar{G}_2$. RC (blue) and BCC (red) lattices. The bulk modulus is the same for both lattices.

For strain localisation tensor $\mathbb{A}_i$ and the shear moduli $\bar{G}_1$, $\bar{G}_2$ there is a visible difference between the cluster model and the classical Mori-Tanaka scheme. As previously, only tiniest volume fractions of inclusions (below $f_i = 1\%$ for strain localisation tensor and below $f_i = 5\%$ for effective shear moduli) present insignificant impact of interactions between inclusions. It shows that the cluster model gives a chance to tackle the problem of describing the interaction effects between inclusions that the original scheme lacks. The bulk modulus $\bar{K}$, depending only on the volume fraction of inclusions, is the same for both models. When comparing the two lattices, the Mori-Tanaka scheme gives results between them, although always closer to the BCC lattice, i.e. the "less anisotropic one". Also, the similar behaviour of the results getting closer to the Mori-Tanaka scheme at the higher volume fractions of inclusions is observed.

2.6 Cluster model for random microstructures

Previous sections concerned regular lattices with cubic symmetry, but the cluster model is also suitable for other types of microstructures, including the random ones. Here, another factor comes into the question: for the same volume fraction of inclusions, the spatial distribution of inclusions (i.e. their layout) might be completely different. Each time a new sample is generated, a completely new layout is produced. The classical Mori-Tanaka scheme would give the identical outcomes for each generation. The cluster model, however, should show at least small differences between them.

Another question is how does the number of inclusions in a sample affect the results? For example, there might be samples with 5, 50 or 500 inclusions inside, but with different sizes - thus all having the same volume fraction of inclusions. Again, the classical scheme would show the same outcomes, no matter the sample type, while the cluster model could provide the consequence of their geometry.

In this section, these random types of microstructures are explored. Different types of samples are generated: with $n = 5, 10, 100, 1000$ randomly-spaced inclusions, all having the same volume fraction of inclusions of $f_i = 20\%$. For each type, 20 different generations are analysed. In each case, the centremost inclusion is selected as the base inclusion. For simplicity, the calculations are performed assuming single-family situation, so it is assumed that all inclusions for the given generation carry the same strain as the base inclusion. Material parameters are listed in table 2.4. Please note that these are only "theoretical" materials, with non-real values of extreme contrast, used in order to emphasize and better visualise the effects of the model.

Table 2.4: Parameters of "theoretical" materials used.

	Matrix: soft	Inclusions: ultra hard
bulk modulus, K [GPa]	2.1667	21667
shear modulus, G [GPa]	1.0000	10000
Poisson's ratio, ν [-]	0.3	0.3
thermal conductivity, k [W/(m·K)]	1	10000

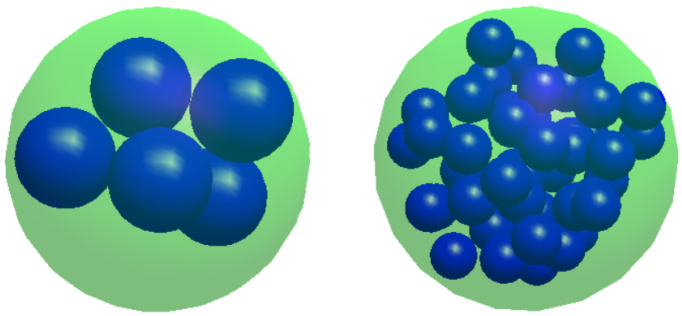

Figure 2.16: Samples with different numbers of randomly-spaced inclusions: 5 (left); and 50 (right).

The tracked outcome values are the same material parameters as in section 2.3, i.e.: macroscopic effective bulk modulus $\bar{K}$, two macroscopic effective shear moduli $\bar{G}_1$, $\bar{G}_2$ and macroscopic coefficient of thermal expansion ($\bar{k}$). Additionally, for each type and generation, the ratio between two shear moduli $\bar{G}_1/\bar{G}_2$ is calculated as a measure of how isotropic each sample is. The results are presented in tables 2.5-2.9, as well as in figures 2.17-2.21 for chosen types of samples. For each type of sample, the mean value, the standard deviation and comparison with the Mori-Tanaka scheme are presented. The latter was calculated as follows:

$$Dev_{MT} = \sqrt{(\mu - MT)^2} \tag{2.56}$$

where μ is a mean value obtained from the cluster model; and MT is a value obtained from the Mori-Tanaka scheme.

It can be observed from the results that the cluster model indeed shows the impact of the specific size, number and spatial distribution of inclusions, even for the same volume fraction of inclusions. At the same time, the classical Mori-Tanaka scheme lacks this possibility, resulting in the same value for each scenario.

Intuitively, the more inclusions are there, the more consistent the results should be. However, it is not observed. For some outcome macroscopic parameters, the standard deviation is the lowest for the 5-inclusion case (bulk modulus, thermal conductivity), while for 1000-inclusion case it is the highest (first and second shear moduli). Comparison to the Mori-Tanaka scheme gives similar conclusions. Moreover, it seems that for the bulk modulus and thermal conductivity, the cluster model generally gives higher outcome values than the Mori-Tanaka schemes. Thus, it is not possible to judge what number of inclusions in random layouts gives results more consistent with the Mori-Tanaka model. Further studies are needed in which, for example, multi-family variant of the cluster model will be used.

Table 2.5: Results for macroscopic bulk modulus $\bar{K}$ for multiple generations of random samples. Different numbers of inclusion and Mori-Tanaka scheme for comparison.

	Bulk modulus $\bar{K}$ [GPa]						
Sample type	5 incl.	10 incl.	50 incl.	100 incl.	500 incl.	1000 incl.	MT
Mean	3.0558	3.0655	3.0554	3.0610	3.0562	3.0560	3.0415
Standard dev.	0.0056	0.0165	0.0075	0.0117	0.0079	0.0076	0.0
Dev_{MT}	0.01428	0.02398	0.01390	0.01953	0.01468	0.01450	0.0

Table 2.6: Results for macroscopic first shear modulus $\bar{G}_1$ for multiple generations of random samples. Different numbers of inclusion and Mori-Tanaka scheme for comparison.

	First shear modulus $\bar{G}_1$ [GPa]						
Sample type	5 incl.	10 incl.	50 incl.	100 incl.	500 incl.	1000 incl.	MT
Mean	1.5305	1.5770	1.5381	1.5575	1.5481	1.5572	1.5249
Standard dev.	0.0274	0.0409	0.0255	0.0394	0.0338	0.0413	0.0
Dev_{MT}	0.00564	0.05216	0.01321	0.03262	0.02326	0.03230	0.0

Table 2.7: Results for macroscopic second shear modulus $\bar{G}_2$ for multiple generations of random samples. Different numbers of inclusion and Mori-Tanaka scheme for comparison.

	Second shear modulus G_2 [GPa]						
Sample type	5 incl.	10 incl.	50 incl.	100 incl.	500 incl.	1000 incl.	MT
Mean	1.5462	1.5389	1.5473	1.5397	1.5394	1.5368	1.5249
Standard dev.	0.0167	0.0227	0.0188	0.0277	0.0252	0.0291	0.0
Dev_{MT}	0.02137	0.01405	0.02245	0.01480	0.01459	0.01193	0.0

Table 2.8: Results for ratio between two macroscopic shear moduli $\bar{G}_1/\bar{G}_2$ for multiple generations of random samples. Different numbers of inclusion and Mori-Tanaka scheme for comparison.

	Shear moduli ratio $\bar{G}_1/\bar{G}_2$ [-]						
Sample type	5 incl.	10 incl.	50 incl.	100 incl.	500 incl.	1000 incl.	MT
Mean	0.9901	1.0252	0.9943	1.0122	1.0062	1.0141	1.0000
Standard dev.	0.0284	0.0375	0.0276	0.0418	0.0374	0.0458	0.0
Dev_{MT}	0.00988	0.02519	0.00567	0.01225	0.00620	0.01406	0.0

Table 2.9: Results for isotropised macroscopic thermal conductivity $\bar{k}$ for multiple generations of random samples. Different numbers of inclusion and Mori-Tanaka scheme for comparison.

	Isotropised hermal conductivity k [W/(m·k)]						
Sample type	5 incl.	10 incl.	50 incl.	100 incl.	500 incl.	1000 incl.	MT
Mean	1.7821	1.8029	1.7799	1.7912	1.7820	1.7794	1.7497
Standard dev.	0.0127	0.0417	0.0159	0.0249	0.0183	0.0161	0.0
Dev_{MT}	0.03245	0.05320	0.03016	0.04153	0.03230	0.02973	0.0

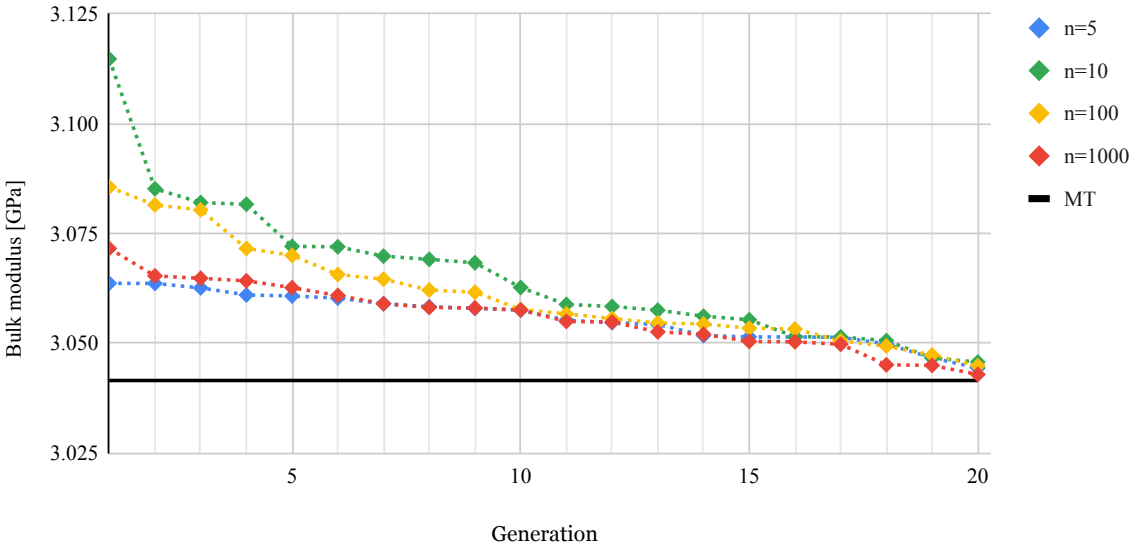

Figure 2.17: Distribution of results for different generations of samples for macroscopic bulk modulus $\bar{K}$. Samples with $n = 5, 10, 100, 1000$ inclusions compared with the Mori-Tanaka (black) scheme. Values sorted from the largest to the lowest.

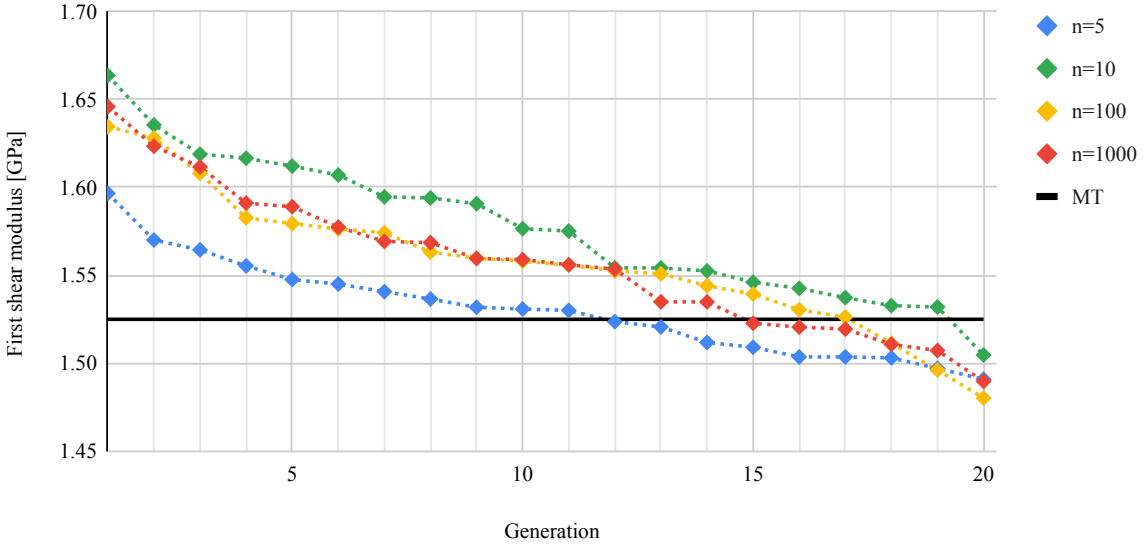

Figure 2.18: Distribution of results for different generations of samples for macroscopic first shear modulus $\bar{G}_1$. Samples with $n = 5, 10, 100, 1000$ inclusions compared with the Mori-Tanaka (black) scheme. Values sorted from the largest to the lowest.

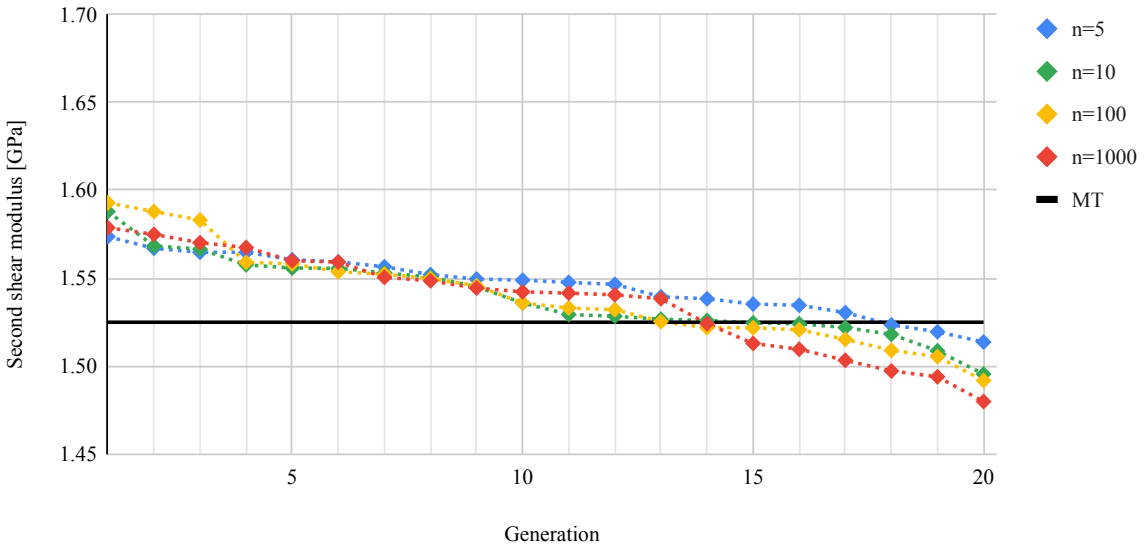

Figure 2.19: Distribution of results for different generations of samples for macroscopic second shear modulus $\bar{G}_2$. Samples with $n = 5, 10, 100, 1000$ inclusions compared with the Mori-Tanaka (black) scheme. Values sorted from the largest to the lowest.

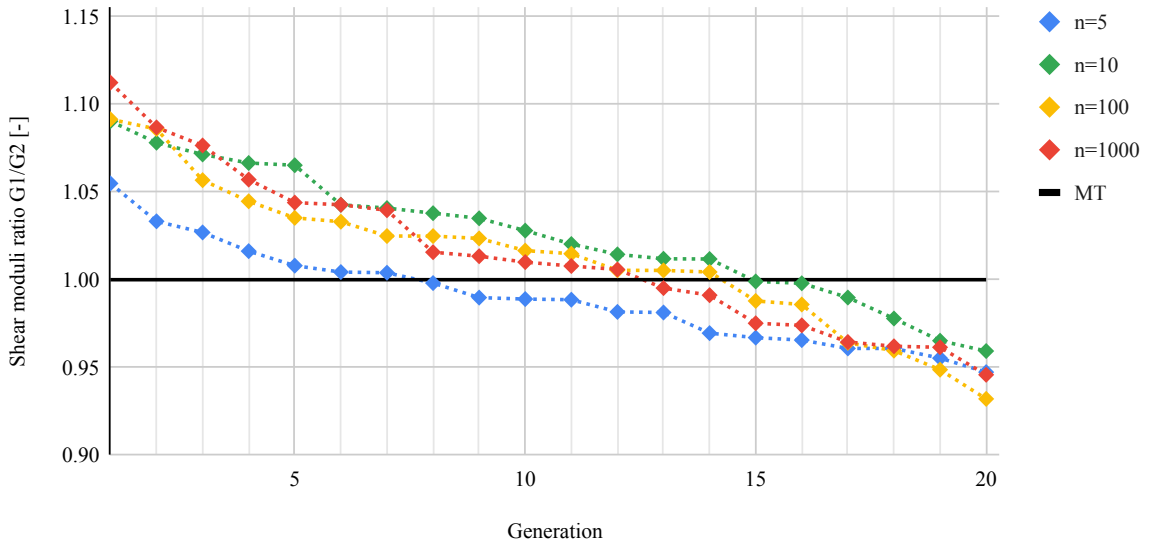

Figure 2.20: Distribution of results for different generations of samples for ratio between two macroscopic shear moduli $\bar{G}_1/\bar{G}_2$. Samples with $n = 5, 10, 100, 1000$ inclusions compared with the Mori-Tanaka (black) scheme. Values sorted from the largest to the lowest.

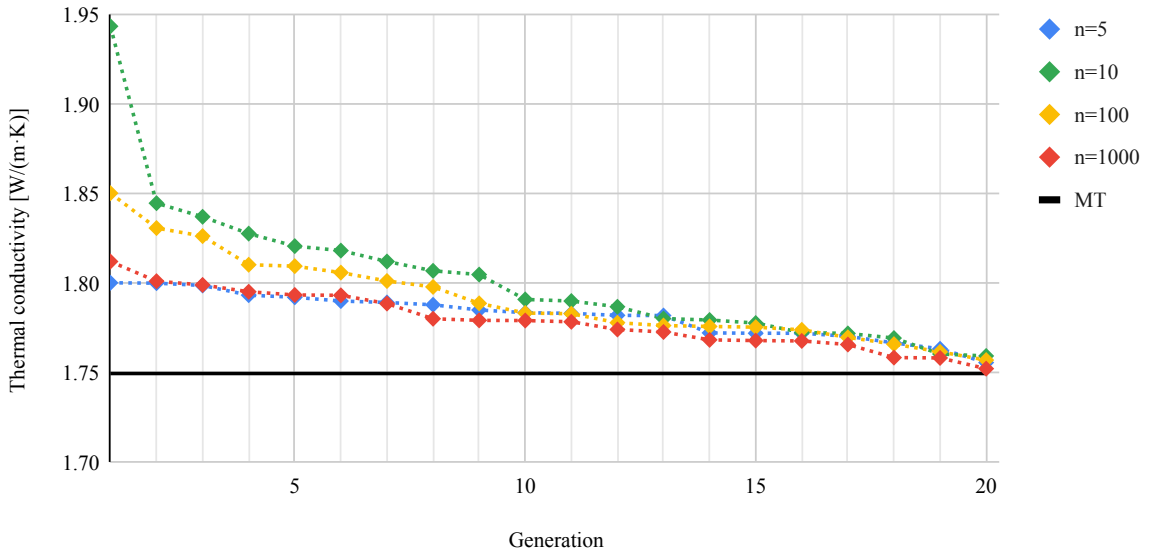

Figure 2.21: Distribution of results for different generations of samples for isotropised macroscopic thermal conductivity $\bar{k}$. Samples with $n = 5, 10, 100, 1000$ inclusions compared with the Mori-Tanaka (black) scheme. Values sorted from the largest to the lowest.

2.7 Summary

The cluster model is an extension of the classical Mori-Tanaka mean-field model, aiming to describe the average macroscopic parameters of a material with a given microstructure. The core principle is to take into account the interactions between inclusions within the analysed space, in addition to the interactions between the inclusions and the matrix. To achieve this, the analysis is performed for a spherical cluster of inclusion. It is established by choosing a reference inclusion within the basic unit cell (usually, the centremost one) and then defining a sphere, with its centre point in this reference inclusion. In calculations, only inclusions with centre points located within this sphere are considered.

In order to capture and represent the proper behaviour of the material, the cluster should have appropriate size. Three regular lattices are examined: regular cubic (RC), body-centred cubic (BCC) and face-centred cubic (FCC), as they are the most prevalent lattices in the field of micromechanics. Comparison of mechanical and thermal results from different cluster sizes suggests that, in order to achieve stable and representative results, the cluster should have diameter equal to at least 16 unit cell widths for RC and BCC lattices, or 15 unit cell widths for FCC lattice.

When compared to the classical Mori-Tanaka Model, aforementioned interactions seem to play the most visible role with distances between centres of inclusions equalling up to 4.00 inclusion diameters for a simple case of single inclusions in an infinite matrix. When comparing regular lattices, the impact is visible practically for any scenario. Only tiniest volume fractions of inclusions (below $f_i = 1\%$) show negligible effects. The cluster model captures the impact the microstructure on the anisotropy of the macroscopic material parameters of the composite, what classical mean-field models, e.g. Mori-Tanaka scheme, lack.

The cluster model allows to perform calculations not only for regular lattices, but also for irregular ones. Even with the same volume fraction of inclusions, the effective material parameters of a composite can still vary depending on the size, number and spatial distribution of inclusions. Each generation of a cell with randomly spaced inclusions can produce slightly different results. However, more inclusions within the sample does not necessarily mean more stable results among generations.

The core of the cluster model is the interaction tensor, calculation of which is the most time-consuming part of the process. However, it depends only on: inclusion size, unit cell size and material parameters for the matrix. Thus, as long as the inclusions are spherical, the lattice is regular, and identical material properties for the matrix are applied, the interaction tensor will always be the same. This allows to find pre-defined formulas for most prevalent regular lattices that are compact and consume much less calculation time when implemented, making the cluster model an efficient tool for tasks requiring multiple calculations and iterations.

Chapter 3

Validation of the cluster model in the elastic regime

3.1 Introduction

This chapter consists of validation of the cluster model in the elastic regime. The mail tool used for this purpose is the numerical homogenisation employing the finite elements method (FEM). This allows to compare prediction of the analytical mean-field model (i.e macroscopic elastic properties, mean stress and strains per phase obtained under assumptions of uniform fields within the phases) to a numerical full-field model (i.e. the same quantities resulted from numerical averaging over the non-uniform fields obtained in FE analysis). A significant part of the chapter is devoted to mesh convergence tests, as a proper definition of mesh size is vital for obtaining reliable results when using numerical methods. Finally, experimental data from initial experiments on 3D-printed porous samples are also used for the model validation.

3.2 Numerical finite element homogenisation

3.2.1 Mesh convergence test for a single-inclusion cell

In the finite elements method results may be dependent not only on the geometry, boundary conditions and material parameters, but also on the mesh size of finite elements discretisation. The same input models can produce different results for different mesh sizes. Thus, it is important to perform the mesh convergence test which aims to find the appropriate mesh size for the results to be trustworthy.

Unlike the cluster model, in the FEM, the sample is a unit volume element: a cube with periodic boundary conditions which imply that if any two FEM mesh nodes A and B lie on one side of a volume element, while nodes C and D are their periodic images, respectively, on the opposite side of the volume element, then:

$$\mathbf{u}_A - \mathbf{u}_C = \mathbf{u}_B - \mathbf{u}_D \tag{3.1}$$

where $\mathbf{u}_A$, $\mathbf{u}_B$, $\mathbf{u}_C$ and $\mathbf{u}_D$ are displacements of the respective nodes. To implement the periodic displacement boundary conditions for a given macroscopic strain tensor $\bar{\boldsymbol{\varepsilon}}$ of the unit volume element, the nodes at four vertices of the volume element are assigned displacements of the form:

$$\mathbf{u}_i = \bar{\boldsymbol{\varepsilon}} \cdot \mathbf{X}_i, \quad i \in \{0, 1, 2, 3\} \tag{3.2}$$

where $\mathbf{X}_0 = (0, 0, 0)$, $\mathbf{X}_1 = (1, 0, 0)$, $\mathbf{X}_2 = (0, 1, 0)$ and $\mathbf{X}_3 = (0, 0, 1)$, while all periodic relations in equations (3.1) are enforced during the FEM solution by taking node A as vertex 0 and C as vertex 1, 2 or 3, depending on the wall pairing. Examples are visualised in figure 3.1.

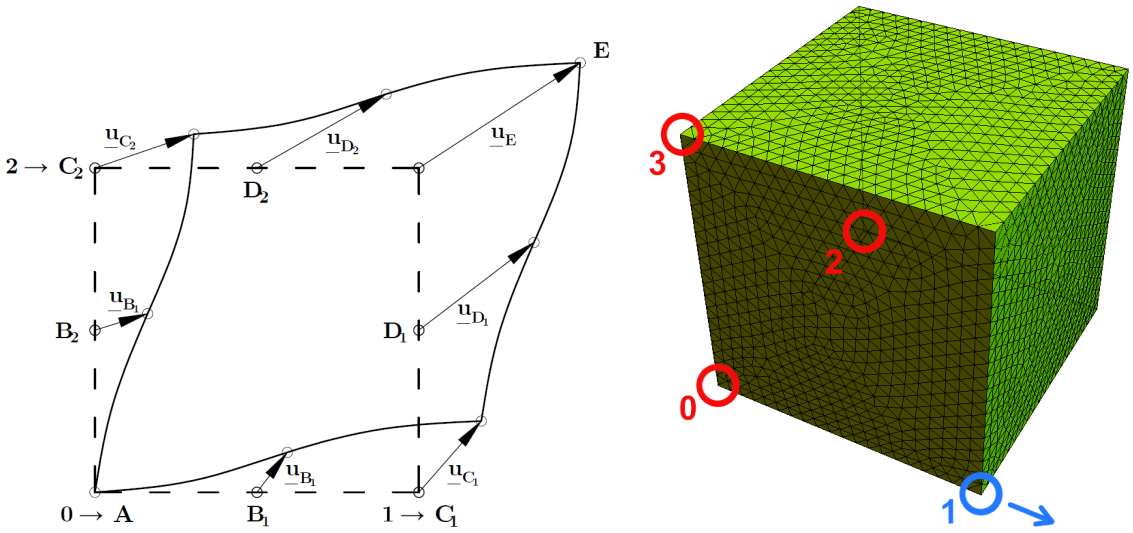

Figure 3.1: Periodic boundary conditions. A 2D general example (left); and 3D case used in the mesh convergence test.

The first convergence test is performed on the simplest possible case of a single inclusion inside the middle of a cube, as in figure 3.2. The inclusion size is $r_i = 0.40$m, and the cube (and thus the unit cell) size is 1x1x1m (in fact, any length unit can be taken as the presented results are not dependent on the length scale). Material parameters are listed in table 3.1. The model is meshed with different sizes of mesh, from very coarse to very fine, with mesh size: 0.50m, 0.25m, 0.15m, 0.10m, 0.05m and 0.03m, where mesh size is defined as the maximum element size. Difference between meshes can be seen in figure 3.3. Four-node tetrahedral elements with linear shape functions and one Gauss point are used. In this case, stresses and strains are uniform within an element. The sample is subject to periodic boundary conditions, with the overall uniaxial strain along the (1,0,0) direction, i.e. the unit cell's edge, as specified below:

$$\bar{\varepsilon} = \begin{bmatrix} 0.01 & 0 & 0 \\ 0 & 0 & 0 \\ 0 & 0 & 0 \end{bmatrix} \tag{3.3}$$

Table 3.1: Parameters of materials used for mesh convergence test

	matrix: soft	inclusions: hard
Young Modulus, E [GPa]	30.0	200
shear modulus, G [GPa]	12.5	76.92
Poisson's ratio, ν [-]	0.2	0.3

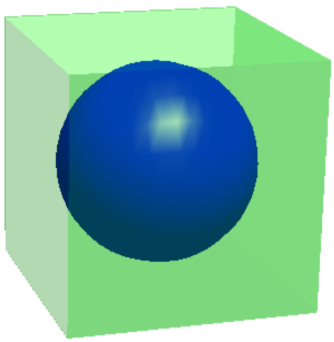

Figure 3.2: Single-inclusion cell for mesh convergence test.

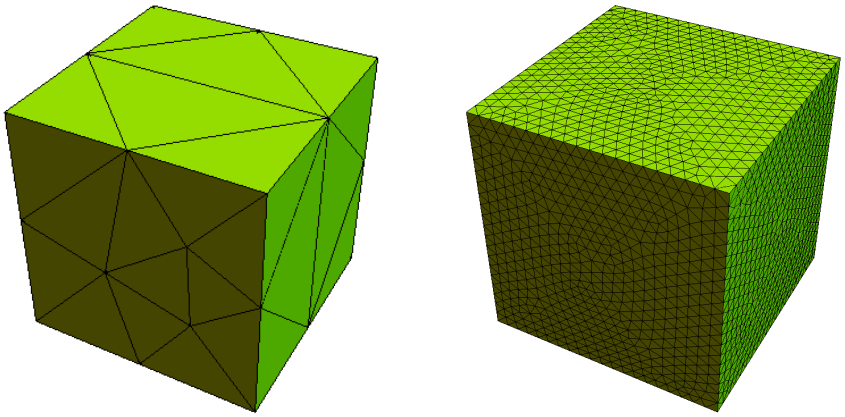

Figure 3.3: Different meshes for the single-inclusion cell. Mesh size: 0.50 m (left); and 0.05 m (right).

Tracked results are tensile components: of macroscopic stress $\bar{\boldsymbol{\sigma}}$, of stress in matrix $\boldsymbol{\sigma}_m$ and of stress in inclusion $\boldsymbol{\sigma}_i$ along the (1,0,0) direction, i.e. the unit cell's edge. They are shown in the figure 3.4, relative to the mesh size or to the number of total finite elements. The results converge to a certain value and the difference between the results gets lower as the mesh is denser.

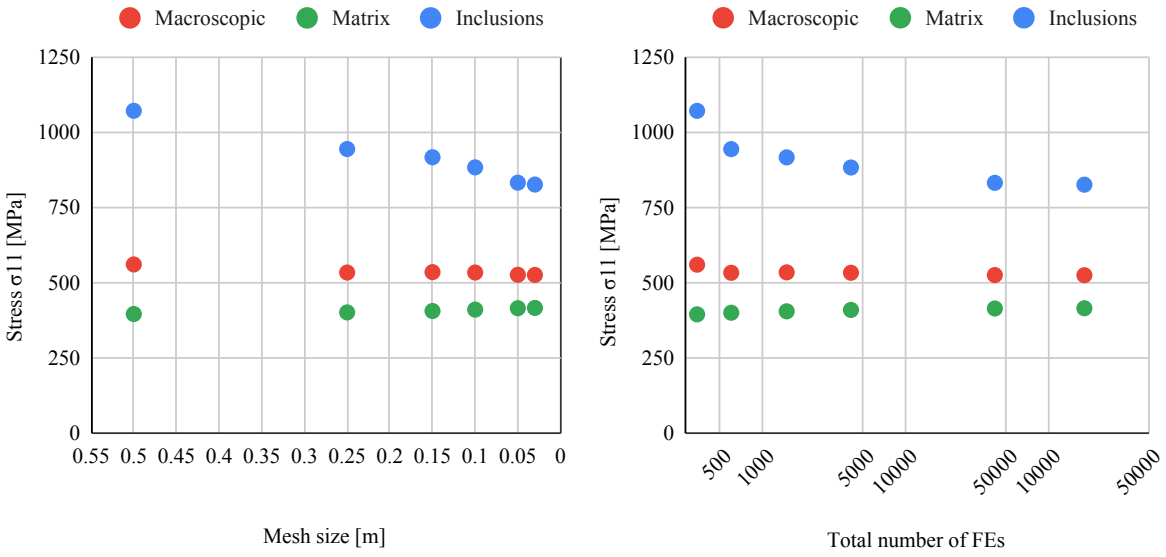

(a) (b)

Figure 3.4: Dependence of σ_{11} stress component on: mesh size (a); and total number of finite elements (b). Single-inclusion model.

It is well visible that the results are changing along with the mesh sizes. The biggest difference is seen among the stresses in the inclusion. The reason might be the fact that the inclusion is a sphere that loses its shape after meshing. Finite elements have straight edges which cause loss of the real curvature of the sphere. The finer the mesh, the smaller the elements and smaller the difference between the approximated shape and the real one, as visualised in figure 3.5. When meshing, only the maximum size of a finite element is set. It means that by the mesh size defined to e.g. 0.25 m, the software tries to mesh it as coarse as possible, but not exceeding this value. On the other hand, there is no minimum size, so when it is impossible to mesh with elements of size of 0.25 m, the software generates smaller elements. It is visible when comparing two most coarse meshes: 0.50m and 0.25m. In these cases, the number of finite elements in the sphere is the same, meaning that the software assumes that 0.50m is too coarse to mesh a spherical inclusion.

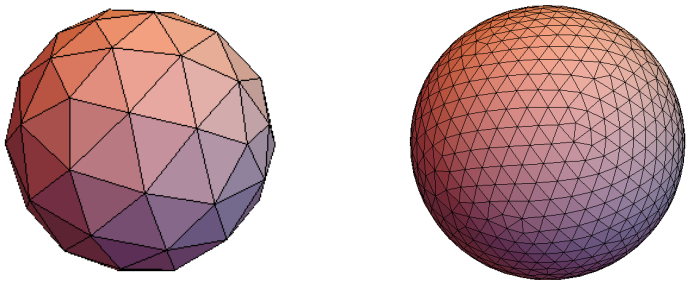

Figure 3.5: Different meshes for the inclusion. Mesh size: 0.50 m (left); and 0.05 m (right).

As the biggest differences occur among the results for the inclusion, it is reasonable to concentrate on these and explore, for example, the relationship between the outcomes and the average volume of one finite element in the inclusion. The inclusion radius is $r_i = 0.40m$, thus its volume is $V_i = 0.2681m^3$. Dividing the volume by the number of finite elements in the inclusion, we achieve the average volume of one finite element in the inclusion:

$$V_{fe.av.i} = \frac{V_i}{n_{fe.i}} \tag{3.4}$$

where $V_{fe.av.i}$ is average volume of finite element in inclusion; V_i is volume of inclusion; and $n_{fe.i}$ is number of finite elements in the inclusion. Its relationship to σ_{11} stresses is shown in figure 3.6a.

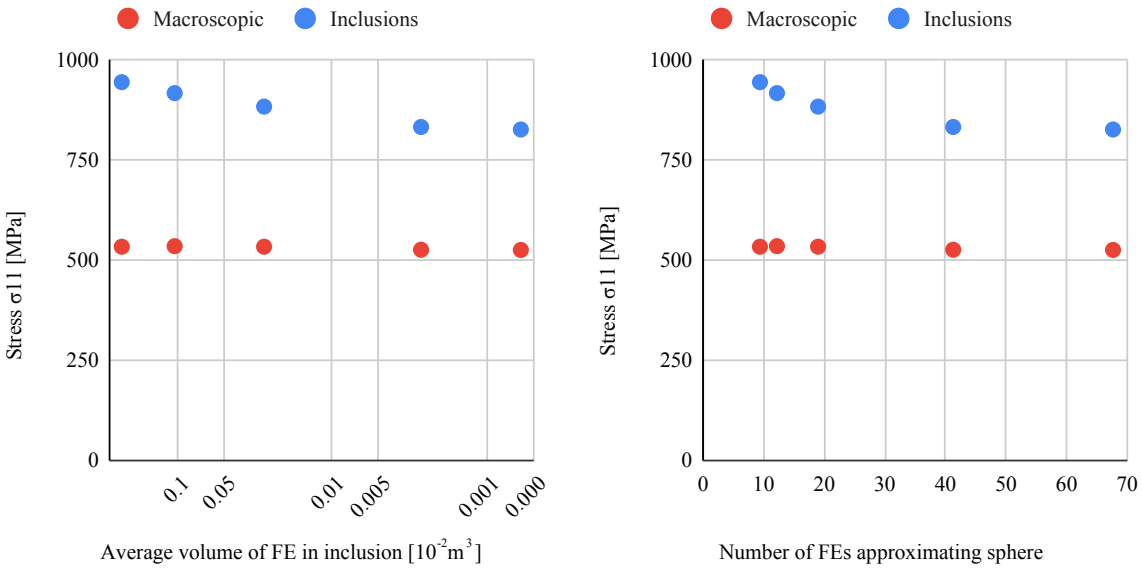

Figure 3.6: Dependence of σ_{11} stress component on: average size of one finite element in the inclusion (a); and number of elements approximating the sphere perimeter (b). Single-inclusion model.

The above mentioned value is a volumetric characteristic. Intuitively, we can guess that some linear measurement of how well the curvature of the inclusion is represented could also be used as a description. The inclusion radius is $r_i = 0.40m$, thus its perimeter is $l_i = 2.5133m$. As the maximum mesh size does not always correspond to the actual size of finite elements in the inclusion (as the number of finite elements in the inclusion is the same for 0.50m and 0.25m mesh), to approximate the average size of one finite element, we need to take its average volume calculated in equation (3.4). As the mesh consists of four-node tetrahedral elements, we can assume that, in average, they will be

close to regular tetrahedrons. The formula for a regular tetrahedron edge is as following:

$$a_{tetr} = \sqrt[3]{\frac{12V_{tetr}}{\sqrt{2}}} \tag{3.5}$$

where a_{tetr} is length of edge of average tetrahedron (i.e. average size of finite element in inclusion); and $V_{av.i}$ is volume of average tetrahedron (which can be assumed as previously calculated average volume of finite element in inclusion $V_{fe.av.i}$). This time, the ratio of inclusion perimeter to average size of finite element was taken into consideration, giving an estimation of how many elements are used to approximate the sphere. This relationship is presented in figure 3.6b.

$$n_{eax} = \frac{l_i}{a} \tag{3.6}$$

where n_{eax} is number of elements approximating a spherical inclusion; l_i perimeter of an inclusion; and a_{tetr} is length of edge of an average tetrahedron (average size of finite element in inclusion).

All those convergence tests aim to verify at which granularity the mesh is reliable enough by comparing all the results and verifying discrepancies between them. To visualise it, the σ_{11} stresses for the finest mesh (the most detailed mesh available) is set as a reference value. For each mesh, the ratio of σ_{11} to reference σ_{11} value was calculated and shown on the Y axis. X axis shows the number of finite elements approximating the sphere in the figure 3.7a. The same ratio was shown on the figure 3.7b, but the X axis shows the mesh size, so the comparison of the stress in the matrix is possible.

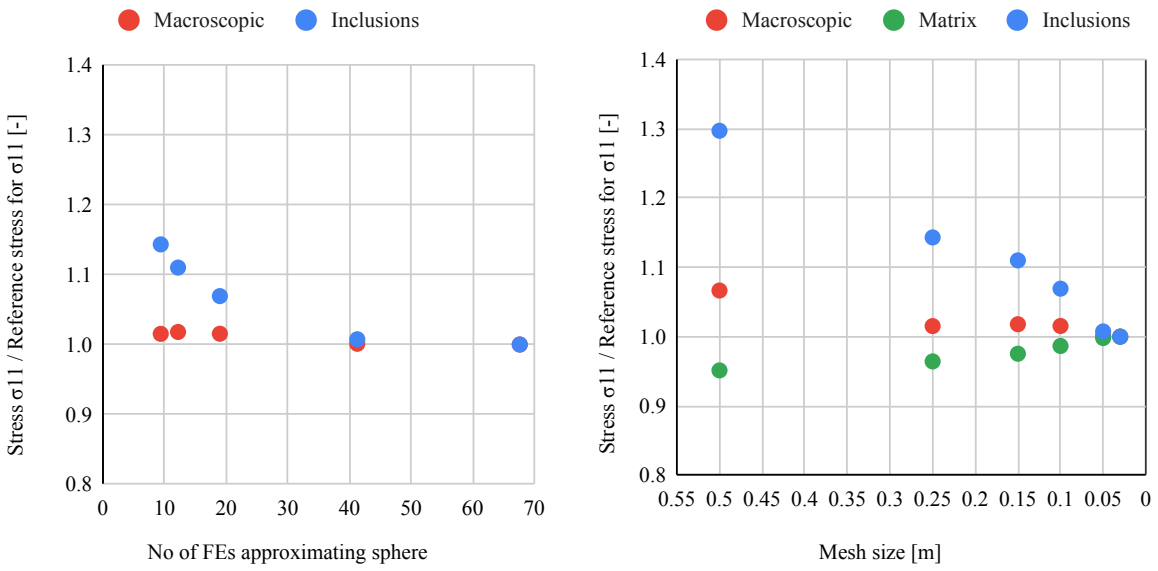

(a) (b)

Figure 3.7: Dependence of σ_{11}/reference σ_{11} ratio on: number of elements approximating the sphere (a); and mesh size (b). Single-inclusion model.

As it can be seen, the finer the mesh, the smaller the discrepancies. The results for the inclusion are especially prone to mesh granularity. For this example of an inclusion with radius $r_i = 0.40$m, the 0.05m mesh seems to be the coarsest acceptable one for further analysis, as the discrepancies are less than 1% relative to the reference mesh. In terms of dimensionless values, it translates to a sphere that is approximated with around 40 elements on its perimeter.

3.2.2 Mesh convergence test for a single inclusion cell with second-order finite elements

In the previous subsection, the calculations have been performed for four-node tetrahedron finite elements with linear shape functions. To achieve the acceptable mesh convergence, very fine meshes

are needed which corresponds to longer computation time. The other approach of achieving more precise results is to increase the order of shape functions for finite elements. In this subsection, the calculations are repeated for the same geometry and material data, with the only difference being the ten-node tetrahedron finite elements with quadratic shape functions, instead of linear ones. In this case, stresses and strains are not uniform within an element.

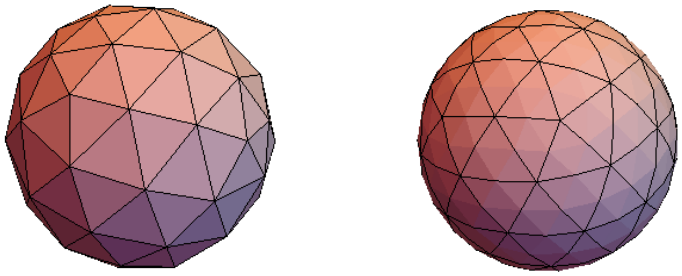

Figure 3.8: Different types of tetrahedron finite elements: with linear shape functions (left); and quadratic (right).

Similar to the previous subsection, the model is meshed with different sizes of mesh, from very coarse to fine: 0.50m, 0.25m, 0.15m, 0.10m and 0.05m, where mesh size is defined as the maximum element size. The mesh size of 0.03m was impossible to calculate, because the file size became too big for the script to run properly. The sample is subject to the exactly same periodic boundary conditions with the overall strain along the (1,0,0) direction, i.e. the unit cell's edge. As in the examples with linear shape functions, first it was tested what is the relationship between stress and mesh size or number of finite elements, as shown in figure 3.9.

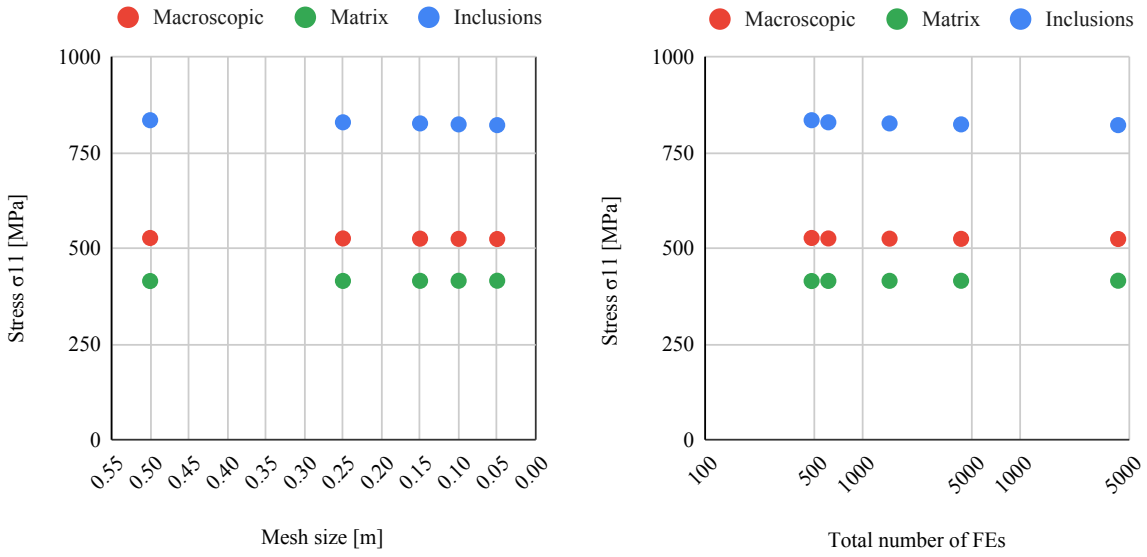

(a) (b)

Figure 3.9: Dependence of σ_{11} stress component on: mesh size (a); and to total number of finite elements (b). Single-inclusion model with quadratic elements.

As previously, with finer mesh, the results approach some asymptote value. However, differences between the coarser and finer meshes are much smaller than for the elements with linear shape functions. Thus, to visualise the trend, a reference value was set as the σ_{11} stresses for the finest mesh (0.05m - the most detailed mesh available). For each mesh size, the ratio σ_{11} to reference value of σ_{11} is calculated and shown on the Y axis. X axis shows the number of elements approximating the spheres (figure 3.10a) or the mesh size (figure 3.10b).

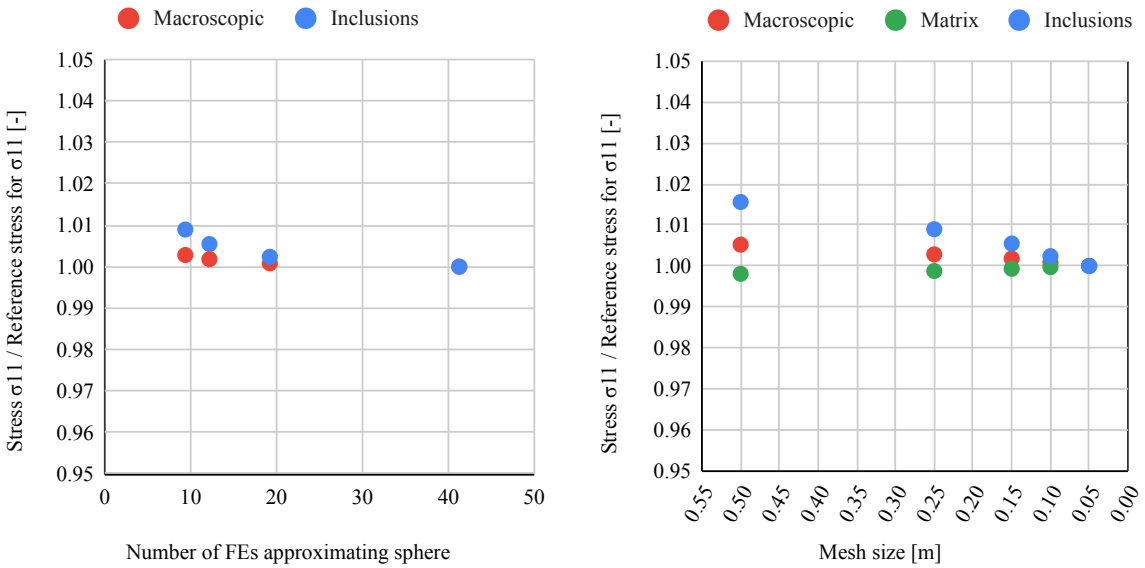

(a) (b)

Figure 3.10: Dependence on σ_{11}/reference σ_{11} ratio on: number of elements approximating the sphere (a); and to mesh size (b). Single-inclusion model with quadratic elements.

For the single-inclusion model with elements with linear shape functions, the acceptable mesh size was defined as 0.05 m (i.e. 40 finite elements approximating the sphere), where discrepancies were lowered to less than 1%. In the model with quadratic shape functions, such a level of convergence is reached for the 0.25m mesh (i.e. 10 finite elements approximating the sphere). That is a significant improvement, allowinng for much shorter calculation times.

3.2.3 Mesh convergence test for a cell with 5x5x5 regularly-spaced inclusions

Each cell has periodic boundary conditions. It means that on each wall, the displacements (in terms of the shape change of the wall) are the same as on the opposite wall (see figure 3.1). Such a setup mimics a cell that is a small cut-out from a bigger environment that has exactly the same setups copied in each direction. Theoretically, the results for a single-cell model should be the same as for a model of any number of inclusions placed in a regular cubic lattice. This section aims to test if the application of periodic boundary condition is correct.

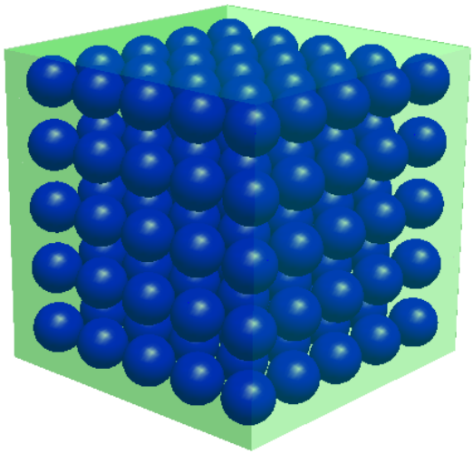

Figure 3.11: Regular 5x5x5 regular cubic lattice of inclusions for mesh convergence test.

The sample model is a unit cell with 125 regularly spaced inclusions forming a 5x5x5 regular cubic (RC) lattice, as visualised in figure 3.11. The sample size is thus 5x5x5m. Ten-node finite elements with quadratic shape functions are used. The same material data is used as in the single-cell scenarios. The model is meshed with different sizes of mesh, from very coarse to medium: 0.50m, 0.25m, 0.15m, where mesh size is defined as the maximum element size. Finer meshes were not possible to calculate, because of the file size becoming too big for the script to run properly. The unit cell is subject to the exactly same periodic boundary conditions, with the overall strain along the (1,0,0) direction, i.e. the unit cell edge. Results are shown in figures 3.12-3.13.

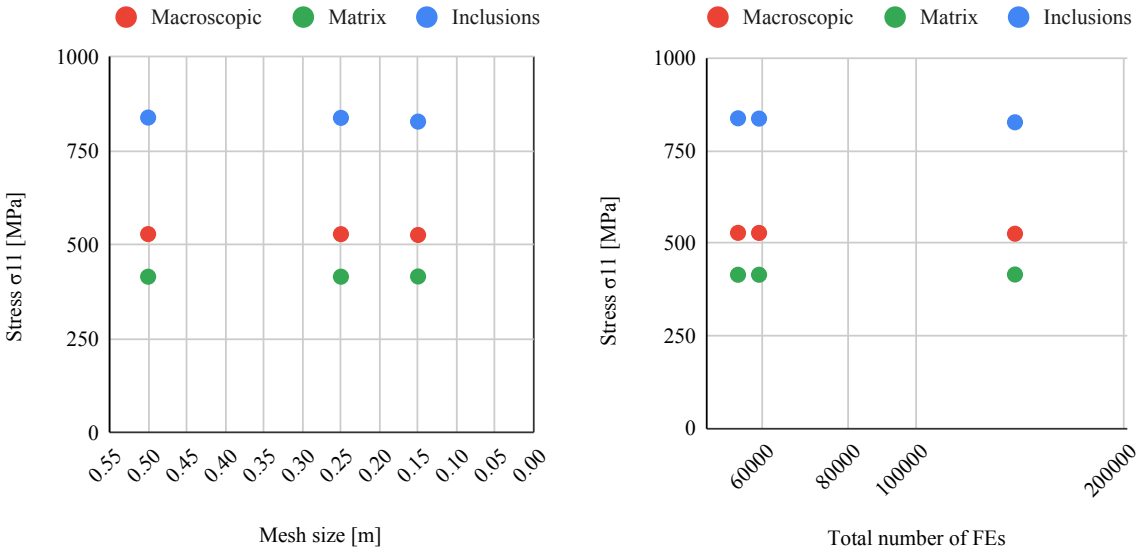

(a) (b)

Figure 3.12: Dependence of σ_{11} stress component on: mesh size (a); and total number of finite elements (b). Regular cubic 5x5x5 model with quadratic elements.

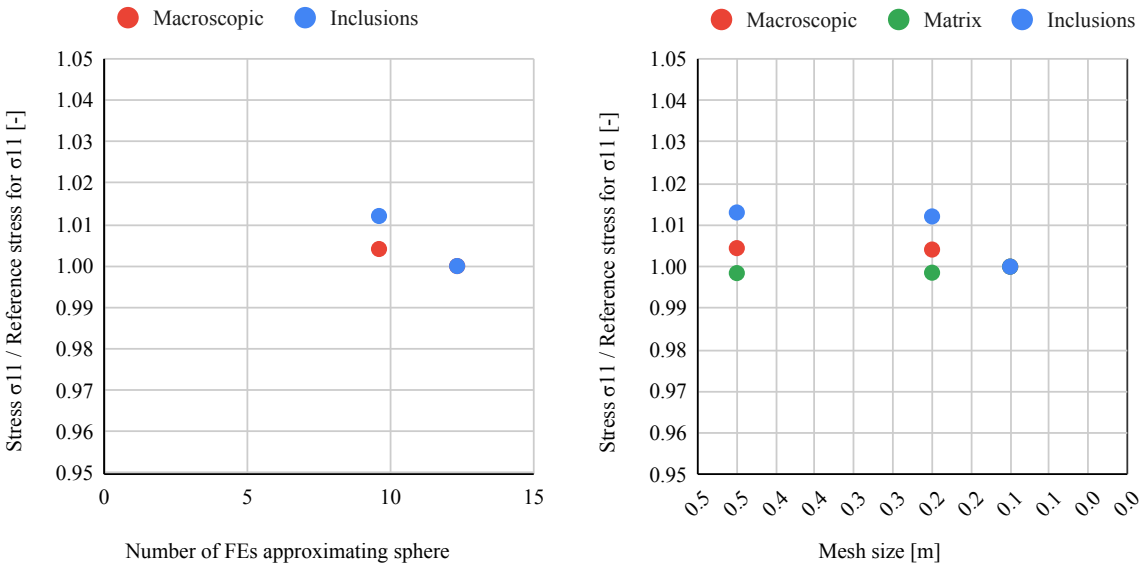

(a) (b)

Figure 3.13: Dependence of σ_{11}/reference σ_{11} ratio on: number of elements approximating the sphere (a); and mesh size (b). Regular cubic 5x5x5 model with quadratic elements.

The data set is much smaller than in the previous points, due to limitation of available computing power. However, it is possible to conclude that the inclusion stress value for the 0.15m mesh is $\bar{\sigma}_{11} = 826.83MPa$ for the 5x5x5 RC model, while for the corresponding single-inclusion model, such value was $\bar{\sigma}_{11} = 825.88MPa$. These values are very close to each other, showing that a single-inclusion setup, with proper periodic boundary conditions, can indeed act as a representative unit cell for bigger setups with a regular mesh.

3.2.4 Comparison of results and conclusion for mesh convergence tests

To compare different models, element orders and mesh sizes, following results are used:

1. macroscopic stress component in direction 1: $\bar{\sigma}_{11}$;
2. matrix stress component in direction 1: $\sigma_{m.11}$;
3. inclusion stress component in direction 1: $\sigma_{i.11}$.

Results are shown in tables 3.2 - 3.4. Each model has the same inclusion radii of $r_i = 0.40$m, so the resulting volume fraction of inclusions is $f_i = 26.81\%$.

Table 3.2: Results for macroscopic stress in direction 1 ($\bar{\sigma}_{11}$) for all models.

Mesh size	0.50m	0.25m	0.15m	0.10m	0.05m	0.03m
Single linear	559.72	532.79	534.19	532.88	525.34	524.78
Single quadratic	527.04	525.79	525.26	524.74	524.31	-
5x5x5 quadratic	527.81	527.63	525.47	-	-	-

Table 3.3: Results for stress in matrix in direction 1 ($\sigma_{m.11}$) for all models.

Mesh size	0.50m	0.25m	0.15m	0.10m	0.05m	0.03m
Single linear	394.78	400.17	404.78	409.43	414.17	415.00
Single quadratic	414.69	414.98	415.21	415.38	415.49	-
5x5x5 quadratic	414.51	414.55	415.15	-	-	-

Table 3.4: Results for stress in inclusions in direction 1 ($\sigma_{i.11}$) for all models.

Mesh size	0.50m	0.25m	0.15m	0.10m	0.05m	0.03m
Single linear	1070.87	943.75	916.38	882.70	831.74	825.51
Single quadratic	834.23	828.76	825.88	823.36	821.40	-
5x5x5 quadratic	837.61	836.82	826.83	-	-	-

All models show stability and their results converge to a certain value. For the model with elements with linear shape function, the differences among various mesh sizes, in terms of the macroscopic stress and matrix stress values, are relatively small (5-7%). However, the biggest differences are visible for stresses in inclusions (up to 30%). This can be a result of poor approximation of shape of spherical inclusions when using first-order elements (i.e. with linear shape functions). To lower the differences to the acceptable level (below 5%), the mesh size has to be no larger than 0.05m for a sphere of radius $r_i = 0.40$m. This refers to around 40 finite elements approximating the sphere on its perimeter.

For models with finite elements with quadratic shape functions, the situation is different. The convergence test shows acceptable results even for the coarsest mesh of 0.50m (discrepancies at around 1.5%). For the 0.25m mesh (around 10 finite elements approximating the sphere) the discrepancy levels are even below 1%. Second order elements give much higher accuracy and reliability, while also dramatically improving the calculation time. For the single-inclusion example, the acceptable mesh consisted of 42 455 first-order finite elements resulting in 1 612 kB input file size. On the other hand, only 608 second-order elements were needed for achieving similar accuracy, resulting in 74 kB input file size.

Number of finite elements approximating the sphere perimeter might be a good dimensionless indicator of what mesh size is needed to achieve an acceptable level of accuracy. This was visualised

in figure 3.14. 40 finite elements were needed for single-order finite elements and 10 finite elements for second-order finite elements.

The results show that the single-cell model may be used as a representative unit cell for entire microstructures, e.g. a cell with 5x5x5 inclusions in the RC lattice. Table 3.5 presents a comparison between these two models. Both examples are of second-order finite elements with 0.15m mesh size. The biggest difference between the outcome values is only 0.114%.

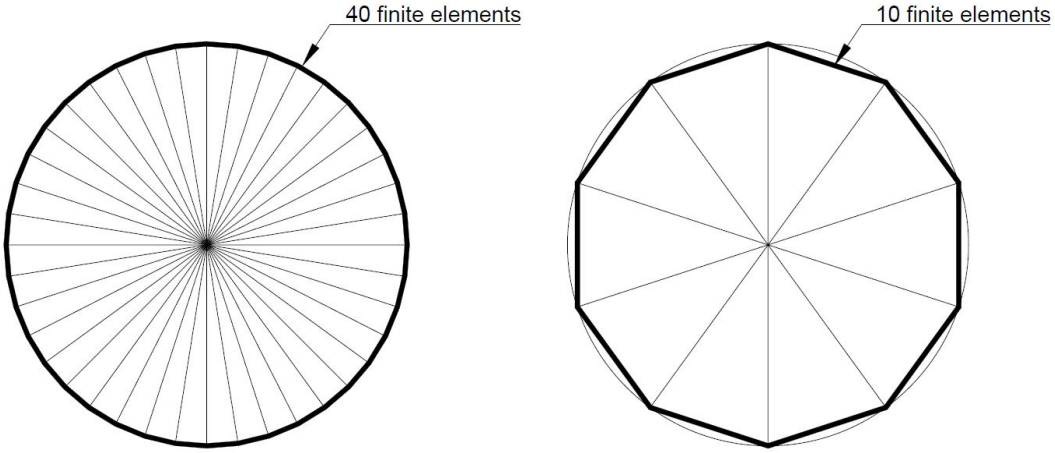

Figure 3.14: Cross-section visualisation through an inclusion. To achieve the acceptable level of accuracy, there should be at least 40 first-order elements (left) or 10 second order elements (right) on the perimeter.

Table 3.5: Comparison of results between single quadratic and 5x5x5-RC quadratic models for 0.15m mesh size.

Stress	$\bar{\sigma}_{11}$	$\sigma_{m.11}$	$\sigma_{i.11}$
Single quadratic	525.26	415.21	825.88
5x5x5 quadratic	525.47	415.15	826.83
Difference	0.040%	0.013%	0.114%

3.3 Numerical verification of the cluster model

In this section, the cluster model is directly confronted with the finite elements method, as a form of an "external" verification. This allows to explore whether the results from both methods are consistent with each other. As in the previous sections, three different lattices are considered: regular cubic (RC), body-centred cubic (BCC) and face-centred cubic (FCC). Parameters of a theoretical material are listed in table 3.6. Two scenarios are considered: reference matrix with ultra hard inclusions (UHI) and reference matrix with ultra soft inclusions (USI). Please note that these are only "theoretical" materials, with non-real values of extreme contrast, used in order to emphasize and better visualise the effects of the model.

Table 3.6: Materials used for mesh convergence test

	Matrix: reference	Inclusions: ultra hard	Inclusions: ultra soft
Young Modulus, E [GPa]	1.0	10000	0.00010
shear modulus, G [GPa]	2.6	26000	0.00026
Poisson's ratio, ν [-]	0.3	0.3	0.3

The verification consists of calculating macroscopic bulk modulus ($\bar{K}$) and calculating shear moduli ($\bar{G}_1$, $\bar{G}_2$) for different volume fractions of inclusions. For the cluster model, it is performed for a cluster with pre-defined gamma functions (i.e. equivalent to a cluster of size $D = 40d$, see sections 2.1 and

2.4). The FEM verification consisted of modelling a unit cell with periodic boundary conditions that is subjected to external unit strain of $\bar{\varepsilon} = 0.01$. Two strain scenarios are performed: uniaxial tension and shearing, as defined in equation (3.7) and shown in figure 3.15.

$$\bar{\boldsymbol{\varepsilon}} = \bar{\varepsilon} \begin{bmatrix} 1 & 0 & 0 \\ 0 & 0 & 0 \\ 0 & 0 & 0 \end{bmatrix} \qquad \bar{\boldsymbol{\varepsilon}} = \bar{\varepsilon} \begin{bmatrix} 0 & 1 & 0 \\ 1 & 0 & 0 \\ 0 & 0 & 0 \end{bmatrix} \tag{3.7}$$

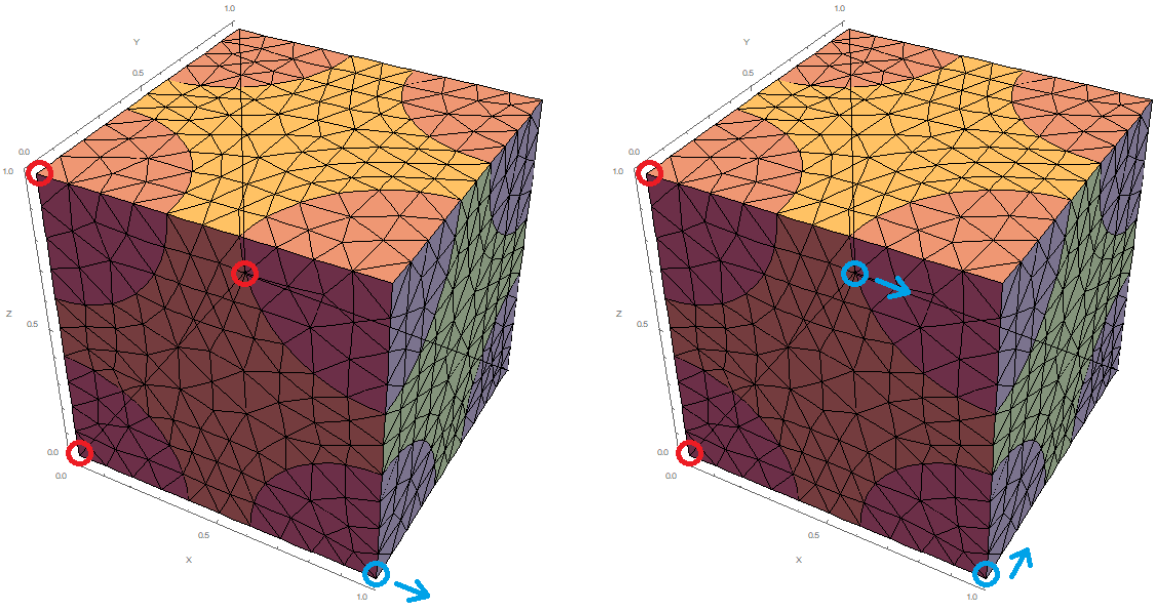

Figure 3.15: Boundary conditions: uniform tension (left); and shearing (right). Red circles show the fixed points. Blue circles show the point with applied strain.

The results from the FEM are macroscopic stress tensors averaged for the entire sample. Based on this, it was possible to calculate macroscopic bulk modulus ($\bar{K}$) and macroscopic shear moduli ($\bar{G}_1$, $\bar{G}_2$). For a sample with cubic symmetry, it done using following formulas:

$$3\bar{K} = 1/3\left(\bar{C}_{1111} + \bar{C}_{2222} + \bar{C}_{3333}\right) + 2/3\left(\bar{C}_{1122} + \bar{C}_{1133} + \bar{C}_{2233}\right) \tag{3.8}$$

$$2\bar{G}_1 = 1/3\left(\bar{C}_{1111} + \bar{C}_{2222} + \bar{C}_{3333}\right) - 1/3\left(\bar{C}_{1122} + \bar{C}_{1133} + \bar{C}_{2233}\right) , \tag{3.9}$$

$$\bar{G}_2 = 1/3\left(\bar{C}_{2323} + \bar{C}_{1313} + \bar{C}_{1212}\right) . \tag{3.10}$$

where $\bar{K}$ is macroscopic bulk modulus; $\bar{G}_1$ is macroscopic first shear modulus; $\bar{G}_2$ is macroscopic second shear modulus; and $\bar{C}_{ijkl}$ are components of the macroscopic stiffness tensor $\bar{\mathbb{C}}$.

The results are presented in figures 3.16 - 3.18. As it can be seen, the cluster model generally gives results very close to the ones obtained from the finite elements method, both in quantitative, as well as in qualitative terms. A significant discrepancy between the cluster model and FEM arises when reaching the maximum possible volume fraction of inclusions for the given lattice. It is especially visible in scenarios with inclusions stiffer than the matrix. If the acceptable threshold of discrepancy between cluster and FEM is assumed as 5%, then the limit volume fraction of inclusions is around $f_i = 35\%$ for hard inclusions and around $f_i = 40\%$ for the soft inclusions. If the threshold is set to 15%, then the limit volume fraction is around $f_i = 50\%$ and $f_i = 55\%$ respectively.

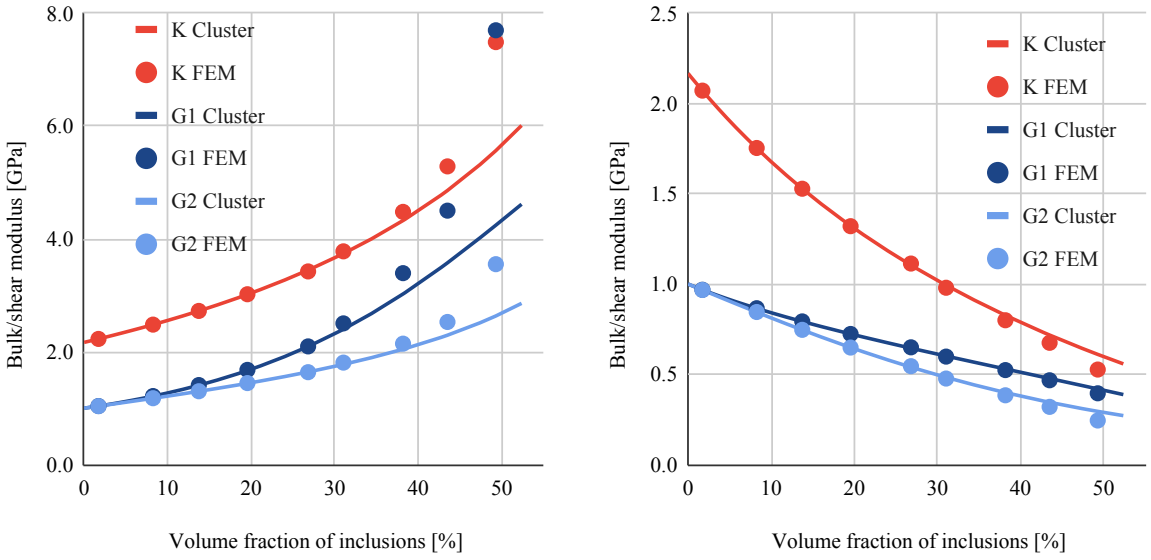

(a) (b)

Figure 3.16: Macroscopic bulk ($\bar{K}$) and shear ($\bar{G}_1$, $\bar{G}_2$) moduli comparison between the cluster model and finite elements method (FEM). RC lattice. Ultra hard (a); and ultra soft (b) inclusions. Note different scale on Y axes.

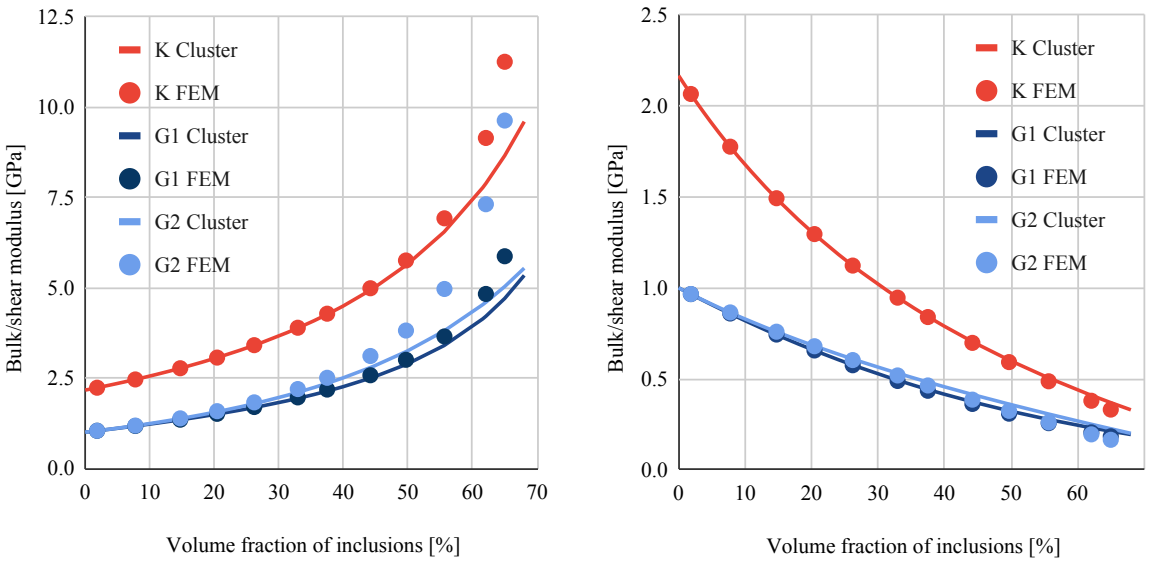

(a) (b)

Figure 3.17: Macroscopic bulk ($\bar{K}$) and shear ($\bar{G}_1$, $\bar{G}_2$) moduli comparison between the cluster model and finite elements method (FEM). BCC lattice. Ultra hard (a); and ultra soft (b) inclusions. Note different scale on Y axes.

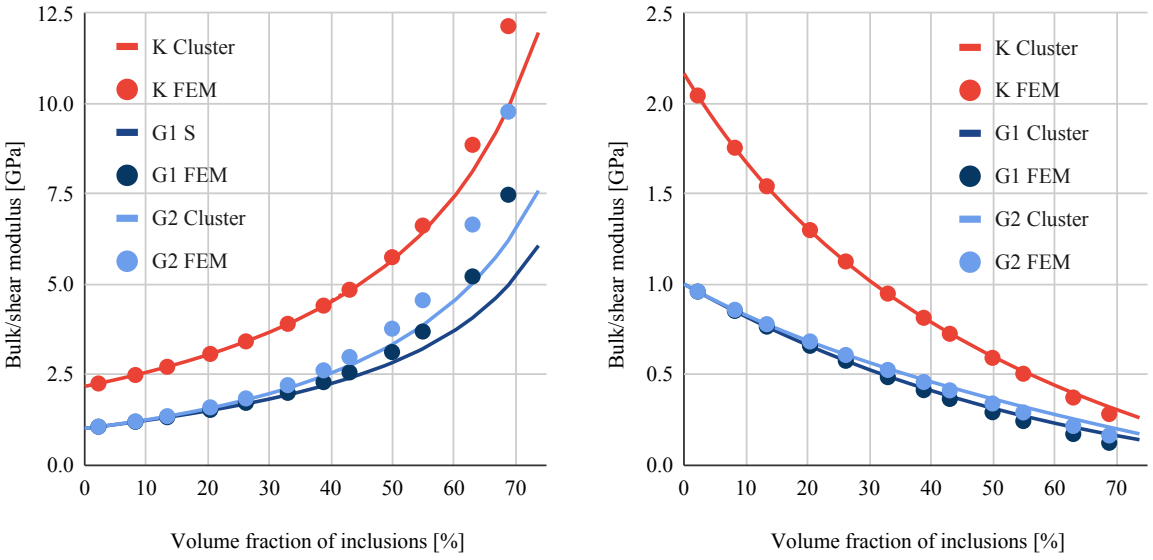

(a) (b)

Figure 3.18: Macroscopic bulk ($\bar{K}$) and shear ($\bar{G_1}$, $\bar{G_2}$) moduli comparison between the cluster model and finite elements method (FEM). FCC lattice. Ultra hard (a); and ultra soft (b) inclusions. Note different scale on Y axes.

Additionally, it is possible to make a comparison of the macroscopic values between the RC, BCC and FCC lattices themselves, both for the cluster and FEM models. Each type of material property is treated separately, i.e. bulk modulus ($\bar{K}$) and shear moduli ($\bar{G_1}$, $\bar{G_2}$) are plotted in separate graphs 3.19 - 3.21. For the sake of clarity, the figures show the range of volume fraction of inclusions up to $f_i = 70\%$.

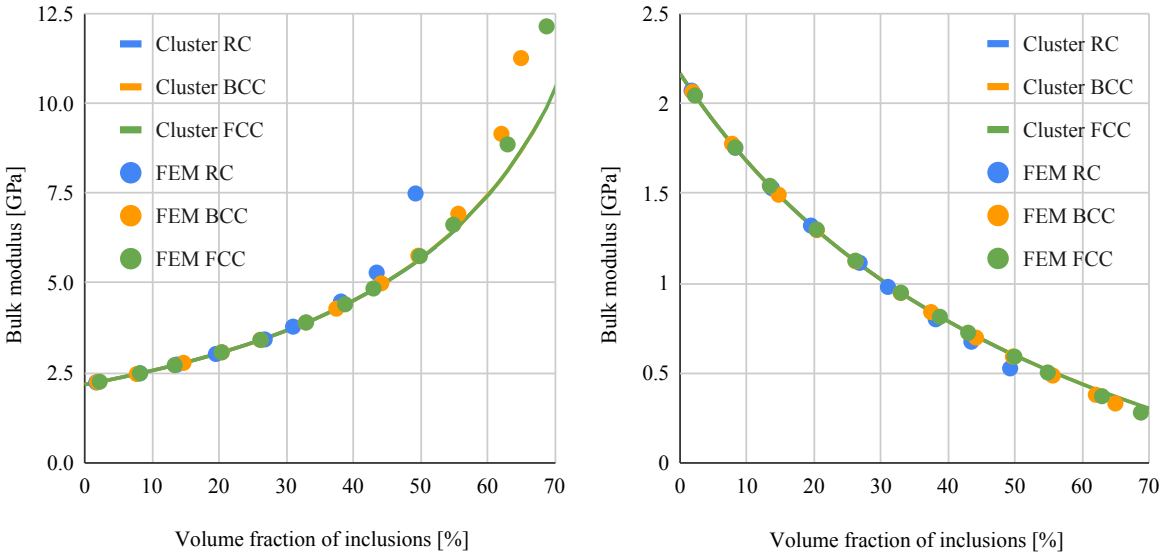

(a) (b)

Figure 3.19: Comparison of macroscopic bulk modulus ($\bar{K}$) for different lattice for the cluster model and finite elements method (FEM). Ultra hard (a); and ultra soft (b) inclusions. Note different scale on Y axes.

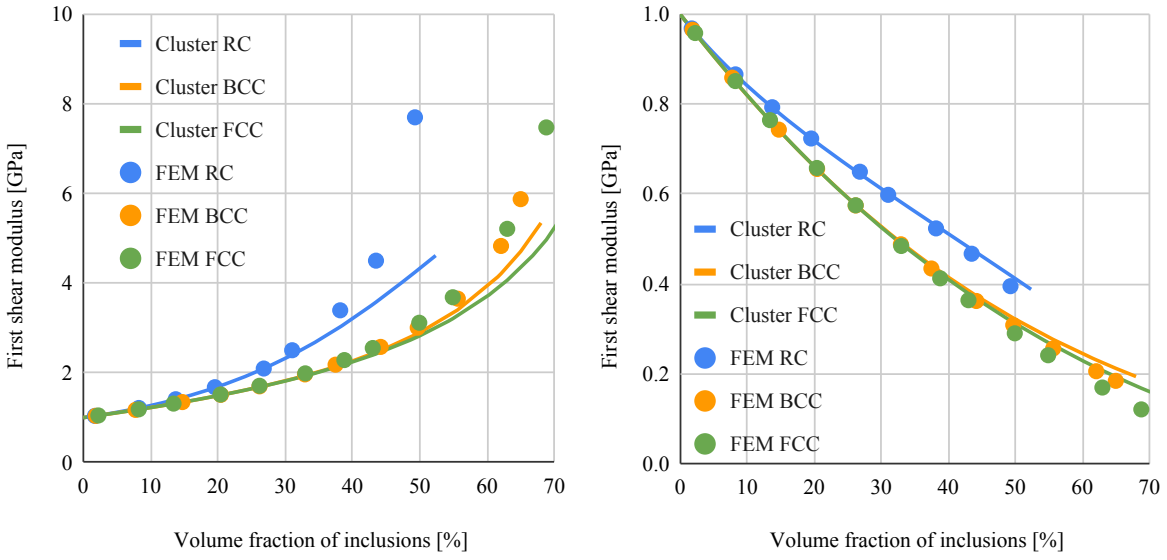

Figure 3.20: Comparison of macroscopic first shear modulus ($\bar{G}_1$) for different lattice for the cluster model and finite elements method (FEM). Ultra hard (a); and ultra soft (b) inclusions. Note different scale on Y axes.

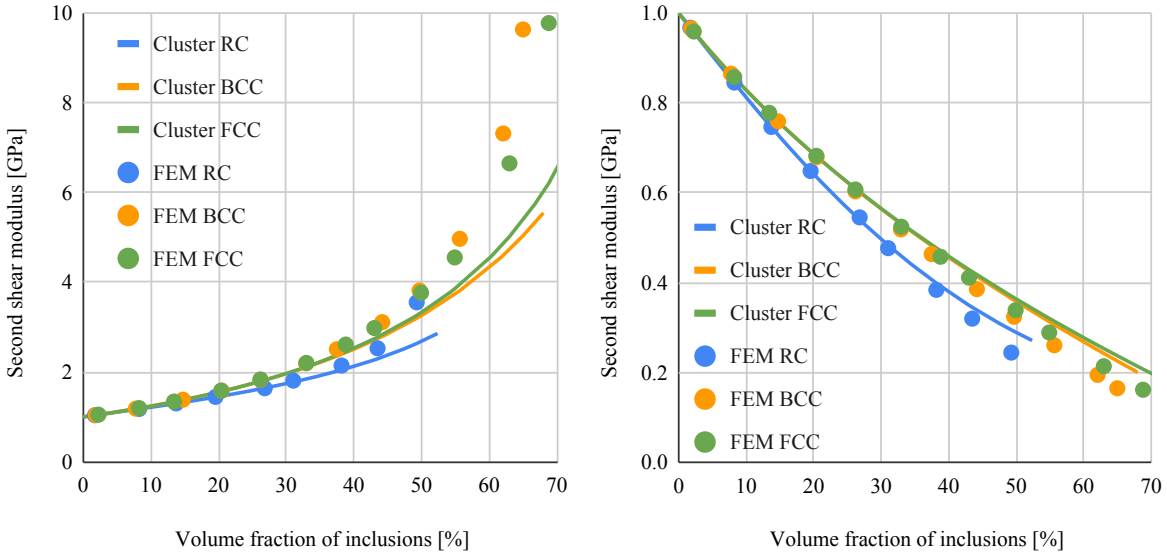

Figure 3.21: Comparison of macroscopic second shear modulus ($\bar{G}_2$) for different lattice for the cluster model and finite elements method (FEM). Ultra hard (a); and ultra soft (b) inclusions. Note different scale on Y axes.

It is visible that the macroscopic bulk modulus ($\bar{K}$) for the cluster model is identical in all three lattices. It is not, however, when comparing values from the FEM. The difference between RC, BCC, and FCC for the FEM becomes visible for the volume fraction of inclusions above $f_i = 40\%$. Macroscopic shear moduli ($\bar{G}_1$, $\bar{G}_2$) show clear differences between each of three lattices, especially for the RC vs BCC/FCC. The two latter ones show values very close to each other, although in the ultra-hard-inclusions scenario they seem to be "mirrored" (e.g. in FEM values for BCC are higher than

for FCC, while in cluster values for BCC are lower than for FCC). In all cases, the ultra-soft-inclusions scenario shows much smaller discrepancies than the ultra-hard-inclusions one. For all further analyses, the volume fraction of inclusions equal to $f_i = 40\%$ is assumed as the applicability limit for the cluster model.

3.4 Experimental validation of the cluster model

Alongside the numerical methods, experimental validation of the model has also been approached. In this case, however, for a porous material. Thus, only samples with the matrix phase and voids are considered. The task has been performed by the team of prof. Tomasz Zieliński from IPPT PAN and described in detail in paper Kowalczyk-Gajewska et al. (2024).

Physical samples were produced of acrylonitrile butadiene styrene (ABS) polymer material using a 3D printing technique. Their sizes are: diameter 24 mm and height 32 mm. RC, BCC and FCC lattices were produced with five nominal values of pore diameters used to create geometries used for 3D printing, namely d_p =1.7, 2.15, 2.5, 3.1 and 3.5 mm, with the nominal unit cell size of 4 mm. The produced pores were oriented in such a manner, as to achieve loading along the unit cell edge (i.e. (0,0,1) direction) or the diagonal (i.e. (1,1,1) direction). Additionally, several fully solid samples were also 3D printed and tested to evaluate the polymer matrix stiffness to provide the reference for porous specimens.

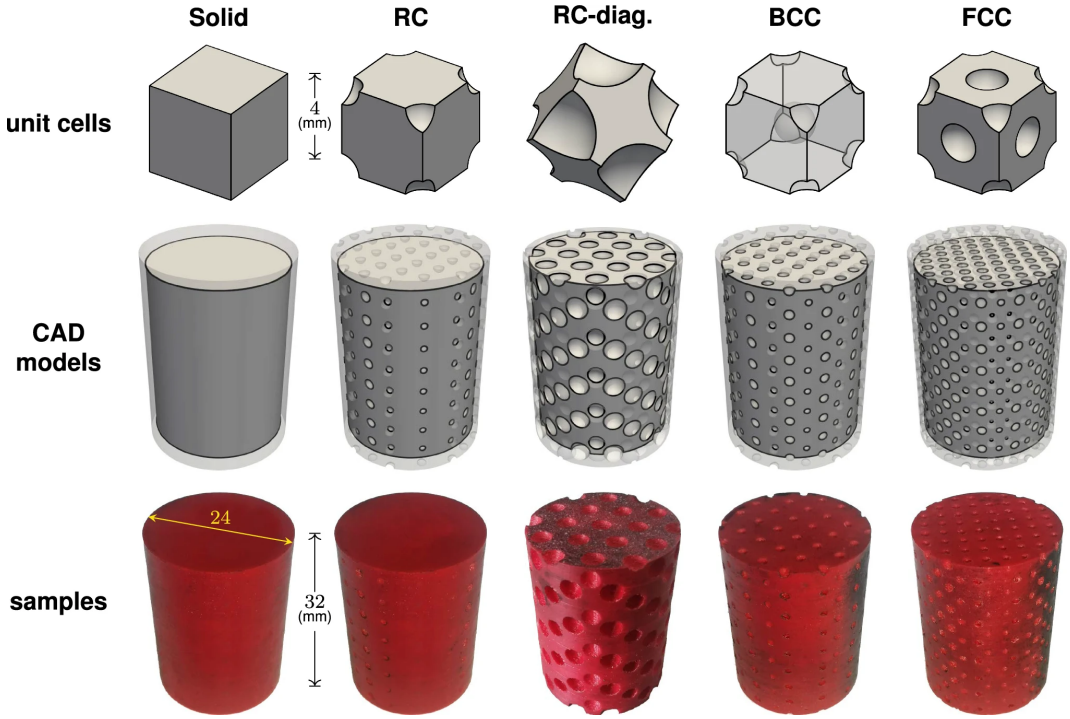

Figure 3.22: Cubic unit cells and CAD models as well as 3D printed and machined samples with cubic distributions of spherical pores (RC, RC-diag., BCC, FCC), or without pores (solid). Source: Kowalczyk-Gajewska et al. (2024).

The experiment consisted of a uniaxial displacement-controlled compression test, conducted using the MTS 858 hydraulic testing machine. To determine the mean strain in the loading direction, a so-called "virtual extensometer" was used in frame of a digital image correlation technique. The obtained experimental results (listed in table 3.7) demonstrated that there is a non-negligible influence of the microstructure on the developed anisotropy degree of the macroscopic stiffness of a porous material, as predicted with the virtual models. When comparing the results from the measurements and modelling (i.e. from the cluster model and finite element method), as shown in figure 3.23, it is visible that they are qualitatively in good agreement in terms of the impact of the porosity and microstructure type on the macroscopic Young's modulus. Although, the quantitative assessment is more challenging, mainly

due to the inherent inaccuracy of 3D printed geometries and possible variation of solid properties within the samples.

Please note that the experiments described in this section are just the initial step of real-life validation of the cluster model. There is still room for further research and a deepened experimental validation, e.g. by employing 3D printed samples produced by more accurate printing techniques, or by use of metallic materials and techniques enabling production of two-phase materials.

Table 3.7: Results of measurements of the macroscopic Young's modulus for cylindrical solid and porous samples (average ± standard deviation). Source: Kowalczyk-Gajewska et al. (2024).

Unit cell type	Compression direction	Nominal pore size [mm]	Actual pore size [mm]	Porosity [%]	Young modulus [GPa]
Solid	-	-	-	0.0	2.340 ± 0.058
RC	Edge (0,0,1)	1.7	1.59	3.3	2.098
		2.15	2.04	7.1	1.950
		2.5	2.39	11.3	1.852 ± 0.073
		3.1	2.99	22.2	1.721 ± 0.029
		3.5	3.39	32.4	1.103
	Diagonal (1,1,1)	3.1	2.99	22.2	1.372
		3.5	3.39	32.4	0.922
BCC	Edge (0,0,1)	1.7	1.59	6.7	2.013
		2.15	2.04	14.1	1.659
		2.5	2.39	22.7	1.428
		3.1	2.99	44.4	0.500 ± 0.006
FCC	Edge (0,0,1)	1.7	1.59	13.4	1.555
		2.15	2.04	28.2	1.032
		2.5	2.39	45.4	0.562

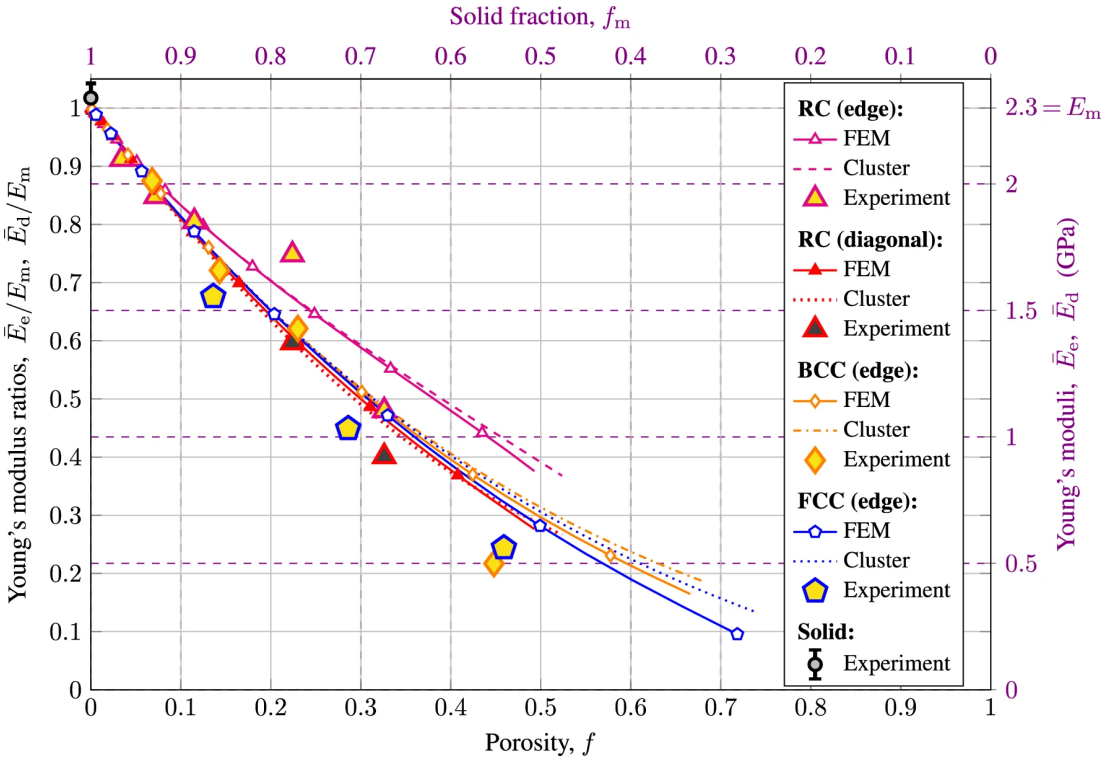

Figure 3.23: Young's moduli vs. porosity and solid volume fraction for solid and porous materials with RC, BCC, and FCC arrangements of spherical pores. Source: Kowalczyk-Gajewska et al. (2024).

3.5 Optimisation in the elastic regime

A huge advantage of composites is the possibility of joining materials of different parameters and extracting their best characteristics. One material could have high strength, while the other could act as a good thermal insulator. By joining them together, we could possibly obtain a composite material that would posses those two advantages together. This, of course, has limits and the result depends on the proportion of each phase. If we use more soft lightweight inclusions, we lose strength. If we try to maximise strength, our material becomes less insulating. Moreover, the spatial distribution of each phase or direction of applied loads also play a huge role in the process. There is a need to find a proper balance among all used phases and that is where different methods of optimisations are used.

3.5.1 Theoretical stiff and insulating material

Let us consider a theoretical (i.e. not following any particular real-world material) composite material consisting of a dense and stiff matrix along with ultra-light, low-stiffness insulating inclusions. Three regular lattices of inclusions are considered: RC, BCC and FCC. Their parameters are listed in table 3.8. The cluster model with pre-defined gamma functions is used, as this is the most time-efficient method for multiple calculations.

Table 3.8: Parameters of materials used for optimisation (hard and insulating).

	Matrix: hard	Inclusions: insulating
Young Modulus, E [GPa]	36.0	2.4
shear modulus, G [GPa]	15.0	1.0
Poisson's ratio, ν [-]	0.2	0.2
CTE, α [1/K]	$1.5{\cdot}10^{-5}$	$1.5{\cdot}10^{-5}$
thermal conductivity, k [W/(m·K)]	1.0	0.01
density, ρ [kg/m^3]	25000	1

In this example, three different macroscopic properties are considered: mechanical (stiffness, i.e. Young's modulus), thermal (thermal conductivity) and density. Optimisation aims to find the best balance between all these values. To find this balance, an objective (or cost) function ϕ is specified as a sum n components, one for each material property. For each component, zero means the best solution. The scenario that gives the lowest value of the objective function ϕ is considered the best. Similar approach was proposed in Kursa et al. (2014). The objective function is defined as follows:

$$\phi = \sum_{i}^{n} \left(\frac{\text{macroscopic outcome value}}{\text{reference value}} - \delta \right)^2 \tag{3.11}$$

where δ depends on whether the given material parameter is desired to be as low ($\delta = 0$) or as high ($\delta = 1$) as possible. The reference values are the maximum possible values, so it is ensured that each component ranges between 0 and 1.

In this case, the objective function ϕ depends on the volume fraction of inclusions f_i and is defined as a sum of $n = 3$ components (one for each property). For this scenario, a perfect material would have high stiffness (thus $\delta = 1$), low thermal conductivity and low density (thus $\delta = 0$). The objective function takes the following shape:

$$\phi(f_i) = w_1 \left(\frac{\bar{E}_1}{E_m} - 1 \right)^2 + w_2 \left(\frac{\bar{k}}{k_m} - 0 \right)^2 + w_3 \left(\frac{\bar{\rho}}{\rho_m} - 0 \right)^2 \tag{3.12}$$

where $\bar{E}_1$ is macroscopic first Young's (defining the stiffness of the material when loaded along a unit cell edge); E_m is Young's modulus of matrix; $\bar{k}$ is macroscopic thermal conductivity (trace of a 3x3 matrix $\bar{k}$); k_m is thermal conductivity of matrix; $\bar{\rho}$ is macroscopic density; ρ_m is density of matrix; and w_1, w_2, w_3 are weight functions for each material parameter. Additional constraints of e.g. minimum stiffness or maximum thermal conductivity etc. can be applied for even more detailed optimisation procedure (see Kursa et al. (2014)).

Calculations are performed for different volume fractions of inclusions varying from $f_i = 0\%$ to the maximum possible one for each lattice (i.e. $f_i = 52\%$ for RC, $f_i = 68\%$ for BCC and $f_i = 74\%$ for

FCC). Figure 3.24a shows the relation of each effective property to volume fraction of inclusions for the RC lattice (graphs for other lattices are omitted for simplicity). The next step is to sum up all the components with appropriate weight functions assigned. Choice of the weight functions is crucial and strongly affects the result. It is a representation of design goals and requirements in the expected application of the material. In this case, three different sets of weight functions are used:

1. 0.500 × mechanical + 0.500 × thermal + 0.000 × density (weight-irrelevant);
2. 0.333 × mechanical + 0.333 × thermal + 0.333 × density (all-equal);
3. 0.500 × mechanical + 0.250 × thermal + 0.250 × density (mechanical-dominated).

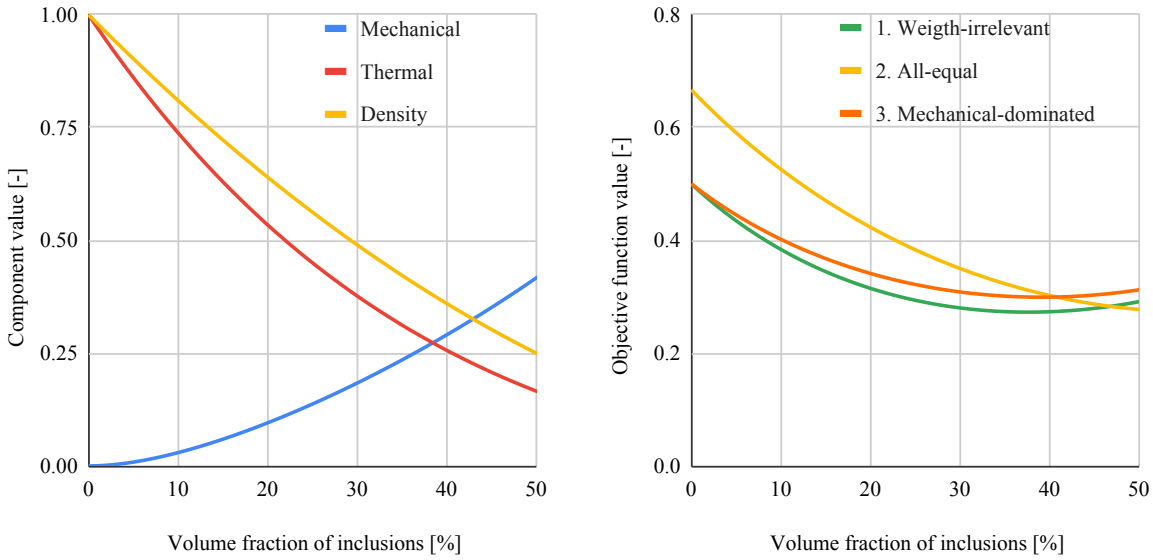

(a) (b)

Figure 3.24: Values of each component of objective function (a); and objective functions for different set of weights (b).

Table 3.9: Optimal volume fractions f_i and corresponding objective function values $\phi(f_i)$ for different lattices.

objective function	RC lattice		BCC lattice		FCC lattice	
	f_i	$\phi(f_i)$	f_i	$\phi(f_i)$	f_i	$\phi(f_i)$
weight-irrelevant	39.7%	0.2632	35.4%	0.3003	34.7%	0.3013
all-equal	out of range		out of range		67.7%	0.2826
mechanical-dominated	42.3%	0.2888	36.7%	0.3277	36.0%	0.3289

Table 3.10: Material parameters of an optimal metallic-matrix composite found using the mechanical-dominated set of weight functions.

	RC lattice	BCC lattice	FCC lattice
first Young's modulus, $\bar{E}_1$ [GPa]	16.46	15.99	16.21
thermal conductivity, $\bar{k}_{iso}$ [W/(m·K)]	0.4827	0.5404	0.5485
density, $\bar{\rho}$ [kg/m^3]	14423	15817	16008

Figure 3.24b shows objective functions for these three sets for the RC lattice. Table 3.9 lists the optimal volume fractions of inclusions and corresponding objective function value for each set. Table 3.10 lists the macroscopic material parameters for an optimal composite found using the mechanical-dominated set of weight functions. It can be seen that the choice of the spatial distribution of inclusions

(i.e. the lattice) affects the results. For the same objective functions, different minimum values are achieved and they correspond to different volume fraction of inclusions.

3.5.2 Theoretical metal-matrix composite

After trials with a theoretical hard and insulating material, the next step is to perform the optimisation for a composite similar to ones used in real applications, with implementation of an external load and a failure criteria. A theoretical combination of a metallic matrix and ceramic inclusions is used. Their parameters are listed in table 3.11.

Table 3.11: Materials used for optimisation (metal-ceramic composite).

	Matrix: metallic	Inclusions: ceramic
Young Modulus, E [GPa]	117	393
shear modulus, G [GPa]	43.66	161.1
Poisson's ratio, ν [-]	0.34	0.22
CTE, α [1/K]	$1.69 \cdot 10^{-5}$	$0.65 \cdot 10^{-5}$
thermal conductivity, k [W/(m·K)]	339	35
density, ρ [kg/m^3]	8940	3990
yield stress, Y_0 [MPa]	276	379

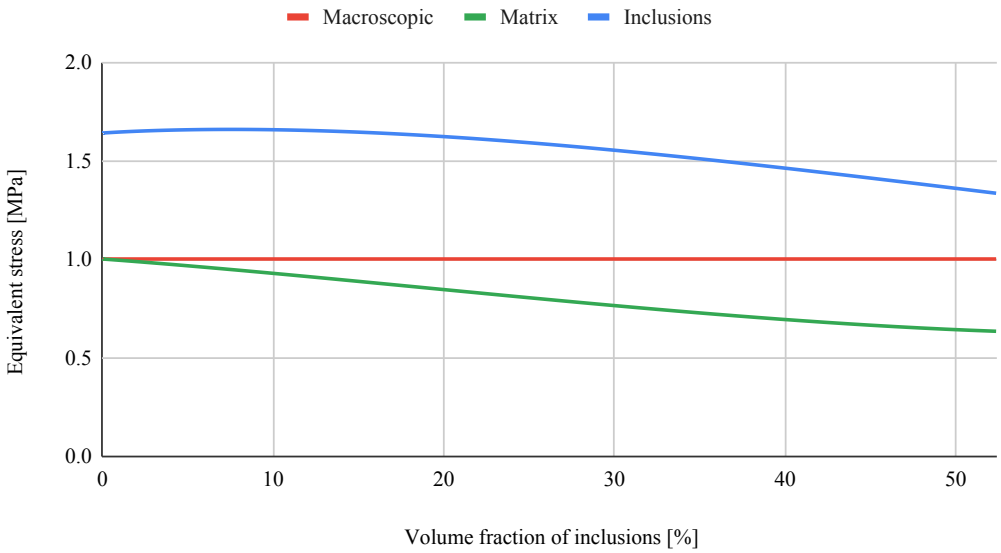

Figure 3.25: Von Mises stresses: macroscopic, matrix and inclusions. RC lattice for metal-ceramic composite.

The sample is subjected to external unit uniaxial tension load of $\bar{\sigma} = 1$ MPa along the unit cell edge. The figure 3.25 shows the distribution of stresses in both phases depending on the volume fraction of inclusions. While the problem is linear, knowing the limit stress (yield stress) for both matrix and inclusions, it is possible to calculate the value of external load, at which one of the phases fails:

$$\lambda_r = \frac{Y_{0.r}}{\sigma_{1MPa.r}} \tag{3.13}$$

$$\sigma_{failure.r} = \lambda_r \cdot 1[\text{MPa}] \tag{3.14}$$

where λ_r is failure coefficient for phase r; $Y_{0.r}$ is yield stress for phase r; $\sigma_{1Mpa.r}$ is stress in a phase r when external load is set to $\bar{\sigma} = 1$ MPa; and $\sigma_{failure.r}$ is external load at which failure in phase r occurs.

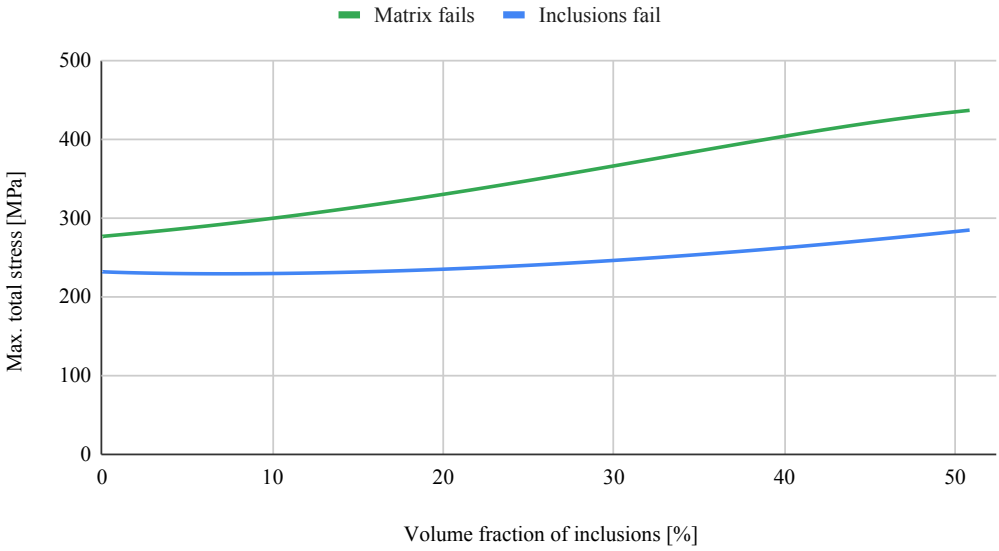

Figure 3.26: Macroscopic stress (external load) at which failure occurs in matrix (green) or inclusions (blue). RC pattern for metal-ceramic composite.

Values of external load at which failure occurs in matrix or inclusions are shown in figure 3.26. In this example, the bearing capacity for each phase rises along with the volume fraction of inclusions. Moreover, the inclusions are the phase that would fail first. In such a case, it is possible to assume that even after the failure of inclusions occurs, the matrix (which here is assumed to be a continuous medium) should still be able to carry the load, at least to some extent. For this reason, the same calculations are performed with the same material parameters for the matrix, but with inclusions assumed as having nearly zero strength and stiffness. Values of external load at which failure occurs in such non-load-bearing inclusions (when only the matrix works) are shown in figure 3.27 as a light green line.

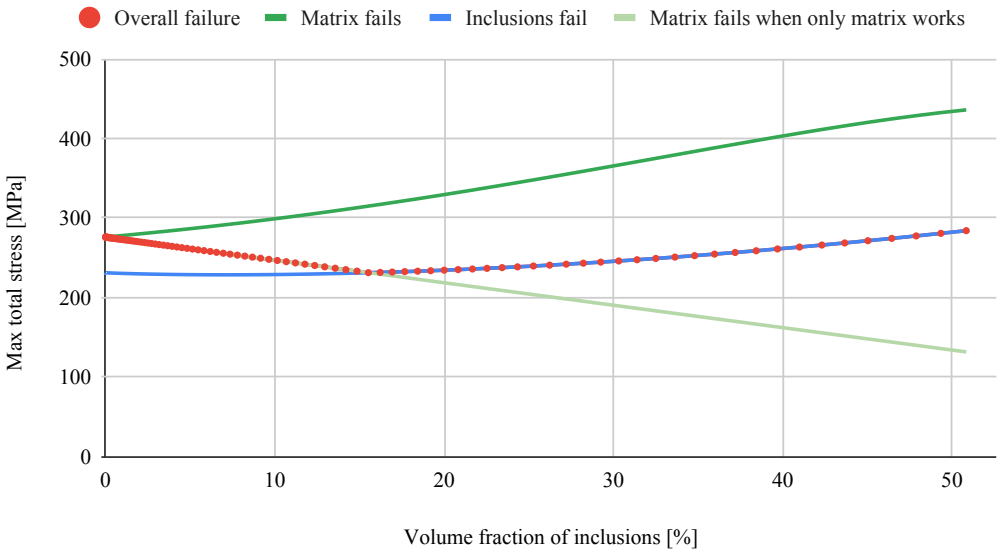

Figure 3.27: Macroscopic stress (external load) at which failure occurs in matrix (green), full-working inclusions (blue) or non-load-bearing inclusions (light green). Red dotted lines is a combination of all phases, indicating the overall failure of the entire sample.

As it can be seen, in case of non-load-bearing inclusions, the overall strength decreases along with the volume fraction of inclusions. Eventually at some point, the load-bearing capacity of the pure matrix is lower than for the sample with fully working inclusions. Since then, the overall bearing capacity is determined by the strength of inclusions. The overall bearing capacity is thus depicted on the graph with a red dotted line. This strength parameter can be used as an extra input into the objective function for the optimisation. Moreover, the coefficient of thermal expansion is also added as the fifth parameter.

In the following example, the optimisation scenario would resemble a design of a metallic-matrix composite for a braking disc. In that case, a perfect material would have high thermal conductivity coefficient (to disperse heat easily), high strength, high stiffness, low coefficient of thermal expansion and low density. With this material and objective choice, the stiffness, mass, and coefficient of thermal expansion are better when volume fraction of inclusions is high. Thermal conductivity gives the best value when no inclusions are present. The strength of the composite is non-monotonous and it is the weakest for volume fraction of inclusion of around $f_i = 0.15$. Thus, the new objective function is defined as below:

$$\phi(f_i) = w_1 \left(\frac{\bar{E}_1}{E_i} - 1 \right)^2 + w_2 \left(\frac{\bar{k}}{k_m} - 1 \right)^2 + w_3 \left(\frac{\bar{\rho}}{\rho_m} \right)^2 + w_4 \left(\frac{\bar{\alpha}}{\alpha_m} \right)^2 + w_5 \left(\frac{\bar{\sigma}_{failure}}{Y_{0.i}} - 1 \right)^2 \quad (3.15)$$

where $\bar{E}_1$ is macroscopic first Young modulus; E_i is Young's modulus of inclusions; $\bar{k}_{iso}$ is macroscopic thermal conductivity (trace of a 3x3 matrix $\bar{\mathbf{k}}$); k_m is thermal conductivity of matrix; $\bar{\rho}$ is macroscopic; ρ_m is density of matrix; $\bar{\alpha}$ is macroscopic coefficient of thermal expansion; α_m is coefficient of thermal expansion of matrix; $\bar{\sigma}_{failure}$ is macroscopic strength (max. load that could be applied to sample before failure); $Y_{0.i}$ is yield stress of inclusions; and w_1, w_2, w_3, w_4, w_5 are weight functions for each material parameter.

Four different sets of weight functions are considered applied. Three of them are the same as in the example from the previous subsection (weight-irrelevant, all-equal, mechanical-dominated). The fourth one is an extended set and consists of: thermal conductivity, mass, thermal expansion and strength components with emphasis on the thermal conductivity part.

1. 0.500 × mechanical + 0.500 × thermal + 0.000 × density + 0.000 × CTE + 0.000 × strength;
2. 0.333 × mechanical + 0.333 × thermal + 0.333 × density + 0.000 × CTE + 0.000 × strength;
3. 0.500 × mechanical + 0.250 × thermal + 0.250 × density + 0.000 × CTE + 0.000 × strength;
4. 0.000 × mechanical + 0.500 × thermal + 0.150 × density + 0.100 × CTE + 0.250 × strength.

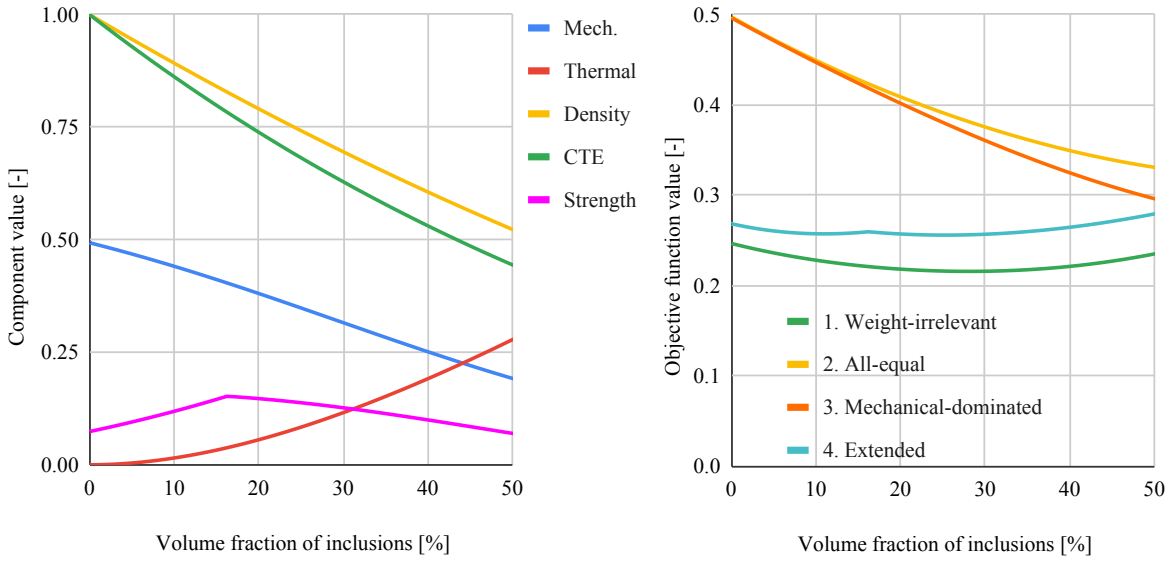

(a) (b)

Figure 3.28: Values of each component of objective function (a); and objective functions for different set of weights (b). Metallic-ceramic composite.

The relation of each component to volume fraction of inclusions for the RC lattice is shown in figure 3.28a, while the objective functions are shown on figure 3.28b (graphs for other lattices are omitted for simplicity). In table 3.12 are listed optimal volume fractions of inclusions and corresponding objective function value for each set, while in table 3.13 are listed the macroscopic material parameters for an optimal composite found using the extended set of weight functions.

Table 3.12: Optimal volume fractions f_i and corresponding objective function values $\phi(f_i)$ for different lattices

objective function	RC lattice		BCC lattice		FCC lattice	
	f_i	$\phi(f_i)$	f_i	$\phi(f_i)$	f_i	$\phi(f_i)$
weight-irrelevant	28.2%	0.2156	19.4%	0.2262	19.4%	0.2262
all-equal	out of range		out of range		out of range	
mechanical-dominated	out of range		out of range		out of range	
extended	25.3%	0.2558	26.1%	0.2394	30.9%	0.2555

Table 3.13: Macroscopic material parameters of an optimal metallic-matrix composite found using the extended set of weight function.

	RC lattice	BCC lattice	FCC lattice
first Young's modulus, $\bar{E}_1$ [GPa]	16.16	15.51	16.33
thermal conductivity, $\bar{k}_{iso}$ [W/(m·K)]	240	237	221
density, $\bar{\rho}$ [kg/m^3]	7689	7649	7411
CTE, $\bar{\alpha}[1/K]$	$1.393{\cdot}10^{-5}$	$1.384{\cdot}10^{-5}$	$1.330{\cdot}10^{-5}$
yield stress, $\bar{\sigma}_{failure}[MPa]$	238.6	278.8	286.9

Above-mentioned examples show the efficiency of the cluster model. Thanks to short calculation time, it is possible to test multiple different scenarios in complex multi-criteria optimisation procedures, finding e.g.: the optimal microstructure, volume fraction of inclusions or material composition. Such tools based on the cluster model might be used in initial stages of the design process to quickly test and verify various design choices, even if the next phase would involve more detailed methods of verification.

3.6 Summary

It has been demonstrated that the cluster model gives consistent results with the computational homogenization employing finite element method, both in quantitative and qualitative terms. The obtained values are close to each other in both methods. Impact of the microstructure and its anisotropy on the macroscopic material parameters of the composite is well-visible and correctly captured. Numerical verification shows that the maximum applicable volume fraction of inclusion for the cluster model is $f_i = 40\%$. Above this value, significant discrepancies between these two methods are observed, especially for the case when inclusion phase is stiffer than the matrix phase.

It has been observed that within the computational homogenization, meshing applied in the finite elements method is a significant factor which may affect the results. Therefore, the mesh converge test has been performed to find the acceptable mesh size. The biggest impact of mesh size is seen in mean stresses and strains calculated for the inclusion phase. Thus, the acceptable mesh size is mostly linked to the acceptable approximation of the inclusion geometry. The meshing should give no fewer than 10 finite elements along the inclusion perimeter for a second-order finite element. A single unit cell with applied periodic boundary conditions is sufficient to represent the entire cluster of a regular structure.

Limited experimental validation shows that the results from the cluster model are in good qualitative agreements with real-life samples. However, the quantitative assessment is significantly more challenging, mainly due to inherent inaccuracy of 3D printed geometries and possible variation of solid properties, even within the samples of the same material and geometry.

Effective optimisation procedures are possible thanks to short calculation time for the cluster model. It allows for use of multi-criteria optimisation in order to find the optimal microstructure,

volume fraction of inclusions or material composition. Presented analyses of two different design scenarios demonstrated the potential of the proposed model for application on initial stages of the design process of composite materials.

Chapter 4

Extension of the cluster model to elastoplasticity

4.1 Introduction

This chapter concerns the extension of the cluster model to elastic-plastic composites. Most of the results presented in this chapter have been published in Bieniek et al. (2024).

Originally, the cluster model was derived in the framework of linear thermoelasticity of the matrix material. So, in particular, it was assumed in the derivation that the matrix stiffness tensor $\mathbb{C}_m$ and the thermal stress tensor $\boldsymbol{\beta}_m\theta$ were constant within the matrix phase. This chapter explains extension of the cluster model for elastic–plastic composites. Due to the involved non-linearity of the constitutive law of the metal matrix, the extension of any mean-field model for this case requires additional assumptions. In the case of the cluster model, this means that three additional steps must be incorporated: linearisation, uniformisation and isotropisation. In this section, the general idea behind these steps is presented. The detailed mathematical background of this process is next explained in section 4.2.

4.1.1 Linearisation

Plastic regime involves a non-linear response of the material to the external loading. Thus, application of a mean-field model, in particular the cluster model, which was developed assuming the linear matrix response, requires some linearisation of non-linear behaviour. Classically, two approaches are present: tangent, or secant, which are schematically illustrated in figure 4.1.

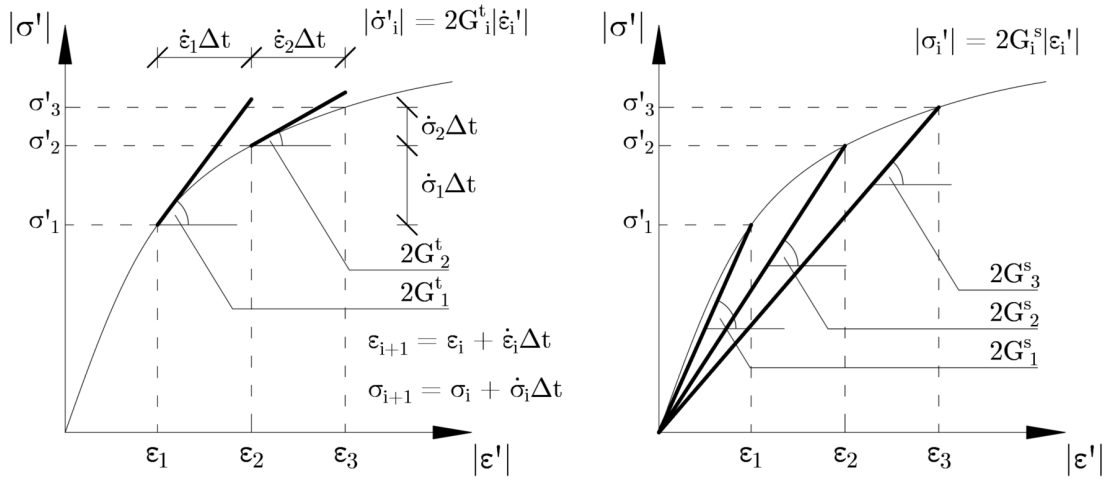

Figure 4.1: Generic stress-strain curve for a plastic loading case with difference between: tangent (left); and secant (right) linearisation.

The obtained tangent or secant moduli are changing along the loading process depending on the accumulated plastic deformation. For the cluster model, the first approach, i.e. tangent linearization, has been chosen, as - contrary to the secant linearisation - it is not restricted to the proportional loading processes and can be performed for any deformation path. In both approaches, the load is applied step by step in time increments.

4.1.2 Uniformisation

For elastic-plastic materials, tangent (or secant) modulus depends on the current strain or stress in the material, as explained in the previous section. At the same time, the cluster model is a mean-field model, meaning that it approximates the stress or strain field in the entire phase with one value. In reality, however, strain and stress (and thus tangent or secant moduli) vary in different parts of the unit cell. It can be seen in FEM calculations where e.g. there is a concentration of stresses in the matrix in the areas near the inclusions or voids (as visualised in figure 4.2). The goal of this step is to find an acceptable approximation to replace the spatially varying tangent modulus with a uniform one (in space, but still changing with time) to implement it to the cluster model. Uniformisation can be performed using either the mean values of a given field within the phase (so called first moment) or higher order averaged values as second moments.

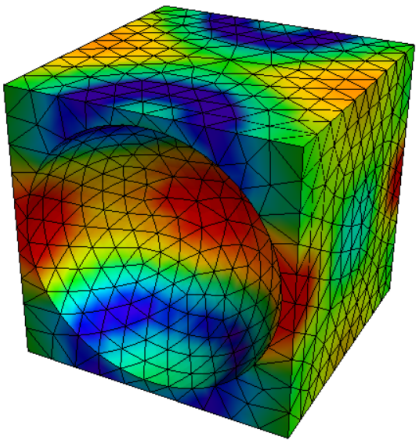

Figure 4.2: Example map of equivalent stresses inside a sample with voids from FEM analyses. Local concentrations of stresses are visible.

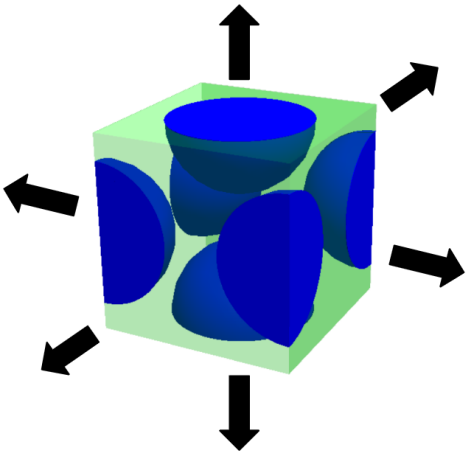

Figure 4.3: External loading conditions (strain) applied to the sample during a hydrostatic loading case.

As explained before, the cluster model is a mean-field model, meaning that it approximates the entire phase with one value, averaged on the entire matrix, which is then used to calculate tangent (or secant) moduli. In most cases, such approach leads to acceptable results, however, it may also lead to significant discrepancies as compared to the full-field results. It is especially visible for a hydrostatic loading case (visualised in figure 4.3). To explain this issue, let us first recall that every stress tensor can be divided into a hydrostatic and deviatoric part.

$$\boldsymbol{\sigma} = \boldsymbol{\sigma}^{\mathrm{H}} + \boldsymbol{\sigma}^{\mathrm{D}} \tag{4.1}$$

where $\boldsymbol{\sigma}$ is stress tensor; $\boldsymbol{\sigma}^{\mathrm{H}}$ is hydrostatic part of the stress tensor; and $\boldsymbol{\sigma}^{\mathrm{D}}$ is deviatoric part of the stress tensor.

Within the plastic flow theory, the plastic strain are initiated when some equivalent stress reaches the yield stress. In J_2 flow theory, the equivalent stress is described by the Huber-von Mises yield function with the associated flow rule and the power-law isotropic hardening. The equivalent von Mises stress depends only on the deviatoric part of the stress tensor and is described as follows:

$$\sigma_{eq} = \sqrt{3J_2} \tag{4.2}$$

or:

$$\sigma_{eq} = \sqrt{\frac{(\sigma_{11}-\sigma_{22})^2 + (\sigma_{22}-\sigma_{33})^2 + (\sigma_{33}-\sigma_{11})^2 + 6(\sigma_{12}^2+\sigma_{13}^2+\sigma_{23}^2)}{2}} \tag{4.3}$$

where σ_{eq} is equivalent von Mises stress; J_2 is second invariant of the deviatoric part of the stress tensor; and σ_{ij} are components of the stress tensor.

In a hydrostatic loading case for a mean-field model, only the hydrostatic part of stress is present in the mean stress of the matrix, while the deviatoric one is equal to zero. It means that the equivalent von Mises stress would also be equal to zero, so the matrix will never reach the yield point. Thus, such loading conditions are known to pose important difficulties for many mean-field models of metal matrix elastic–plastic composites (Naili & Doghri, 2023). As they make use of mean values of stress (the first moment) to perform the uniformisation step, they predict a purely elastic response of the phases, even though plastic yielding of the metal matrix is observed in the full-field calculations, e.g. in FEM. The non-homogenous microstructure induces areas of local non-hydrostatic stress conditions, especially around inclusions/voids, meaning that the plastic yielding actually occurs. This needs to be taken into consideration.

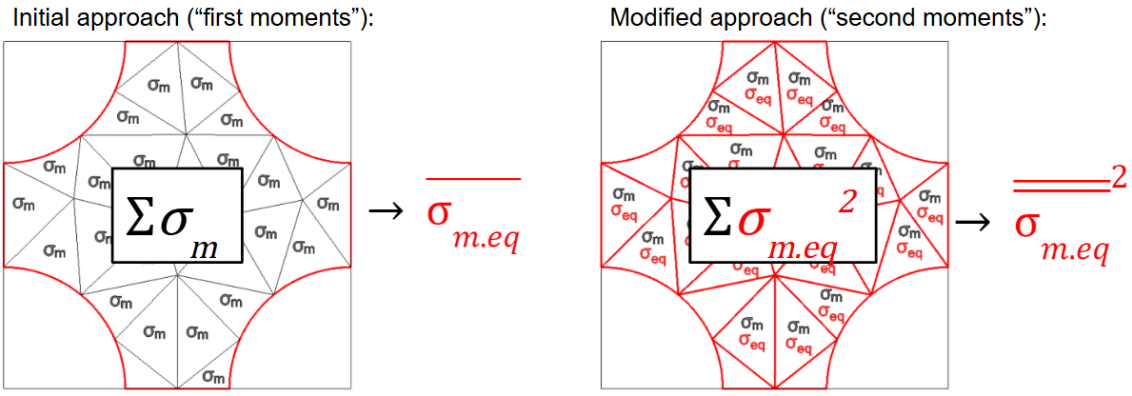

Figure 4.4: Difference between the "first moments" (left); and "second moments" (right) approach visualised on a graph with "finite elements". Please note that this is a metaphor in order to explain the idea of the method. The cluster is a mean field model, meaning that, in the end, there are no finite elements, but a continuous medium described by a single value.

The general idea is to change the way by which the averaged equivalent stress for the matrix is calculated in the algorithm. The initial approach (so called "first moments") consists of averaging the stress tensor in the matrix σ_m first, and then calculating the equivalent stress $\sigma_{m.eq}$. The modified approach (so called "second moments") aims to calculate the local equivalent stresses $\sigma_{m.eq}$ first and then perform the volume averaging. Thanks to this approach, the local plastic conditions are not zeroed and they sum up to give a non-zero global equivalent stress, allowing for a better representation of the behaviour of a real composite. In figure 4.4 the difference is explained using a metaphor of finite element discretisation of the unit cell.

4.1.3 Isotropisation

The cluster model assumes that the matrix material is isotropic. It is true in the elastic regime, but as the plastic effects occur, it is no longer the case. The tangent stiffness tensor is anisotropic (and thus the shear stiffness) and depends on the shear loading direction. If shear loading agrees with the direction of plastic strain rate, we have plastic shear modulus G^t, while for other directions the modulus remains elastic G (as per schematic figure 4.5).

In order to implement the plastic regime into the cluster model, it is necessary to find an acceptable isotropic approximation of the anisotropic shear moduli. Based on the literature (Chaboche et al., 2005), following approach is proposed where the values of the shear modulus are assumed to be equal in each direction of shearing and calculated as a weighted sum of the elastic and plastic ones:

$$G_r^{iso} = (1 - \psi)G_r^t + \psi G_r \tag{4.4}$$

where G_r^{iso} is isotropic elastic-plastic shear modulus for a given phase r; G_r is elastic shear modulus for a given phase r; G_r^t is plastic shear modulus for a given phase r; and ψ is weight factor depending on the isotropisation method. In the literature, the value of the isotropisation weight factor ψ is usually

assumed as 0.8 (so called “hard isotropisation”) or 0.0 (“soft isotropisation) where only plastic part is considered. In this thesis, the "soft" isotropisation (i.e. with $\psi = 0.0$) is used, as this selection of isotropisation method was demonstrated as being more efficient (Doghri & Friebel, 2005; Kursa et al., 2018).

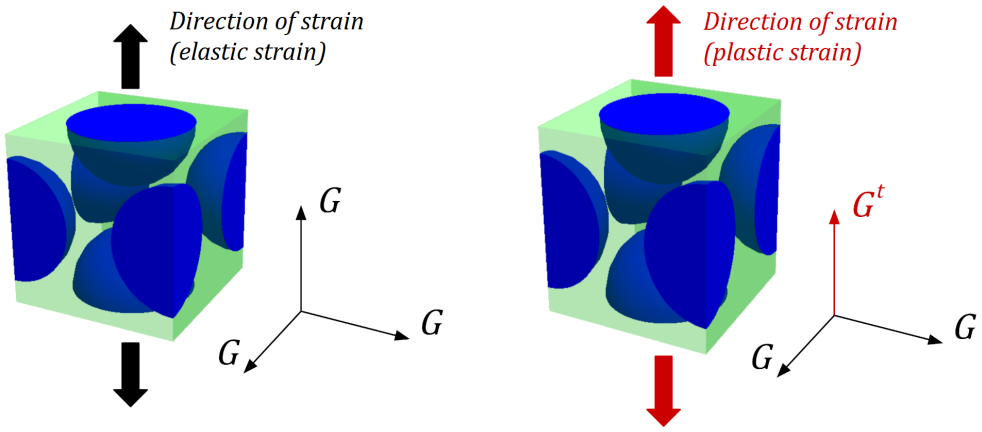

Figure 4.5: Values of the shear modulus of the matrix in different directions are equal in the elastic regime (left), but changes in the plastic regime (right), meaning that the matrix becomes anisotropic. Large arrows denote the direction of isochoric tension.

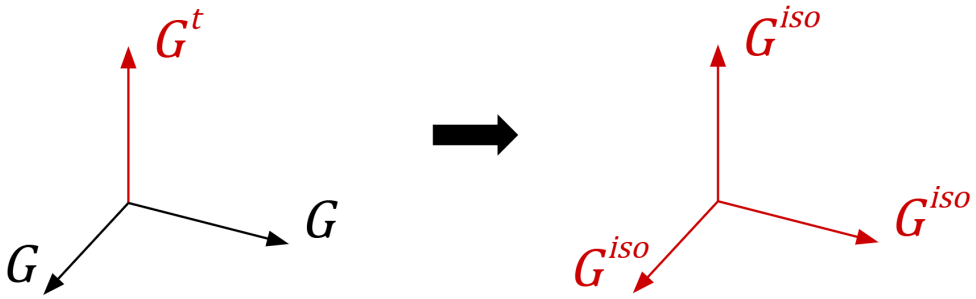

Figure 4.6: General idea: the averaged (isotropised) values are assumed for each direction, making the matrix material isotropic again for calculation purposes. It must be remembered that the stiffness tensor $\mathbb{C}$ (on which the shear moduli are dependent) is in fact a fourth-order tensor (the figure should be done in 5D space not 3D space).

4.2 Theoretical formulation

In the analysis, it is assumed that in the plastic regime the metal matrix is locally described by the Huber-von Mises yield function with the associated flow rule (the so-called isotropic J_2 plasticity) and the power-law isotropic hardening (see table 4.1 for the respective equations). In the model, the strain and strain rate are additively decomposed into the elastic and plastic parts and the stress or stress rate can be obtained from the linear Hooke’s law for the elastic part of the strain or strain rate, namely:

$$\dot{\boldsymbol{\sigma}} = \mathbb{C}^{\mathrm{e}}_{\mathrm{m}} \cdot (\dot{\boldsymbol{\varepsilon}} - \dot{\boldsymbol{\varepsilon}}^{\mathrm{p}}(\boldsymbol{\sigma}, \varepsilon^{\mathrm{p}}_{\mathrm{eq}}))\,, \quad \boldsymbol{\sigma} = \mathbb{C}^{\mathrm{e}}_{\mathrm{m}} \cdot (\boldsymbol{\varepsilon} - \boldsymbol{\varepsilon}^{\mathrm{p}}(\boldsymbol{\sigma}, \varepsilon^{\mathrm{p}}_{\mathrm{eq}}))\,. \tag{4.5}$$

Moreover, in the plastic regime, a one-to-one relation exists between the equivalent plastic strain and the equivalent von Mises stress:

$$\sigma_{\mathrm{eq}} = Y_0 + h\,\left(\varepsilon^{\mathrm{p}}_{\mathrm{eq}}\right)^n \quad \rightarrow \quad \varepsilon^{\mathrm{p}}_{\mathrm{eq}}(\sigma_{\mathrm{eq}}) = \left(\frac{\sigma_{\mathrm{eq}} - Y_0}{h}\right)^{1/n}. \tag{4.6}$$

where Y_0 is initial yield stress of matrix; n is exponent in the hardening law; and h is hardening modulus of the matrix material.

The above-listed equations cannot be directly used to find the respective cluster model formula, as the plastic strain evolves in a non-linear way and is spatially non-uniform within the matrix. As mentioned in the previous subsection, some additional steps must be taken to incorporate those equations into the cluster model framework, i.e.: linearisation, uniformisation and isotropisation.

Table 4.1: Local constitutive relations for the elastic-plastic metal matrix.

Elastic-plastic model of the matrix material		
Yield condition	$f(\boldsymbol{\sigma}) = \sigma_{\mathrm{eq}} - Y(\varepsilon^{\mathrm{p}}_{\mathrm{eq}}) \leq 0$	$\boldsymbol{\sigma}^{\mathrm{D}} = \mathrm{dev}(\boldsymbol{\sigma})$, $\sigma_{\mathrm{eq}} = \sqrt{\frac{3}{2}\boldsymbol{\sigma}^{\mathrm{D}} \cdot \boldsymbol{\sigma}^{\mathrm{D}}}$
Flow rule	$\dot{\boldsymbol{\varepsilon}}^{\mathrm{p}} = \lambda \frac{3\boldsymbol{\sigma}^{\mathrm{D}}}{2Y}$	$\dot{\boldsymbol{\varepsilon}}^{\mathrm{p}} = \dot{\boldsymbol{\varepsilon}} - \dot{\boldsymbol{\varepsilon}}^{\mathrm{e}}$
Consistency conditions	$\lambda f = 0 \quad \wedge \quad \lambda \dot{f} = 0$	
Hardening law	$Y\left(\varepsilon^{\mathrm{p}}_{\mathrm{eq}}\right) = Y_0 + h\,\left(\varepsilon^{\mathrm{p}}_{\mathrm{eq}}\right)^n$	$\dot{\varepsilon}^{\mathrm{p}}_{\mathrm{eq}} = \sqrt{\frac{2}{3}\dot{\boldsymbol{\varepsilon}}^{\mathrm{p}} \cdot \dot{\boldsymbol{\varepsilon}}^{\mathrm{p}}} = \lambda$

The first step is linearisation. The elastic–plastic relations are written in the thermoelastic-like (affine) incremental or non-incremental form as follows:

$$\dot{\boldsymbol{\sigma}} = \mathbb{C}^{\mathrm{ep,aff}}_{\mathrm{m}}(\boldsymbol{\sigma}, \varepsilon^{p}_{\mathrm{eq}}) \cdot \dot{\boldsymbol{\varepsilon}} - \boldsymbol{\beta}^{\mathrm{aff}}_{\mathrm{m}}(\boldsymbol{\sigma}, \varepsilon^{\mathrm{p}}_{\mathrm{eq}}) \tag{4.7}$$

or

$$\boldsymbol{\sigma} = \mathbb{C}^{\mathrm{ep,aff}}_{\mathrm{m}}(\boldsymbol{\sigma}, \varepsilon^{\mathrm{p}}_{\mathrm{eq}}) \cdot \boldsymbol{\varepsilon} - \boldsymbol{\beta}^{\mathrm{aff}}_{\mathrm{m}}(\boldsymbol{\sigma}, \varepsilon^{\mathrm{p}}_{\mathrm{eq}})\,, \tag{4.8}$$

where the definitions of $\mathbb{C}^{\mathrm{ep,aff}}_{\mathrm{m}}(\boldsymbol{\sigma}, \varepsilon^{\mathrm{p}}_{\mathrm{eq}})$ and $\boldsymbol{\beta}^{\mathrm{aff}}_{\mathrm{m}}(\boldsymbol{\sigma}, \varepsilon^{\mathrm{p}}_{\mathrm{eq}})$ depend on the applied linearisation method and are not the same for incremental and non-incremental formulations. In the second "uniformisation" step, the quantities $\boldsymbol{\sigma}$ and $\varepsilon^{\mathrm{p}}_{\mathrm{eq}}$ are approximated by some values, uniform within the matrix material, denoted as $\hat{\boldsymbol{\sigma}}$ and $\hat{\varepsilon}^{\mathrm{p}}_{\mathrm{eq}}$:

$$\mathbb{C}^{\mathrm{ep,aff}}_{\mathrm{m}}(\boldsymbol{\sigma}, \varepsilon^{\mathrm{p}}_{\mathrm{eq}}) \approx \mathbb{C}^{\mathrm{ep,aff}}_{\mathrm{m}}(\hat{\boldsymbol{\sigma}}, \hat{\varepsilon}^{\mathrm{p}}_{\mathrm{eq}})\,, \quad \boldsymbol{\beta}^{\mathrm{aff}}_{\mathrm{m}}(\boldsymbol{\sigma}, \varepsilon^{\mathrm{p}}_{\mathrm{eq}}) \approx \boldsymbol{\beta}^{\mathrm{aff}}_{\mathrm{m}}(\hat{\boldsymbol{\sigma}}, \hat{\varepsilon}^{\mathrm{p}}_{\mathrm{eq}})\,. \tag{4.9}$$

Additionally, in the case of the cluster model, to make use of the closed-form formulas and preserve computational robustness of the model, in the third step the elastic-plastic stiffness $\mathbb{C}^{\mathrm{ep,aff}}_{\mathrm{m}}(\hat{\boldsymbol{\sigma}}, \hat{\varepsilon}^{\mathrm{p}}_{\mathrm{eq}})$ is isotropised, so that equations (4.7)-(4.8) are finally approximated as:

$$\dot{\boldsymbol{\sigma}} = \mathbb{C}^{\mathrm{ep,aff,iso}}_{\mathrm{m}}(\hat{\boldsymbol{\sigma}}, \hat{\varepsilon}^{\mathrm{p}}_{\mathrm{eq}}) \cdot \dot{\boldsymbol{\varepsilon}} - \boldsymbol{\beta}^{\mathrm{aff}*}_{\mathrm{m}}(\hat{\boldsymbol{\sigma}}, \hat{\varepsilon}^{\mathrm{p}}_{\mathrm{eq}}) \tag{4.10}$$

or

$$\boldsymbol{\sigma} = \mathbb{C}^{\mathrm{ep,aff,iso}}_{\mathrm{m}}(\hat{\boldsymbol{\sigma}}, \hat{\varepsilon}^{\mathrm{p}}_{\mathrm{eq}}) \cdot \boldsymbol{\varepsilon} - \boldsymbol{\beta}^{\mathrm{aff}*}_{\mathrm{m}}(\hat{\boldsymbol{\sigma}}, \hat{\varepsilon}^{\mathrm{p}}_{\mathrm{eq}})\,, \tag{4.11}$$

where:

$$\mathbb{C}^{\mathrm{ep,aff,iso}}_{\mathrm{m}}(\hat{\boldsymbol{\sigma}}, \hat{\varepsilon}^{\mathrm{p}}_{\mathrm{eq}}) = 3K_{\mathrm{m}}\mathbb{I}^{\mathrm{P}} + 2G^{\mathrm{ep,aff,iso}}_{\mathrm{m}}(\hat{\boldsymbol{\sigma}}, \hat{\varepsilon}^{\mathrm{p}}_{\mathrm{eq}})\mathbb{I}^{\mathrm{D}}\,, \tag{4.12}$$

where $\boldsymbol{\beta}^{\mathrm{aff}*}_{\mathrm{m}}(\hat{\boldsymbol{\sigma}}, \hat{\varepsilon}^{\mathrm{p}}_{\mathrm{eq}})$ is the form of $\boldsymbol{\beta}^{\mathrm{aff}}_{\mathrm{m}}(\hat{\boldsymbol{\sigma}}, \hat{\varepsilon}^{\mathrm{p}}_{\mathrm{eq}})$ after isotropisation of $\mathbb{C}^{\mathrm{ep,aff}}_{\mathrm{m}}(\hat{\boldsymbol{\sigma}}, \hat{\varepsilon}^{\mathrm{p}}_{\mathrm{eq}})$, K_{m} is the constant elastic bulk modulus of the matrix, $G^{\mathrm{ep,aff,iso}}_{\mathrm{m}}(\hat{\boldsymbol{\sigma}}, \hat{\varepsilon}^{\mathrm{p}}_{\mathrm{eq}})$ is the isotropic affine shear modulus of the matrix, and $\mathbb{I}^{\mathrm{P}}$, $\mathbb{I}^{\mathrm{D}}$ are defined in section 2.2 of chapter 2.

With such an approximation of the local matrix law, we may proceed with applying the cluster model with the reservation that $\hat{\boldsymbol{\sigma}}_{\mathrm{m}}$ and $\hat{\varepsilon}^{\mathrm{p}}_{\mathrm{eq}}$ evolve as deformation advances, so the solution must be obtained step-by-step. Note that the relation between the mean stress (or stress rate) and mean strain (or strain rate) in the matrix, resulting from equation (4.12), takes the form equivalent to equation (2.1) in section 2.1 of chapter 2:

$$\dot{\boldsymbol{\sigma}}_{\mathrm{m}} = \mathbb{C}^{\mathrm{ep,aff,iso}}_{\mathrm{m}}(\hat{\boldsymbol{\sigma}}, \hat{\varepsilon}^{\mathrm{p}}_{\mathrm{eq}}) \cdot \dot{\boldsymbol{\varepsilon}}_{\mathrm{m}} - \boldsymbol{\beta}^{\mathrm{aff}*}_{\mathrm{m}}(\hat{\boldsymbol{\sigma}}, \hat{\varepsilon}^{\mathrm{p}}_{\mathrm{eq}}) \tag{4.13}$$

or

$$\boldsymbol{\sigma}_{\mathrm{m}} = \mathbb{C}^{\mathrm{ep,aff,iso}}_{\mathrm{m}}(\hat{\boldsymbol{\sigma}}, \hat{\varepsilon}^{\mathrm{p}}_{\mathrm{eq}}) \cdot \boldsymbol{\varepsilon}_{\mathrm{m}} - \boldsymbol{\beta}^{\mathrm{aff}*}_{\mathrm{m}}(\hat{\boldsymbol{\sigma}}, \hat{\varepsilon}^{\mathrm{p}}_{\mathrm{eq}})\,, \tag{4.14}$$

where the argument $\hat{\boldsymbol{\sigma}}$ is not necessarily equal to $\boldsymbol{\sigma}_{\mathrm{m}}$ and, similarly, the current $\hat{\varepsilon}^{\mathrm{p}}_{\mathrm{eq}}$ is not necessarily calculated based on mean values of stress and strain tensors (which are also called the first stress and strain moments).

As mentioned previously, only the tangent linearisation is considered for the cluster model. There are three variants possible: incremental tangent, non-incremental tangent (affine) and modified tangent schemes. The tangent elastic–plastic moduli are defined using the rate form of the local relations (4.5). The local flow rule and consistency relation lead to the following definition of the anisotropic tangent elastic–plastic modulus:

$$\dot{\boldsymbol{\sigma}} = \mathbb{C}_{\mathrm{m}}^{\mathrm{ep,t}}(\boldsymbol{\sigma}, \varepsilon_{\mathrm{eq}}^{\mathrm{p}}) \cdot \dot{\boldsymbol{\varepsilon}} \quad \text{with} \quad \mathbb{C}_{\mathrm{m}}^{\mathrm{ep,t}}(\boldsymbol{\sigma}, \varepsilon_{\mathrm{eq}}^{\mathrm{p}}) = \mathbb{C}_{\mathrm{m}}^{\mathrm{e}} \quad \text{if} \quad \lambda(\boldsymbol{\sigma}, \varepsilon_{\mathrm{eq}}^{\mathrm{p}}) = 0 \tag{4.15}$$

and:

$$\mathbb{C}_{\mathrm{m}}^{\mathrm{ep,t}}(\boldsymbol{\sigma}, \varepsilon_{\mathrm{eq}}^{\mathrm{p}}) = 3K_{\mathrm{m}}\mathbb{I}^{\mathrm{P}} + 2G_{\mathrm{m}}^{\mathrm{ep,t}}(\varepsilon_{\mathrm{eq}}^{\mathrm{p}})\mathbb{N}^{\mathrm{D}} + 2G_{\mathrm{m}}(\mathbb{I}^{\mathrm{D}} - \mathbb{N}^{\mathrm{D}}) \quad \text{if} \quad \lambda(\boldsymbol{\sigma}, \varepsilon_{\mathrm{eq}}^{\mathrm{p}}) > 0\,, \tag{4.16}$$

where the fourth order tensor $\mathbb{N}^{\mathrm{D}}$ is:

$$\mathbb{N}^{\mathrm{D}} = \mathbf{N}^{\mathrm{D}} \otimes \mathbf{N}^{\mathrm{D}} \tag{4.17}$$

and $\mathbf{N}^{\mathrm{D}}$ is the direction of the stress deviator $\boldsymbol{\sigma}^{\mathrm{D}}$, while the modulus $G_{\mathrm{m}}^{\mathrm{ep,t}}(\varepsilon_{\mathrm{eq}}^{\mathrm{p}})$ decreases with the accumulated plastic strain:

$$\mathbf{N}^{\mathrm{D}} = \frac{\boldsymbol{\sigma}^{\mathrm{D}}}{\sqrt{\boldsymbol{\sigma}^{\mathrm{D}} \cdot \boldsymbol{\sigma}^{\mathrm{D}}}}\,, \quad G_{\mathrm{m}}^{\mathrm{ep,t}}(\varepsilon_{\mathrm{eq}}^{\mathrm{p}}) = G_{\mathrm{m}} \frac{Y'(\varepsilon_{\mathrm{eq}}^{\mathrm{p}})}{Y'(\varepsilon_{\mathrm{eq}}^{\mathrm{p}}) + 3G_{\mathrm{m}}} = G_{\mathrm{m}} \frac{nh(\varepsilon_{\mathrm{eq}}^{\mathrm{p}})^{n-1}}{nh(\varepsilon_{\mathrm{eq}}^{\mathrm{p}})^{n-1} + 3G_{\mathrm{m}}}\,, \tag{4.18}$$

where $Y'(\varepsilon_{\mathrm{eq}}^{\mathrm{p}})$ denotes the derivative of $Y(\varepsilon_{\mathrm{eq}}^{\mathrm{p}})$ with respect to $\varepsilon_{\mathrm{eq}}^{\mathrm{p}}$; and G_{m} is the constant elastic shear modulus of the matrix.

The three mentioned variants of tangent linearisation and "uniformisation" rely on the tangent modulus (4.16) and specify $\mathbb{C}_{\mathrm{m}}^{\mathrm{ep,aff,iso}}(\hat{\boldsymbol{\sigma}}, \hat{\varepsilon}_{\mathrm{eq}}^{\mathrm{p}})$ and $\boldsymbol{\beta}_{\mathrm{m}}^{\mathrm{aff}*}(\hat{\boldsymbol{\sigma}}, \hat{\varepsilon}_{\mathrm{eq}}^{\mathrm{p}})$ as in the following points:

- **The Tangent model.** The affine local relation (4.10) is postulated with $G_{\mathrm{m}}^{\mathrm{ep,aff,iso}}(\hat{\boldsymbol{\sigma}}, \hat{\varepsilon}_{\mathrm{eq}}^{\mathrm{p}}) = G_{\mathrm{m}}^{\mathrm{ep,t}}(\bar{\varepsilon}_{\mathrm{eq}}^{\mathrm{p}})$ for $\lambda(\boldsymbol{\sigma}_m, \bar{\varepsilon}_{\mathrm{eq}}^{\mathrm{p}}) > 0$, so it is calculated based on the mean values of the stress and strain field in the matrix (the so-called first moments). In particular, using relation (4.6), we use the mean value of stress in the matrix phase to calculate $\hat{\varepsilon}_{\mathrm{eq}}^{\mathrm{p}}$ ($\hat{\sigma}_{\mathrm{eq}} := \bar{\sigma}_{\mathrm{eq}}$):

$$\varepsilon_{\mathrm{eq}}^{\mathrm{p}} \approx \hat{\varepsilon}_{\mathrm{eq}}^{\mathrm{p}} := \bar{\varepsilon}_{\mathrm{eq}}^{\mathrm{p}}(\bar{\sigma}_{\mathrm{eq}}) = \left(\frac{\bar{\sigma}_{\mathrm{eq}} - Y_0}{h}\right)^{1/n} \quad \text{where} \quad \bar{\sigma}_{\mathrm{eq}} = \sqrt{\frac{3}{2}\boldsymbol{\sigma}_{\mathrm{m}}^{\mathrm{D}} \cdot \boldsymbol{\sigma}_{\mathrm{m}}^{\mathrm{D}}}\,, \tag{4.19}$$

  with $\boldsymbol{\sigma}_{\mathrm{m}}^{\mathrm{D}}$ being the deviatoric part of $\boldsymbol{\sigma}_{\mathrm{m}}$. The free term $\boldsymbol{\beta}_{\mathrm{m}}^{\mathrm{aff}*}(\hat{\boldsymbol{\sigma}}, \hat{\varepsilon}_{\mathrm{eq}}^{\mathrm{p}})$ in equation (4.10) incorporates the anisotropic part of the tangent stiffness tensor and is specified as:

$$\boldsymbol{\beta}_{\mathrm{m}}^{\mathrm{aff}*}(\hat{\boldsymbol{\sigma}}, \hat{\varepsilon}_{\mathrm{eq}}^{\mathrm{p}}) \approx \boldsymbol{\beta}_{\mathrm{m}}^{\mathrm{aff}*}(\boldsymbol{\sigma}_{\mathrm{m}}, \bar{\varepsilon}_{\mathrm{eq}}^{\mathrm{p}}) = 2(G^{\mathrm{ep,t}}(\bar{\varepsilon}_{\mathrm{eq}}^{\mathrm{p}}) - G_{\mathrm{m}})(\mathbb{I}^{\mathrm{D}} - \mathbb{N}^{\mathrm{D}}(\boldsymbol{\sigma}_{\mathrm{m}})) \cdot \dot{\boldsymbol{\varepsilon}}_{\mathrm{m}}\,, \tag{4.20}$$

  so again, it is calculated using the mean values of the stress and strain fields in the matrix phase. This isotropic approximation of the tangent stiffness is justified by the fact that for the proportional loading process, in which $\mathbf{N}'$ remains constant at a given material point of the matrix phase, we have:

$$\dot{\boldsymbol{\sigma}} = \mathbb{C}_{\mathrm{m}}^{\mathrm{ep,t}}(\boldsymbol{\sigma}, \varepsilon_{\mathrm{eq}}^{\mathrm{p}}) \cdot \dot{\boldsymbol{\varepsilon}} = \mathbb{C}_{\mathrm{m}}^{\mathrm{ep,t,iso}}(\varepsilon_{\mathrm{eq}}^{\mathrm{p}}) \cdot \dot{\boldsymbol{\varepsilon}}\,. \tag{4.21}$$

  It is worth mentioning that in the case of the proposed tangent linearisation and unformisation based on the first moments, the analogical equality for mean values, namely:

$$\dot{\boldsymbol{\sigma}}_{\mathrm{m}} = \mathbb{C}_{\mathrm{m}}^{\mathrm{ep,t}}(\boldsymbol{\sigma}_{\mathrm{m}}, \bar{\varepsilon}_{\mathrm{eq}}^{\mathrm{p}}) \cdot \dot{\boldsymbol{\varepsilon}}_{\mathrm{m}} = \mathbb{C}_{\mathrm{m}}^{\mathrm{ep,t,iso}}(\bar{\varepsilon}_{\mathrm{eq}}^{\mathrm{p}}) \cdot \dot{\boldsymbol{\varepsilon}}_{\mathrm{m}}\,, \tag{4.22}$$

  remains valid for most of the processes considered in the present chapter: hydrostatic extension and isochoric tension in the direction of an edge or diagonal of cubic RC, BCC and FCC unit cells, so in these cases $\boldsymbol{\beta}_{\mathrm{m}}^{\mathrm{aff}*}(\hat{\boldsymbol{\sigma}}, \hat{\varepsilon}_{\mathrm{eq}}^{\mathrm{p}}) = \mathbf{0}$. On the other hand, in general, the condition is not fulfilled, as for example for isochoric tension in an arbitrary direction within the cubic unit cell.

- **The Non-incremental Tangent (Affine) model**. In Masson et al. (2000) it was proposed to consider the local law in the matrix in the non-incremental form while employing the tangent modulus. Following this proposal, for the non-incremental relation (4.12) we set $G_{\mathrm{m}}^{\mathrm{ep,aff,iso}}(\hat{\boldsymbol{\sigma}}, \hat{\varepsilon}_{\mathrm{eq}}^{\mathrm{p}}) = G_{\mathrm{m}}^{\mathrm{ep,t}}(\bar{\varepsilon}_{\mathrm{eq}}^{\mathrm{p}})$ where $G_{\mathrm{m}}^{\mathrm{ep,t}}(\bar{\varepsilon}_{\mathrm{eq}}^{\mathrm{p}})$ is given by equation (4.18). Then, the "thermal stress"-like term is given by

$$\boldsymbol{\beta}_{\mathrm{m}}^{\mathrm{aff}*}(\hat{\boldsymbol{\sigma}}, \varepsilon_{\mathrm{eq}}^{\mathrm{p}}) = \mathbb{C}_{\mathrm{m}}^{\mathrm{ep,t,iso}}(\bar{\varepsilon}_{\mathrm{eq}}^{\mathrm{p}}) \cdot \boldsymbol{\varepsilon}_{\mathrm{m}} - \boldsymbol{\sigma}_{\mathrm{m}}\,, \tag{4.23}$$

so again, "uniformisation" is performed using the mean quantities (first moments) per phase. In practice, in the numerical step-by-step algorithm, the $\boldsymbol{\beta}$-term for step $t+\Delta t$ is calculated as:

$$\boldsymbol{\beta}_{\mathrm{m}}^{\mathrm{aff}*}(t+\Delta t)=\mathbb{C}_{\mathrm{m}}^{\mathrm{ep,t,iso}}(t+\Delta t)\cdot\boldsymbol{\varepsilon}_{\mathrm{m}}(t)-\boldsymbol{\sigma}_{\mathrm{m}}(t)-(\mathbb{C}_{\mathrm{m}}^{\mathrm{ep,t}}(t+\Delta t)-\mathbb{C}_{\mathrm{m}}^{\mathrm{ep,t,iso}}(t+\Delta t))\cdot\Delta\boldsymbol{\varepsilon}_{\mathrm{m}}\,, \tag{4.24}$$

where $\Delta\boldsymbol{\varepsilon}_{\mathrm{m}}=\boldsymbol{\varepsilon}_{\mathrm{m}}(t+\Delta t)-\boldsymbol{\varepsilon}_{\mathrm{m}}(t)$, and the last term in equation (4.24) vanishes for the proportional processes mentioned above.

- **The modified Tangent model.** A less common method of "uniformisation" of the affine moduli is based on the use of the so-called second moment of stress (Suquet, 1997), namely:

$$\bar{S}_{\mathrm{m}}=\mathbb{I}^{\mathrm{D}}\cdot\langle\boldsymbol{\sigma}\otimes\boldsymbol{\sigma}\rangle_{\mathrm{m}}=\left\langle\boldsymbol{\sigma}^{\mathrm{D}}\cdot\boldsymbol{\sigma}^{\mathrm{D}}\right\rangle_{\mathrm{m}}=\frac{2}{3}\left\langle\sigma_{\mathrm{eq}}^{2}\right\rangle_{\mathrm{m}}\,, \tag{4.25}$$

so that:

$$\varepsilon_{\mathrm{eq}}^{\mathrm{p}}\approx\hat{\varepsilon}_{\mathrm{eq}}^{\mathrm{p}}=\bar{\bar{\varepsilon}}_{\mathrm{eq}}^{\mathrm{p}}(\bar{\bar{\sigma}}_{\mathrm{eq}})\quad\text{where}\quad\bar{\bar{\sigma}}_{\mathrm{eq}}=\sqrt{\left\langle\sigma_{\mathrm{eq}}^{2}\right\rangle_{\mathrm{m}}}=\sqrt{\frac{3}{2}\bar{S}_{\mathrm{m}}} \tag{4.26}$$

and $\hat{\varepsilon}_{\mathrm{eq}}^{\mathrm{p}}=\bar{\bar{\varepsilon}}_{\mathrm{eq}}^{\mathrm{p}}$ is used to calculate the isotropic tangent shear modulus and the $\boldsymbol{\beta}$-term in equation (4.12). Also, the yield condition is checked based on $\bar{\bar{\sigma}}_{\mathrm{eq}}$. Because this value is independent of $\boldsymbol{\sigma}_{\mathrm{m}}$ and $\boldsymbol{\varepsilon}_{\mathrm{m}}$, which could be found using the set of equations of the cluster model, an additional relation is needed to track the value of $\bar{S}_{\mathrm{m}}$ in the course of calculations. To this end in (Berbenni, 2021), in the context of elastic-viscoplastic two-phase materials and another mean-field approach, it was proposed to use the Hill-Mandel lemma (Hill, 1967) in the form:

$$\bar{\boldsymbol{\sigma}}\cdot\dot{\bar{\boldsymbol{\varepsilon}}}=\langle\boldsymbol{\sigma}\cdot\dot{\boldsymbol{\varepsilon}}\rangle=f_{\mathrm{i}}\left\langle\boldsymbol{\sigma}\cdot\dot{\boldsymbol{\varepsilon}}\right\rangle_{\mathrm{i}}+(1-f_{\mathrm{i}})\left\langle\boldsymbol{\sigma}\cdot\dot{\boldsymbol{\varepsilon}}\right\rangle_{\mathrm{m}}\,. \tag{4.27}$$

Next, observing that the heterogeneity of fields within the inclusion phase and the hydrostatic part of fields in the matrix are less pronounced, the formula was simplified as follows:

$$\bar{\boldsymbol{\sigma}}\cdot\dot{\bar{\boldsymbol{\varepsilon}}}=f_{\mathrm{i}}\boldsymbol{\sigma}_{\mathrm{i}}\cdot\dot{\boldsymbol{\varepsilon}}_{\mathrm{i}}+3(1-f_{\mathrm{i}})\sigma_{\mathrm{m}}^{\mathrm{H}}\dot{\varepsilon}_{\mathrm{m}}^{\mathrm{H}}+(1-f_{\mathrm{i}})\left\langle\boldsymbol{\sigma}^{\mathrm{D}}\cdot\dot{\boldsymbol{\varepsilon}}^{\mathrm{D}}\right\rangle_{\mathrm{m}}\,, \tag{4.28}$$

where $\sigma_{\mathrm{m}}^{\mathrm{H}}\mathbf{I}$ and $\varepsilon_{\mathrm{m}}^{\mathrm{H}}\mathbf{I}$ are the hydrostatic parts of $\boldsymbol{\sigma}_{\mathrm{m}}$ and $\boldsymbol{\varepsilon}_{\mathrm{m}}$, respectively, while $\boldsymbol{\varepsilon}^{\mathrm{D}}$ is the deviatoric part of $\boldsymbol{\varepsilon}$. As it is seen, following this simplification regarding the inclusion phase and the hydrostatic part of fields in the elastic-plastic matrix, only the mean values of fields per phase are taken into account. The last term, employing the deviatoric part of the stress and strain rate fields in the matrix, is expanded and approximated by introducing equation (4.12) with:

$$\begin{aligned}\mathbb{C}_{\mathrm{m}}^{\mathrm{ep,t,iso}}(\varepsilon_{\mathrm{eq}}^{\mathrm{p}})&\approx\mathbb{C}_{\mathrm{m}}^{\mathrm{ep,t}}(\bar{\bar{\varepsilon}}_{\mathrm{eq}}^{\mathrm{p}})=3K_{\mathrm{m}}\mathbb{I}^{\mathrm{P}}+2G_{\mathrm{m}}^{\mathrm{ep,t}}(\bar{\bar{\varepsilon}}_{\mathrm{eq}}^{\mathrm{p}})\mathbb{I}^{\mathrm{D}}\,, &(4.29)\\ \boldsymbol{\beta}_{\mathrm{m}}^{\mathrm{aff}*}(\hat{\boldsymbol{\sigma}},\hat{\varepsilon}_{\mathrm{eq}}^{\mathrm{p}})&\approx\boldsymbol{\beta}_{\mathrm{m}}^{\mathrm{aff}*}(\boldsymbol{\sigma}_{\mathrm{m}},\bar{\bar{\varepsilon}}_{\mathrm{eq}}^{\mathrm{p}})=2(G_{\mathrm{m}}^{\mathrm{ep,t}}(\bar{\bar{\varepsilon}}_{\mathrm{eq}}^{\mathrm{p}})-G_{\mathrm{m}})(\mathbb{I}^{\mathrm{D}}-\mathbb{N}^{\mathrm{D}}(\boldsymbol{\sigma}_{\mathrm{m}}))\cdot\dot{\boldsymbol{\varepsilon}}_{\mathrm{m}}\,, &(4.30)\end{aligned}$$

after which it is obtained:

$$\begin{gathered}\left\langle\boldsymbol{\sigma}^{\mathrm{D}}\cdot\dot{\boldsymbol{\varepsilon}}^{\mathrm{D}}\right\rangle_{\mathrm{m}}\approx\frac{1}{2G_{\mathrm{m}}^{\mathrm{ep,t}}}\left\langle\boldsymbol{\sigma}^{\mathrm{D}}\cdot(\dot{\boldsymbol{\sigma}}^{\mathrm{D}}+\boldsymbol{\beta}_{\mathrm{m}}^{\mathrm{aff}*})\right\rangle_{\mathrm{m}}=\\ \frac{1}{2G_{\mathrm{m}}^{\mathrm{ep,t}}}\left(\left\langle\boldsymbol{\sigma}^{\mathrm{D}}\cdot\dot{\boldsymbol{\sigma}}^{\mathrm{D}}\right\rangle_{\mathrm{m}}+\boldsymbol{\sigma}_{\mathrm{m}}^{\mathrm{D}}\cdot\boldsymbol{\beta}_{\mathrm{m}}^{\mathrm{aff}*}\right)=\frac{1}{2G_{\mathrm{m}}^{\mathrm{ep,t}}}\left\langle\boldsymbol{\sigma}^{\mathrm{D}}\cdot\dot{\boldsymbol{\sigma}}^{\mathrm{D}}\right\rangle_{\mathrm{m}}\,.\end{gathered} \tag{4.31}$$

Based on the definition (4.25) we observe that:

$$\dot{\bar{S}}_{\mathrm{m}}=2\left\langle\boldsymbol{\sigma}^{\mathrm{D}}\cdot\dot{\boldsymbol{\sigma}}^{\mathrm{D}}\right\rangle_{\mathrm{m}}\,, \tag{4.32}$$

so the following relation is obtained for the time rate of the second moment:

$$\dot{\bar{S}}_{\mathrm{m}}=\frac{4G_{\mathrm{m}}^{\mathrm{ep,t}}}{1-f_{\mathrm{i}}}\left(\bar{\boldsymbol{\sigma}}\cdot\dot{\bar{\boldsymbol{\varepsilon}}}-f_{\mathrm{i}}\boldsymbol{\sigma}_{\mathrm{i}}\cdot\dot{\boldsymbol{\varepsilon}}_{\mathrm{i}}-3(1-f_{\mathrm{i}})\sigma_{\mathrm{m}}^{\mathrm{H}}\dot{\varepsilon}_{\mathrm{m}}^{\mathrm{H}}\right)\,. \tag{4.33}$$

In Berbenni (2021), the current value of $\bar{S}_m$ was found from the evolution equation: $\bar{S}_{\mathrm{m}}(t+\Delta t)=\bar{S}_{\mathrm{m}}(t)+\dot{\bar{S}}_{\mathrm{m}}(t)\Delta t$. However, since $\bar{S}_{\mathrm{m}}$ is a quadratic function of $\boldsymbol{\sigma}$, it has been found, in the present context of the elastic-plastic matrix, that for a computationally efficient update of $\bar{S}_{\mathrm{m}}$ we will

also require the second time rate of $\bar{S}_{\mathrm{m}}$. This quantity can be found using Hill's condition presented fully in rate form, namely:

$$\dot{\bar{\boldsymbol{\sigma}}} \cdot \dot{\bar{\boldsymbol{\varepsilon}}} = \langle \dot{\boldsymbol{\sigma}} \cdot \dot{\boldsymbol{\varepsilon}} \rangle = f_{\mathrm{i}} \langle \dot{\boldsymbol{\sigma}} \cdot \dot{\boldsymbol{\varepsilon}} \rangle_{\mathrm{i}} + (1 - f_{\mathrm{i}}) \langle \dot{\boldsymbol{\sigma}} \cdot \dot{\boldsymbol{\varepsilon}} \rangle_{\mathrm{m}} , \tag{4.34}$$

which, after the same simplifications as in equation (4.28), reduces to:

$$\dot{\bar{\boldsymbol{\sigma}}} \cdot \dot{\bar{\boldsymbol{\varepsilon}}} = f_{\mathrm{i}} \dot{\boldsymbol{\sigma}}_{\mathrm{i}} \cdot \dot{\boldsymbol{\varepsilon}}_{\mathrm{i}} + 3(1 - f_{\mathrm{i}}) \dot{\sigma}_{\mathrm{m}}^{\mathrm{H}} \dot{\varepsilon}_{\mathrm{m}}^{\mathrm{H}} + (1 - f_{\mathrm{i}}) \left\langle \dot{\boldsymbol{\sigma}}^{\mathrm{D}} \cdot \dot{\boldsymbol{\varepsilon}}^{\mathrm{D}} \right\rangle_{\mathrm{m}} . \tag{4.35}$$

After substituting equation (4.12), the last term is found as:

$$\left\langle \dot{\boldsymbol{\sigma}}^{\mathrm{D}} \cdot \dot{\boldsymbol{\varepsilon}}^{\mathrm{D}} \right\rangle_{\mathrm{m}} \approx \frac{1}{2G_{\mathrm{m}}^{\mathrm{ep,t}}} \left\langle \dot{\boldsymbol{\sigma}}^{\mathrm{D}} \cdot (\dot{\boldsymbol{\sigma}}^{\mathrm{D}} + \dot{\boldsymbol{\beta}}_{\mathrm{m}}^{\mathrm{aff}*}) \right\rangle_{\mathrm{m}} = \frac{1}{2G_{\mathrm{m}}^{\mathrm{ep,t}}} \left(\left\langle \dot{\boldsymbol{\sigma}}^{\mathrm{D}} \cdot \dot{\boldsymbol{\sigma}}^{\mathrm{D}} \right\rangle_{\mathrm{m}} + \dot{\boldsymbol{\sigma}}_{\mathrm{m}}^{\mathrm{D}} \cdot \dot{\boldsymbol{\beta}}_{\mathrm{m}}^{\mathrm{aff}*} \right) . \tag{4.36}$$

On the other hand, it is assumed that:

$$\ddot{\bar{S}}_{\mathrm{m}} = 2 \left\langle \boldsymbol{\sigma}^{\mathrm{D}} \cdot \ddot{\boldsymbol{\sigma}}^{\mathrm{D}} + \dot{\boldsymbol{\sigma}}^{\mathrm{D}} \cdot \dot{\boldsymbol{\sigma}}^{\mathrm{D}} \right\rangle_{\mathrm{m}} \approx 2 \left\langle \dot{\boldsymbol{\sigma}}^{\mathrm{D}} \cdot \dot{\boldsymbol{\sigma}}^{\mathrm{D}} \right\rangle_{\mathrm{m}} , \tag{4.37}$$

that is we assume that the stress increment along Δt is sufficiently smooth to neglect $\ddot{\boldsymbol{\sigma}}'$. Combing equations (4.35)-(4.37), we find:

$$\ddot{\bar{S}}_{\mathrm{m}} = \frac{4G_{\mathrm{m}}^{\mathrm{ep,t}}}{1 - f_{\mathrm{i}}} \left(\dot{\bar{\boldsymbol{\sigma}}} \cdot \dot{\bar{\boldsymbol{\varepsilon}}} - f_{\mathrm{i}} \dot{\boldsymbol{\sigma}}_{\mathrm{i}} \cdot \dot{\boldsymbol{\varepsilon}}_{\mathrm{i}} - 3(1 - f_{\mathrm{i}}) \dot{\sigma}_{\mathrm{m}}^{\mathrm{H}} \dot{\varepsilon}_{\mathrm{m}}^{\mathrm{H}} \right) - 2 \dot{\boldsymbol{\sigma}}_{\mathrm{m}}^{\mathrm{D}} \cdot \dot{\boldsymbol{\beta}}_{\mathrm{m}} . \tag{4.38}$$

Using equations (4.33) and (4.37), the value of $\bar{S}_{\mathrm{m}}$ is updated according to:

$$\bar{S}_{\mathrm{m}}(t + \Delta t) = \bar{S}_{\mathrm{m}}(t) + \dot{\bar{S}}_{\mathrm{m}} \Delta t + \frac{1}{2} \ddot{\bar{S}}_{\mathrm{m}} \Delta t^2 \tag{4.39}$$

and then used in equation (4.26) to find the current value of $\bar{\bar{\sigma}}_{\mathrm{eq}}$.

Note that the modified (incremental) tangent scheme was also employed in Doghri et al. (2011); however, authors calculated, the second moments using the algorithmic tangent modulus for the elastic predictor step, based on the finite increments of strain and stress in the matrix. Moreover, instead of the Hill-Mandel lemma, the second moments were specified based on differentiation of the effective elastic stiffness with respect to the shear modulus, as proposed in Suquet (1995).

It should be noted that the extension of the cluster scheme to elastic-plastic materials can also be performed using the classical or modified secant scheme model. It has been decided not to follow this path since the definition of the secant elastic-plastic modulus is restricted to the proportional loading processes. By contrast, the tangent elastic-plastic modulus $\mathbb{C}_{\mathrm{m}}^{\mathrm{ep,t}}(\boldsymbol{\sigma}, \varepsilon_{\mathrm{eq}}^{\mathrm{p}})$ in equation (4.16) can be calculated for any deformation path. As mentioned above, the difficulty of the tangent linearisation method, as compared to the secant model, is the anisotropy of the exact tensor $\mathbb{C}_{\mathrm{m}}^{\mathrm{ep,t}}(\boldsymbol{\sigma}, \varepsilon_{\mathrm{eq}}^{\mathrm{p}})$ (even though the plasticity model is isotropic). This tensor is orthotropic with the orthotropy directions induced by the principal axes of the plastic strain rate or, equivalently, stress in the matrix. Although there exist specifications of the polarisation tensor $\mathbb{P}_0$ and the interaction tensor between two inclusions $\boldsymbol{\Gamma}^{IJ}$ for an anisotropic matrix material (Berveiller et al., 1987), their application requires numerical integration to be performed and the closed-pre-defined gamma functions (explained section 2.4 of chapter 2) and, consequently, equations (2.52)-(2.54) cannot be applied. This strongly affects the computational efficiency and robustness of the method which are supposed to be the main advantages of the mean-field schemes, making them suitable for use in large-scale FEM computations (Sadowski et al., 2017). As demonstrated above, the issue here has been solved by using the isotropic $\mathbb{C}_{\mathrm{m}}^{\mathrm{ep,aff,iso}}$ specified by equations (4.12), with $G^{\mathrm{ep,t}}(\hat{\varepsilon}_{\mathrm{eq}}^{\mathrm{p}})$ as the shear modulus, to preserve the relative algebraic simplicity of the scheme in the elastic regime. The assumed isotropic approximation corresponds to the so-called "soft isotropisation" proposed in Chaboche et al. (2005).

It should be stressed that all three steps, i.e.: linearisation, uniformisation and isotropisation, introduce additional approximations to the mean-field model, as compared to the elastic regime, which may further affect the quality of predictions. Thus, a selection of the most appropriate approach must be based on verification with respect to full-field solutions, obtained e.g. by numerical FEM homogenisation, as it was previously done for the pure elastic regime. Such verification is reported in the next subsection.

4.3 Results

For the calculations in the elastic-plastic regime, two type of samples are considered: a metal matrix reinforced with ceramic inclusions (MMC), and a metal matrix weakened with voids. Material parameters of phases are listed in table 4.2.

Table 4.2: Parameters of materials used for analysis in elasto-plastic regime.

	Matrix: metallic	Inclusions: ceramic	Voids
Young Modulus, E [GPa]	75.0	400.0	-
shear modulus, G [GPa]	28.9	166.7	-
Poisson's ratio, ν [-]	0.3	0.2	-
yield stress, Y_0 [MPa]	75.0	-	-
plastic modulus, h [MPa]	416.0	-	-
exponent, n [-]	0.3895	-	-

Firstly, the analytical estimation of the cluster model is compared to the classic Mori-Tanaka scheme, with both models using tangent and modified tangent linearisation. In the case of the cluster model, the composite response for two directions of isochoric tension are compared: (0,0,1) and (1,1,1) with respect to the unit cell edges. Inclusions in the materials are arranged in the RC or BCC lattice. Results are presented in figures 4.7-4.8. Contrary to the Mori-Tanaka scheme, the cluster model captures the anisotropic response in two extreme directions of the isochoric extension test. In the case of the metal matrix composite reinforced with ceramic particles (figure 4.7), the linearisation method has a strong impact on the estimated overall response of the material, especially on the cluster model's assessment for the isochoric extension along the unit cell's edge, i.e. (0,0,1) direction. This is in contrast to the metal matrix with voids (figure 4.8) where the linearisation scheme has a much less visible influence. The reason for this are the stiff ceramic particles which play a crucial role in shaping the material's response in the isochoric extension test in the (0,0,1) direction for RC and in the (1,1,1) direction for the BCC arrangement. It can be seen that, in all cases, the stiffest response for a given mean field model is predicted by the standard tangent method.

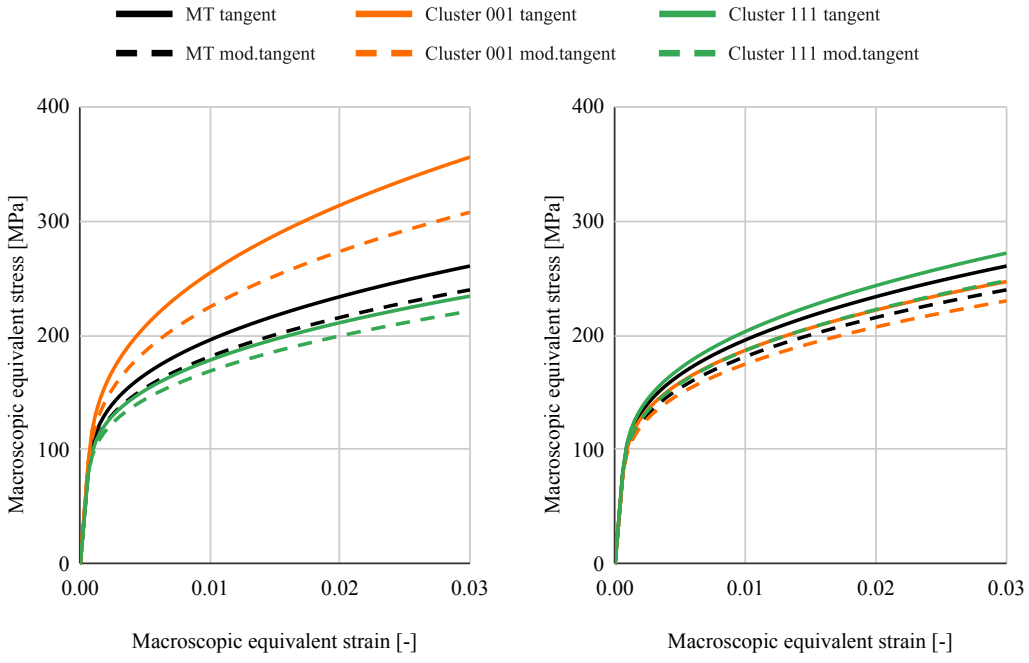

(a) (b)

Figure 4.7: Macroscopic von Mises equivalent stress vs macroscopic equivalent strain for the elastic–plastic response of a metal matrix reinforced with ceramic particles (MMC). Volume fraction of inclusions equal to $f_i = 30\%$. Tangent and modified tangent linearisation of Mori-Tanaka and cluster model. Two directions of load: (0,0,1) and (1,1,1). RC (a); and BCC (b) lattices.

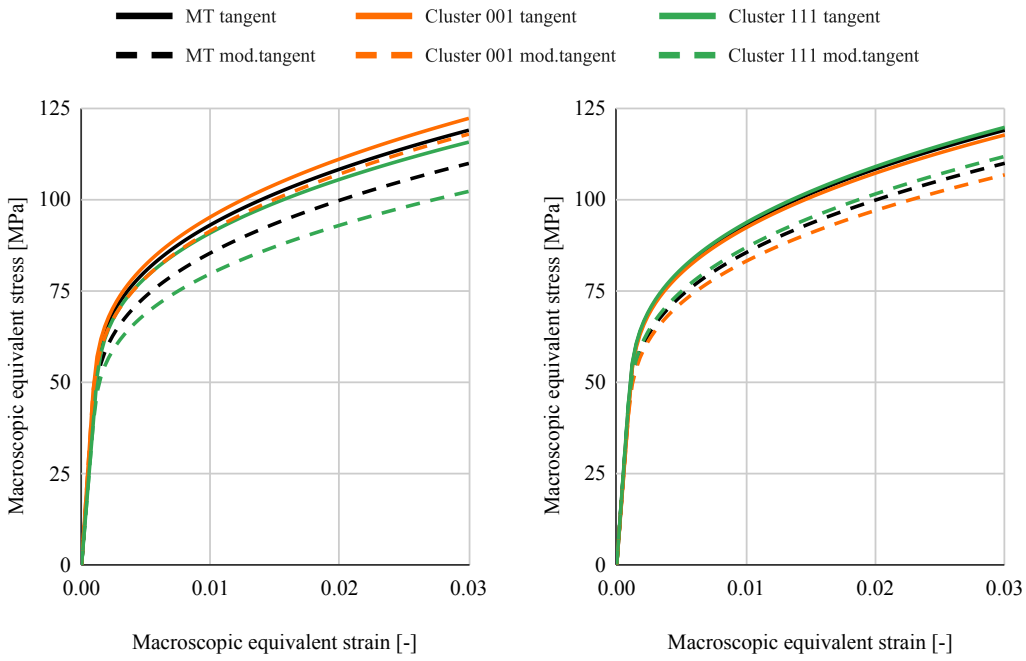

Figure 4.8: Macroscopic von Mises equivalent stress vs macroscopic equivalent strain for the elastic–plastic response of a metal matrix weakened with voids. Volume fraction of voids equal to $f_i = 30\%$. Tangent and modified tangent linearisation of Mori-Tanaka and cluster model. Two directions of load: (0,0,1) and (1,1,1). RC (a); and BCC (b) lattices.

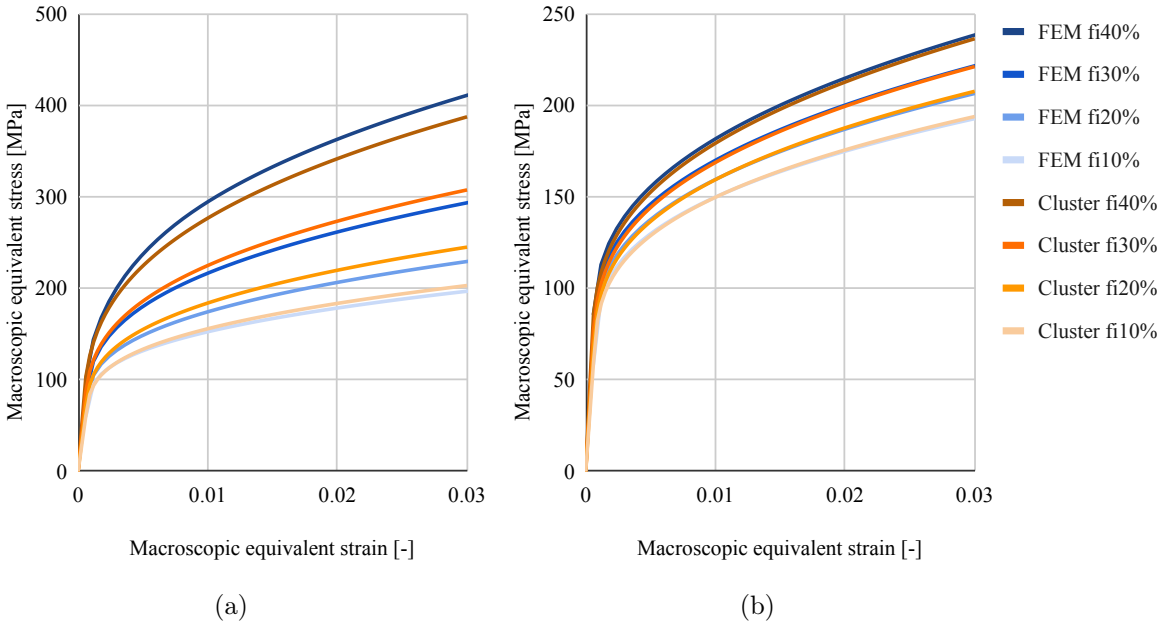

Figure 4.9: Macroscopic equivalent von Mises stress vs macroscopic equivalent strain for the elastic–plastic response of a metal matrix reinforced with ceramic particles (MMC) in RC lattice. Volume fractions of inclusions: $f_i = 10\%, 20\%, 30\%, 40\%$. Results from the cluster model (orange) and FEM (blue). Direction of load (0,0,1) (a); and (1,1,1) (b). Note different scale on Y axes.

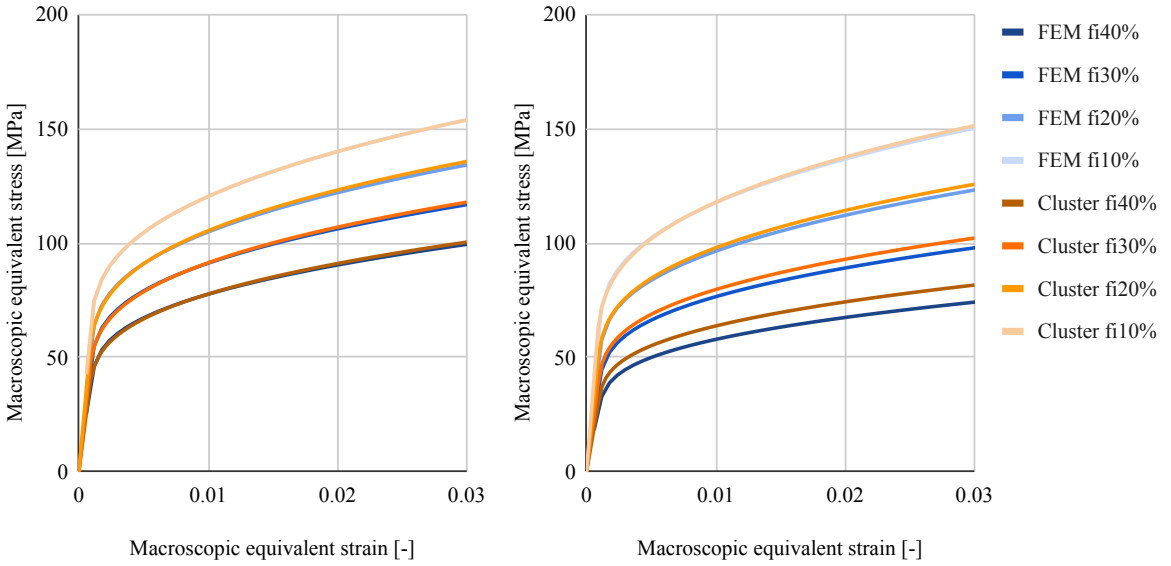

(a) (b)

Figure 4.10: Macroscopic equivalent von Mises stress vs macroscopic equivalent strain for the elastic–plastic response of a metal matrix weakened with voids in RC lattice. Volume fractions of inclusions: $f_i = 10\%, 20\%, 30\%, 40\%$. Results from the cluster model (orange) and FEM (blue). Direction of load (0,0,1) (a); and (1,1,1) (b).

As in the previous chapter, the results from the cluster model are confronted with the finite elements method (FEM) as a means of verification. Solely the results for the modified tangent linearisation method will be demonstrated in the rest of the analysis. This method has an additional advantage compared to the two remaining methods based on the first moments, as it enables to predict matrix yielding under overall hydrostatic stress. This property will be shown in the next part of this section.

The results of the numerical homogenisation and the cluster mean-field model almost coincide for the direction (1,1,1) for the MMC material. For the stiff direction (0,0,1), the mean-field model slightly overestimates the FEM reference results for $f_i = 10\%$–30% and underestimates for the 40% volume fraction, as seen in figure 4.9a. In general, the cluster model estimates are qualitatively and quantitatively similar to the results obtained by the FEM. By comparing the two figures 4.9a and 4.9b, one can observe a strong impact of the tension direction when both methods are in good agreement in estimating this anisotropic response. Similar results are observed for the metal matrix weakened by voids in the RC lattice, as demonstrated in figure 4.10, where an even better quantitative agreement between the cluster model and the reference FEM results is observed. Note that the weakening of the material caused by the presence of voids is more pronounced for the (1,1,1) loading direction.

Next, let us focus on how the direction of load affects the non-linear response of the composite. Results for the Mori-Tanaka scheme, cluster model, and FEM are compared. Both the RC and BCC lattices are considered. Figure 4.11 shows the macroscopic response of a metal matrix reinforced with ceramic particles, while figure 4.12 shows a metal matrix weakened with voids.

For the RC lattice, the influence of the direction of load on the macroscopic response of the material is more visible than in the case of the BCC lattice. It is worth noting that, no matter whether the inhomogeneities are stiffer or softer than the matrix material, the RC lattice manifests a stiffer response in the direction (0,0,1) than along (1,1,1), while for the BCC lattice, the relationship is reversed. Those observations are true for both the FEM and the cluster model predictions. Note that the Mori–Tanaka scheme provides the same response for both unit cells and is not sensitive to the loading direction. The predictions of the Mori-Tanaka are always between the cluster estimates for the two extreme directions. While comparing the cluster with the FEM, there is a good quantitative correlation up to the volume fraction of 40% what has been observed in the previous parts of this thesis as well.

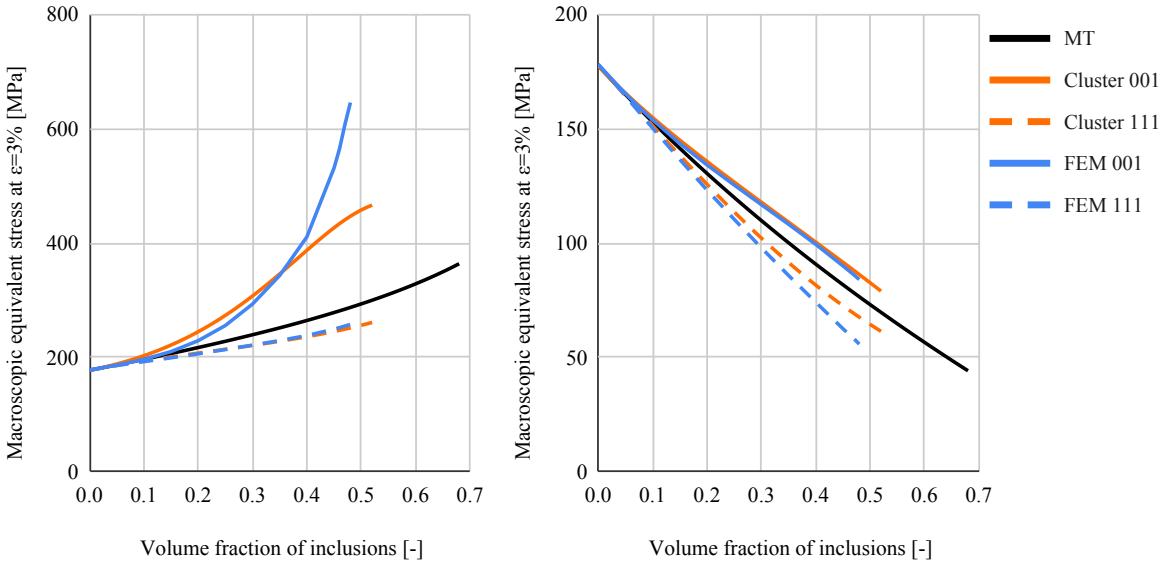

(a) (b)

Figure 4.11: Macroscopic equivalent von Mises stress values at macroscopic strain equal to $\bar{\varepsilon} = 3\%$. Metal matrix reinforced with ceramic inclusions (MMC). Different volume fractions of inclusions, two directions of load: (0,0,1); and (1,1,1). RC (a) and BCC (b) lattices. Note different scale on Y axes.

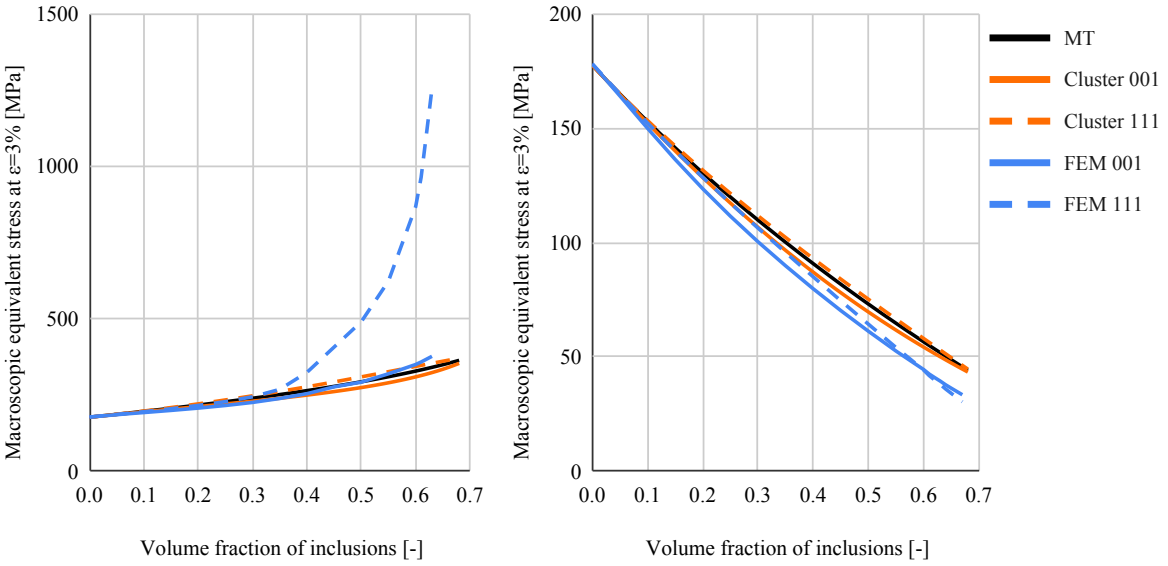

(a) (b)

Figure 4.12: Macroscopic equivalent von Mises stress values at macroscopic strain equal to $\bar{\varepsilon} = 3\%$. Metal matrix weakened with voids. Different volume fractions of voids, two directions of load: (0,0,1) and (1,1,1). RC (a); and BCC (b) lattices. Note different scale on Y axes.

Apart from the isochoric tension cases, a hydrostatic tension is also examined, both with the cluster and FEM models. Same material parameters are used as in the previous analysis. The results are shown in the figures 4.13-4.14. For a unit cell of a cubic symmetry, this results in the hydrostatic macroscopic stress. As described in the previous subsections, such loading conditions are known to pose important difficulties for many mean-field models of metal matrix elastic–plastic composites (Naili & Doghri, 2023). For this reason, the second stress moment is used in the uniformisation step.

However, the extent of plastic yielding may be not correctly estimated. This problem seems to be of prime importance when plastic yielding of porous metals is analysed and when void growth phenomena are of interest.

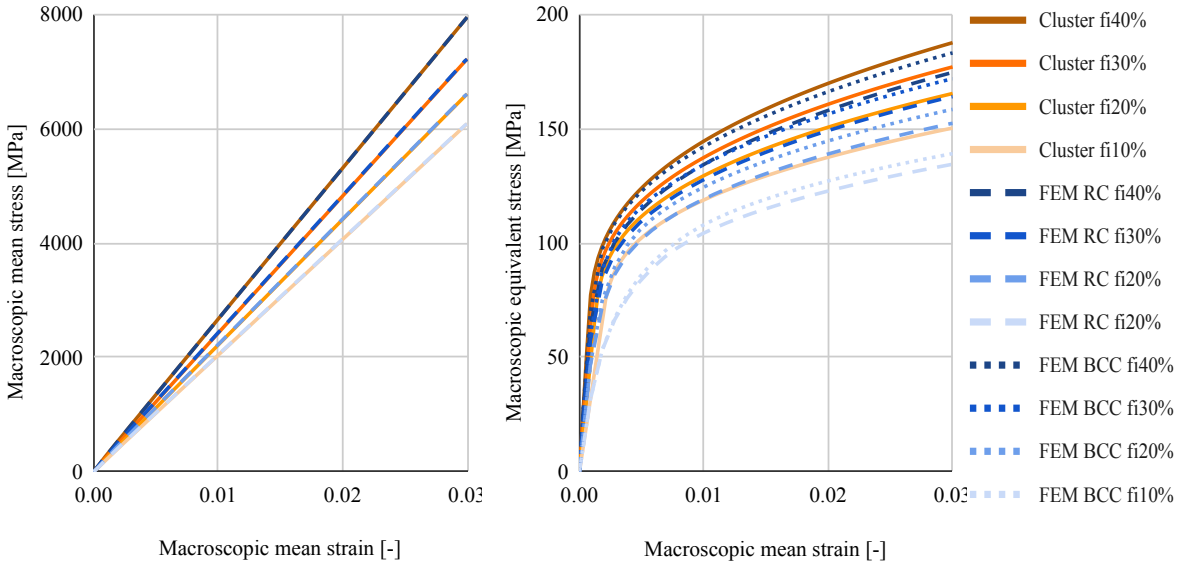

(a) (b)

Figure 4.13: Macroscopic stress vs macroscopic mean strain for the elastic–plastic response of a metal matrix reinforced with ceramic particles (MMC). Volume fractions of inclusions: $f_i = 10\%, 20\%, 30\%, 40\%$. Hydrostatic tension. Results from the cluster model (orange) and FEM (blue) for both lattices. Macroscopic mean stress (a); and macroscopic equivalent stress $\bar{\bar{\sigma}}_{\mathrm{eq}}$ (second moment) (b). Note different scale on Y axes.

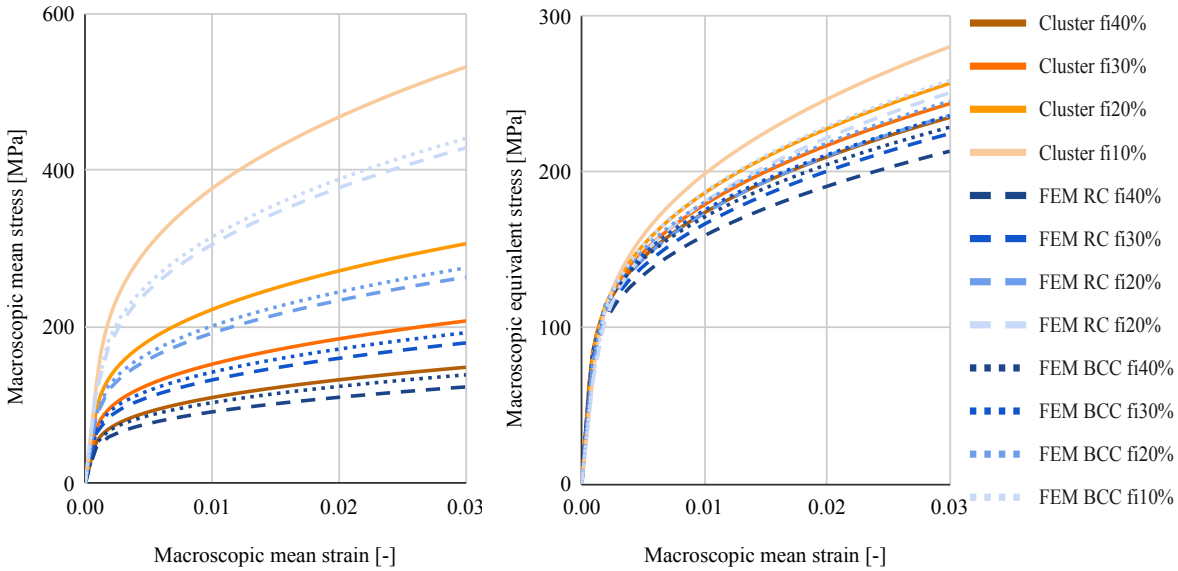

(a) (b)

Figure 4.14: Macroscopic stress vs macroscopic mean strain for the elastic–plastic response of a metal matrix weakened with voids. Volume fractions of voids: $f_i = 10\%, 20\%, 30\%, 40\%$. Hydrostatic tension. Results from the cluster model (orange) and FEM (blue) for both lattices. Macroscopic mean stress (a); and macroscopic equivalent stress $\bar{\bar{\sigma}}_{\mathrm{eq}}$ (second moment) (b). Note different scale on Y axes.

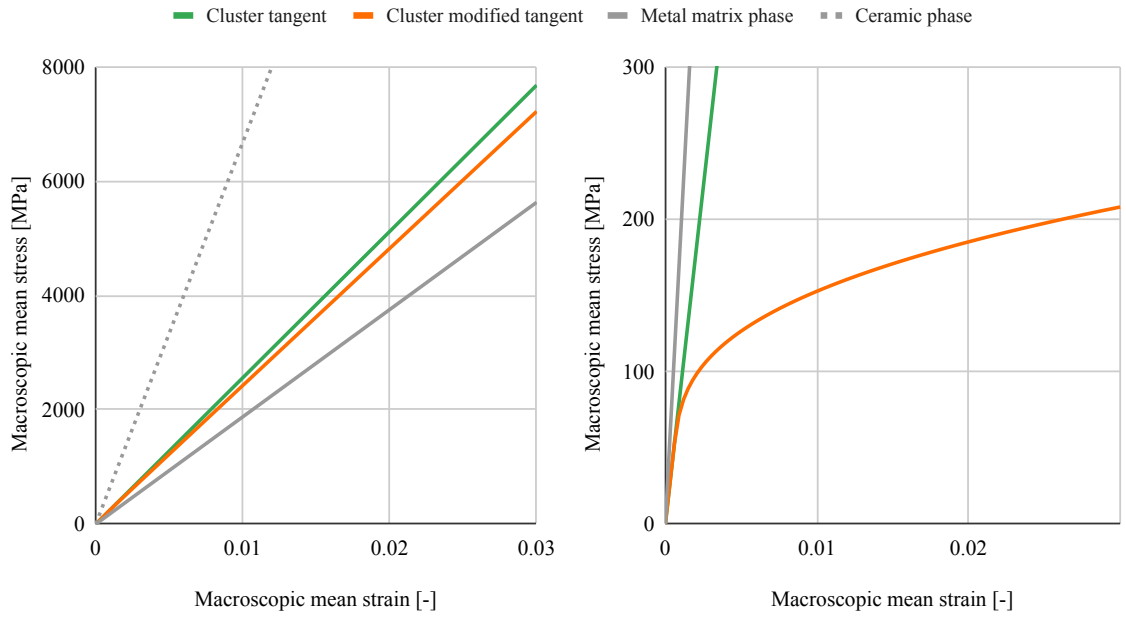

(a) (b)

Figure 4.15: Macroscopic mean stress vs macroscopic mean strain for the elastic–plastic response calculated with the original tangent (green) and modified tangent (orange) linearisation, with comparison to response of pure phases (grey). Volume fractions of voids $f_i = 30\%$. Hydrostatic tension. Metal matrix reinforced with ceramic particles (a); and metal matrix weakened with voids (b).

As concerns the macroscopic mean stress in MMC (figure 4.13a), the analytical estimates are in perfect agreement with FEM calculations. It should be noted that in terms of these results, there is no visible difference between the composite response for the RC and BCC lattices both in the cluster and FEM predictions. In the case of stress fluctuations described by the second moment of stress in the matrix (figure 4.13b), the cluster model overpredicts the magnitude of $\bar{\bar{\sigma}}_{eq}$, especially for the smallest volume fractions of inclusions $f_i = 10\%$, but the results are of the same order of magnitude. Contrary to the mean-field approach, the FEM calculations exhibit some slight difference between the lattices, with the values for the BCC being slightly larger than those for the RC.

As concerns the matrix with voids, a significantly larger difference is observed, especially for the smallest volume fraction of inclusions $f_i = 10\%$. The macroscopic mean stress in the porous metal (figure 4.14a) is overpredicted by the modified tangent cluster approach. However, the predictions are of reasonable quality compared to the classical tangent linearisation, with the plastic yielding of the composite well predicted, contrary to the standard (i.e. of first moment) tangent linearisation, as seen in figure 4.15. As in the MMC case, the cluster model overestimates the magnitude of $\bar{\sigma}_{eq}$ in the metal matrix with respect to FEM outcomes, with some slight difference between the FEM BCC and FEM RC responses.

When comparing MMC with the matrix with voids, it can be seen that at the same level of the macroscopic mean strain, the latter one exhibits larger values of equivalent stress $\bar{\bar{\sigma}}_{eq}$, so more plasticity develops in the porous material than in the metal matrix composite under hydrostatic loading.

4.4 Optimisation in the elastic-plastic regime

As described in section 3.5, during the design process for composite materials, there is a need to find a proper balance between the volume fraction of phases and their space distribution to achieve desired parameters. Similar to the elastic case in chapter 3, a multi-criteria optimisation procedure is engaged for the plastic regime. Macroscopic density, as well as mechanical and thermal parameters are examined. Calculations are performed for different volume fractions of inclusions varying from $f_i = 0\%$ to $f_i = 50\%$, for two lattices: RC and BCC. A composite of a metallic matrix and ceramic inclusions is considered, with parameters specified in table 4.3.

Table 4.3: Parameters of materials used for optimisation (metal-ceramic composite) in elasto-plastic regime.

	Matrix: metallic	Inclusions: ceramic
Young Modulus, E [GPa]	75.0	400.0
shear modulus, G [GPa]	28.9	166.7
Poisson's ratio, ν [-]	0.3	0.2
CTE, α [1/K]	$2.35{\cdot}10^{-5}$	$0.65{\cdot}10^{-5}$
thermal conductivity, k [W/(m·K)]	237	35
density, ρ [kg/m^3]	2700	3990
yield stress, Y_0 [MPa]	75.0	380.0
limit strain, ε_{lim} [-]	1.5%	-
plastic modulus, h [MPa]	416.0	-
exponent, n [-]	0.3895	-

The sample is subjected to external strain that increases incrementally to $\bar{\varepsilon} = 3\%$ along the direction (0,0,1), i.e. along the unit cell's edge. The metallic matrix is modelled to show the elastic-plastic behaviour, while the inclusions are assumed to be brittle, meaning that they only work within the elastic regime. Both equivalent stresses and equivalent strains in each phase are tracked and are shown in figure 4.16.

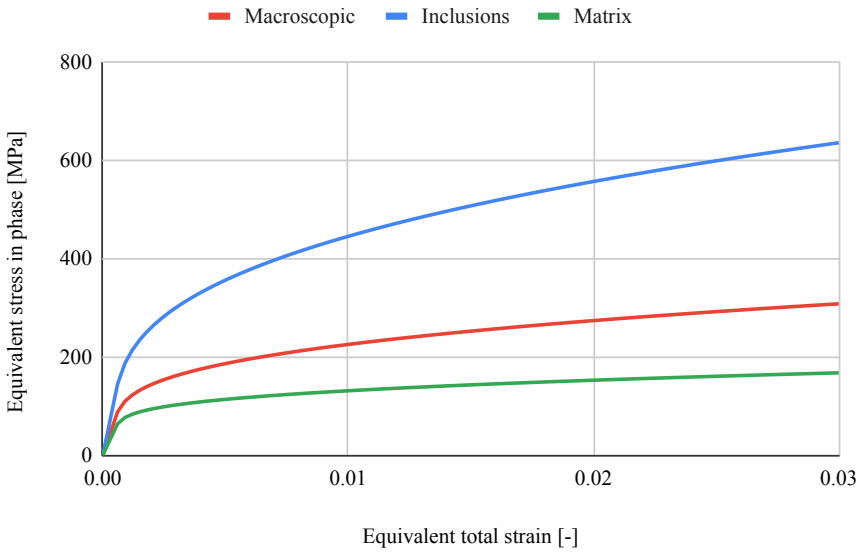

Figure 4.16: Stress-macroscopic strain relationship for each phase. RC lattice, (0,0,1) direction, $f_i = 30\%$.

As mentioned before, the purely elastic inclusions are assumed to be brittle, meaning that they fail after reaching yield stress (equal to $Y_{0.i} = 380MPa$). The plastic matrix, on the other hand, would fail after reaching the equivalent strain of $\varepsilon_{lim.m} = 1.5\%$, simulating a serviceability limit state. The strength (bearing capacity) of the entire composite would be the macroscopic equivalent stress at which one of the phases fails.

As it can be seen in figure 4.17, for the RC lattice at lower fractions of inclusions, it is the matrix that reaches its serviceability limit first. The threshold is around $f_i = 14\%$ after which the inclusions are deciding on the bearing capacity of the entire composite. The BCC lattice gives simpler results, as the inclusions do not fail under the given external strain and only the matrix' serviceability limit is the deciding factor. This will be one of the parameters applied to the objective function and referred to as the strength of the composite.

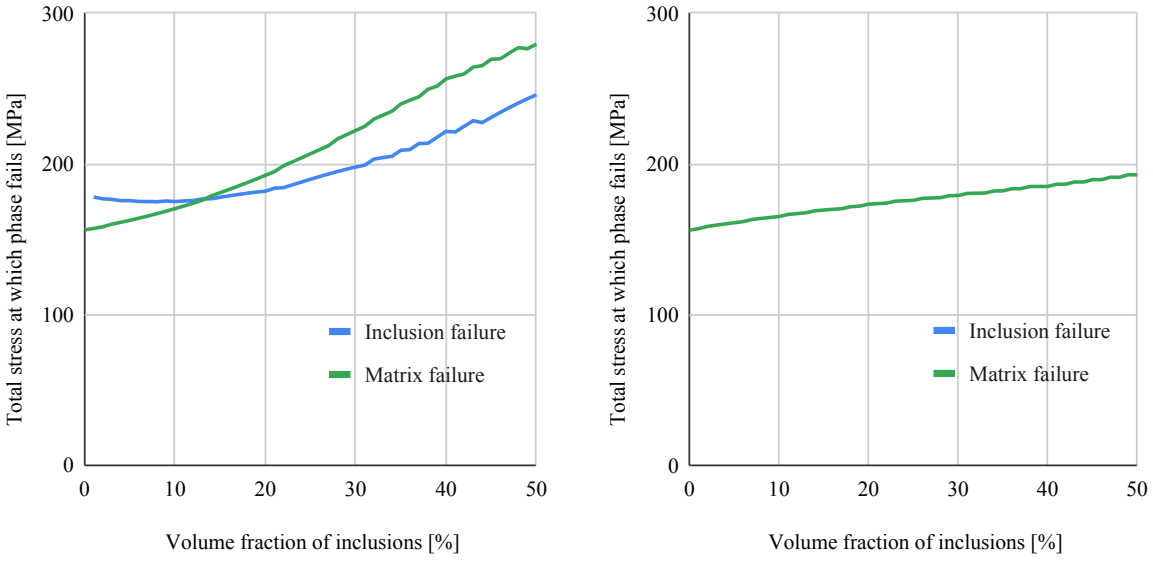

Figure 4.17: Macroscopic external stress at which one of the phases fails. (0,0,1) direction of load. RC (a); and BCC (b) lattices. Note: external strain equal to $\bar{\varepsilon} = 3\%$ was not sufficient to damage the inclusions in the BCC lattice.

As in the optimisation procedure for the elastic regime in section 3.5 of chapter 3, the objective function ϕ is defined as a sum n components, one for each material property. For each component, zero means the best solution. The scenario that gives the lowest value of the objective function ϕ is considered the best. The objective function takes following shape:

$$\phi = \sum_{i}^{n} \left(\frac{\text{macroscopic outcome value}}{\text{reference value}} - \delta \right)^2 \tag{4.40}$$

where δ depends on whether the given material parameter is desired to be as low ($\delta = 0$) or as high ($\delta = 1$) as possible. The reference values are the maximum possible values, so it is ensured that each component ranges between 0 and 1.

Four different macroscopic properties of the composite are considered: strength (bearing capacity), thermal conductivity, coefficient of thermal expansion and density. The first two are desired to be as high as possible (strong and easily radiating out the heat), while the other two as low as possible (lightweight and hardly expanding).

$$\phi(f_i) = w_1 \left(\frac{\bar{\sigma}_{fail}}{Y_{0.i}} - 1 \right)^2 + w_2 \left(\frac{\bar{k}}{k_m} - 1 \right)^2 + w_3 \left(\frac{\bar{\rho}}{\rho_i} - 0 \right)^2 + w_4 \left(\frac{\bar{\alpha}}{\alpha_i} - 0 \right)^2 \tag{4.41}$$

where $\bar{\sigma}_{fail}$ is macroscopic strength (i.e. maximal external stress that could be applied to sample before one of the phases fail); $Y_{0.i}$ is yield stress of inclusions; $\bar{k}$ is macroscopic thermal conductivity (trace of a 3x3 matrix $\bar{\mathbf{k}}$); k_m is thermal conductivity of matrix; $\bar{\rho}$ is macroscopic density; ρ_i is density of inclusions; $\bar{\alpha}$ is macroscopic coefficient of thermal expansion; α_i is coefficient of thermal expansion of inclusions; and w_1, w_2, w_3, w_4 are weight functions for each material parameter.

Figure 4.18 shows how each compents behaves in relation to volume fraction of inclusions. With this material choice, the coefficient of thermal expansion is better, the more inclusions there are. On the other hand, for thermal conductivity and mass, the results are better with pure matrix only. Similarly with the bearing capacity, although it has a less monotonous relation to the volume fraction of inclusions. Three different sets of weight functions are applied:

1. 0.25 × strength + 0.25 × thermal + 0.25 × CTE + 0.25 × densisty (all-equal);
2. 0.50 × strength + 0.25 × thermal + 0.00 × CTE + 0.25 × densisty (mechanical-dominated);
3. 0.00 × strength + 0.65 × thermal + 0.35 × CTE + 0.00 × densisty (heat-resistant).

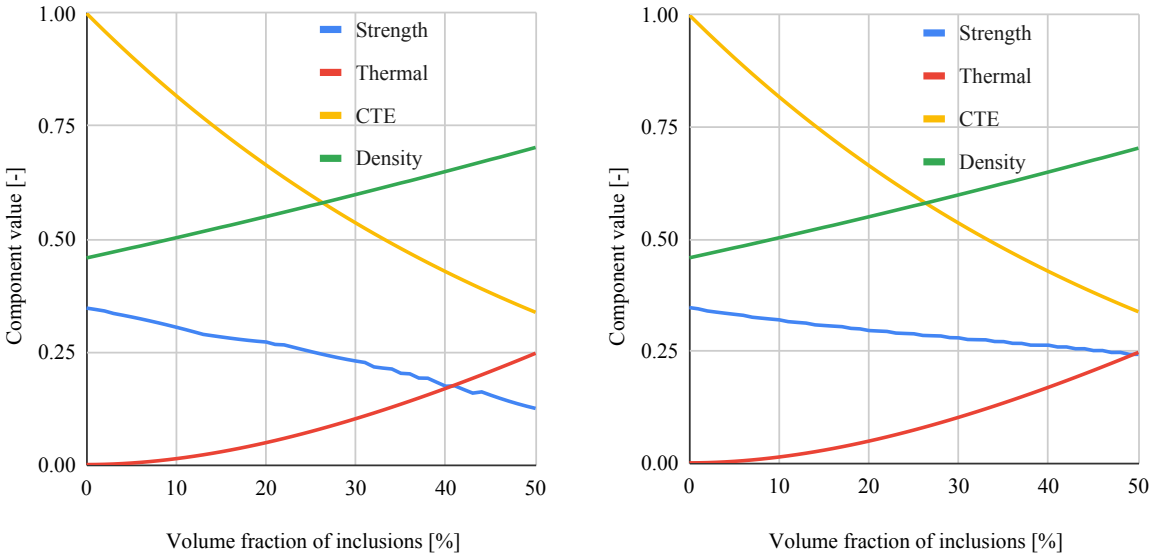

Figure 4.18: Values of each component of objective function. RC (a); and BCC (b) lattices.

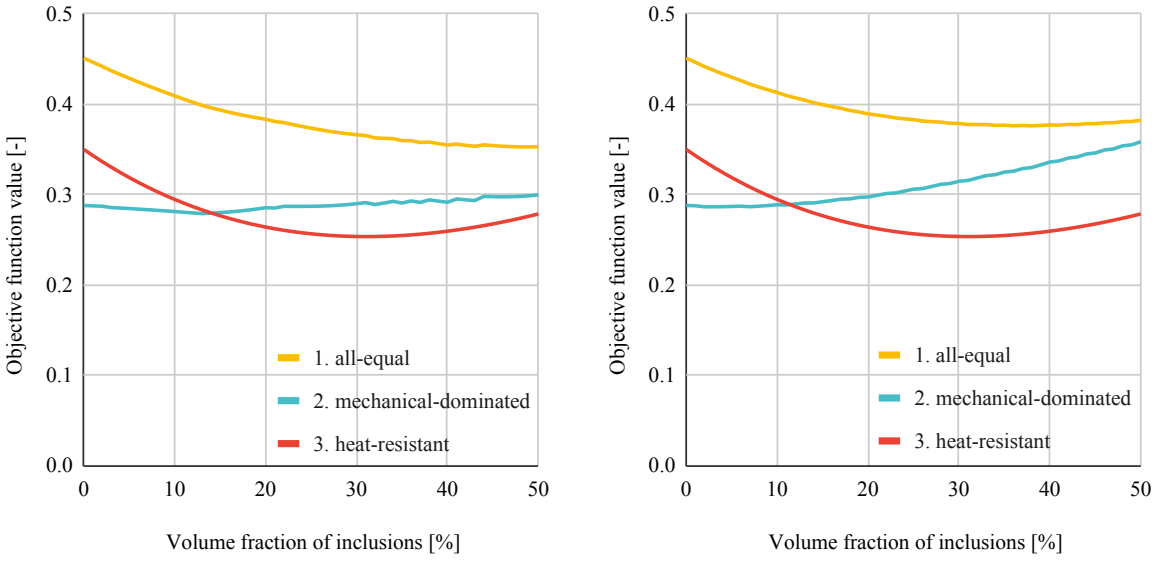

Figure 4.19: Values of objective functions ϕ. RC (a); and BCC (b) lattices.

Table 4.4: Optimal volume fractions f_i and corresponding objective function values $\phi(f_i)$ for different lattices.

objective function	RC		BCC	
	f_i	$\phi(f_i)$	f_i	$\phi(f_i)$
all-equal	49%	0.3528	38%	0.3760
mechanical-dominated	13%	0.2788	3%	0.2864
heat-resistant	31%	0.2534	31%	0.2534

Table 4.5: Material parameters of an optimal composite found using given set of weight functions.

	all-equal		mec.-dominated		heat-resistant	
	RC	BCC	RC	BCC	RC	BCC
strength, $\bar{\sigma}_{fail}$ [MPa]	243.3	185.1	175.9	159.5	199.2	180.5
thermal conductivity, $\bar{k}$ [W/(m·K)]	121.3	143.8	202.1	228.6	159.1	159.1
CTE, $\bar{\alpha}$ [1/K]	1.382	1.572	2.060	2.281	1.700	1.700
density, $\bar{\rho}$ [kg/m^3]	3332	3190	2868	2739	3100	3100

Figure 4.19 shows objective functions for these three sets of weight functions. In table 4.4 are listed the optimal volume fractions of inclusions and corresponding objective function values, while in table 4.5 are listed the macroscopic material parameters for an optimal composite found using each set of weight functions. It can be seen that changing the spatial distribution (i.e. the lattice) of inclusions affects the results. For the same objective functions, the difference minimum values are achieved and they correspond with different volume fraction of inclusions.

Such calculations based on the cluster model might be used for optimisation in the initial phase of the design process. Thanks to short calculation time, it is possible to test multiple different scenarios in complex multi-criteria optimisation procedures, finding e.g.: the optimal microstructure, volume fraction of inclusions or material composition, even if the next phase would involve more detailed methods of verification.

4.5 Summary

The goal of this chapter is to propose an extension of the cluster model into the elastic-plastic response of composite materials. To this end, we adopted and further developed the cluster model. Extension of the cluster model to the elastic-plastic cases requires incorporation of three additional steps, i.e.: linearisation, uniformisation and isotropisation. In this respect a new modified tangent linearization method for the matrix response is formulated. In the method, the second moment of stress $\bar{\bar{\sigma}}_{\mathrm{eq}}$ is used to calculate the tangent elastic–plastic modulus of the matrix. The evolution of $\bar{\bar{\sigma}}_{\mathrm{eq}}$ is tracked by an additional relation stemming from the Hill–Mandel lemma. To preserve the computational efficiency of the framework, isotropisation of the tangent elastic–plastic stiffness was performed. Moreover, with the same goal, at each time increment the second moment of stress was updated based on its first and second rates.

Full-field FEM calculations are used as benchmarks for checking the soundness of the cluster model predictions. These computations are performed on microstructural unit cells with applied periodic displacement boundary conditions.

Isochoric extension of a composite material in two directions is analysed: along the unit cell's edges (0,0,1) and along the cell's main diagonals (1,1,1), as well as their volumetric (hydrostatic) extension. Contrary to the Mori-Tanaka scheme, the cluster model accounts for the anisotropic non-linear response for different directions of the isochoric extension test. The results of computational homogenisation are in good agreement with the cluster model predictions for volume fractions up to around 40%. A strongly increasing role of the tension direction is observed when the volume content of inhomogeneities rose above 5%, with the cluster model and the finite element method being in good agreement in estimating this phenomenon. The analysis of hydrostatic loading cases shows that the use of the modified version of tangent linearisation enables the model to provide satisfactory predictions for the case of hydrostatic loading. The problem of accounting for yielding initiation under volumetric extension is overcome by the use of the second moments of stress within the "uniformisation" step. This allows the extent of plastic yielding to be satisfactorily estimated for both the reinforced and voided cases. It should be remarked that similarly to the bulk modulus in the elastic regime, the response under hydrostatic loading predicted by the cluster model is insensitive to the particular arrangement of inhomogeneities if only it is of cubic symmetry, whereas some differences between arrangements are detected by full-field numerical homogenisation.

It is shown that effective optimisation procedures are possible thanks to short calculation time for the cluster model, even after introducing the plasticity and time increments into the algorithm. It allows for use of multi-criteria optimisation in order to find the optimal microstructure, volume fraction of inclusions, or material parameters. Quick analyses of many different design scenarios demonstrates the potential of the model for initial stages of the design process of composite materials.

Chapter 5

Extension of the cluster model to elastoviscoplasticity

5.1 Introduction

In this chapter the extension of the cluster model to the case when composite phases are elastic-viscoplastic is presented and analyzed. Due to the involved non-linearity of the constitutive laws in viscoplastic regime, the extension of any mean-field model for this case requires additional assumptions, just like it was for the elastic-plastic scenario in chapter 4, i.e.: linearisation, uniformisation and isotropisation. However, additional difficulty in the elastic-viscoplastic case is that the strain rate in the phase depends not only on the stress rate, as is the case in the incremental form of elastic-plastic constitutive law, but also on the stress.

In this thesis, the solution of this problem proposed by Molinari (2002) was chosen, i.e. the additive interaction law with the tangent linearisation for the viscoplastic part. Uniformisation, necessary for using closed-form relations from 2, is conducted with use of a tangent shear modulus of the matrix specified by mean-field value of stress, i.e. without the modification by the second moments of stress. Possible isotropisation methods will be discussed in detail in this chapter. The FEM calculations performed for the verification purpose, are using the non-linear Perzyna law for the viscoplastic regime.

Worth noting is the fact that in Kowalczyk-Gajewska et al. (2021), which the later part of this chapter refers to, the cluster model was formulated for the general non-linear viscoplasticity, but was implemented and verified by comparison with FEM only for the linear and isotropic viscoelasticity. Thus, the problem of proper linearisation, uniformisation and isotropisation was not discussed in that paper.

5.2 Theory

The theoretical framework described in this section follows Kowalczyk-Gajewska et al. (2021) and presents extension of the cluster model combined with the additive interaction law due to Molinari (2002) for elastic-viscoplastic composite materials.

5.2.1 Local constitutive law

Compared to previous chapters, the constitutive behavior is changed. Each phase is now governed by an elastic-viscoplastic law of the Maxwell-type (see figure 5.1). For a given phase r we have:

$$\dot{\boldsymbol{\varepsilon}} = \dot{\boldsymbol{\varepsilon}}^e + \dot{\boldsymbol{\varepsilon}}^v = \mathbb{M}_r \cdot \dot{\boldsymbol{\sigma}} + \boldsymbol{F}_r(\boldsymbol{s}) \tag{5.1}$$

where the strain rate $\dot{\boldsymbol{\varepsilon}}$ is the sum of elastic $\dot{\boldsymbol{\varepsilon}}^e$ and viscoplastic parts $\dot{\boldsymbol{\varepsilon}}^v$; $\boldsymbol{s}$ is the deviator of the Cauchy stress $\boldsymbol{\sigma}$; and $\mathbb{M}_r$ is a fourth order tensor of elastic compliance, defined as inverse of the stiffness tensor $\mathbb{C}_r$, i.e.:

$$\mathbb{M}_r = (\mathbb{C}_r)^{-1} \tag{5.2}$$

and tensorial function $\boldsymbol{F}_r(\boldsymbol{s})$ is a constitutive relation by which viscoplastic strain rate is related to stress tensor deviator $\boldsymbol{s}$. In the present thesis, the Perzyna viscoplastic model is adopted for $\boldsymbol{F}_r(\boldsymbol{s})$ with an over-stress function Φ (Perzyna, 1986):

$$\dot{\boldsymbol{\varepsilon}}^v = \boldsymbol{F}_r(\boldsymbol{s}) = \Phi \frac{\partial f}{\partial \boldsymbol{s}} \tag{5.3}$$

with:

$$f = \sigma_{eq} - Y_0 - R(\varepsilon_{eq}), \quad \Phi = \dot{\boldsymbol{\varepsilon}}_0 \left(\frac{\langle f \rangle}{Y_0 + R(\varepsilon_{eq})} \right)^{\frac{1}{M}} \tag{5.4}$$

where σ_{eq} is the equivalent stress; Y_0 is the yield stress; ε_{eq} is the cumulated plastic strain rate; $\dot{\boldsymbol{\varepsilon}}_0$ is reference strain rate; M is strain rate sensitivity; and function $R(\varepsilon_{eq})$ describes the strain hardening behaviour of the phase. Macaulay brackets $\langle \quad \rangle$ deonotes a ramp function, i.e. $\langle x \rangle = x$ if $x > 0$ and $\langle x \rangle =$ otherwise.

In the overstress model described by equation (5.4), the viscoplastic flow is initiated when function f is positive. Both strain rate sensitivity and reference strain rate represent the rate dependence of the viscoplastic flow rule and Y_0 is the stress at which the viscoplastic flow starts. The non-linearity of the flow rule is defined with the power law exponent $1/M$.

Because of the fact that the Maxwell's model is used, purely viscoplastic and purely elastic problems are considered separately before addressing the elastic-viscoplastic case. The diagram of the Maxwell's model is presented in figure 5.1. It consists of a spring and a dashpot connected in series, i.e. they experience the same value of stress. Spring continues to extend only when $\dot{\boldsymbol{\sigma}}$ is non-zero. When $\dot{\boldsymbol{\sigma}} = 0$ only the dashpot extends in a creep-type process.

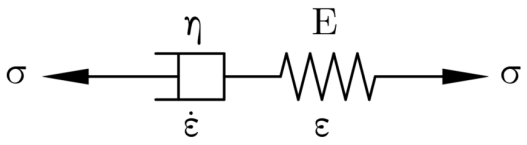

Figure 5.1: Schematic diagram of the 1D Maxwell's model. The spring is described by the stiffness modulus E and the dashpot by the coefficient of viscosity η, both sharing the same value of stress σ. For the 3D case, E is replaced by the stiffness tensor $\mathbb{C}$ and coefficient of viscosity by a viscous tangent stiffness $\mathbb{C}^v$ resulting from non-linear relations (5.3)-(5.4).

5.2.2 Pure viscoplastic case

First, let us consider a case of a purely viscoplastic response, i.e. the creep-type process in which we may assume that $\dot{\boldsymbol{\sigma}} = 0$. By adopting the tangent linearisation proposed by Molinari et al. (1987), the non-linear response of phase r is approximated by affine-like relation, similar to the one discussed in chapter 4 for thermoelastic material:

$$\dot{\boldsymbol{\varepsilon}}^v = \mathbb{M}^t(\boldsymbol{s}_r) \cdot \boldsymbol{s} + \dot{\boldsymbol{\varepsilon}}_r^{ref}(\boldsymbol{s}_r) \tag{5.5}$$

where $\boldsymbol{s}_r$ is the mean deviatoric stress in phase r; and:

$$\mathbb{M}_r^t(\boldsymbol{s}_r) = \frac{\partial \boldsymbol{F}_r}{\partial \boldsymbol{s}}(\boldsymbol{s}_r) \tag{5.6}$$

$$\dot{\boldsymbol{\varepsilon}}_r^{ref}(\boldsymbol{s}_r) = \boldsymbol{F}_r(\boldsymbol{s}_r) - \mathbb{M}_r^t(\boldsymbol{s}_r) \cdot \boldsymbol{s}_r \tag{5.7}$$

where $\mathbb{M}_r^t(\boldsymbol{s}_r)$ is a viscous tangent compliance tensor; and $\dot{\boldsymbol{\varepsilon}}_r^{ref}$ is a reference strain rate. The mean strain rate associated to $\boldsymbol{s}_r$ is given by equation obtained after averaging (5.5) over the phase volume:

$$\dot{\boldsymbol{\varepsilon}}_r^v = \boldsymbol{F}_r(\boldsymbol{s}_r) = \mathbb{M}_r^t(\boldsymbol{s}_r) \cdot \boldsymbol{s}_r + \dot{\boldsymbol{\varepsilon}}_r^{ref}(\boldsymbol{s}_r) \tag{5.8}$$

The second equality in equation (5.8) results from the fact that the tangent law (5.5) coincides at $\boldsymbol{s}_r$ with the non-linear response $\boldsymbol{F}_r(\boldsymbol{s}_r)$ as indicated by (5.7). The relationship (5.5) can be inverted into:

$$\boldsymbol{s} = \mathbb{C}_r^t(\boldsymbol{s}_r) \cdot \dot{\boldsymbol{\varepsilon}}^v + \boldsymbol{s}_r^{ref}(\boldsymbol{s}_r) \tag{5.9}$$

with:

$$\boldsymbol{s}_r^{ref} = -\mathbb{C}_r^t(\boldsymbol{s}_r) \cdot \dot{\boldsymbol{\varepsilon}}_r^{ref} \tag{5.10}$$

Taking as a reference medium the homogeneous material with constitutive response given by the matrix tangent law (equation (5.9) with $r = m$), from the results obtained for thermoelastic composite in section 2.1, we find:

$$\dot{\boldsymbol{\varepsilon}}_i^v = \dot{\boldsymbol{\varepsilon}}_0^v - \bar{\boldsymbol{\Gamma}}^v \cdot (\Delta\mathbb{C}_i^t \cdot \dot{\boldsymbol{\varepsilon}}_i^v + \Delta\boldsymbol{s}_i^{ref}) \tag{5.11}$$

with:

$$\Delta\mathbb{C}_i^t = \mathbb{C}_i^t - \mathbb{C}_m^t, \quad \Delta\boldsymbol{s}_i^{ref} = \boldsymbol{s}_i^{ref} - \boldsymbol{s}_m^{ref} \tag{5.12}$$

We have also introduced the following polarisation tensor:

$$\bar{\boldsymbol{\Gamma}}^v(\mathbb{C}_m^t) = -\sum_{J \neq I} \boldsymbol{\Gamma}^{IJ.v} \tag{5.13}$$

The tensors $\boldsymbol{\Gamma}^{IJ.v}(J = 1, 2, ...)$ are defined by equation (2.9) with $\boldsymbol{\Gamma}$ obtained from the Green functions depending upon the tangent modulus $\mathbb{C}_m^t(\boldsymbol{s}_r)$ of the reference medium.

In this interaction model, $\dot{\boldsymbol{\varepsilon}}_0^v$ is an integration constant appearing in the Lipman-Schwinger-Dyson integral equation and is specified as:

$$\dot{\boldsymbol{\varepsilon}}_0^v = \dot{\bar{\boldsymbol{\varepsilon}}}^v + f_i\mathbb{P}_0^v \cdot (\Delta\mathbb{C}_i^t \cdot \dot{\boldsymbol{\varepsilon}}_i^v + \Delta\boldsymbol{s}_i^{ref}) \tag{5.14}$$

where $\dot{\bar{\boldsymbol{\varepsilon}}}^v$ is macroscopic applied strain rate, and:

$$\mathbb{P}_0^v = -\boldsymbol{\Gamma}^{II.v}(sphere) \tag{5.15}$$

$\boldsymbol{\Gamma}^{II.v}(sphere)$ is calculated with equation (2.9) for an inclusion of spherical shape and with the tangent modulus $\mathbb{C}_m^t$ of the matrix. Thus, $\mathbb{P}_0^v$ is solely function of $\mathbb{C}_m^t$ and for isotropic matrix is specified by equation (2.31).

We define the deviatoric stress $\boldsymbol{s}_0$ as being related to $\dot{\boldsymbol{\varepsilon}}_0^v$ by the tangent law of the reference medium (equation (5.9) with $r = m$):

$$\boldsymbol{s}_0 = \mathbb{C}_m^t(\boldsymbol{s}_m) \cdot \dot{\boldsymbol{\varepsilon}}_0^v + \boldsymbol{s}_m^{ref}(\boldsymbol{s}_m) \tag{5.16}$$

Substracting equation (5.16) from the inclusion's tangent law (equation (5.9) with $r = i$) we obtain (for simplicity, the dependence of $\mathbb{C}_m^t$ and $\boldsymbol{s}_m^{ref}$ on $\boldsymbol{s}_m$ is omitted further on):

$$\boldsymbol{s}_i - \boldsymbol{s}_0 = \mathbb{C}_i^t \cdot \dot{\boldsymbol{\varepsilon}}_i^v - \mathbb{C}_m^t \cdot \dot{\boldsymbol{\varepsilon}}_0^v + \Delta\boldsymbol{s}_i^{ref} \tag{5.17}$$

Using this relationship to eliminate $\Delta\boldsymbol{s}_i^{ref}$ in equation (5.11), leads to the following interaction laws:

$$\left(\mathbb{C}_m^t - \left(\bar{\boldsymbol{\Gamma}}^v\right)^{-1}\right) \cdot (\dot{\boldsymbol{\varepsilon}}_i^v - \dot{\boldsymbol{\varepsilon}}_0^v) = \boldsymbol{s}_i - \boldsymbol{s}_0 \tag{5.18}$$

or:

$$\dot{\boldsymbol{\varepsilon}}_i^v - \dot{\boldsymbol{\varepsilon}}_0^v = \left(\mathbb{C}_m^t - \left(\bar{\boldsymbol{\Gamma}}^v\right)^{-1}\right)^{-1} \cdot (\boldsymbol{s}_i - \boldsymbol{s}_0) \tag{5.19}$$

The definition (5.14) of $\dot{\boldsymbol{\varepsilon}}_0^v$ given by the cluster model can be written as:

$$\dot{\bar{\boldsymbol{\varepsilon}}}^v - \dot{\boldsymbol{\varepsilon}}_0^v = \left(\mathbb{C}_m^t - (\mathbb{P}_0^v)^{-1}\right)^{-1} \cdot (\dot{\bar{\boldsymbol{s}}} - \boldsymbol{s}_0) \tag{5.20}$$

where $\dot{\bar{\boldsymbol{s}}}$ is the deviator of the macroscopic stress. Equations (5.19)-(5.20) can be written as:

$$\dot{\boldsymbol{\varepsilon}}_i^v - \dot{\boldsymbol{\varepsilon}}_0^v = -\mathbb{M}_*^v \cdot (\boldsymbol{s}_i - \boldsymbol{s}_0) \tag{5.21}$$

$$\dot{\bar{\boldsymbol{\varepsilon}}}^v - \dot{\boldsymbol{\varepsilon}}_0^v = -\mathbb{M}_{*0}^v \cdot (\boldsymbol{s}_i - \boldsymbol{s}_0) \tag{5.22}$$

with:

$$\mathbb{M}_*^v = \left((\bar{\boldsymbol{\Gamma}}^v)^{-1} - \mathbb{C}_m^t\right)^{-1} \tag{5.23}$$

$$\mathbb{M}_{*0}^v = \left((\mathbb{P}_0^v)^{-1} - \mathbb{C}_m^t\right)^{-1} \tag{5.24}$$

For the function $\boldsymbol{F}_r$ given by the Perzyna viscoplastic model (equations 5.3-5.4), the viscoplastic tangent stiffness is specified as follows:

$$\mathbb{C}_m^t = 3K_m^v \mathbb{I}^{\mathrm{D}} + 2G_m^{t1}(\sigma_{eq})\mathbf{N}^{\mathrm{D}} \otimes \mathbf{N}^{\mathrm{D}} + 2G_m^{t2}(\sigma_{eq})(\mathbb{I}^{\mathrm{D}} - \mathbf{N}^{\mathrm{D}} \otimes \mathbf{N}^{\mathrm{D}}) \tag{5.25}$$

and is anisotropic. Note the viscous bulk modulus K_m^v is infinite ($K_m^v \to \infty$) as the viscoplastic strain rate is volume-preserving, while:

$$2G_m^{t1} = \frac{2mY_0}{3\dot{\boldsymbol{\varepsilon}}_0}\left(\frac{\langle\sigma_{eq} - Y_0\rangle}{Y_0}\right)^{1-\frac{1}{M}}, \quad 2G_m^{t2} = \frac{2\sigma_{eq}}{3\dot{\boldsymbol{\varepsilon}}_0}\left(\frac{Y_0}{\langle\sigma_{eq} - Y_0\rangle}\right)^{\frac{1}{M}} \tag{5.26}$$

and, similarly to elastic-plastic tangent stiffness (as per equation (4.16)), $\mathbf{N}^{\mathrm{D}}$ is the direction of the stress deviator $\boldsymbol{\sigma}^{\mathrm{D}}$.

5.2.3 Pure elastic case

Now, a purely linearly elastic response is assumed. We can see such process as a instantaneous loading, with infinite strain rate $\dot{\varepsilon} \to \infty$. Thus, the results of this section can be directly obtained by setting $\theta = 0$ in the equation of the thermoelastic case. We express here the problem in the rate form, having in view applications in elasto-viscoplasticity. For each phase, the rate form of the Hooke's law is as follows:

$$\dot{\boldsymbol{\sigma}}_r = \mathbb{C}_r \cdot \dot{\boldsymbol{\varepsilon}}_r^e \tag{5.27}$$

where $\mathbb{C}_r$ is the tensor of elastic moduli; $\dot{\boldsymbol{\sigma}}_r$ is the stress rate; and $\dot{\boldsymbol{\varepsilon}}_r^e$ is elastic strain rate in each phase r. Averages of stress and strain rate per phases are considered.

Using the results from chapter 2, the sets of results equivalent to purely viscoplastic case can be written in the rate form:

$$\dot{\boldsymbol{\sigma}}_0 = \mathbb{C}_m \cdot \dot{\boldsymbol{\varepsilon}}_0^e \tag{5.28}$$

$$\dot{\boldsymbol{\varepsilon}}_i^e - \dot{\boldsymbol{\varepsilon}}_0^e = \left(\mathbb{C}_m - (\bar{\boldsymbol{\Gamma}})^{-1}\right)^{-1} \cdot (\dot{\boldsymbol{\sigma}}_i - \dot{\boldsymbol{\sigma}}_0) \tag{5.29}$$

$$\dot{\bar{\boldsymbol{\varepsilon}}}^e - \dot{\boldsymbol{\varepsilon}}_0^e = \left(\mathbb{C}_m - (\mathbb{P}_0)^{-1}\right)^{-1} \cdot (\dot{\bar{\boldsymbol{\sigma}}} - \dot{\boldsymbol{\sigma}}_0) \tag{5.30}$$

where:

$$\bar{\boldsymbol{\Gamma}}(\mathbb{C}_m) = -\sum_{J \neq I} \boldsymbol{\Gamma}^{IJ} \tag{5.31}$$

$$\mathbb{P}_0 = -\boldsymbol{\Gamma}^{II}(sphere) \tag{5.32}$$

Tensors $\boldsymbol{\Gamma}^{II}(sphere)$ and $\boldsymbol{\Gamma}^{IJ}$ are defined by equation (2.9) with $\boldsymbol{\Gamma}$ obtained from the Green functions associated to the elastic stiffness modulus $\mathbb{C}_m$ of the matrix. $\boldsymbol{\Gamma}^{II}(sphere)$ is calculated for a spherical shape and consequently is solely function of $\mathbb{C}_m$. The integration constant $\dot{\boldsymbol{\varepsilon}}_0^e$ is given by:

$$\dot{\boldsymbol{\varepsilon}}_0^e = \dot{\bar{\boldsymbol{\varepsilon}}^{\boldsymbol{e}}} + f_i \mathbb{P}_0 \cdot (\Delta\mathbb{C}_i \cdot \dot{\boldsymbol{\varepsilon}}_{\boldsymbol{i}}^{\boldsymbol{e}}) \tag{5.33}$$

Equations (5.29)-(5.30) can be written as:

$$\dot{\boldsymbol{\varepsilon}}_i^e - \dot{\boldsymbol{\varepsilon}}_0^e = -\mathbb{M}_*^e \cdot (\dot{\boldsymbol{\sigma}}_i - \dot{\boldsymbol{\sigma}}_0) \tag{5.34}$$

$$\dot{\bar{\boldsymbol{\varepsilon}}}^e - \dot{\boldsymbol{\varepsilon}}_0^e = \mathbb{M}_{*0}^e \cdot (\dot{\bar{\boldsymbol{\sigma}}} - \dot{\boldsymbol{\sigma}}_0) \tag{5.35}$$

with:

$$\mathbb{M}_*^e = \left((\bar{\boldsymbol{\Gamma}})^{-1} - \mathbb{C}_m\right)^{-1} \tag{5.36}$$

$$\mathbb{M}_{*0}^e = \left((\mathbb{P}_0)^{-1} - \mathbb{C}_m\right)^{-1} \tag{5.37}$$

5.2.4 Elastic-viscoplastic case

Combining the two aforementioned processes, an additive interaction law can be conceptually formed by observing that:

$$\dot{\varepsilon}_i = \dot{\varepsilon}_i^e + \dot{\varepsilon}_i^v \tag{5.38}$$

and defining $\dot{\boldsymbol{\varepsilon}}_0$ as:

$$\dot{\boldsymbol{\varepsilon}}_0 = \dot{\boldsymbol{\varepsilon}}_0^e + \dot{\boldsymbol{\varepsilon}}_0^v \tag{5.39}$$

Adding relations (5.33) and (5.34) with (5.21) and (5.22), respectively we obtain:

$$\dot{\varepsilon}_i - \dot{\varepsilon}_0 = -\mathbb{M}_*^e \cdot (\dot{\sigma}_i - \dot{\sigma}_0) - \mathbb{M}_*^v \cdot (\boldsymbol{s}_i - \boldsymbol{s}_0) \tag{5.40}$$

where $\mathbb{M}_*^e$ and $\mathbb{M}_*^v$ are given by equations (5.23) and (5.36).

These heuristically derived Maxwellian interaction law can be rationalised based on several arguments. Hashin (1969) found an analytical solution for the linear viscoelastic problem of a spherical inclusion embedded in an infinite matrix. The material response was of the Maxwell type in both phases and incompressibility was assumed. This solution can be exactly retrieved by using an additive interaction law having the same structure as equation (5.40), see Kouddane et al. (1993).

An additive interaction law was later proposed for solving inclusion problems, for non-linear, anisotropic, compressible material responses, including elasto-viscoplasticity, (Molinari et al., 1997; Molinari, 2002). The instantaneous elastic response due to a jump in the external solicitation appears to be well captured by this type of additive interaction law. On the other hand, for slow loading the quasi-non-linear creep viscoplastic response is also well captured. Moreover, it was verified by Mercier et al. (2005) that, for elastic-viscoplastic materials, the predictions of the additive interaction law for the single inclusion problem were in good agreement with finite element simulations for various loading conditions and strain paths.

Classical homogenisation schemes, such as the Mori-Tanaka model or the self-consistent scheme, have been proposed based on the additive form of the interaction law, (Molinari et al., 1997; Abdul-Latif et al., 1998; Molinari, 2002; Mercier & Molinari, 2009; Kowalczyk-Gajewska & Petryk, 2011; Abdul-Latif et al., 2018; Wang et al., 2010; Zecevic & Lebensohn, 2020). These homogenisation schemes have been validated by comparisons with finite elements calculations (Mercier et al., 2012, 2019; Czarnota et al., 2015) and experimental results (Girard et al., 2021).

Applying additive law similarly for the interaction equations (5.21) and (5.34), the governing equations of the purely elastic and purely viscoplastic cluster models can be blended together within the additive formulation

$$\dot{\bar{\boldsymbol{\varepsilon}}} - \dot{\boldsymbol{\varepsilon}}_0 = -\mathbb{M}_{*0}^e \cdot (\dot{\bar{\boldsymbol{\sigma}}} - \dot{\boldsymbol{\sigma}}_0) - \mathbb{M}_{*0}^v \cdot (\dot{\bar{\boldsymbol{s}}} - \dot{\boldsymbol{s}}_0) \tag{5.41}$$

where $\mathbb{M}_{*0}^v$ and $\mathbb{M}_{*0}^e$ are given by equations (5.24) and (5.37). Equations (5.28) and (5.16) can be inverted into:

$$\dot{\boldsymbol{\varepsilon}}_0^e = \mathbb{M}_m \cdot \dot{\boldsymbol{\sigma}}_0 \tag{5.42}$$

$$\dot{\boldsymbol{\varepsilon}}_0^v = \mathbb{M}_m^t \cdot \dot{\boldsymbol{s}}_0 + \dot{\boldsymbol{\varepsilon}}_m^{ref} \tag{5.43}$$

where $\mathbb{M}_m = (\mathbb{C}_m)^{-1}$, $\mathbb{M}_m^t = (\mathbb{C}_m^t)^{-1}$, and $\dot{\boldsymbol{\varepsilon}}_m^{ref} = -\mathbb{M}_m^t \cdot \boldsymbol{s}_m^{ref}$. Combining equations (5.42)-(5.43) with equation (5.39), we obtain:

$$\dot{\boldsymbol{\varepsilon}}_0 = \mathbb{M}_m \cdot \dot{\boldsymbol{\sigma}}_0 + \mathbb{M}_m^t \cdot \dot{\boldsymbol{s}}_0 + \dot{\boldsymbol{\varepsilon}}_m^{ref} \tag{5.44}$$

With equations (5.1)-(5.5), the linearised form of the constitutive law for matrix is:

$$\dot{\boldsymbol{\varepsilon}} = \mathbb{M}_m \cdot \dot{\boldsymbol{\sigma}} + \mathbb{M}_m^t \cdot \boldsymbol{s} + \dot{\boldsymbol{\varepsilon}}_m^{ref} \tag{5.45}$$

The macroscopic strain rate $\dot{\bar{\boldsymbol{\varepsilon}}}(t)$ is assumed to be prescribed in terms of time (similar assumption might be used for the macroscopic stress $\dot{\bar{\boldsymbol{\sigma}}}(t)$). The relationship between $\dot{\bar{\boldsymbol{\varepsilon}}}(t)$ and mean strain rates in phases takes form:

$$\dot{\bar{\boldsymbol{\varepsilon}}} = f_i \dot{\boldsymbol{\varepsilon}}_i + (1 - f_i) \dot{\boldsymbol{\varepsilon}}_m \tag{5.46}$$

Similar rule applies for macroscopic and mean stress rates per and mean stresses per phases.

5.3 Mesh convergence re-evaluation for the elastic-viscoplastic case

As already observed, in the finite elements method results may be dependent not only on the geometry, boundary conditions or material parameters, but also on the mesh of finite elements. For this reason, before performing the analyses towards cluster model verification, the mesh sensitivity test was performed at the first stages of the thesis, for the elastic regime (see section 3.2 of chapter 3). Conclusions from this test were applied to further calculations with good outcomes. However, it was observed that the viscoplastic model, as a much more complex one, produces bigger discrepancies and results in a higher level of mesh vulnerabilities. For this reason, it was decided that some re-evaluation of assumptions regarding the meshing was necessary.

In the aforementioned mesh convergence test for the elastic regime, a minimum mesh size was described in relation to the inclusion size (at least 10 finite elements per inclusion perimeter), as well as second-order elements were chosen to represent the sample. Following a similar algorithm, a scenario of viscoplastic matrix with no strain hardening and with stiff (only elastic) inclusions is used for this test, as it should refer to the biggest achievable contrast between phases. Material data are specified in table 5.1. Similar materials parameters were used in Czarnota et al. (2015).

Table 5.1: Material parameters used for mesh convergence test in elasto-viscoplastic regime.

	Matrix: elastic-viscoplastic	Inclusions: elastic
Young Modulus, E [GPa]	70.0	400.0
shear modulus, G [GPa]	26.9	166.7
Poisson's ratio, ν [-]	0.3	0.2
yield stress, Y_0 [MPa]	480	-
plastic modulus, K_0 [MPa]	0	-
reference strain rate, $\dot{\varepsilon}_0$ [1/s]	0.001	-
rate sensitivity exponent m [-]	0.1	-

The test is performed for a representative unit cell of size 1x1x1m and volume fraction of inclusions equal to $f_i = 40\%$ (the largest reliable value for the cluster model from the previous analysis) which corresponds to inclusions size of $r_i = 0.457m$ for RC and $r_i = 0.630m$ for BCC lattices respectively (in fact, any length unit can be taken as the presented results are not dependent on the length scale). Two loading directions are defined: (0,0,1) and (1,1,1) with respect to unit cell edges and with maximum total tensile strain of $\bar{\varepsilon} = 0.03$. The mesh sizes vary from 0.1 to 0.04m. The loading was applied with a strain rate of $\dot{\bar{\varepsilon}} = 0.001\frac{1}{s}$ The same periodic boundary conditions are applied, as in the FEM analysis in previous chapters.

As seen in the figures 5.2-5.3, there is a high convergence of results in the elastic range for all mesh sizes, like in the analyses in previous chapters. However, after the simulation enters the viscoplastic regime, significant discrepancies become visible, especially for the RC lattice under (0,0,1) loading direction and for the BCC under (1,1,1) loading direction. The comparison of mesh sizes have been performed in the same way as the initial mesh convergence tests for the elastic regime, as described in detail in section 3.2 of chapter 3. For each mesh size, following values have been calculated and compared:

- number of finite elements in the model (total, for matrix, for inclusions);
- radius, volume and perimeter of inclusion;
- average volume of one finite element in inclusion;
- average edge length of one finite element in inclusion (assuming tetrahedral elements);

The results (macroscopic stresses and mean stresses per phase) for each mesh size are compared to the finest mesh (0.04m), which was set as the reference, and presented in tables 5.2-5.5. It can be seen that for the viscoplastic regime the mesh needs to be finer than for the elastic case. If the acceptable level of discrepancies is assumed as 5% , the mesh size should be no bigger than 0.05m, which corresponds to 48 second-order finite elements approximating the inclusions of spherical shape (resulting in the discrepancy 3% level). It is much more than 10 finite elements that were sufficient for the elastic regime.

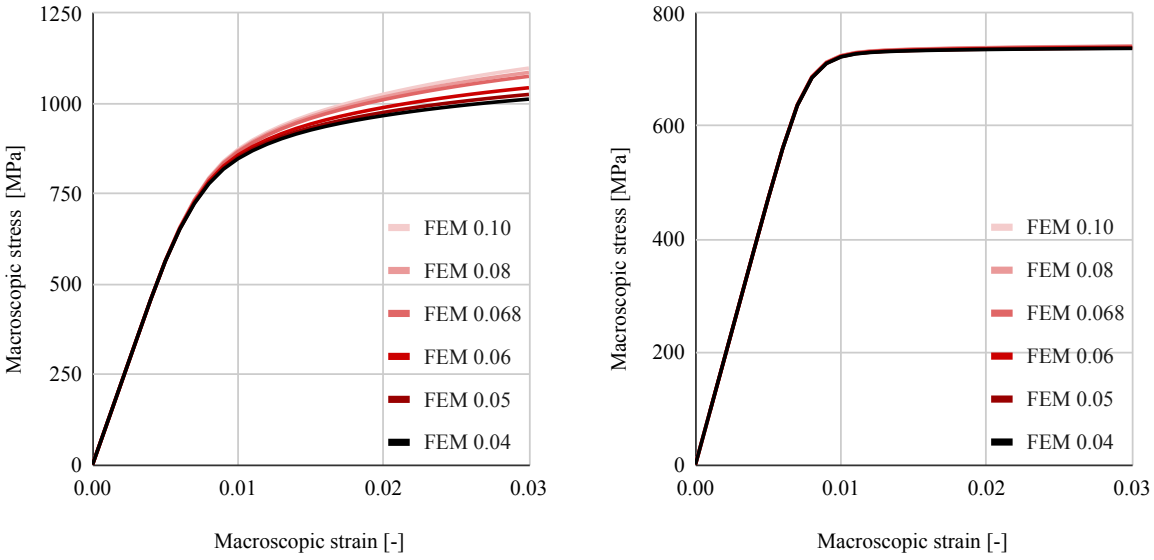

(a) (b)

Figure 5.2: Macroscopic stress vs macroscopic strain for different mesh sizes. RC lattice. Loading direction (0,0,1) (a); and (1,1,1) (b). Note different scale on Y axes.

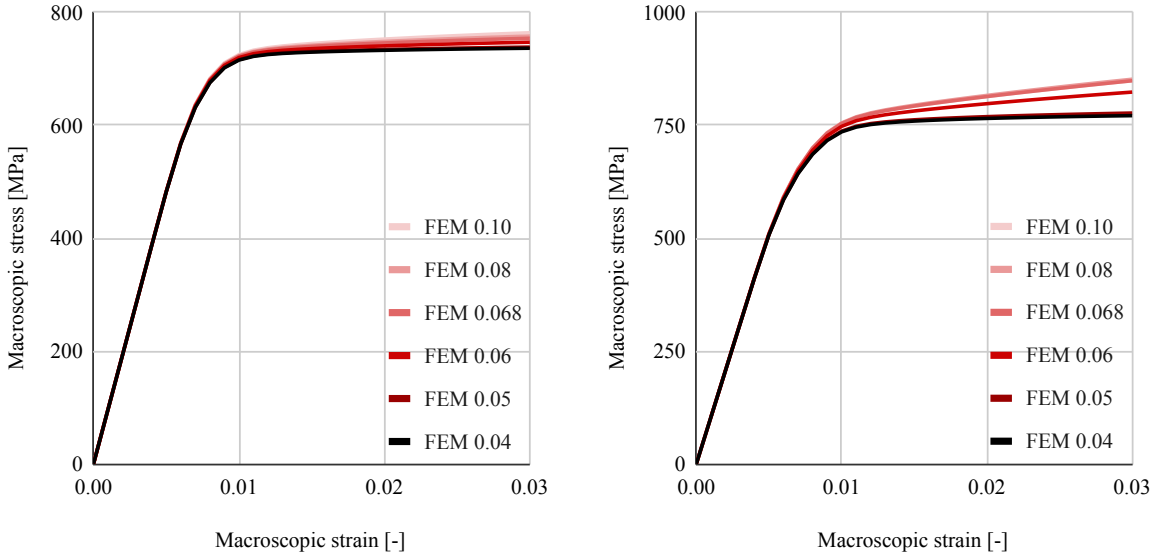

(a) (b)

Figure 5.3: Macroscopic stress vs macroscopic strain for different mesh sizes. BCC lattice. Loading direction (0,0,1) (a); and (1,1,1) (b). Note different scale on Y axes.

Table 5.2: Mesh convergence test for viscoplastic tension. RC lattice, direction (0,0,1).

Mesh	No of FEs approx.	Total		Inclusions		Matrix	
size [m]	the sphere [-]	[MPa]	[%] to ref.	[MPa]	[%] to ref.	[MPa]	[%] to ref.
0.1	23.6	1674	109.1%	3151	114.6%	688.9	95.3%
0.08	26.7	1661	108.2%	3112	113.2%	692.7	95.8%
0.068	30.2	1643	107.1%	3064	111.4%	695.6	96.2%
0.06	38.0	1588	103.5%	2911	105.8%	706.5	97.7%
0.05	48.1	1556	101.4%	2815	102.4%	716.5	99.1%
0.04	56.1	1534	100.0%	2750	100.0%	723.1	100.0%

Table 5.3: Mesh convergence test for viscoplastic tension. RC lattice, direction (1,1,1).

Mesh	No of FEs approx.	Total		Inclusions		Matrix	
size [m]	the sphere [-]	[MPa]	[%] to ref.	[MPa]	[%] to ref.	[MPa]	[%] to ref.
0.1	23.6	1121	100.6%	1475	101.4%	884.4	99.8%
0.08	26.7	1120	100.5%	1473	101.2%	884.4	99.8%
0.068	30.2	1119	100.5%	1470	101.1%	884.4	99.8%
0.06	38.0	1116	100.2%	1462	100.5%	885.0	99.8%
0.05	48.1	1115	100.1%	1458	100.2%	885.6	99.9%
0.04	56.1	1114	100.0%	1455	100.0%	886.4	100.0%

Table 5.4: Mesh convergence test for viscoplastic tension. BCC lattice, direction (0,0,1).

Mesh	No of FEs approx.	Total		Inclusions		Matrix	
size [m]	the sphere [-]	[MPa]	[%] to ref.	[MPa]	[%] to ref.	[MPa]	[%] to ref.
0.1	23.4	1178	103.5%	1656	108.2%	858.8	98.1%
0.08	27.6	1169	102.8%	1632	106.6%	861.2	98.4%
0.068	31.7	1164	102.3%	1616	105.6%	862.1	98.5%
0.06	37.1	1153	101.4%	1584	103.5%	866.5	99.0%
0.05	47.8	1141	100.3%	1542	100.7%	873.4	99.8%
0.04	55.6	1137	100.0%	1531	100.0%	875.2	100.0%

Table 5.5: Mesh convergence test for viscoplastic tension. BCC lattice, direction (1,1,1).

Mesh	No of FEs approx.	Total		Inclusions		Matrix	
size [m]	the sphere [-]	[MPa]	[%] to ref.	[MPa]	[%] to ref.	[MPa]	[%] to ref.
0.1	23.4	1363	111.2%	2170	119.5%	824.9	99.1%
0.08	27.6	1347	109.9%	2127	117.2%	826.4	99.3%
0.068	31.7	1342	109.5%	2112	116.3%	828.3	99.5%
0.06	37.1	1304	106.4%	2014	110.9%	830.4	99.8%
0.05	47.8	1235	100.7%	1841	101.4%	830.6	99.8%
0.04	55.6	1226	100.0%	1816	100.0%	832.3	100.0%

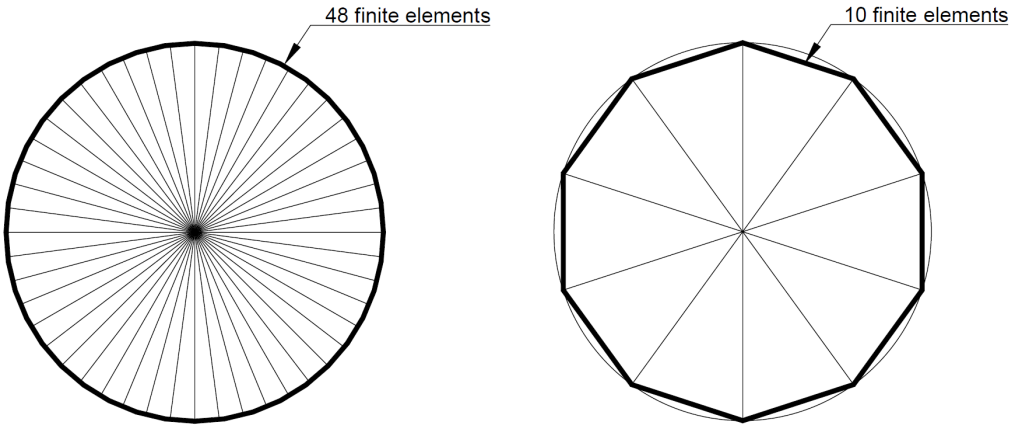

Figure 5.4: Visualisation of the mesh density through the inclusion cross-section and discretisation of its perimeter. To achieve the acceptable level of accuracy for the viscoplastic case, there should be at least 48 second-order finite elements (left) compared to just 10 for the elastic regime (right).

5.4 Results

In the previous chapters, bigger discrepancies in results were observed for the scenario with ultra hard inclusions (UHI) than with ultra soft ones. Thus, for sake of simplicity, only these scenarios are considered in the analysis for the elastic-viscoplastic regime and inclusions are always stiffer than matrix. Moreover, only the RC and BCC lattices are examined, as the FCC one exposed very similar behaviour and results to the BCC lattice. Two material setups are considered:

1. viscoplastic matrix, elastic inclusion;
2. viscoplastic matrix, viscoplastic inclusions.

Two isochoric uniaxial tension scenarios are considered which differ by tension direction: (1,0,0) and (1,1,1). As the elasto-viscoplastic calculations are based on time increments, the external strain is applied in steps, corresponding to the strain rate of $\dot{\bar{\varepsilon}} = 0.001\frac{1}{s}$, reaching $\bar{\varepsilon} = 0.1$ in the last time step. It needs to be mentioned that the cluster model applies only to the small strain theory. Such a large strain has been chosen only for testing purposes and limitations of the model need to be kept in mind. Calculations for this test are performed for a single volume fraction of inclusions $f_i = 40\%$. The periodic boundary conditions are applied in all FE analyses.

As already mentioned in section 5.2.2, the viscoplastic tangent stiffness in the case of Perzyna law is anisotropic and given by (5.26). Therefore, there is a question of choosing the isotropisation method which might have a significant impact on the results. The general formula, analogous to (4.4), which can be applied to establish isotropic viscoplastic shear modulus was proposed by Czarnota et al. (2015):

$$\psi G_1^v + (1-\psi) G_2^v \tag{5.47}$$

where ψ is an isotropisation weight factor. In the literature, two isotropisation methods have mostly been used: "soft" ($\psi = 0.0$) and "hard" ($\psi = 0.8$). However, in order to better understand the model behaviour and find the best fitting solution, calculations for a series of different values of isotropisation weight factor were performed: 0.0, 0.2, 0.4, 0.6, 0.8 and 1.0.

5.4.1 Elastic-viscoplastic matrix, elastic inclusions

For the calculations in the elastic-viscoplastic regime, an composite of a elastic-viscoplastic metallic matrix and purely elastic ceramic inclusions is considered. Material data are specified in table 5.8. The results are presented in the form of macroscopic stress-strain curves for the entire sample, as well as relationships between stresses and strains (per-phase or overall/macroscopic) for each phase. The results are shown in figures 5.5-5.11 for the RC lattice and in figures 5.12-5.14 for the BCC lattice. For sake of concisness, only the stress-strain curves relative to the macroscopic strain $\bar{\varepsilon}$ are shown for the BCC lattice.

Table 5.6: Material parameters used for analysis of two-phase composite in elasto-viscoplastic regime.

	Matrix: elastic-viscoplastic	Inclusions: elastic
Young Modulus, E [GPa]	70.0	400.0
shear modulus, G [GPa]	26.9	166.7
Poisson's ratio, ν [-]	0.3	0.2
yield stress, Y_0 [MPa]	480	-
plastic modulus, K_0 [MPa]	0	-
reference strain rate, $\dot{\varepsilon}_0$ [1/s]	0.001	-
rate sensitivity exponent m [-]	0.1	-

It is visible that for both models the stress level stabilises at a certain point. However, there are giant discrepancies between the results obtained for varying values of ψ in the cluster model, with better accordance with the FEM model at lower ones (ranging between $\psi = 0.2$ and $\psi = 0.4$). Discrepancies are most visible for the RC (0,0,1) scenario which seems to be the most demanding case in this respect for both mean-field and full-field models (as seen in the mesh-convergence study). For other cases, these discrepancies are significantly smaller, as well as the point at which the stresses stabilise is reached for lower strains. The advanced viscous flow regime is well represented as concerns

the stabilised stress levels, while the most difficult range to estimate is the transition from the elastic to viscoplastic regime where the two approaches show different behaviour.

The FEM model produces a gradual and smooth transition, while the cluster model gives a more sudden change from the linear elastic regime, especially for the lower isotropisation factors where a "dent" is visible in graphs, even if they later align well with the numerical model. This might be explained by the fact, that the cluster is a mean-field model in which the transition occurs at single moment for the entire matrix phase, while in the full-field FEM calculations it can happen in different time steps for each finite element. Similar observations were also made in Sadowski et al. (2021) where the additive law, combined with the Perzyna law for the matrix phase, was employed in the context of the Mori-Tanaka model. In that paper, it was demonstrated that a non-monotonous overall response of the composite materials delivered by the mean-field approach is related to switch from purely elastic localization relation to the elastic-viscoplastic one, which can happen for the higher overall stress level than the asymptotic stress achieved in purely viscoplastic regime. The switch happens when the yield stress threshold (5.4) is reached in the matrix phase.

Inclusions respond only elastically and are well represented in both models. However, the maximum strain that they reach is different and depends on the isotropisation value as well. There is a significant drop in the bearing capacity of the matrix in FEM results, especially for the RC (0,0,1), which is not visible in the cluster model. This might be explained by possible unloading of some individual finite elements which is not possible in the mean-field cluster model. The isotropisation value does seem to significantly impact the results. Strong impact of spatial distribution of inclusions and anisotropy of lattices is successfully reproduced by the cluster model.

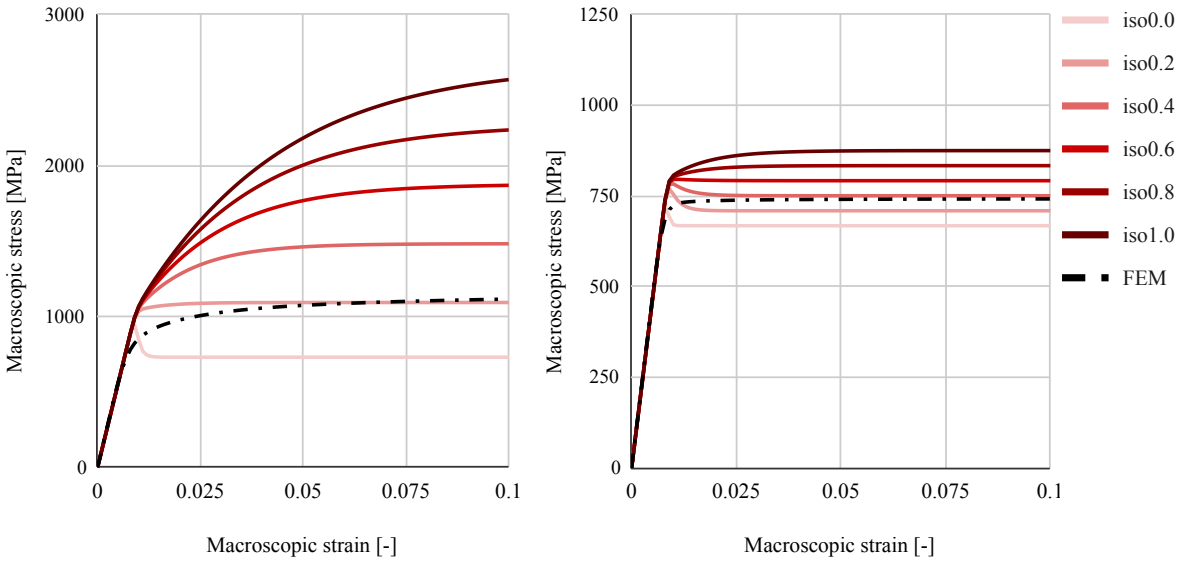

(a) (b)

Figure 5.5: Macroscopic stress vs macroscopic strain for different values of isotropisation weight factor. Volume fraction of inclusions $f_i = 40\%$, elastic inclusions, RC lattice. Loading direction (0,0,1) (a); and (1,1,1) (b). Note different scale on Y axes.

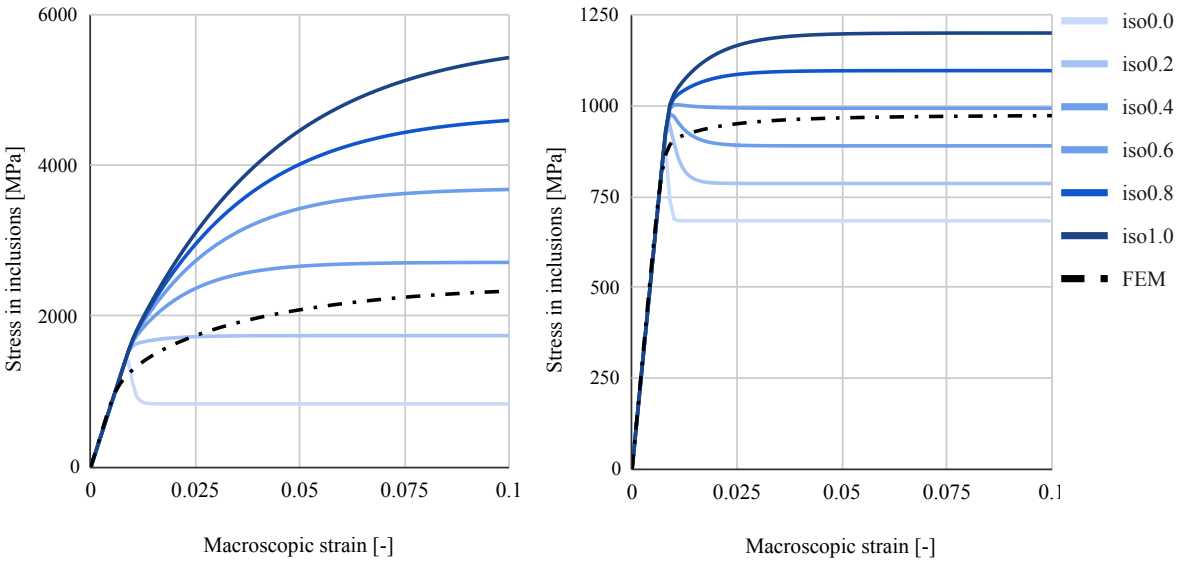

(a) (b)

Figure 5.6: Stress in inclusions vs macroscopic strain for different values of isotropisation weight factor. Volume fraction of inclusions $f_i = 40\%$, elastic inclusions, RC lattice. Loading direction (0,0,1) (a); and (1,1,1) (b). Note different scale on Y axes.

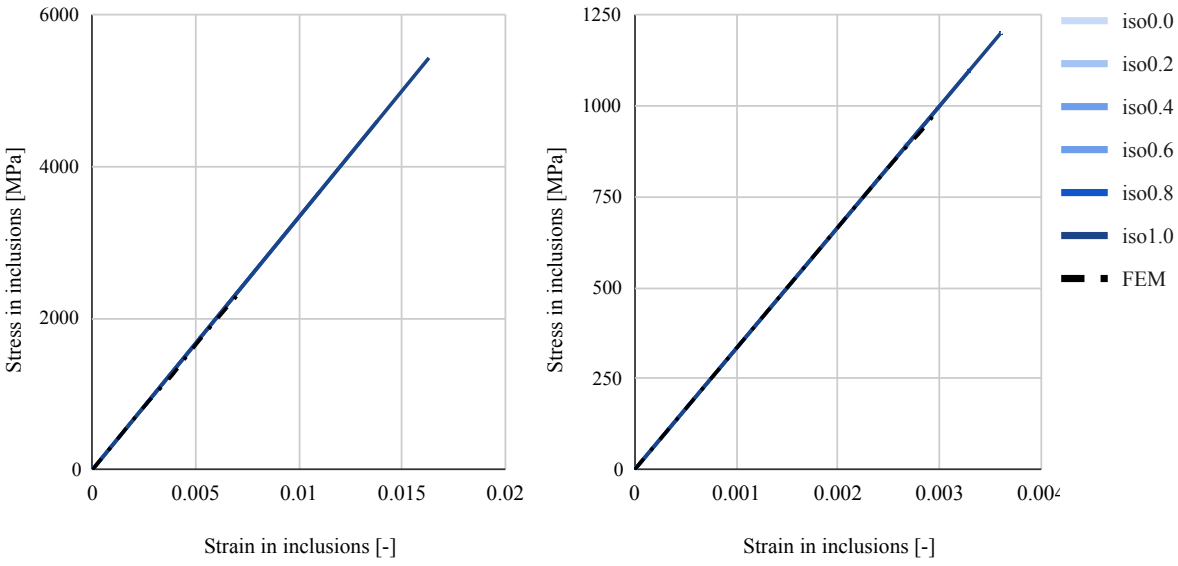

(a) (b)

Figure 5.7: Stress in inclusions vs strain in inclusions for different values of isotropisation weight factor. Volume fraction of inclusions $f_i = 40\%$, elastic inclusions, RC lattice. Loading direction (0,0,1) (a); and (1,1,1) (b). Note different scale on Y axes.

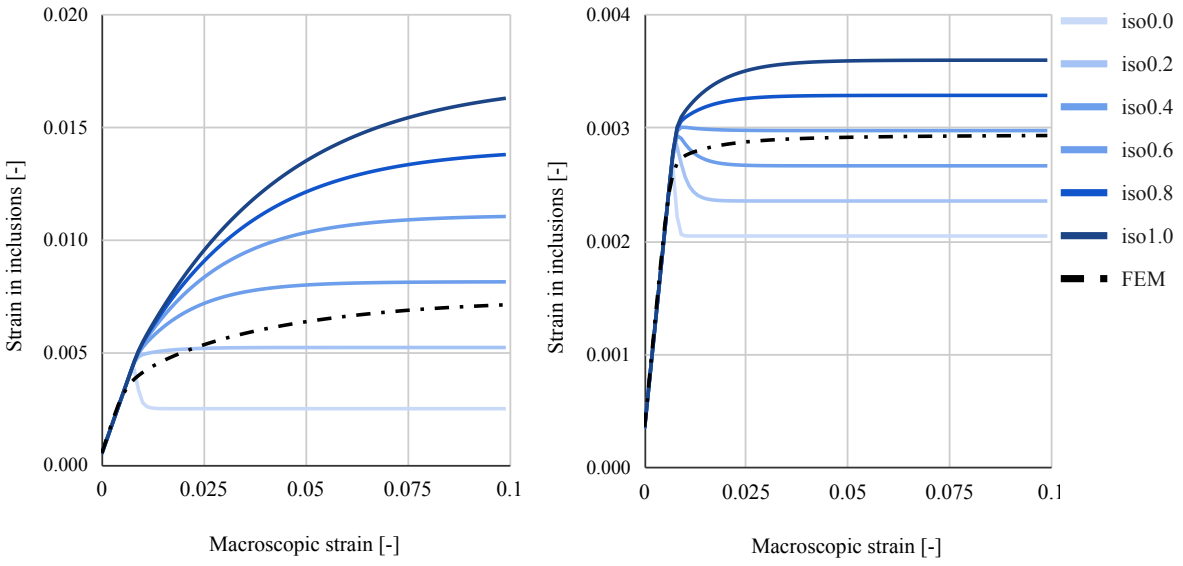

(a) (b)

Figure 5.8: Strain in inclusions vs macroscopic strain for different values of isotropisation weight factor. Volume fraction of inclusions $f_i = 40\%$, elastic inclusions, RC lattice. Loading direction (0,0,1) (a); and (1,1,1) (b). Note different scale on Y axes.

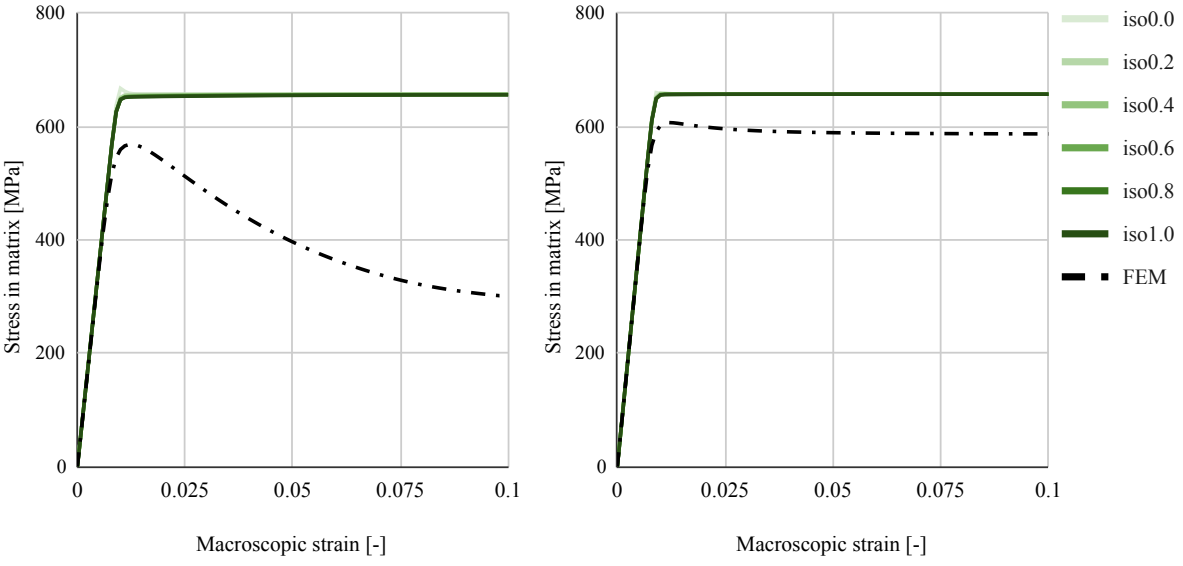

(a) (b)

Figure 5.9: Stress in matrix vs macroscopic strain for different values of isotropisation weight factor. Volume fraction of inclusions $f_i = 40\%$, elastic inclusions, RC lattice. Loading direction (0,0,1) (a); and (1,1,1) (b).

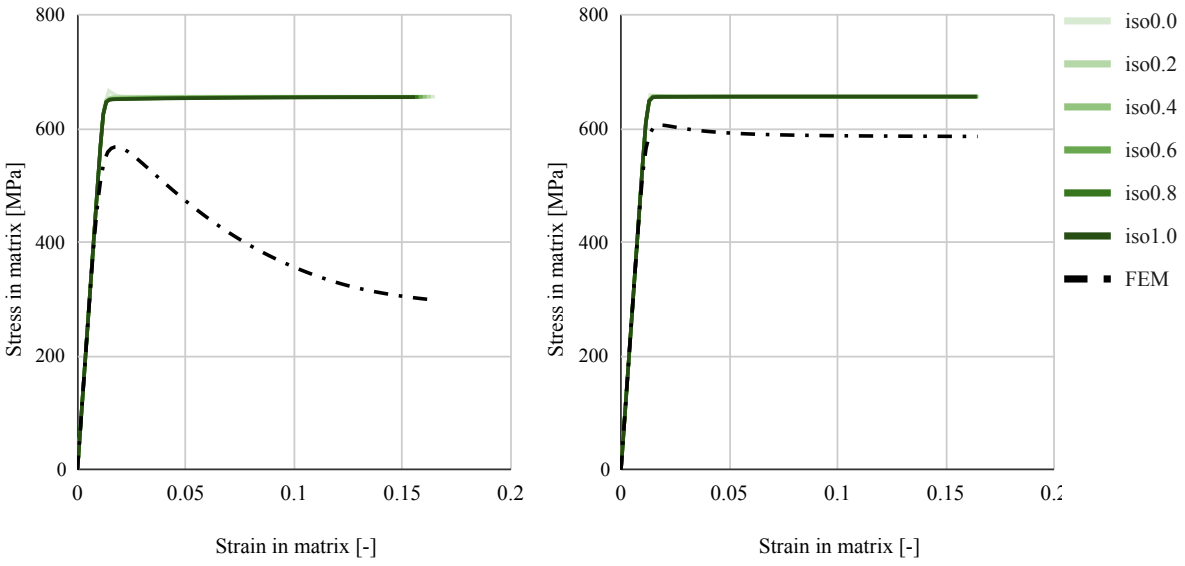

(a) (b)

Figure 5.10: Stress in matrix vs strain in matrix for different values of isotropisation weight factor. Volume fraction of inclusions $f_i = 40\%$, elastic inclusions, RC lattice. Loading direction (0,0,1) (a); and (1,1,1) (b).

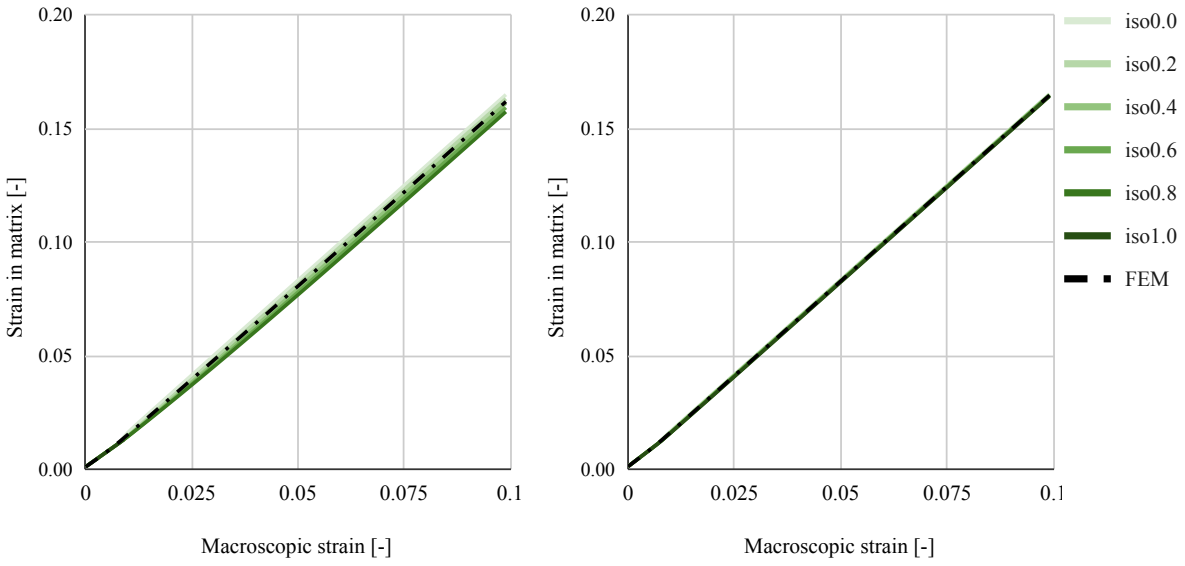

(a) (b)

Figure 5.11: Strain in matrix vs macroscopic strain for different values of isotropisation weight factor. Volume fraction of inclusions $f_i = 40\%$, elastic inclusions, RC lattice. Loading direction (0,0,1) (a); and (1,1,1) (b).

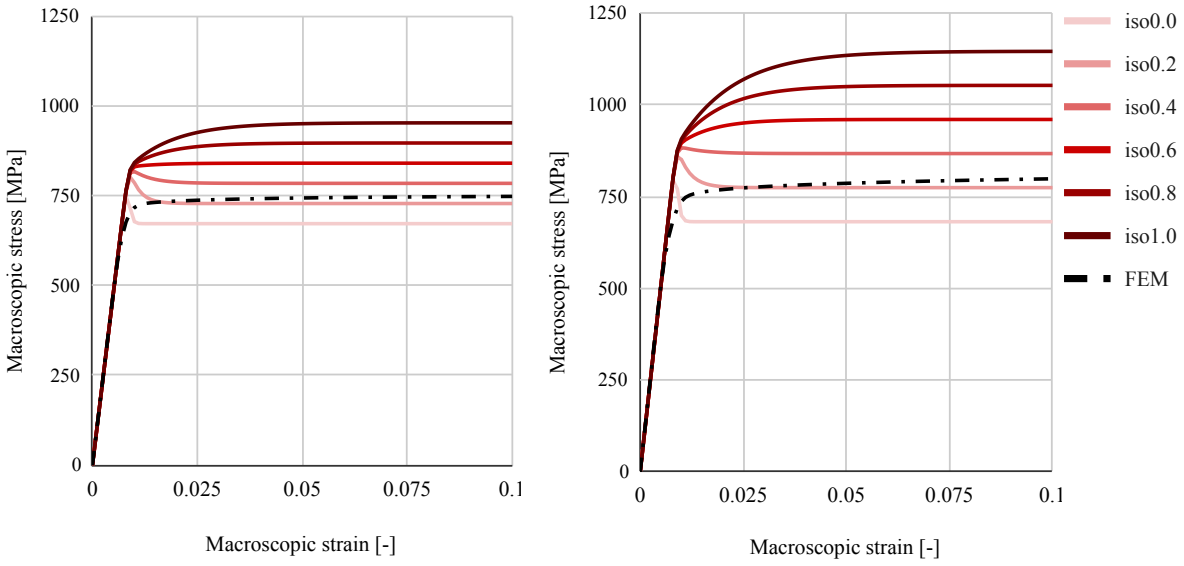

(a) (b)

Figure 5.12: Macroscopic stress vs macroscopic strain for different values of isotropisation weight factor. Volume fraction of inclusions $f_i = 40\%$, elastic inclusions, BCC lattice. Loading direction (0,0,1) (a); and (1,1,1) (b).

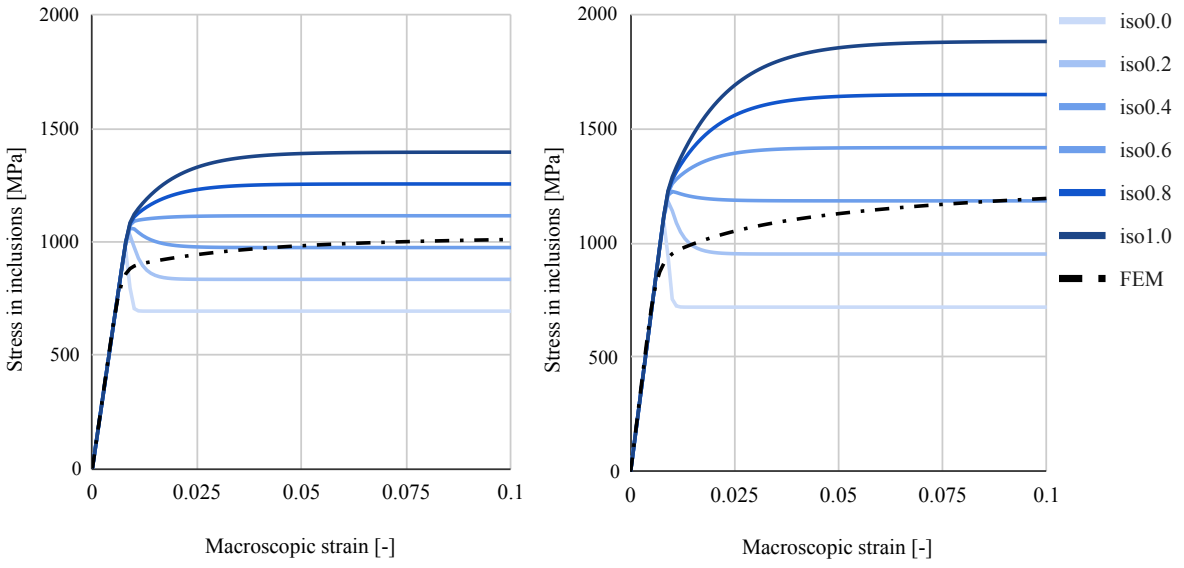

(a) (b)

Figure 5.13: Stress in inclusions vs macroscopic strain for different values of isotropisation weight factor. Volume fraction of inclusions $f_i = 40\%$, elastic inclusions, BCC lattice. Loading direction (0,0,1) (a);and (1,1,1) (b).

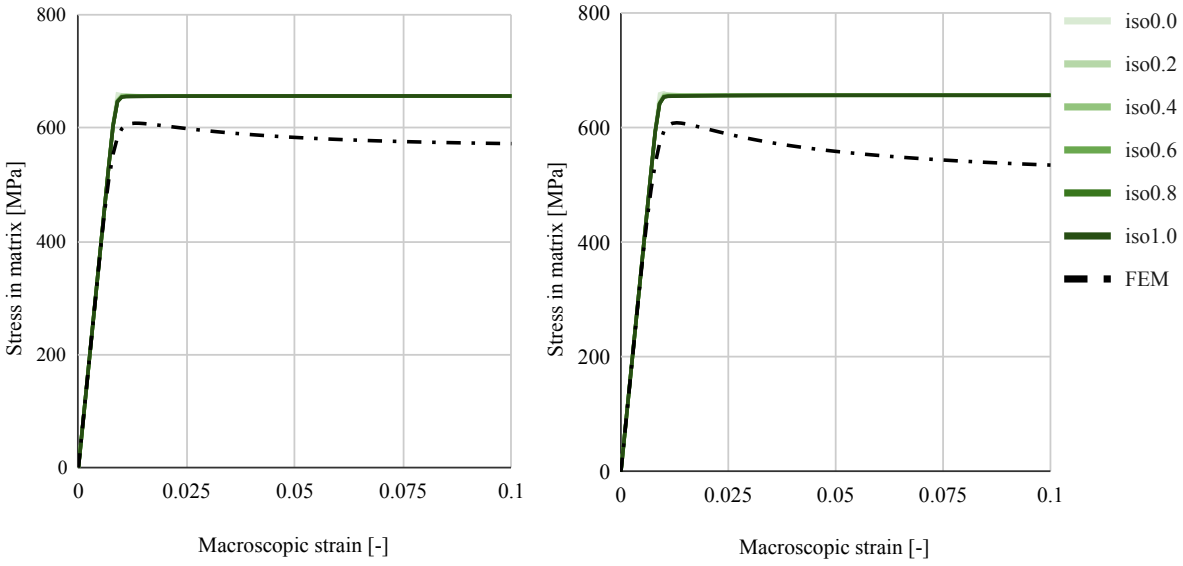

(a) (b)

Figure 5.14: Stress in matrix vs macroscopic strain for different values of isotropisation weight factor. Volume fraction of inclusions $f_i = 40\%$, elastic inclusions, BCC lattice. Loading direction (0,0,1) (a); and (1,1,1) (b).

Results demonstrate that, in general, some form of model calibration should be performed at the beginning of the calculation process in order to select the most suitable isotropisation value. For this specific material and loading scenarios, the best fitting isotropisation value was chosen as 0.2. For this value, results of mean - and full-field models for different volume fractions of inclusions are compared ($f_i = 20\%, 30\%, 40\%$). The macroscopic response is presented in figures 5.15-5.16.

Similar conclusions can be taken for each volume fraction of inclusions considered. Elasticity and the advanced viscous flow regime are well represented, while the transition from the elastic to viscoplastic regime shows discrepancy between the cluster model and the FE results. Big difference in stress levels between $f_i = 40\%$ and smaller volume fractions is observed for the first scenario, i.e. RC (0,0,1). A reason might be the fact that the volume fraction of inclusions equal to $f_i = 40\%$ is much closer to the limit for the RC lattice (max $f_i = 52\%$) than for the BCC (max $f_i = 68\%$). Similar trend was observed in the previous chapters.

Additionally, the value of the macroscopic strain, at which the macroscopic stress stabilises, were listed for each case and presented in table 5.7. Stabilisation was assumed as the point at which the stress level between time increments changes by no more than 0.1%. For the cluster model, the 0.2 isotropisation value was considered. The results stabilise at similar ranges between $\bar{\varepsilon} = 0.016$ and $\bar{\varepsilon} = 0.025$ mostly depending on the loading scenario and less on the volume fraction of inclusions. The RC (0,0,1) case seems to be the most demanding in this regard, especially in FEM calculations, which for $f_i = 40\%$ it needs to reach $\bar{\varepsilon} = 0.061$ to obtain relatively stabilised values.

Table 5.7: Level of macroscopic strain at which the macroscopic stress stabilises.

	RC 001	RC 111	BCC 001	BCC 111
cluster fi40%	0.024	0.018	0.019	0.021
cluster fi30%	0.022	0.02	0.021	0.021
cluster fi20%	0.025	0.021	0.022	0.023
FEM fi40%	0.061	0.015	0.018	0.026
FEM fi30%	0.037	0.015	0.015	0.017
FEM fi20%	0.028	0.016	0.016	0.017

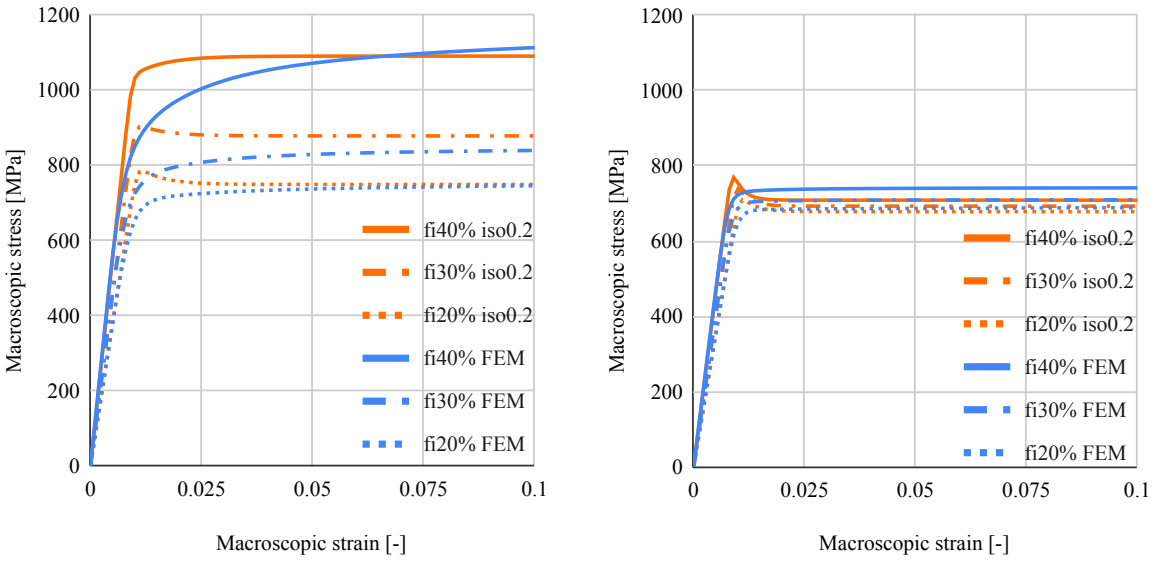

(a) (b)

Figure 5.15: Macroscopic stress-strain response for $f_i = 20\%, 30\%, 40\%$ volume fractions of inclusions. FEM (blue) and cluster model with isotropisation weight factor $\psi = 0.2$ (orange). RC lattice, elastic inclusions. Loading direction (0,0,1) (a); and (1,1,1) (b).

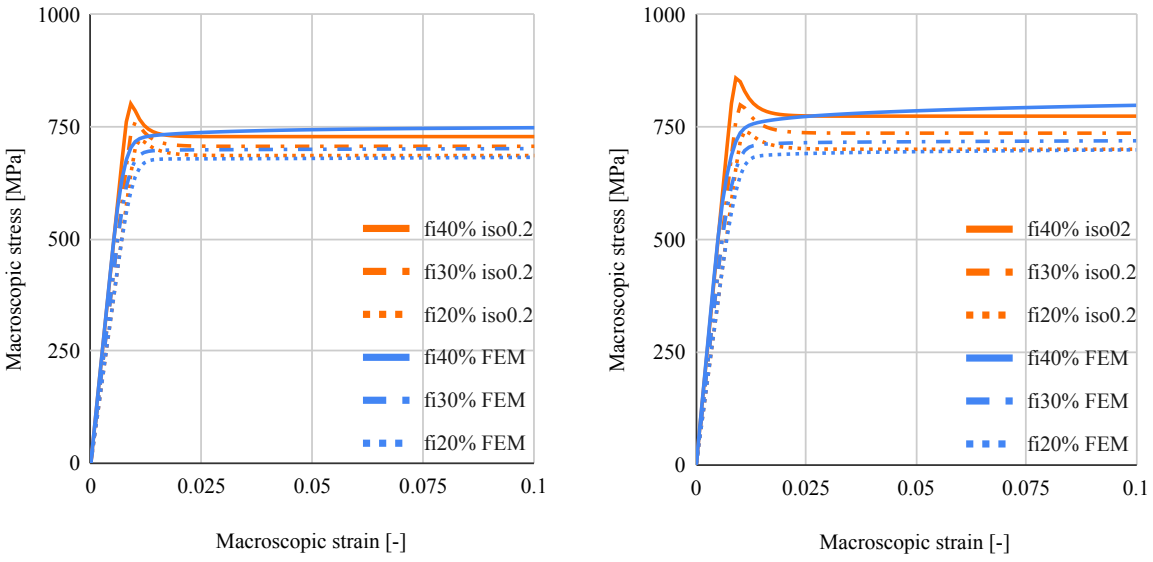

(a) (b)

Figure 5.16: Macroscopic stress-strain response for $f_i = 20\%, 30\%, 40\%$ volume fractions of inclusions. FEM (blue) and cluster model with isotropisation weight factor $\psi = 0.2$ (orange). BCC lattice, elastic inclusions. Loading direction (0,0,1) (a); and (1,1,1) (b).

5.4.2 Elastic-viscoplastic matrix, viscoplastic inclusions

Apart from purely elastic stiff inclusions, a scenario with elastic-viscoplastic inclusions has been considered as well. The same parameters for matrix are used, while the inclusions have been updated with parameters necessary for viscoplastic analysis, as listed in table 5.8. The results are presented in the form of the macroscopic stress-strain curves for the entire sample, as well as evolution of mean stresses and strains for each phase. The results are shown in figures 5.17-5.23 for the RC lattice and in figures 5.24-5.26 for the BCC lattice. For sake of brevity, only the stress-strain response relative to the macroscopic strain $\bar{\varepsilon}$ is shown for the BCC lattice.

It is visible that the case with elastic-viscoplastic inclusions produces smaller differences between the estimates of the cluster and the results of the FEM analyses. Also, within the cluster model itself, results are less dispersed for different isotropisation weight factors. In the previous scenario, during the matrix undergoing the viscoplastic flow, the purely elastic inclusions were stiff. However, when inclusions are elastic-viscoplastic, the contrast between phase stiffness is significantly smaller and there is some redistribution of strain between them. Still, the most difficult range to estimate is the transition from the elastic to viscoplastic regime where both models behave differently.

Worth noting is that the isotropisation weight factor of $\psi = 0.0$ gives unexpected results. Not only does it produce a significantly softer overall response, but the stress-strain response within the inclusions shows some kind of unloading with completely halting strain increase in this phase at a certain time point. Still, as in the case with purely elastic inclusions, the best accordance with FEM results is obtained with isotropisation weight factor ranging between $\psi = 0.2$ and $\psi = 0.4$.

Table 5.8: Material parameters used for analysis of two-phase composite in elasto-viscoplastic regime.

	Matrix: elastic-viscoplastic	Inclusions: elastic-viscoplastic
Young Modulus, E [GPa]	70.0	400.0
shear modulus, G [GPa]	26.9	166.7
Poisson's ratio, ν [-]	0.3	0.2
yield stress, Y_0 [MPa]	480	960
plastic modulus, K_0 [MPa]	0	0
reference strain rate, $\dot{\varepsilon}_0$ [1/s]	0.001	0.001
rate sensitivity exponent m [-]	0.1	0.1

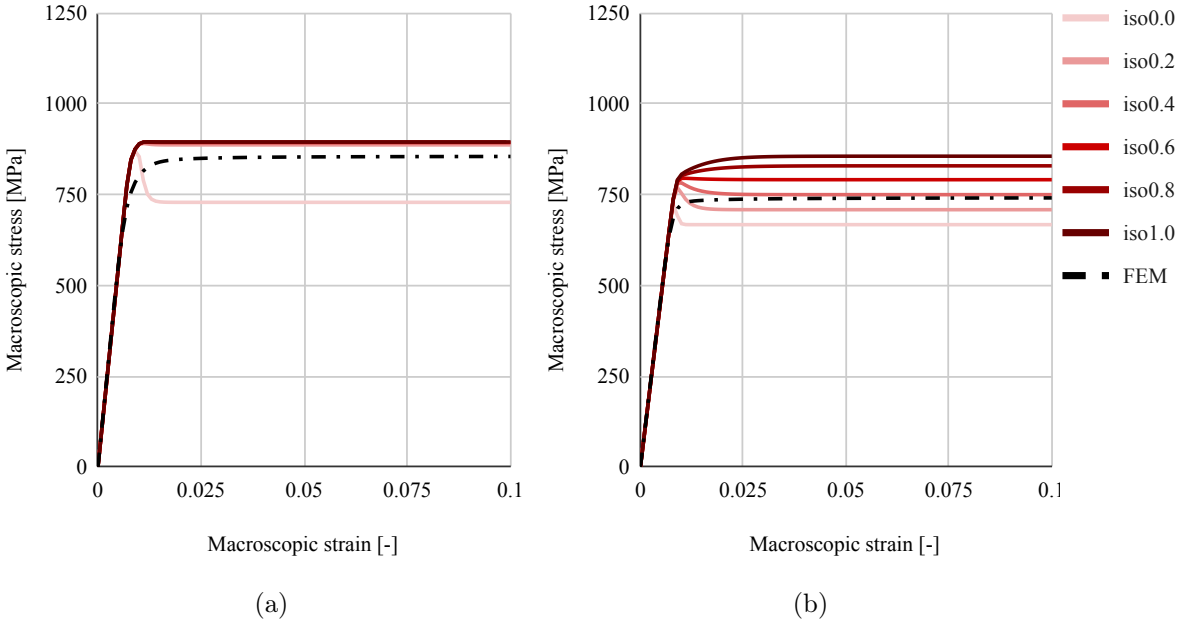

(a) (b)

Figure 5.17: Macroscopic stress vs macroscopic strain for different values of isotropisation weight factor. Volume fraction of inclusions $f_i = 40\%$, elastic-viscoplastic inclusions, RC lattice. Loading direction (0,0,1) (a); and (1,1,1) (b).

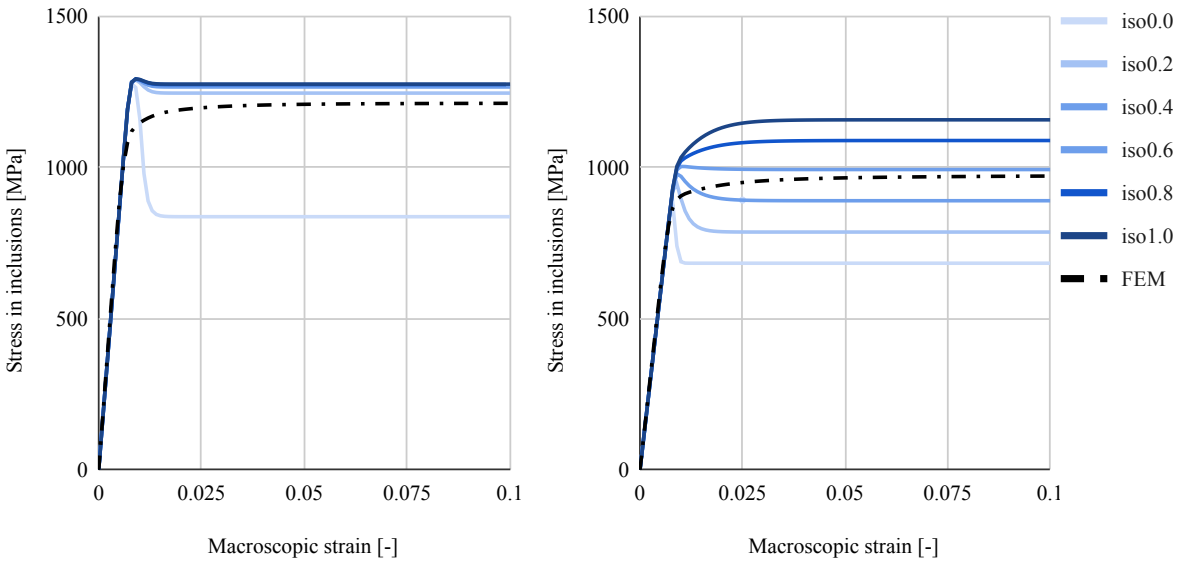

(a) (b)

Figure 5.18: Stress in inclusions vs macroscopic strain for different values of isotropisation weight factor. Volume fraction of inclusions $f_i = 40\%$, elastic-viscoplastic inclusions, RC lattice. Loading direction (0,0,1) (a); and (1,1,1) (b).

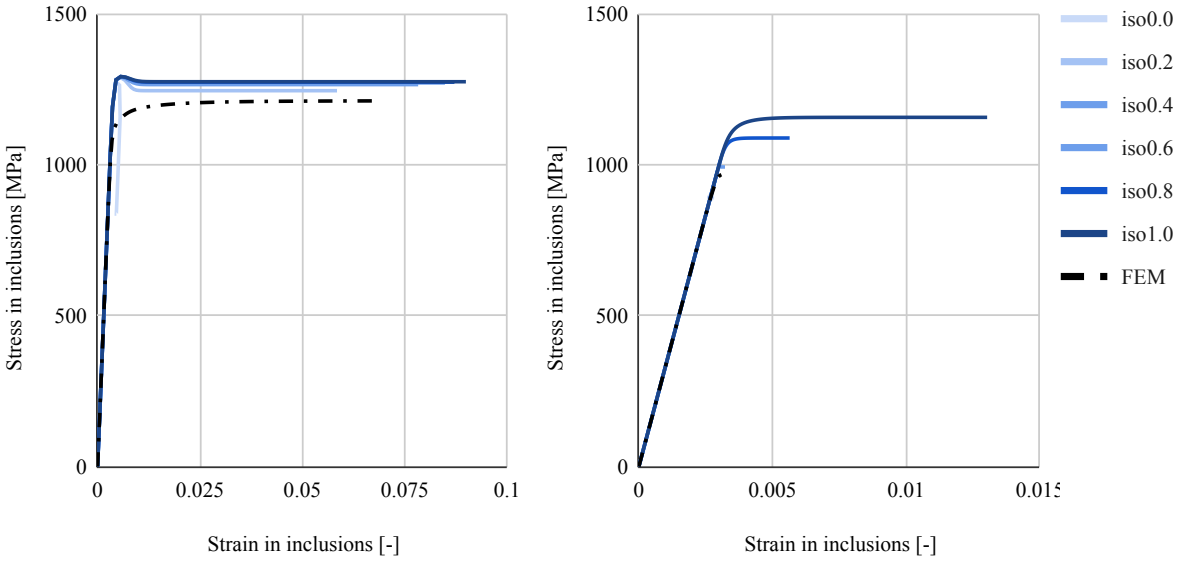

(a) (b)

Figure 5.19: Stress in inclusions vs strain in inclusions for different values of isotropisation weight factor. Volume fraction of inclusions $f_i = 40\%$, elastic-viscoplastic inclusions, RC lattice. Loading direction (0,0,1) (a); and (1,1,1) (b).

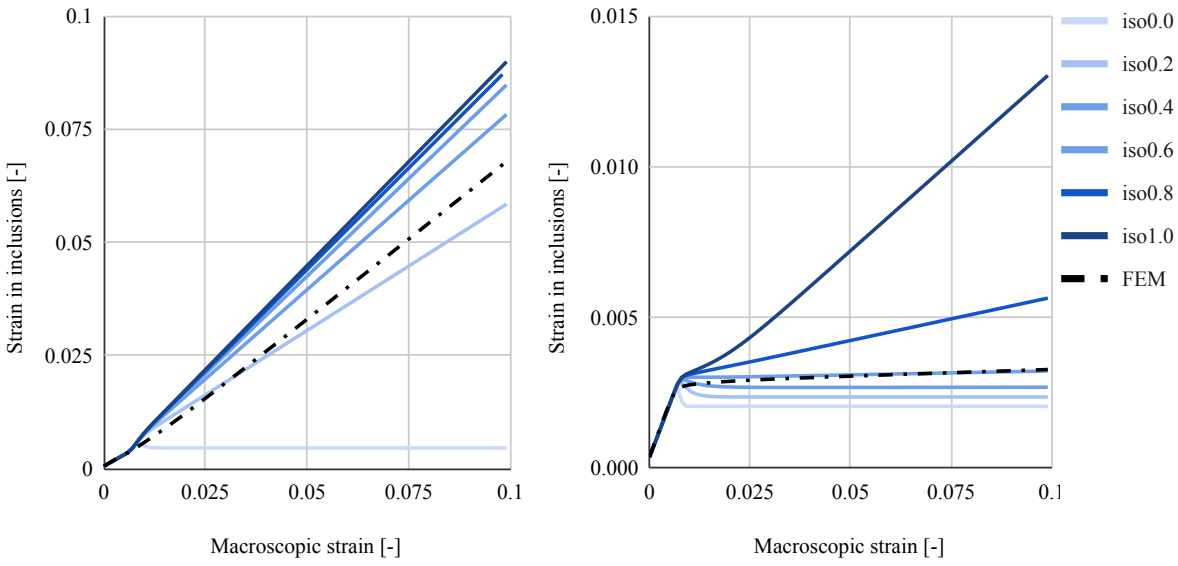

(a) (b)

Figure 5.20: Strain in inclusions vs macroscopic strain for different values of isotropisation weight factor. Volume fraction of inclusions $f_i = 40\%$, elastic-viscoplastic inclusions, RC lattice. Loading direction (0,0,1) (a); and (1,1,1) (b). Note different scale on Y axes.

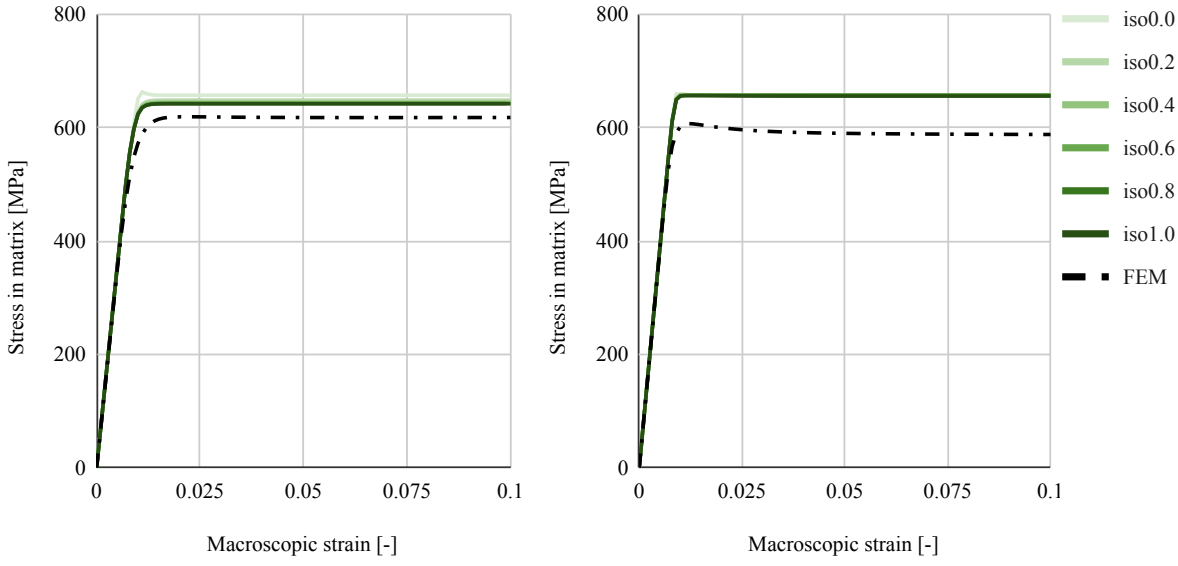

(a) (b)

Figure 5.21: Stress in matrix vs macroscopic strain for different values of isotropisation weight factor. Volume fraction of inclusions $f_i = 40\%$, elastic-viscoplastic inclusions, RC lattice. Loading direction (0,0,1) (a); and (1,1,1) (b).

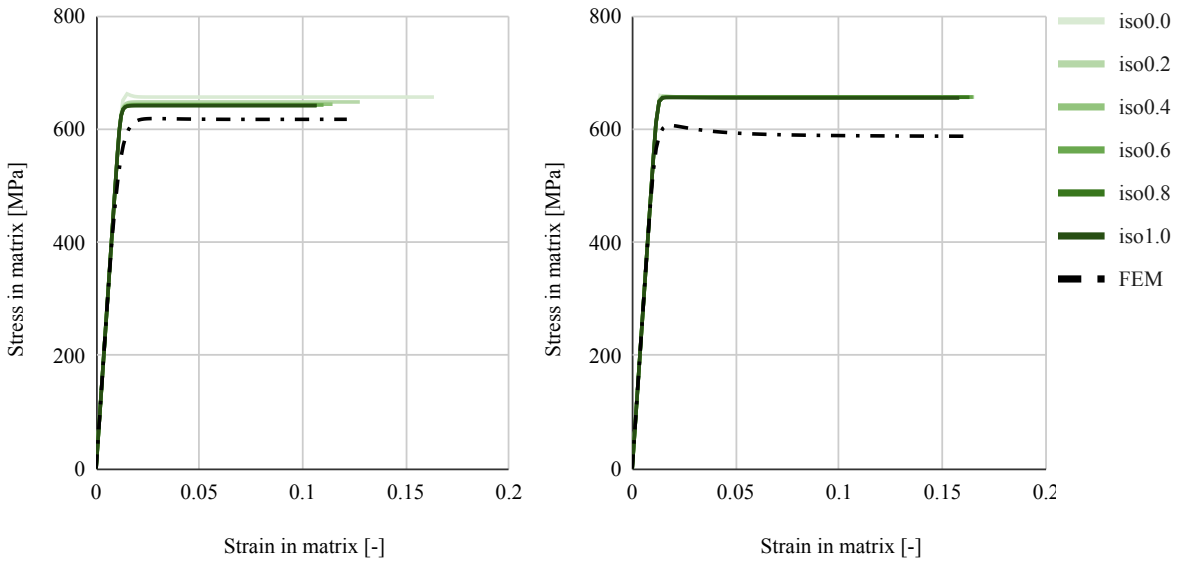

(a) (b)

Figure 5.22: Stress in matrix vs strain in matrix for different values of isotropisation weight factor. Volume fraction of inclusions $f_i = 40\%$, elastic-viscoplastic inclusions, RC lattice. Loading direction (0,0,1) (a); and (1,1,1) (b).

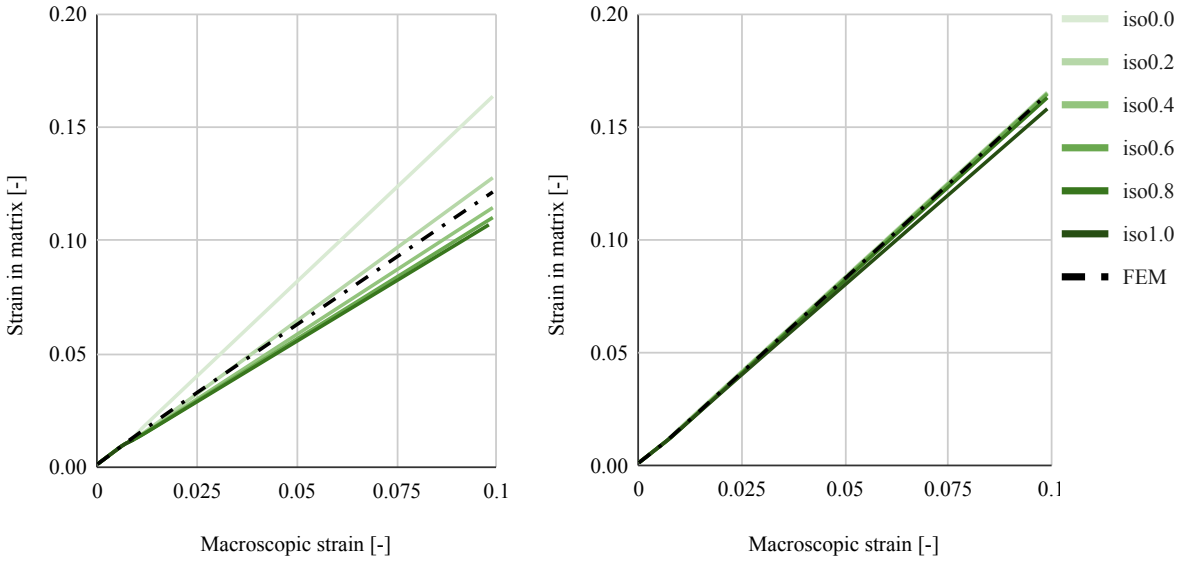

(a) (b)

Figure 5.23: Strain in matrix vs macroscopic strain for different values of isotropisation weight factor. Volume fraction of inclusions $f_i = 40\%$, elastic-viscoplastic inclusions, RC lattice. Loading direction (0,0,1) (a); and (1,1,1) (b).

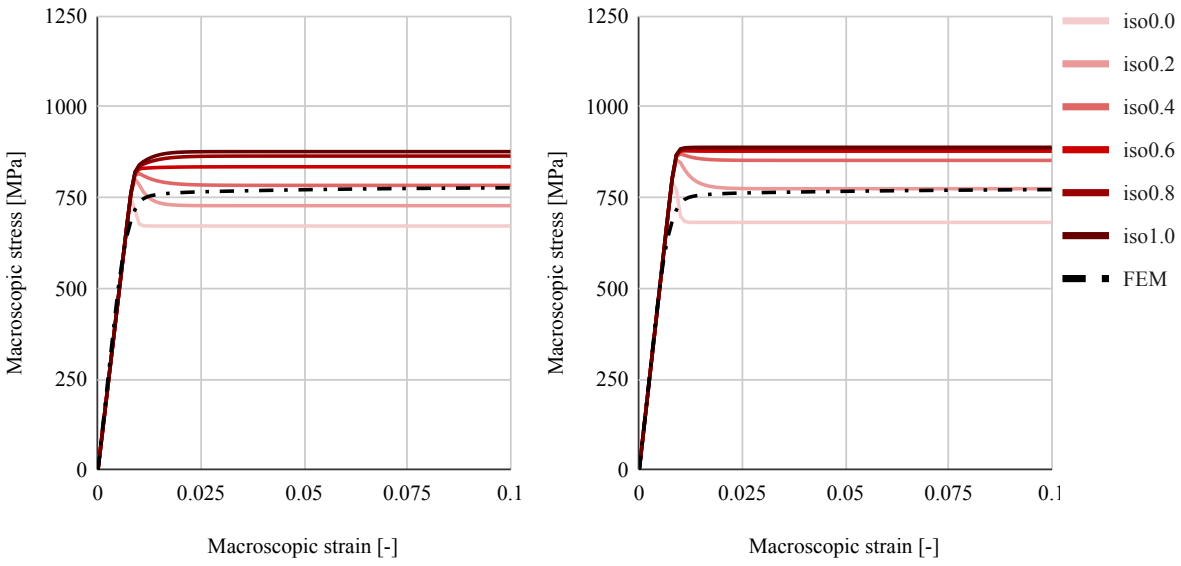

(a) (b)

Figure 5.24: Macroscopic stress vs macroscopic strain for different values of isotropisation weight factor. Volume fraction of inclusions $f_i = 40\%$, elastic-viscoplastic inclusions, BCC lattice. Loading direction (0,0,1) (a); and (1,1,1) (b).

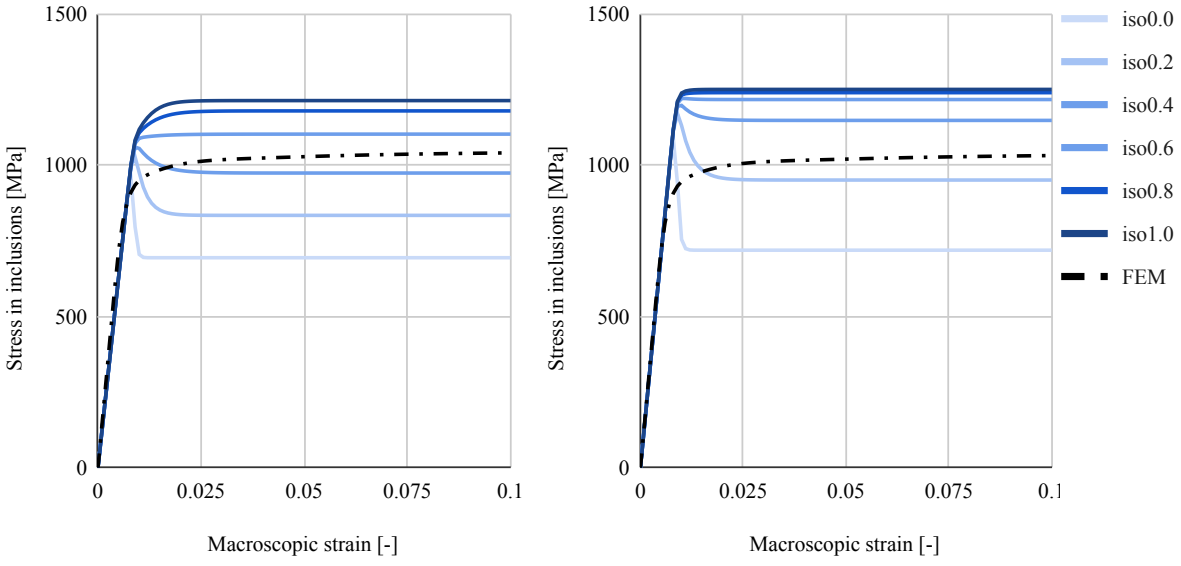

(a) (b)

Figure 5.25: Stress in inclusions vs macroscopic strain for different values of isotropisation weight factor. Volume fraction of inclusions $f_i = 40\%$, elastic-viscoplastic inclusions, BCC lattice. Loading direction (0,0,1) (a); and (1,1,1) (b).

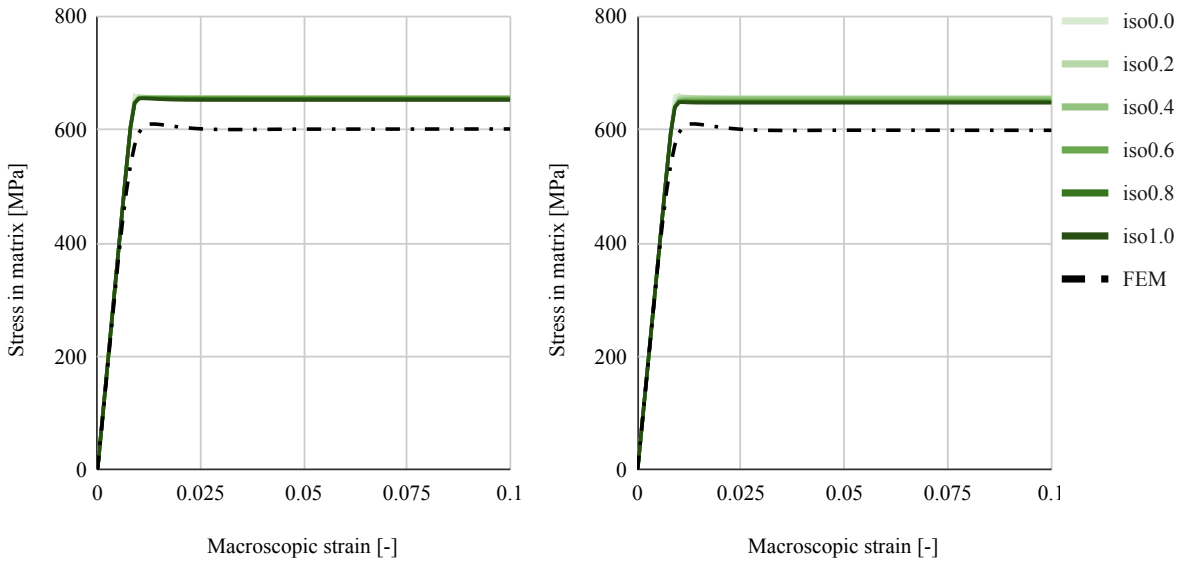

(a) (b)

Figure 5.26: Stress in matrix vs macroscopic strain for different values of isotropisation weight factor. Volume fraction of inclusions $f_i = 40\%$, elastic-viscoplastic inclusions, BCC lattice. Loading direction (0,0,1) (a); and (1,1,1) (b).

5.5 Summary

Extension of the cluster model to the elastic-viscoplastic cases requires incorporation of the Maxwell-type constitutive law into the mean-field modelling framework. The idea of the additive tangent interaction law proposed in Kowalczyk-Gajewska et al. (2021) has been used in the present thesis. The law has been formulated assuming tangent linearisation of the Perzyna viscoplastic law for the matrix and calculating the viscous tangent compliance $\mathbb{M}^v$ employing the mean stress (first moment) in the matrix. Next, in order to benefit from the closed-form relations available for the cluster model in the case of isotropic matrix material, the isotropisation of $\mathbb{M}^v$ needs to be performed. It was shown that results achieved using the cluster model rely a lot on the chosen isotropisation method applied to the viscous tangent stiffness. In the literature, usually two are described: "soft" and "hard", where the isotropisation weight factor in equation (5.47) is equal to $\psi = 0.0$ or $\psi = 0.8$, respectively. In this chapter multiple isotropisation weight factors were examined which showed large discrepancies between the respective estimates. In general, the best compliance between the cluster and FEM models was found for softer ones, around $\psi = 0.2$. This hints that some form of model calibration should be performed at the beginning of the calculation process for the viscoplastic regime in order to choose the most suitable isotropisation value for a given scenario.

The ranges of pure elasticity and advanced viscous flow are well represented in the cluster model as it gives results very close to the FEM analyses. However, the transition from the elastic to viscoplastic regime is the most difficult range to estimate, as the two models show different behaviour. The FEM model produces a gradual and smooth transition, while the cluster model gives a more sudden change, especially for the lowest isotropisation values where some sort of "dent" is visible. This type of a spurious response has been already observed for the additive tangent Mori-Tanaka model in Sadowski et al. (2021).

Representation of the viscoplastic regime poses a much bigger level of difficulty compared to e.g. plasticity. Still, more research and model adjustments are required in this field in order to obtain reliant analytical tools for viscous effects. Possible remedies may be sought either by using a fully anisotropic viscoplastic tangent compliance (which would require the numerical integration to find tensors $\bar{\mathbf{\Gamma}}^v$ and $\mathbb{P}_0^v$) and/or calculating this fourth order tensor by means of the second moment of stress as done for the elastic-plastic composite in chapter 4.

Mesh convergence tests for FEM models show that much denser meshes are required in order to

achieve an acceptable level of accuracy. For the elastic-viscoplastic case, there should be at least 48 second-order finite elements on the perimeter of inclusions compared to just 10 for calculations in the elastic regime.

Chapter 6

Additional study on microstructure

6.1 Introduction

During the research reported in this thesis, several features regarding the microstructure of inclusion-matrix composites have been observed. This included e.g. direction-dependent behaviour of regular cubic (RC) and body-centred cubic (BCC) lattices, as well as risk of possible geometrical instabilities of matrix in porous materials. This chapter aims to propose some geometry-based measures which could explain differences between the mechanical response of different unit cells. Moreover, a simplified analysis of porous microstructure stability is performed.

6.2 Comparison of regular cubic and body-centred cubic lattices

Throughout the thesis, the most concern has been given to regular cubic (RC) and body-centred Cubic (BCC) lattices, as these are one of the most prevalent regular spatial arrangements of particles studied in the context of micromechanical modelling. During various numerical and analytical analyses, an interesting phenomena has been observed. When samples are subject to uniaxial tension in two different directions: the one along the sample edge (0,0,1) and the one along the diagonal (1,1,1), both layouts show a strongly anisotropic response. This was expected, based on their microstructure, however they behave in an "opposite" way to one another, i.e.: for the RC the stiffer response is observed for the (0,0,1) direction, while for BCC it is for the (1,1,1) direction, which can be seen e.g. in figure 5.5 or 5.12. This chapter seeks a deeper look into microstructure of these lattices to see if there are any geometrical traits that may give foresight of their mechanical properties even before the start of mechanical analysis.

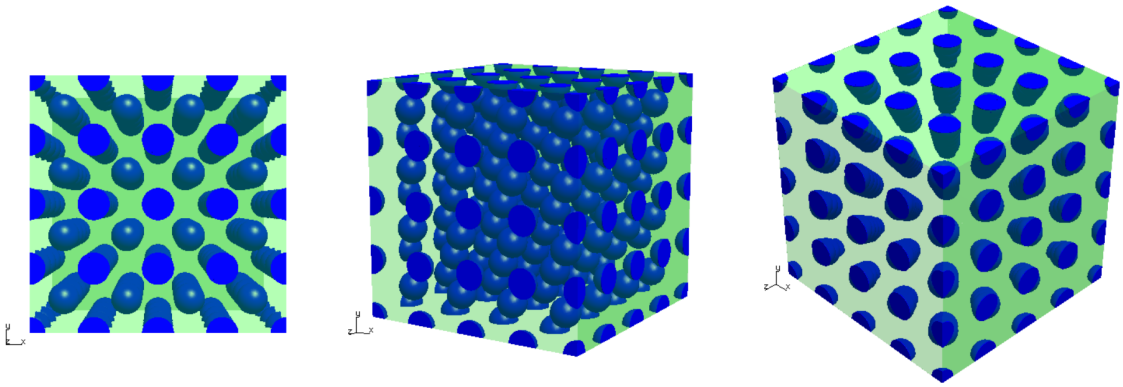

Figure 6.1: Different viewing angles of the BCC lattice.

As mentioned previously, the first step is to search for some geometrical explanation. With a simple visual comparison of samples, different pictures are visible depending on the viewing angle.

From some views all inclusions are perfectly aligned, showing a view through the entire matrix, while from other angles all that can be seen is a tight cluster of inclusions. It is illustrated in figure 6.1. The matrix is visualised as semi-transparent for clarity.

An intuitive trace to look for are the distances between centres of inclusions. In the RC lattice, these distances are significantly different depending on the direction. For the (0,0,1) direction (i.e. along the bottom edge) the inclusions are close together, while along the diagonal there is more "weak" space between them. At the same time, in the BCC arrangement, this "weak" space is filled with an additional inclusion, thus "reinforcing" this direction. It is visualised in figure 6.2.

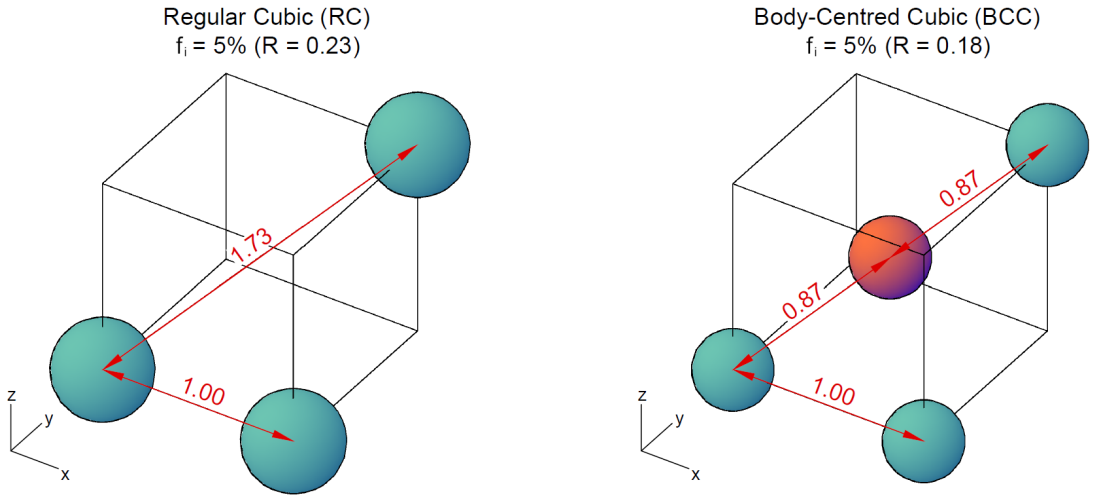

Figure 6.2: Distances between inclusions for (0,0,1) and (1,1,1) directions in RC (left); and BCC (right) lattices.

Kowalczyk-Gajewska et al. (2021) described this characteristic as directional compacity index λ. It is defined as the ratio of the inclusion radius r_i to the distance between two centres of the closest inclusions s, with this distance being measured in the loading direction, i.e. (0,0,1) or (1,1,1).

$$\lambda = \frac{r_i}{s} \tag{6.1}$$

Table 6.1: Directional compacity index for different lattices and loading scenarios.

f_i	RC lattice		BCC lattice	
	(0,0,1)	(1,1,1)	(0,0,1)	(1,1,1)
5%	0.23	0.13	0.18	0.21
10%	0.29	0.17	0.23	0.26
20%	0.36	0.21	0.29	0.33
40%	0.46	0.26	0.36	0.42
50%	0.49	0.28	0.39	0.45

In table 6.1 directional compacity indices listed for different volume fractions of inclusions. It is visible that for the RC lattice this directional compacity index is higher for the (0,0,1) direction, while for the BCC lattice the index is higher for the (1,1,1) direction. Moreover, the RC lattice shows the more extreme behaviour, as it produces both the biggest and the smallest value of this index for any given volume fraction of inclusions. This might explain both the stronger anisotropy of RC than BCC lattice, as well as the observed "opposite" outcomes for two arrangements in the analyses.

The directional compacity index might be a useful tool to describe spatial distribution of inclusions, however it needs the selection of a specific line that connects the centres of inclusions and goes through the sample in one specific location. This might be seen as an arbitrary choice. Moreover, as it explains well the observed differences for composite reinforced by inclusions stiffer than the matrix, it fails to explain why the voided material is still stiffer in (0,0,1) direction than along the diagonal, while reverse

behaviour is seen for BCC case (see figures: 3.16, 3.17, 4.10, 4.9). For this reason, an additional method where no specific position is necessary to be chosen, is tried.

First, the direction of load is selected and straight lines going throughout the sample are drawn parallel to this direction. Then, it is checked how much of this line goes through the inclusions and through the "weak" space of the matrix - similarly to geotechnical boreholes that are made to investigate the soil on the future construction sites. Multiple "boreholes" are "drilled" from the top surface of the cubic sample. Their distribution can be regular (e.g. in a mesh) or random. It was visualised on figures 6.3-6.4 for "drilling" parallelly to (0,0,1) direction.

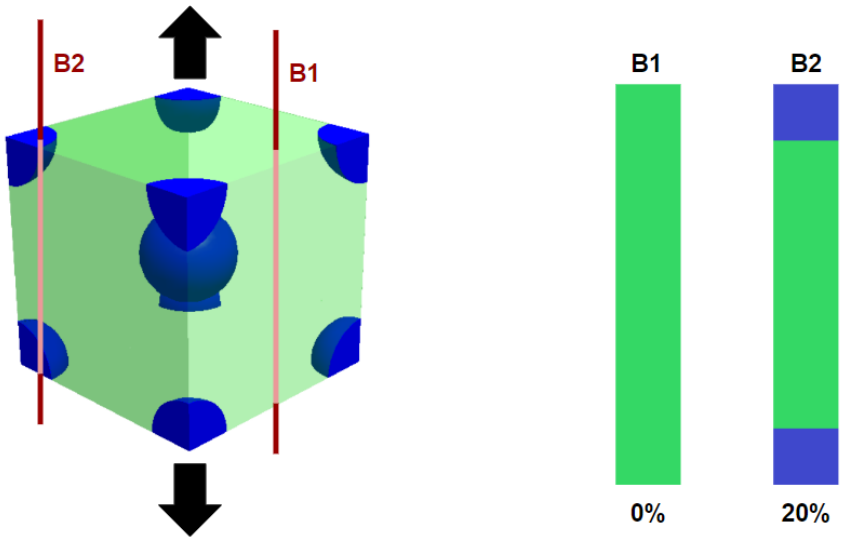

Figure 6.3: Example of "boreholes" that are "drilled" through the sample.

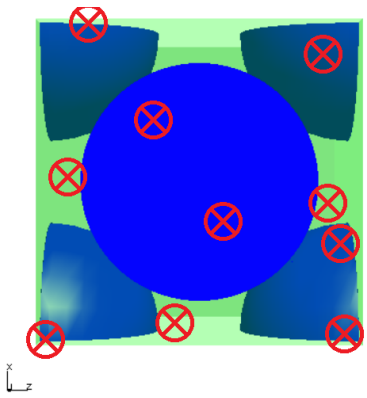

Figure 6.4: Random distribution of boreholes - top view.

At first, 100 randomly distributed boreholes are chosen to be "drilled" along the "vertical" direction (0,0,1), both for RC and BCC lattices. The sample size is equal to $1x1x1m$ (equal to the distance between centres of inclusions of the basic RC mesh) and the volume fraction of inclusions is equal to $f_i = 40\%$. In fact, any length unit can be taken as the presented results are not dependent on the length scale. For each borehole, the encountered volume fraction of inclusion f_i^{bore} was plotted on a graph, as seen in the figure 6.5a. As expected, the average encountered volume fraction (in fact, length fraction) of inclusions among all boreholes is close to the real volume fraction of inclusion: $f_i^{bore.av} = 44.8\%$ for RC, $f_i^{av} = 41.9\%$ for BCC. After the results were sorted in a descending order, as per figure 6.5b, they showed an interesting pattern - even if both samples have the same volume fraction of inclusions, their distribution is different. The BCC lattice is much more uniform, with fewer "empty" boreholes (i.e. boreholes going through the matrix material only).

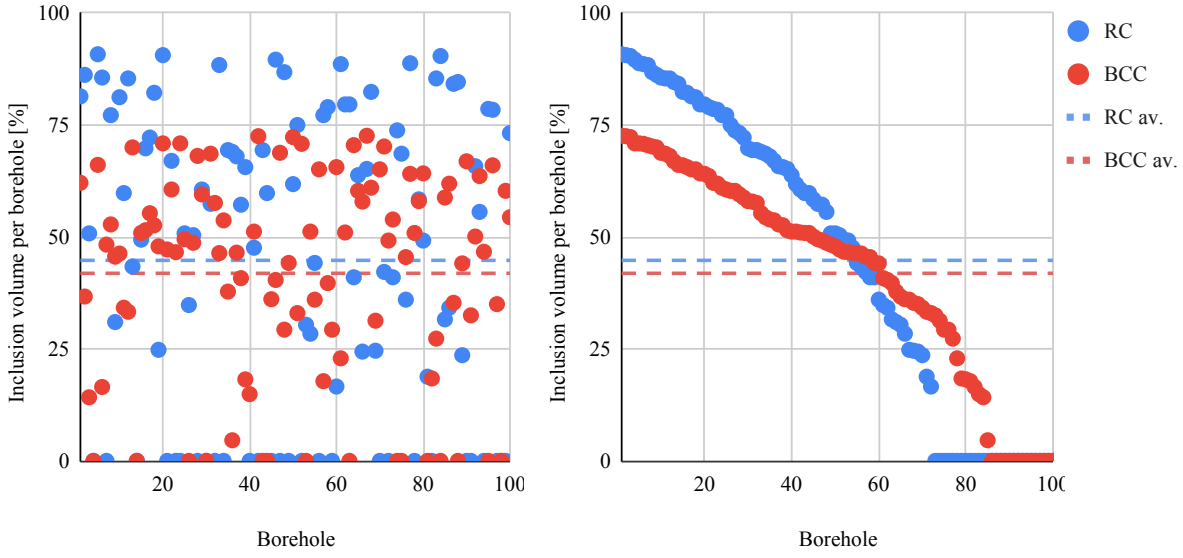

(a) (b)

Figure 6.5: Volume fraction of inclusions in each borehole. 100 randomly distributed boreholes. RC and BCC lattices, (0,0,1) direction. Raw data export (a); and sorted in descending order (b).

The analysis was repeated for the same samples, although this time using a regular 10x10 mesh of boreholes (100 in total, as in the random case). Results are shown in figure 6.6. The outcome is similar, although because of the regular mesh, the boreholes intersect symmetrically-corresponding points within the sample, thus effectively lowering the "resolution" and making the interpretations more challenging. For this reason, it was decided to stick to the random distribution of boreholes.

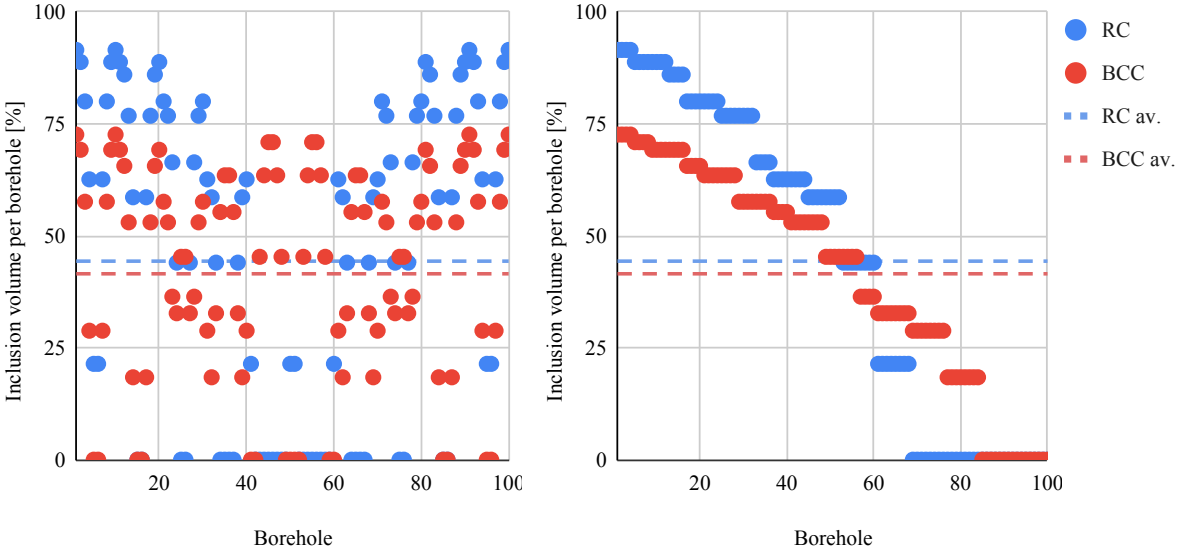

(a) (b)

Figure 6.6: Volume fraction of inclusions in each borehole. 100 regularly distributed boreholes. RC and BCC lattices, (0,0,1) direction. Raw data export (a); and sorted in descending order (b).

After the preliminary verification of the concept, in the next step, the number of "boreholes" in a random distribution was increased to 1000 in order to increase resolution of the analysis, as well as the sample size was increased to 3x3x3 unit cells (more inclusions contained within the sample).

Moreover, two drilling directions were compared, i.e.: (0,0,1) and (1,1,1), for the two lattices. The diagonal direction was achieved by rotating the sample cube to align with the (1,1,1) basis vector of the original coordinate system, as visualised in figure 6.7.

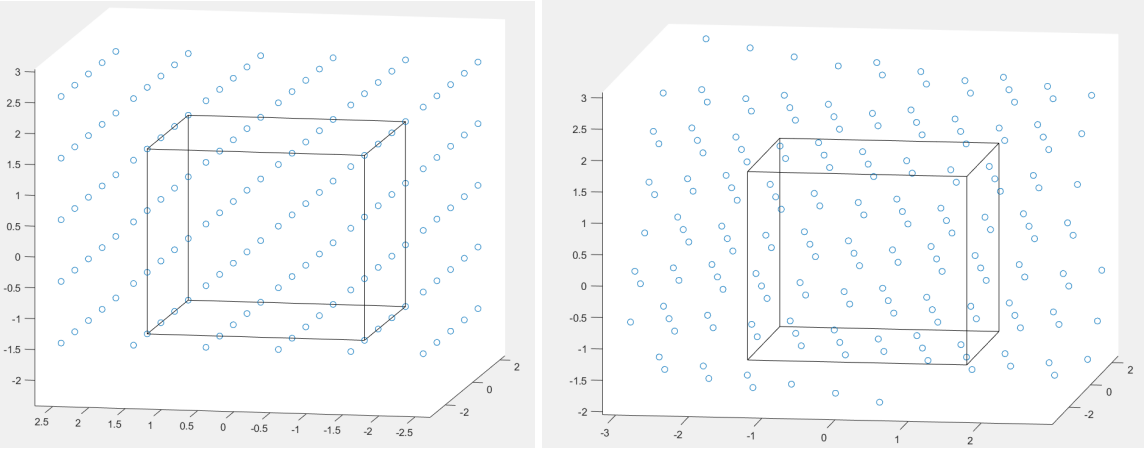

Figure 6.7: Cubic samples inside a cluster of inclusions for RC lattice where sample cube is aligned with direction (0,0,1) (left); and (1,1,1) (right).

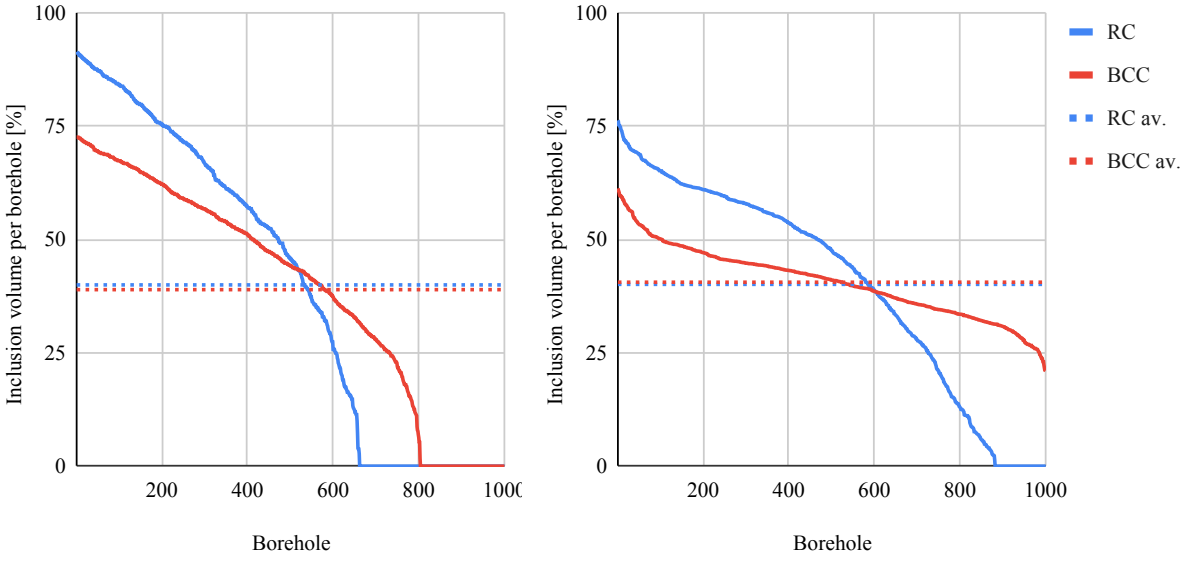

(a) (b)

Figure 6.8: Volume fraction of inclusions in each borehole, sorted in descending order. 1000 randomly distributed boreholes. RC and BCC lattices. Directions: (0,0,1) (a); and (1,1,1) (b).

As seen in figure 6.8, the (1,1,1) direction gives more uniformly distributed results for both layouts. Interestingly, for the BCC sample there are no “empty” boreholes at all, while the fraction of empty boreholes in the case of RC is smaller than for (0,0,1) "drilling" direction. This may explain why direction (0,0,1) remains stiffer than (1,1,1) for RC lattice when the voided material is concerned, and RC unit cell is, in general, responding in a stiffer way than BCC in such case. These outcomes are not clear when analysing the compacity index. The average volume fraction of inclusions achieved during the “drilling” along the (1,1,1) direction is higher for BCC, while along the (0,0,1) direction for RC, however, the difference is very small and rather insignificant to definitely answer the question which direction and for which cell should be stiffer. The results are presented in the table 6.2, along with the slope of the line of regression calculated in MS Excel for each layout.

Table 6.2: Results for different "drilling" scenarios.

lattice and direction	av. volume of inclusions	share of "empty" boreholes	regression line slope	R^2
RC (0.0.1)	0.3995	0.338	-0.00113	0.948
BCC (0.0.1)	0.389	0.196	-0.000813	0.952
RC (1.1.1)	0.4007	0.118	-0.000779	0.945
BCC (1.1.1)	0.4054	0	-0.000264	0.967

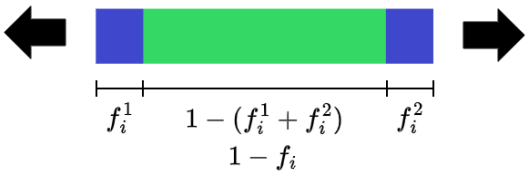

Figure 6.9: Single borehole as subjected to linear tension test.

As in the borehole approach no significant difference is visible in purely geometrical parameters, next step was to add some mechanical meaning to them. First, let us imagine each borehole as a sample of length L undergoing a linear tension test with a known external strain value $\bar{\varepsilon}$, as per figure 6.9. In this case, the macroscopic strain $\bar{\varepsilon}$ is equal to the weighted sum of strains in each phase ε_i,ε_m:

$$\bar{\varepsilon} = \varepsilon_i \frac{L_i}{L} + \varepsilon_m \frac{L_m}{L} \tag{6.2}$$

where weight can be identified as the volume fraction of phases encountered in each borehole:

$$\frac{L_i}{L} = f_i^{bore}, \quad \frac{L_m}{L} = (1 - f_i^{bore}) \tag{6.3}$$

Then the equation 6.2 can be written as:

$$\bar{\varepsilon} = \varepsilon_i f_i^{bore} + \varepsilon_m (1 - f_i^{bore}) \tag{6.4}$$

By replacing the strain by relation of stress σ to Young's moduli in each phase we obtain:

$$\frac{\bar{\sigma}}{\bar{E}} = \frac{\sigma_i}{E_i} f_i^{bore} + \frac{\sigma_m}{E_m} (1 - f_i^{bore}) \tag{6.5}$$

As the microstructure of the borehole can be treated as a laminate, the tensile stresses are the same in each phase ($\sigma_i = \sigma_m = \bar{\sigma}$):

$$\frac{1}{\bar{E}} = \frac{1}{E_i} f_i^{bore} + \frac{1}{E_m} (1 - f_i^{bore}) \tag{6.6}$$

Which finally gives following equation for the macroscopic elastic modulus (later called as "mechanical" elastic modulus):

$$\bar{E} = 1 / \left(\frac{1}{E_i} f_i^{bore} + \frac{1}{E_m} (1 - f_i^{bore}) \right) \tag{6.7}$$

Next, two simpler methods of calculating the macroscopic Young's modulus were added for comparison. First one, as a simple arithmetical weighted sum (later called as "arithmetical" elastic modulus) equivalent to so-called rule of mixtures (or equal strain assumption):

$$\bar{E} = E_i f_i^{bore} + (1 - f_i^{bore}) E_m \tag{6.8}$$

and second one, as a weighted geometric mean (later called as "logarithmic-geometric" elastic modulus):

$$\bar{E} = exp \left(\frac{ln(E_i) f_i^{bore} + ln(E_m)(1 - f_i^{bore})}{f_i^{bore} + (1 - f_i^{bore})} \right) \tag{6.9}$$

For all calculations, material parameters of phases are assumed as $E_i = 100MPa$ and $E_m = 10MPa$ which represents a case of hard inclusions in a soft matrix. The results have been shown on figures 6.10 - 6.11. As previously, no clear indication of opposite behaviour for RC and BCC lattice is visible on the graphs when comparing the lattices within one direction of loading.

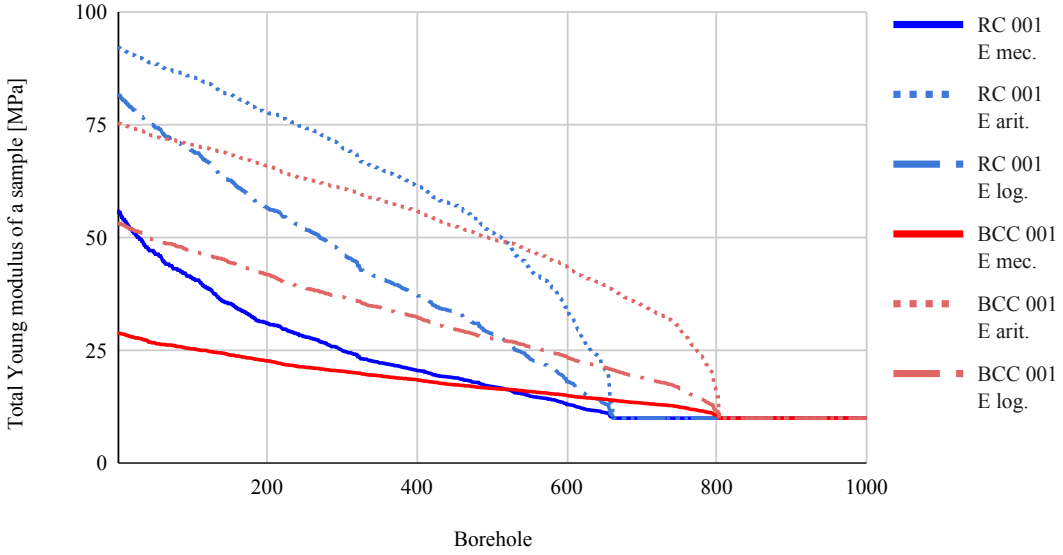

Figure 6.10: Macroscopic Young's moduli for each borehole. Sorted in descending order for 1000 randomly distributed boreholes. RC and BCC lattices, (0,0,1) direction.

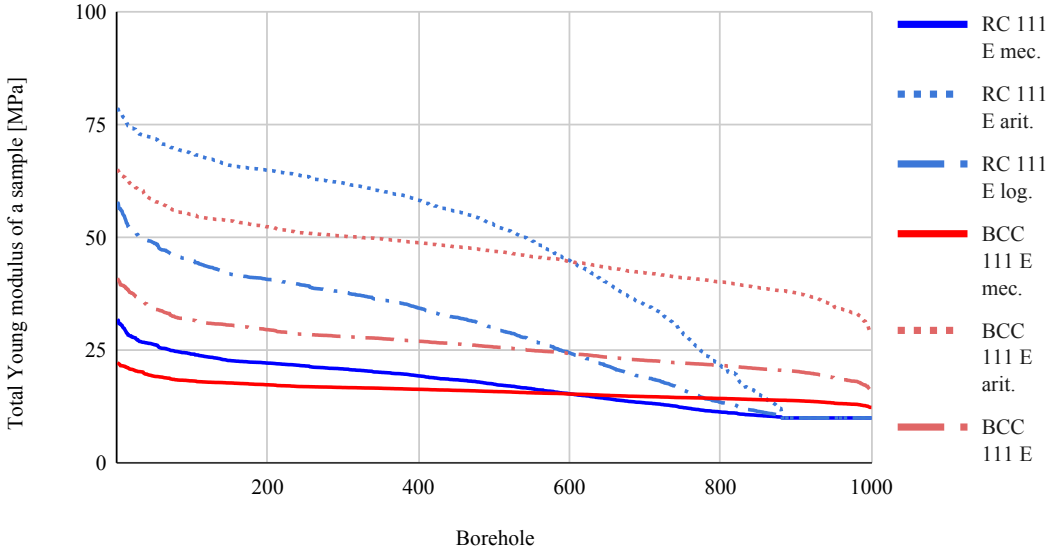

Figure 6.11: Macroscopic Young's moduli for each borehole. Sorted in descending order for 1000 randomly distributed boreholes. RC and BCC lattices, (1,1,1) direction.

Lastly, all original results are plotted in one graph (figure 6.12), to compare results within each lattice separately. In this case, there is an interesting outcome. While the "stiffer" cases (RC 0,0,1 and BCC 1,1,1) are far apart from each other, the "weaker" (RC 1,1,1 and BCC 0,0,1) ones seem to be well-aligned. To better illustrate this, the previously-calculated average Young moduli are plotted for the "weaker" cases which also shows a good alignment between these two ones (figure 6.13).

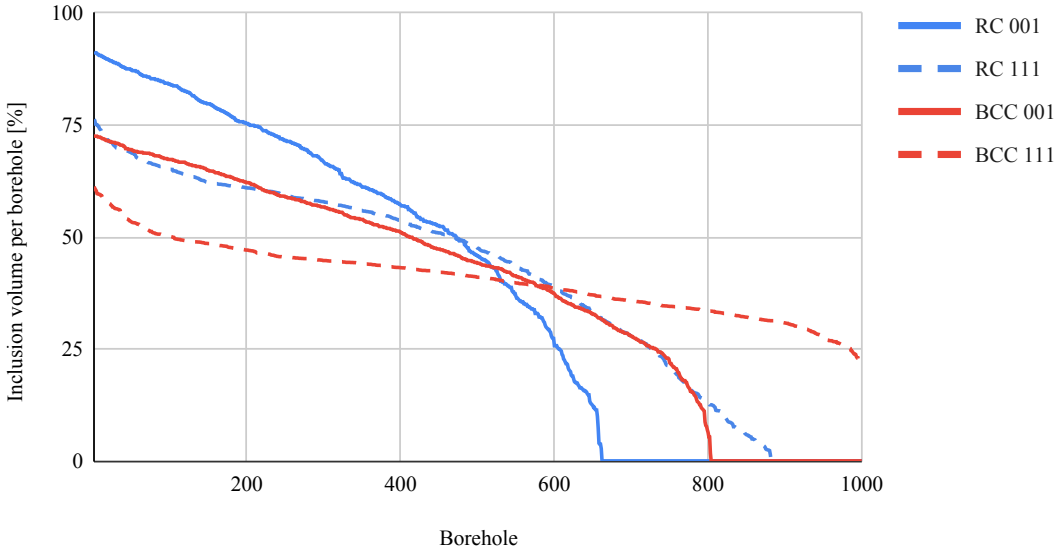

Figure 6.12: Volume fraction of inclusions in each borehole. Sorted in descending order for 1000 randomly distributed boreholes. RC and BCC lattices, (0,0,1) and (1,1,1) directions.

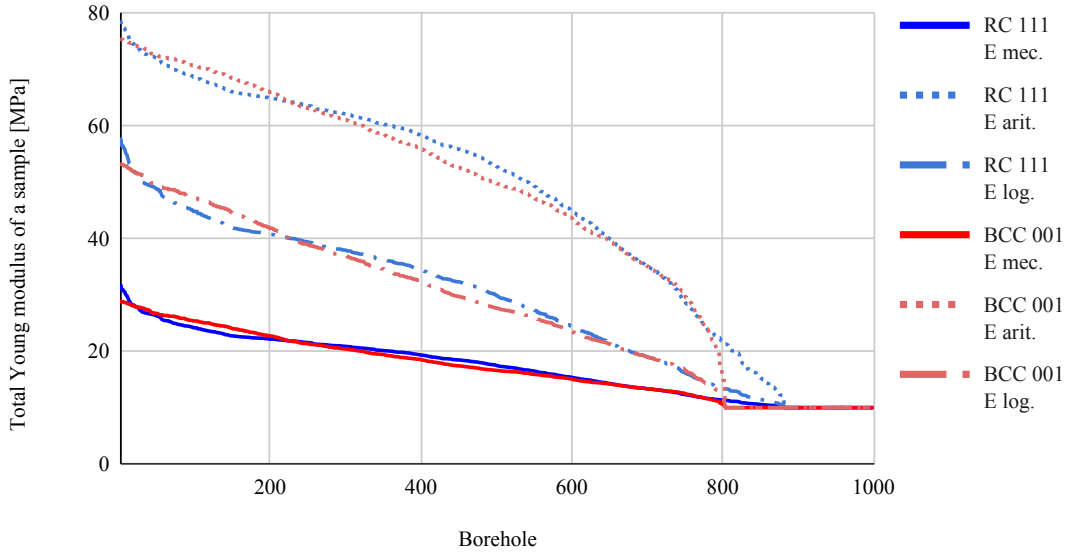

Figure 6.13: Macroscopic Young's moduli for each borehole. Sorted in descending order for 1000 randomly distributed boreholes. RC (1,1,1) and (BCC 0,0,1) (i.e. "weaker" cases).

In conclusion, when analysing the samples from the geometrical point of view, significant differences between regular cubic and body-centred cubic lattices are observed. The directional compacity index for RC lattice is bigger for the (0,0,1) direction, while for BCC it is the (1,1,1) direction. This might explain the "opposite" outcomes observed in the analysis in previous chapters, as higher value of directional compacity index corresponds with stiffer macroscopic response of the composite. Moreover, the RC lattice gives much more anisotropic response and the results are more dependent on the direction of load than for the BCC lattice. The latter produces more uniform results.

When comparing both lattices using the "borehole" method, similar results are observed. The RC lattice is more anisotropic and less uniform than the BCC one. Although, there is no visible indication of "opposite" behaviour of two lattices when the responses for two loading directions are concerned.

The distributions of boreholes for "weaker" cases, i.e. RC (1,1,1) and BCC (0,0,1), qualitatively and quantitatively give very similar results for both lattices. However, the "stiffer" cases, i.e. RC (0,0,1) and BCC (1,1,1), give results far apart from each other. The RC samples show a bigger number of "empty" boreholes, i.e. lines that pass only through the matrix. Within each sample the diagonal direction (1,1,1) gives more uniform distribution of results for both lattices.

6.3 Possible instabilities in samples with voids

This thesis concentrated mostly on scenarios with hard inclusions embedded in a soft matrix, as such scenarios seemed to be more difficult ones in terms of the capacity of the cluster model. The opposite cases, i.e. soft inclusions in a hard matrix, or even porous materials - also prevalent in the field of micromechanics - are also possible to analyse with use of the cluster model. However, as it is a mean-field model, it lacks the ability to predict what happens on the sub-local levels, e.g. if certain parts of the matrix are under tension or compression. This poses a question of other possible failure scenarios in this sub-local level, like buckling. In porous materials with a high volume fraction of voids, the matrix might locally become thin and slender and have no neighbouring inclusions that could support these parts of the sample. This means that even if calculations show that the analysed porous sample can withstand the imposed load, in reality the buckling at microscopic level might occur and lead to the unpredicted failure. Thus, this subsection presents simplified analysis of the critical load with respect to this phenomena.

As previously, regular cubic (RC) and body-centred cubic (BCC) lattices are considered. The identified "weakest" spot, that might be under the risk of buckling, is the thin ligament of material between the voids. It is different for RC and BCC lattices. For the RC lattice, the shortest distance between centres of voids is along the (1,0,0) direction, while in the BCC it is along the (1,1,1) direction, as seen in figure 6.2. This means that different load conditions are critical depending on the given microstructure of the sample and failure might occur in different points within the matrix, as shown in figure 6.14.

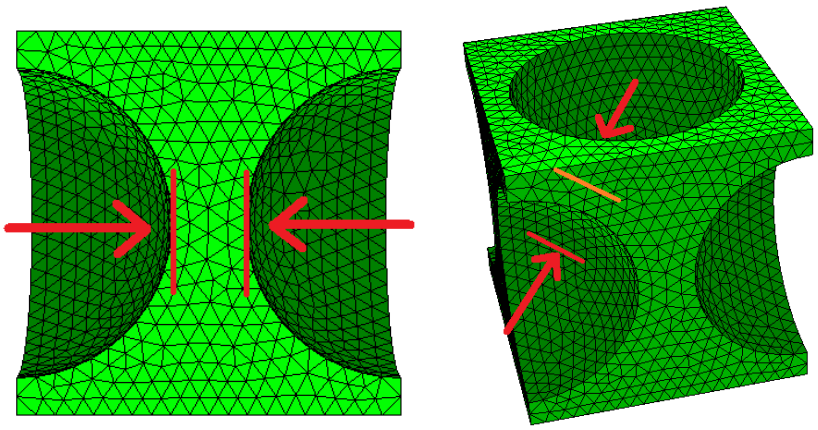

Figure 6.14: Possible weakest spots in the microstructure of regular cubic (left); and body-centred cubic (right) lattice.

Let us imagine a virtual column located between two voids, as in the figure 6.15. The distance between centres of the voids is equal to a. For sake of simplicity, it is assumed that the column has a constant cross-section, with its thickness equal to the thinnest part of the matrix material b. The cross-section might be assumed as a square or a circle. The trickiest part is how to define the unsupported length of the column, as well as its static scheme. Here, the unsupported length is assumed as the void diameter equal to $2r$, and its cross-section as a circle - both of which are simpler and safer assumptions. The column would be treated as a beam fixed on both ends, which translates to column effective length factor $\mu = 1/2$.

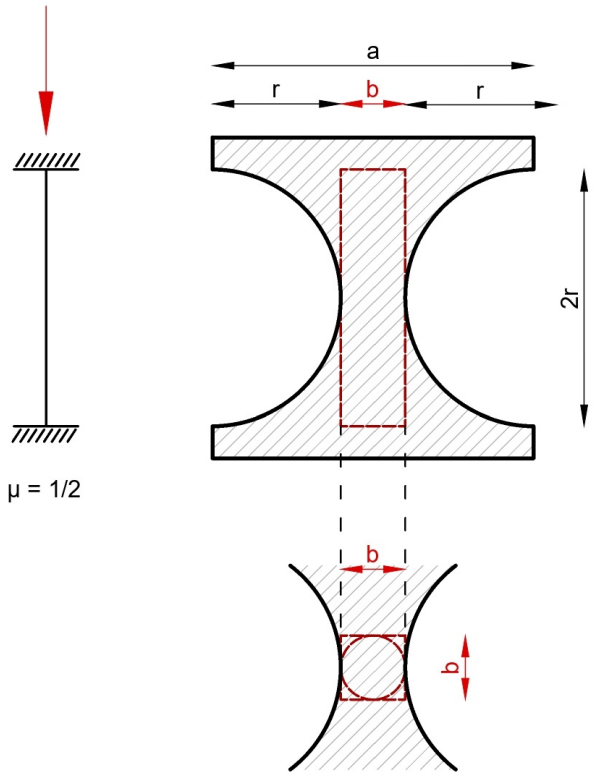

Figure 6.15: Cross-section through a sample: matrix with spherical voids.

In the literature of civil engineering, it is most often assumed that the critical compressive force (and thus, critical the compressive stress) acting on a column is given by the Euler's formula:

$$N_{cr} = \frac{\pi^2 EI}{\mu L} \tag{6.10}$$

$$\sigma_{cr} = \frac{N_{cr}}{A} \tag{6.11}$$

where N_{cr} is critical compressing force; σ_{cr} is critical compressing stress; E is Young's modulus; I is area moment of inertia of the cross section of the column; μ is column effective length factor; L is unsupported length of the column; and A is area of the cross-section of the column. The critical compressive stress for different volume fraction of inclusions f_i is calculated for both RC and BCC lattice. The results are shown in figure 6.16a. Additionally, the slenderness ratio is also often used when verifying whether a column is prone to buckling. This is given by the following formula:

$$S = \frac{\mu L}{i_{min}} \tag{6.12}$$

where S is the slenderness ratio; and i_{min} is smallest radius of gyration of the cross-section. As the cross-section of the column is assumed as circular, the radius of gyration is the same in each direction and is equal to $i_{min} = b/4$. The slenderness ratio for different volume fraction of inclusions f is calculated for both RC and BCC lattice. Distance between centres of closest inclusions is set to $a = 1.000m$ for the RC lattice and $a = 0.867m$ for the BCC lattice. The results are shown in figure 6.16b.

In the previous chapters, the volume fraction inclusions of $f_i = 40\%$ was identified as the reliability limit for the cluster model. For this value, the slenderness is equal to $S = 21.3$ for the RC and $S = 10.3$ for the BCC lattice, while the critical stress is equal to $\sigma_{cr} = 485$ MPa and $\sigma_{cr} = 2060$ MPa respectively. The obtained values of the critical stress are higher than the yield strength of materials considered in the present thesis. Thus, it is safe to assume that for samples with volume fraction of

inclusions up to $f_i = 40\%$, the buckling will not be the type of failure to occur first and the cluster model can be reliably used for mechanical calculations of porous materials.

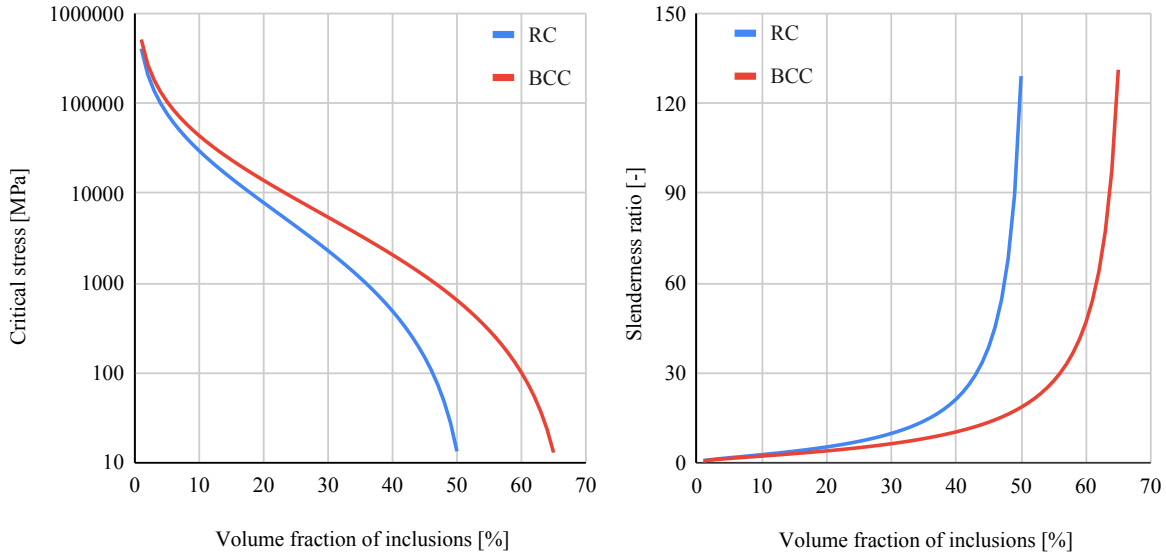

(a) (b)

Figure 6.16: Critical stress (a); and slenderness (b). RC (blue) and BCC (red) lattices.

6.4 Summary

Two additional topics related to the geometry of samples were examined: finding a proper geometry-based indicator which could explain differences in mechanical response observed for RC and BCC lattices loaded in different directions, as well as risk of possible geometrical instabilities of matrix in porous materials.

Regular cubic (RC) and body-centred cubic (BCC) lattices were compared, concentrating on their geometrical features using directional compacity index (Kowalczyk-Gajewska et al., 2021) and the newly proposed "borehole" method. Significant differences between the two lattices are observed. The directional compacity index for RC lattice is bigger for the (0,0,1) direction, while for BCC it is the (1,1,1) direction. This might explain the "opposite" outcomes observed in the analyses in previous chapters, as higher value of directional compacity index corresponds with stiffer macroscopic response of the composite. Moreover, the RC lattice gives much more anisotropic response and the results are more dependent on the direction of load than for the BCC lattice. The latter produces more uniform results. When comparing both lattices with the "borehole" method, similar results are observed. The RC lattice is more anisotropic and less uniform than the BCC one. Although, the method does not provide clear indication for an "opposite" response of both lattices when considering two loading directions.

Analysis of instabilities explores other possible failure scenarios in sub-local level, like buckling. In porous materials with a high volume fraction of voids, the matrix might locally become thin and slender, while having no neighbouring inclusions that could support these parts of the material. The identified "weakest" spot, that might be under the risk of buckling, was the thin part of material between voids that, for purposes of calculations, was simplified to a column. Analyses concentrated on critical compressive force (and thus, the critical compressive stress) given by the Euler's formula. For volume fractions of voids not exceeding $f_i = 40\%$ (which was previously identified as the applicability limit of the cluster model), the obtained values of the critical stress were higher than the yield strength of materials considered in the present thesis. Thus, it was assumed that for samples with volume fraction of inclusions up to $f_i = 40\%$, the buckling will not be the type of failure to occur first and the cluster model can be reliably used for mechanical calculations of porous materials.

Chapter 7

Summary

The thesis has been focused on understanding the relation between microstructure morphological features, in particular, space distribution of phases and anisotropy of macroscopic properties of heterogeneous materials. The main tool used for this purpose was a mean-field cluster model, originally proposed by Molinari & El Mouden (1996) for thermoelastic composite materials. The main goal of the present thesis was: (i) to extend and provide numerical verification of this semi-analytical mean-field scheme in the non-linear regime of material response (elasto-plasticity and elasto-viscoplasticity); and (ii) to formulate computationally efficient procedures for applying this model in finding the optimal microstructure of the composite at the preliminary stage of material design process.

The thesis has been divided into several chapters. Chapter 1 provided the introduction to the topic of composite material analyses, explaining the motivation, goals and the literature review. Chapter 2 explained the principles of the cluster model, its theory, application procedure and explored its behaviour. Chapter 3 focused on the verification of the cluster model in case of thermoelastic properties with main tool used for this purpose being the finite elements method. However, a set of 3D-printed porous samples were also employed for a limited experimental validation. Multi-criteria optimisation procedures were proposed for composites working in the elastic regime. Chapter 4 provided the extension of the cluster model to elasto-plasticity, with necessary steps such as: linearisation, uniformisation and isotropisation with so-called "second stress moments" introduced to tackle the issues with proper prediction of stresses in pure hydrostatic cases. Results were compared with the finite elements method. Additionally, multi-criteria optimisation procedures were proposed for composites working in the elastic-plastic regime. Chapter 5 provided the extension of the cluster model to elasto-viscoplasticity, with focus on the choice of the isotropisation method and its influence on the results which were compared with the outcomes of the FE analyses. Chapter 6 included a supplementary study on geometric traits of the most prevalent regular microstructures.

The key novel contributions of the thesis are as follows:

1. formulating computationally effective procedures of finding the fourth-order interaction tensor describing the impact of microstructure morphology in the mean-field cluster model for the elastic range, in particular, deriving the closed form formulas for the components of this tensor for the most often used regular inclusion arrangements (RC, BCC, FCC).
2. Numerical verification of the cluster model for linear thermoelastic materials, performed by finite element analyses of unit cells. The analyses indicated the limitations of the model for both scenarios of hard or soft inhomogeneities. The applicability range was identified as volume fractions of inclusions/voids up to 40%. The preliminary experimental verification of the model using the 3D printed voided samples was performed with designed layout of spherical voids.
3. Extension of the scheme to non-linear elastic-plastic range of material response, which included three additional steps: linearisation, uniformisation and isotropisation and its numerical verification. As the best solution the modified tangent linearisation of incremental elastic-plastic law of the matrix was prosed, where the tangent matrix moduli were calculated by means of stress fluctuations, assessed by the so-called second stress moments. The proposal provided reliable results for both deviatoric and hydrostatic loading conditions. Specifically, strongly non-linear response seen in the full-field calculations for voided materials were well reproduced, contrary to standard formulation employing only mean stress (so-called first moments).

4. Extension of the scheme to the non-linear elastic-viscoplastic material response, which was done employing the additive tangent interaction law, following Kowalczyk-Gajewska et al. (2021). In that paper the verification of the proposal was performed only for linear viscosity, while in the thesis the non-linear Perzyna-type law for viscous part was analysed. General isotropisation strategies for the viscous compliance tensor were formulated, which employed isotropisation weight factor to find the isotropic viscous shear modulus approximation as a weighted sum of anisotropic moduli. The optimal choice for this factor has been looked for by comparing the mean-field model results with the full-field FE analyses outcomes.
5. Formulation of the microstructure optimisation procedures which use the cluster model estimates of overall material properties, resulting in time-efficient algorithms for finding the optimal microstructure, volume fraction of inclusions or material composition of a composite material.
6. A new geometrical morphology indicator was proposed, based on the concept of "boreholes", which appeared to be a good way to quantify heterogeneity-induced macroscopic materials anisotropy.

There are still areas where further research and fine-tuning of the cluster model is possible and future works may include:

1. exploration of computational effectiveness and numerical verification of a multi-family variant of the cluster scheme, for both linear and non-linear material response;
2. incorporating the stress fluctuation into the extension of the cluster model to elastic-viscoplastic materials;
3. deepened experimental validation of the developed model employing 3D printed samples produced by more accurate printing techniques, as well as use of metallic materials and techniques enabling production of two-phase materials.

Bibliography

Abdul-Latif, A., Dingli, J., & Saanouni, K. (1998). Modeling of complex cyclic inelasticity in heterogeneous polycrystalline microstructure. *Mechanics of Materials*, *30*, 287–305. doi:https://doi.org/10.1016/S0167-6636(98)00054-4.

Abdul-Latif, A., Miad, A.-E., Baleh, R., & Garmestani, H. (2018). Modeling the mechanical behavior of heterogeneous ultrafine grained polycrystalline and nanocrystalline fcc metals. *Mechanics of Materials*, *126*, 1–12. doi:https://doi.org/10.1016/j.mechmat.2018.07.002.

Al-Maharma, A., Patil, S., & Markert, B. (2020). Effects of porosity on the mechanical properties of additively manufactured components: a critical review. *Materials Research Express*, *7*. doi:https://doi.org/10.1088/2053-1591/abcc5d.

Ashby, M. F. (2011). *Materials Selection in Mechanical Design (Fourth Edition*. Butterworth-Heinemann. doi:https://doi.org/10.1016/C2009-0-25539-5.

Ashby, M. F., & Bréchet, Y. J. M. (2003). Designing hybrid materials. *Acta materialia*, *51*, 5801–5821. doi:https://doi.org/10.1016/S1359-6454(03)00441-5.

Berbenni, S. (2021). A time-incremental homogenization method for elasto-viscoplastic particulate composites based on a modified secant formulation. *International Journal of Solids and Structures*, *229*, 111136. doi:https://doi.org/10.1016/j.ijsolstr.2021.111136.

Berveiller, M., Fassi-Fehri, O., & Hihi, A. (1987). The problem of two plastic and heterogeneous inclusions in an anisotropic medium. *International Journal of Engineering Science*, *25*, 691–709. doi:https://doi.org/10.1016/0020-7225(87)90058-9.

Bieniek, K., Majewski, M., Hołobut, P., & Kowalczyk-Gajewska, K. (2024). Anisotropic effect of regular particle distribution in elastic–plastic composites: The modified tangent cluster model and numerical homogenization. *International Journal of Engineering Science*, *203*. doi:https://doi.org/10.1016/j.ijengsci.2024.104118.

Bornert, M., Stolz, C., & Zaoui, A. (1996). Morphologically representative pattern-based bounding in elasticity. *Journal of the Mechanics and Physics of Solids*, *44*, 307–331. doi:https://doi.org/10.1016/0022-5096(95)00083-6.

Brenner, R., & Masson, R. (2005). Improved affine estimates for nonlinear viscoelastic composites. *European Journal of Mechanics - A/Solids*, *24*, 1002–1015. doi:https://doi.org/10.1016/j.euromechsol.2005.06.004.

Chaboche, J., Kanouté, P., & Roos, A. (2005). On the capabilities of mean-field approaches for the description of plasticity in metal matrix composites. *International Journal of Plasticity*, *21*, 1409–1434. doi:https://doi.org/10.1016/j.ijplas.2004.07.001.

Challis, V. J., Roberts, A. P., & Wilkins, A. H. (2008). Design of three dimensional isotropic microstructures for maximized stiffness and conductivity. *International Journal of Solids and Structures*, *45*, 4130–4146. doi:https://doi.org/10.1016/j.ijsolstr.2008.02.025.

Cohen, I. (2004). Simple algebraic approximations for the effective elastic moduli of cubic arrays of spheres. *Journal of the Mechanics and Physics of Solids*, *52*, 2167–2183. doi:https://doi.org/10.1016/j.jmps.2004.02.008.

Courant, R. (1943). Variational methods for the solution of problems of equilibrium and vibration. *Bulletin of the American Mathematical Society*, *49*, 1–23.

Czarnota, C., Kowalczyk-Gajewska, K., Salahouelhadj, A., Martiny, M., & Mercier, S. (2015). Modeling of the cyclic behavior of elastic–viscoplastic composites by the additive tangent Mori–Tanaka approach and validation by finite element calculations. *Int. J. Solids Struct.*, *56–57*, 96–117.

Dizon, J., Espera Jr, A., Chen, Q., & Advincula, R. (2018). Mechanical characterization of 3d-printed polymers. *Additive Manufacturing*, *20*, 44–67. doi:https://doi.org/10.1016/j.addma.2017.12.002.

Doghri, I., Brassart, L., Adam, L., & Gérard, J.-S. (2011). A second-moment incremental formulation for the mean-field homogenization of elasto-plastic composites. *International Journal of Plasticity*, *27*, 352–371. doi:https://doi.org/10.1016/j.ijplas.2010.06.004.

Doghri, I., & Friebel, C. (2005). Effective elasto-plastic properties of inclusion-reinforced composites. study of shape, orientation and cyclic response. *Mechanics of Materials*, *37*, 45–68. doi:https://doi.org/10.1016/j.mechmat.2003.12.007.

El Ghezal, M., & Doghri, I. (2018). Porous plasticity: Predictive second moment homogenization models coupled with gurson's single cavity stress-strain solution. *International Journal of Plasticity*, *108*, 201–221. doi:https://doi.org/10.1016/j.ijplas.2018.05.006.

El Mouden, M., & Molinari, A. (2000). Thermoelastic properties of composites containing ellipsoidal inhomogeneities. *Journal of Thermal Stresses*, *23*, 233–255. doi:10.1080/014957300280425.

Eshelby, J. D. (1957). The determination of the elastic field of an ellipsoidal inclusion, and related problems. *Proc. Royal Society A*, *241*, 376–396. doi:10.1098/rspa.1957.0133.

Fullwood, D., Niezgoda, S., Adams, B., & Kalidindi, S. (2010). Microstructure sensitive design for performance optimization. *Progress in Materials Science*, *21*, 477–562. doi:https://doi.org/10.1016/j.pmatsci.2009.08.002.

Girard, G., Frydrych, K., & Kowalczyk-Gajewska, K. (2021). Cyclic response of electrodeposited copper films. experiments and elastic–viscoplastic mean-field modeling. *Mechanics of Materials*, *153*. doi:https://doi.org/10.1016/j.mechmat.2020.103685.

González, C., Segurado, J., & LLorca, J. (2004). Numerical simulation of elasto-plastic deformation of composites: evolution of stress microfields and implications for homogenization models. *Journal of the Mechanics and Physics of Solids*, *52*, 1573–1593. doi:https://doi.org/10.1016/j.jmps.2004.01.002.

Hashin, Z. (1969). The inelastic inclusion problem. *Int. J. Engng Sci.*, *7*, 11–36.

Hashin, Z. (1983). Analysis of composite materials - a survey. *J. Appl. Mech.*, *50*, 481–505. doi:https://doi.org/10.1115/1.3167081.

Hill, R. (1965). Continuum micro-mechanics of elastoplastic polycrystals. *Journal of the Mechanics and Physics of Solids*, *13*, 89–101. doi:10.1016/0022-5096(65)90023-2.

Hill, R. (1967). The essential structure of constitutive laws for metal composites and polycrystals. *Journal of the Mechanics and Physics of Solids*, *15*, 79–95. doi:https://doi.org/10.1016/0022-5096(67)90018-X.

Hori, M., & Nemat-Nasser, S. (1993). Double-inclusion model and overall moduli of multi-phase composites. *Mechanics of Materials*, *14*, 189–206. doi:https://doi.org/10.1016/0167-6636(93)90066-Z.

Hu, G., & Weng, G. (2000). The connections between the double-inclusion model and the ponte castaneda–willis, mori–tanaka, and kuster–toksoz models. *Mechanics of Materials*, *32*, 495–503. doi:https://doi.org/10.1016/S0167-6636(00)00015-6.

Kanaun, S., & Levin, V. (2008). *Self-Consistent Methods for Composites, Vol. 1: Static Problems*. Springer. doi:https://doi.org/10.1007/978-1-4020-6664-1.

Kouddane, R., Molinari, A., & Canova, G. (1993). Proceedings of the international seminar mecamat 91 fontainebleau/france, . (pp. 129–141).

Kouznetsova, V., Brekelmans, W., & Baaijens, F. (2001). An approach to micro-macro modeling of heterogeneous materials. *Computational Mechanics*, *27*, 37–48. doi:https://doi.org/10.1007/s004660000212.

Kowalczyk-Gajewska, K., Maj, M., Bieniek, K., Majewski, M., Opiela, K. C., & Zieliński, T. G. (2024). Cubic elasticity of porous materials produced by additive manufacturing: experimental analyses, numerical and mean-field modelling. *Archives of Civil and Mechanical Engineering*, *24*. doi:10.1007/s43452-023-00843-z.

Kowalczyk-Gajewska, K., Majewski, M., Mercier, S., & Molinari, A. (2021). Mean field interaction model accounting for the spatial distribution of inclusions in elastic-viscoplastic composites. *Int. J. Solids Struct.*, *224*, 111040. doi:https://doi.org/10.1016/j.ijsolstr.2021.111040.

Kowalczyk-Gajewska, K., & Petryk, H. (2011). Sequential linearization method for viscous/elastic heterogeneous materials. *European Journal of Mechanics - A/Solids*, *30*, 650–664. doi:https://doi.org/10.1016/j.euromechsol.2011.04.002.

de Kruijf, N., Zhou, S., Li, Q., & Mai, Y. (2007). Topological design of structures and composite materials with multiobjectives. *International Journal of Solids and Structures*, *44*, 7092–7109. doi:https://doi.org/10.1016/j.ijsolstr.2007.03.028.

Kröner, E. (1961). Zur plastischen verformung des vielkristalls. *Acta Metallurgica*, *9*, 155–161. doi:https://doi.org/10.1016/0001-6160(61)90060-8.

Kursa, M., Kowalczyk-Gajewska, K., Lewandowski, M., & Petryk, H. (2018). Elastic-plastic properties of metal matrix composites: Validation of mean-field approaches. *European Journal of Mechanics - A/Solids*, *68*, 53 – 66. doi:https://doi.org/10.1016/j.euromechsol.2017.11.001.

Kursa, M., Kowalczyk-Gajewska, K., & Petryk, H. (2014). Multi-objective optimization of thermo-mechanical properties of metal–ceramic composites. *Composites Part B: Engineering*, *60*, 586–596. doi:https://doi.org/10.1016/j.compositesb.2014.01.009.

Kushch, V. (1997). Microstresses and effective elastic moduli of a solid reinforced by periodically distributed spheroidal particles. *International Journal of Solids and Structures*, *34*, 1353–1366. doi:https://doi.org/10.1016/S0020-7683(96)00078-9.

Kushch, V., Mogilevskaya, S., Stolarski, H., & Crouch, S. (2011). Elastic interaction of spherical nanoinhomogeneities with gurtin–murdoch type interfaces. *Journal of the Mechanics and Physics of Solids*, *59*, 1702–1716. doi:https://doi.org/10.1016/j.jmps.2011.06.004.

Lahellec, N., & Suquet, P. (2007). On the effective behavior of nonlinear inelastic composites: I. Incremental variational principles. *J. Mech. Phys. Solids*, *55*, 1932–1963.

Lahellec, N., & Suquet, P. (2013). Effective response and field statistics in elasto-plastic and elasto-viscoplastic composites under radial and non-radial loadings. *International Journal of Plasticity*, *42*, 1–30. doi:https://doi.org/10.1016/j.ijplas.2012.09.005.

Li, D., & Hu, G. (2007). Effective viscoelastic behavior of particulate polymer composites at finite concentration. *Applied Mathematics and Mechanics*, *28*, 297–307. doi:https://doi.org/10.1007/s10483-007-0303-1.

Lu, & Shih-Yuan (1999). Effective conductivities of rectangular arrays of aligned spheroids. *Journal of Applied Physics*, *85*, 264–269. doi:10.1063/1.369439.

Lucchetta, A., Auslender, F., Bornert, M., & Kondo, D. (2021). Incremental variational homogenization of elastoplastic composites with isotropic and armstrong-frederick type nonlinear kinematic hardening. *International Journal of Solids and Structures*, *222-223*, 111000. doi:https://doi.org/10.1016/j.ijsolstr.2021.02.011.

Majewski, M. (2019). Representation of morphological characteristics of microstructure in micromechanical models of composite materials (pol.: Reprezentacja cech morfologicznych mikrostruktury w mikromechanicznych modelach materiałów kompozytowych), phd thesis. URL: `https://www.ippt.pan.pl/repository/doktoraty/open/2017majewski_m_doktorat.pdf`.

Majewski, M., Holobut, P., Kursa, M., & Kowalczyk-Gajewska, K. (2020). Packing and size effects in elastic-plastic particulate composites: Micromechanical modelling and numerical verification. *International Journal of Engineering Science*, *151*, 103271. doi:https://doi.org/10.1016/j.ijengsci.2020.103271.

Majewski, M., Kursa, M., Holobut, P., & Kowalczyk-Gajewska, K. (2017). Micromechanical and numerical analysis of packing and size effects in elastic particulate composites. *Composites: Part B*, *124*, 158–174. doi:https://doi.org/10.1016/j.compositesb.2017.05.004.

Mao, H., Rumpler, R., Gaborit, M., Göransson, P., Kennedy, J., O'Connor, D., Trimble, D., & Rice, H. (2020). Twist, tilt and stretch: from isometric kelvin cells to anisotropic cellular materials. *Materials Design*, *193*. doi:https://doi.org/10.1016/j.matdes.2020.108855.

Mao, H., Rumpler, R., & Göransson, P. (2021). A note on the linear deformations close to the boundaries of a cellular material. *Mechanics Research Communications*, *111*. doi:https://doi.org/10.1016/j.mechrescom.2021.103657.

Marcadon, V., Herve, E., & Zaoui, A. (2007). Micromechanical modeling of packing and size effects in particulate composites. *International Journal of Solids and Structures*, *44*, 8213–8228. doi:https://doi.org/10.1016/j.ijsolstr.2007.06.008.

Masson, R., Bornert, M., Suquet, P., & Zaoui, A. (2000). An affine formulation for the prediction of the effective properties of nonlinear composites and polycrystals. *Journal of the Mechanics and Physics of Solids*, *48*, 1203–1227. doi:https://doi.org/10.1016/S0022-5096(99)00071-X.

McPhedran, R., & McKenzie, D. (1978). The conductivity of lattice of spheres I. The simple cubic lattice. *Proceedings of the Royal Society London A*, *359*, 45–63. doi:https://doi.org/10.1098/rspa.1978.0031.

McPhedran, R., McKenzie, D., & Derrick, G. H. (1978). The conductivity of lattice of spheres II. The body centred and face centred cubic lattices. *Proc. R. Soc. Lond.*, *362*, 211–232. doi:https://doi.org/10.1098/rspa.1978.0129.

Mercier, S., Jacques, N., & Molinari, A. (2005). Validation of an interaction law for the Eshelby inclusion problem in elasto-viscoplasticity. *Int. J. Solids and Struct.*, *42*, 1923–1941.

Mercier, S., Kowalczyk-Gajewska, K., & Czarnota, C. (2019). Effective behavior of composites with combined kinematic and isotropic hardening based on additive tangent mori–tanaka scheme. *Composites Part B: Engineering*, *174*. doi:https://doi.org/10.1016/j.compositesb.2019.107052.

Mercier, S., & Molinari, A. (2009). Homogenization of elastic–viscoplastic heterogeneous materials: Self-consistent and mori-tanaka schemes. *International Journal of Plasticity*, *25*, 1024–1048. doi:https://doi.org/10.1016/j.ijplas.2008.08.006.

Mercier, S., Molinari, A., Berbenni, S., & Berveiller, M. (2012). Comparison of different homogenization approaches for elastic–viscoplastic materials. *Modelling and Simulation in Materials Science and Engineering*, *20*. doi:https://doi.org/10.1088/0965-0393/20/2/024004.

Mercier, S., Molinari, A., & El Mouden, M. (2000). Thermal conductivity of composite material with coated inclusions: Applications to tetragonal array of spheroids. *Journal of Applied Physics*, *87*, 3511–3519. doi:10.1063/1.372374.

Molinari, A. (2002). Averaging models for heterogeneous viscoplastic and elastic viscoplastic materials. *J. Eng. Mater. Technol., Transactions of the ASME*, *124*, 62–70. doi:https://doi.org/10.1115/1.1421052.

Molinari, A., Ahzi, S., & Kouddane, R. (1997). On the self-consistent modeling of elastic-plastic behavior of polycrystals. *Mech. Mater.*, *26*, 43–62.

Molinari, A., Canova, G., & Ahzi, S. (1987). A self consistent approach of the large deformation polycrystal viscoplasticity. *Acta Metallurgica*, *35*, 2983–2994. doi:https://doi.org/10.1016/0001-6160(87)90297-5.

Molinari, A., & El Mouden, M. (1996). The problem of elastic inclusions at finite concentration. *International Journal of Solids and Structures*, *33*, 3131–3150. doi:https://doi.org/10.1016/0020-7683(95)00275-8.

Moradi, M., Aminzadeh, A., Rahmatabadi, D., & Hakimi, A. (2021). Experimental investigation on mechanical characterization of 3d printed pla produced by fused deposition modeling (fdm). *Materials Research Express*, *8*. doi:https://doi.org/10.1088/2053-1591/abe8f3.

Mori, T., & Tanaka, K. (1973). Average stress in matrix and average elastic energy of materials with misfitting inclusions. *Acta Metall.*, *21*, 571–574.

Mueller, J., & Shea, K. (2018). Buckling, build orientation, and scaling effects in 3d printed lattices. *Materials Today. Communications.*, *17*, 69–75. doi:https://doi.org/10.1016/j.mtcomm.2018.08.013.

Muñoz-Morris, M. A., Calderon, N., Gutierrez-Urrutia, I., & Morris, D. G. (2006). Matrix grain refinement in al–tial composites by severe plastic deformation: Influence of particle size and processing route. *Materials Science and Engineering: A*, *425*, 131–137. doi:https://doi.org/10.1016/j.msea.2006.03.027.

Naili, C., & Doghri, I. (2023). Combined mean-field and full-field homogenization of porous elasto-plastic materials and composites under arbitrary stress triaxialities. *Mechanics of Materials*, *187*, 104818. doi:https://doi.org/10.1016/j.mechmat.2023.104818.

Nemat-Nasser, S., & Hori, M. (1999). *Micromechanics: overall properties of heterogeneous materials*. North-Holland Elsevier.

Nemat-Nasser, S., Iwakuma, T., & Hejazi, M. (1982). On composites with periodic structure. *Mechanics of Materials*, *1*, 239–267. doi:https://doi.org/10.1016/0167-6636(82)90017-5.

Nunan, K. C., & Keller, J. B. (1984). Effective elasticity tensor of a periodic composite. *Journal of the Mechanics and Physics of Solids*, *32*, 259–280. doi:https://doi.org/10.1016/0022-5096(84)90024-3.

Paulino, G. H., Silva, E. C. N., & Le, C. H. (2009). Optimal design of periodic functionally graded composites with prescribed properties. *Structural and Multidisciplinary Optimization*, *38*, 469–489. doi:https://doi.org/10.1007/s00158-008-0300-1.

Perzyna, P. (1986). Internal state variable description of dynamic fracture of ductile solids. *Int. J. Solids and Struct.*, *22*, 797–818.

Ponte Castañeda, P., & Willis, J. (1995). The effect of spatial distribution on the effective behavior of composite materials and cracked media. *Journal of the Mechanics and Physics of Solids*, *43*, 1919 – 1951.

Ponte Castañeda, P., & Suquet, P. (1997). Nonlinear composites. *Advances in Applied Mechanics*, *34*, 171–302. doi:https://doi.org/10.1016/S0065-2156(08)70321-1.

Rayleigh, L. (1892). LVI. On the influence of obstacles arranged in rectangular order upon the properties of a medium. *The London, Edinburgh, and Dublin Philosophical Magazine and Journal of Science*, *34*, 481–502. doi:10.1080/14786449208620364.

Rodin, G. J. (1993). The overall elastic response of materials containing spherical inhomogeneities. *International Journal of Solids and Structures*, *30*, 1849–1863. doi:https://doi.org/10.1016/0020-7683(93)90221-R.

Sadowski, P., Kowalczyk-Gajewska, K., & Stupkiewicz, S. (2017). Consistent treatment and automation of the incremental mori-tanaka scheme for elasto-plastic composites. *Computational Mechanics*, *60*, 493–511. doi:https://doi.org/10.1007/s00466-017-1418-z.

Sadowski, P., Kowalczyk-Gajewska, K., & Stupkiewicz, S. (2021). Spurious softening in the macroscopic response predicted by the additive tangent Mori–Tanaka scheme for elastic–viscoplastic composites. *European Journal of Mechanics - A/Solids*, *90*, 104339. doi:https://doi.org/10.1016/j.euromechsol.2021.104339.

Sangani, A., & Acrivos, A. (1982). The effective conductivity of a periodic array of spheres. *Proc. R. Soc. Lond.*, *386*, 263–275. doi:https://doi.org/10.1098/rspa.1983.0036.

Sangani, A. S., & Lu, W. (1987). Elastic coefficients of composites containing spherical inclusions in a periodic array. *Journal of the Mechanics and Physics of Solids*, *35*, 1–21. doi:https://doi.org/10.1016/0022-5096(87)90024-X.

Schjødt-Thomsen, J., & Pyrz, R. (2005). Cubic inclusion arrangement: Effects on stress and effective properties. *Computational Materials Science*, *34*, 129–139. doi:https://doi.org/10.1016/j.commatsci.2004.12.061.

Sevostianov, I. (2014). On the shape of effective inclusion in the maxwell homogenization scheme for anisotropic elastic composites. *Mechanics of Materials*, *75*, 45–59. doi:https://doi.org/10.1016/j.mechmat.2014.03.003.

Sevostianov, I., Mogilevskaya, S., & Kushch, V. (2019). Maxwell's methodology of estimating effective properties: Alive and well. *International Journal of Engineering Science*, *140*, 35–88. doi:https://doi.org/10.1016/j.ijengsci.2019.05.001.

Song, Z., Peng, X., Tang, S., & Fu, T. (2020). A homogenization scheme for elastoplastic composites using concept of mori-tanaka method and average deformation power rate density. *International Journal of Plasticity*, *128*, 102652. doi:https://doi.org/10.1016/j.ijplas.2019.102652.

Suquet, P. (1987). Elements of homogenization for inelastic solid mechanics. In *Homogenization techniques for Composite media* (pp. 193–278). E. Sanchez-Palencia and A. Zaoui (Eds), Springer Berlin. doi:https://doi.org/10.1007/3-540-17616-0_15.

Suquet, P. (1995). Overall properties of nonlinear composites: a modified secant moduli theory and its link with ponte Castañeda's nonlinear variational procedure. *Comptes Rendus de l'Académie des Sciences - Series IIB - Mechanics*, *320*, 563–571.

Suquet, P. (1997). *Effective Properties of Nonlinear Composites. In: Suquet P. (eds) Continuum Micromechanics.*. Vienna: International Centre for Mechanical Sciences (Courses and Lectures), vol 377. Springer. doi:https://doi.org/10.1007/978-3-7091-2662-2-4.

Tandon, G., & Weng, G. (1988). A Theory of Particle-Reinforced Plasticity. *Journal of Applied Mechanics*, *55*, 126–135. doi:10.1115/1.3173618.

Vilchevskaya, E., Kushch, V., Kachanov, M., & Sevostianov, I. (2021). Effective properties of periodic composites: Irrelevance of one particle homogenization techniques. *Mechanics of Materials*, *159*, 103918. doi:https://doi.org/10.1016/j.mechmat.2021.103918.

Wang, H., Wu, P., Tomé, C., & Huang, Y. (2010). A finite strain elastic-viscoplastic self-consistent model for polycrystalline materials. *Journal of the Mechanics and Physics of Solids*, *58*, 594–612. doi:https://doi.org/10.1016/j.jmps.2010.01.004.

Zecevic, M., & Lebensohn, R. (2020). New robust self-consistent homogenization schemes of elasto-viscoplastic polycrystals. *International Journal of Solids and Structures*, *202*, 434–453. doi:https://doi.org/10.1016/j.ijsolstr.2020.05.032.

Zhou, S., & Li, Q. (2008). Computational design of multi-phase microstructural materials for extremal conductivity. *Computational Materials Science*, *43*, 549–564. doi:https://doi.org/10.1016/j.commatsci.2007.12.021.

Zivelonghi, A., & You, J.-H. (2014). Mechanism of plastic damage and fracture of a particulate tungsten-reinforced copper composite: A microstructure-based finite element study. *Materials Science and Engineering: A*, *84*, 318–326. doi:https://doi.org/10.1016/j.commatsci.2013.11.067.

Zohdi, T., & Wriggers, P. (2004). *An Introduction to Computational Micromechanics*. Springer.